UNIVERSITY OF SOUTHAMPTON
FACULTY OF PHYSICAL SCIENCES AND ENGINEERING
Optoelectronics Research Centre

Doughnut-shaped beam generation in solid-state and fibre lasers

By

DI LIN

Thesis for the degree of Doctor of Philosophy

October 2015

UNIVERSITY OF SOUTHAMPTON

ABSTRACT

FACULTY OF PHYSCIAL SCIENCES AND ENGINEERING

OPTOELECTRONICS RESEARCH CENTRE

Doctor of Philosophy

DOUGHNUT-SHAPED BEAM GENERATION IN SOLID-STATE AND FIBRE LASERS

By Di Lin

This thesis focuses on developing new techniques for generating doughnut-shaped beams with a radial polarization state or a vortex phase front.

An all-fibre-based pump beam conditioning element based on a tapered capillary fibre has been developed to provide a ring-shaped pump beam for end-pumped solid-state lasers. This unique pumping scheme provides a simple, efficient and robust approach for generating the doughnut-shaped first higher-order Laguerre-Gaussian (LG_{01}) mode due to its optimized spatial overlap for the LG_{01} mode. However, the analysis of mode composition shows the doughnut-shaped LG_{01} mode is apt to be a 'hybrid' mode consisting of TEM_{01} modes with orthogonal orientations and LG_{01} modes with opposite handedness of helical phase front at axial modes with different frequencies. A novel mode selection element consisting of two nanoscale thickness aluminium strips has been developed by exploiting the fact that the standing wave intensity distribution for the LG_{01}^{+} and LG_{01}^{-} modes inside a laser resonator are different. This scheme has been demonstrated for the first time in a diode-pumped Nd:YAG laser to generate an LG_{01} mode with controllable handedness of helical phase front at output powers ~1 W. Using the ring-shaped pumping scheme, direct generation of a radially-polarized beam has been successfully demonstrated in a Nd:YAG laser by exploiting the fact that the radially-polarized and azimuthally-polarized beams have slightly different spatial overlaps with the ring-shaped pump beam due to bifocusing within the laser crystal, thus resulting in a different threshold for each mode.

The ring-shaped pumping scheme also provides flexibility in transverse mode selection and a significant reduction in adverse thermal lensing effects, offering the

prospect of power scalability in end-pumped lasers. 14 W of linearly-polarized TEM_{00} mode output with a beam quality factor (M^2) <1.1 and 16 W of linearly-polarized doughnut-shaped LG_{01} mode with M^2<2.2 were obtained in a Nd:YVO_4 laser with a slope efficiency of 53% and 55%, respectively. The results showed a reduction in thermal lens strength by approximately 30% compared with traditional fibre-coupled laser diode end pumping.

Furthermore, I have investigated extracavity conversion to radial polarization in both 1μm and 2μm regimes using continuously space-variant λ/4 or λ/2 waveplates (also called S-waveplates), fabricated by a recently developed femtosecond writing technique. In the one-micron wavelength regime, the λ/2 S-waveplate can transform a linearly polarized Gaussian beam into a radially polarized beam with a conversion efficiency of ~75% and M^2 of 2.7, whilst the λ/4 S-waveplate can transform a circularly polarized LG_{01} mode into radial polarization with a conversion efficiency of ~86% and M^2 of 2.9. The S-waveplate has a much better performance in longer wavelength regime due to reduced Rayleigh scattering. We demonstrate highly efficient conversion (~86%) to radial polarization in the 2μm band with wavelength tuning from 1950nm to 2100nm by using a 2μm λ/2 S-waveplate. The resulting radially polarized beam had a M^2 of 2.1 and a maximum polarization extinction ratio (PER) of 17.5dB at 2050nm with a variation of less than 3dB over the full wavelength range.

I finally exploited the λ/2 S-waveplate as an intracavity polarization-controlling element to directly excite radially-polarized TM_{01} mode operation in an Yb-doped fibre laser. The laser yielded ~32W of output power with a radially-polarized TM_{01} mode output beam at 1040nm with a slope efficiency of 66% and polarization purity of 95%. Moreover, I have demonstrated a simple technique for selectively generating the fundamental LP_{01} mode and the next higher order doughnut-shaped LP_{11} mode with a vortex phase front in an Yb-doped fibre laser. This approach exploits the difference in polarization behaviour of individual transverse modes due to transverse variation of birefringence in a few-moded fibre, allowing robust mode discrimination through the use of an appropriately aligned intracavity polarizing element. The laser yielded ~36W of output power for both transverse modes with slope efficiency of 74% and a mode purity of 95%.

Table of Contents

List of tables

List of figures

Declaration of authorship

I, Di Lin, declare that the thesis entitled "Doughnut-shaped beam generation in solid-state and fibre lasers" and the work presented in it are my own and has been generated by me as the result of my own original research. I confirm that:

1. This work was done wholly or mainly while in candidature for a research degree at this University;
2. Where any part of this thesis has previously been submitted for a degree or any other qualification at this University or any other institution, this has been clearly stated;
3. Where I have consulted the published work of others, this is always clearly attributed;
4. Where I have quoted from the work of others, the source is always given. With the exception of such quotations, this thesis is entirely my own work;
5. I have acknowledged all main sources of help;
6. Where the thesis is based on work done by myself jointly with others, I have made clear exactly what was done by others and what I have contributed myself;
7. Parts of this work have been published as the journal papers and conference contributions listed in Appendix.

Signed: .....

Date:.....

Acknowledgements

I would like to express my sincere gratitude to all those who have helped me over the past four years at the ORC. First, I am very grateful to my supervisor, Prof. Andy Clarkson for his insight, inspiration, and guidance for my research, while giving me freedom to pursue my own research interests and ideas. I am also grateful to all my close collaborators: Dr. Jae Daniel, Dr. Peter Shardlow, Dr. Alex Butler, Dr. Martynas Beresna, and Prof. Peter Kazansky. I would like to thank all other ASSL group members: Dr. Jacob Mackenzie, Dr. Rafal Cieslak, Dr. Masaki Tokurakawa, Dr. Matthew Eckold, Dr. Jakub Szela, Mr. Nikita Simakov, Mr. Stan Vassilev, Mr. Antonin Bilaud, Mr. Callum Smith, and Mr. Robin Uren for their kind help and discussions. Finally, I would like to thank my family: my parents, my parents in law, elder sister and my beloved wife for always encouraging, supporting and being with me.

Abbreviations

ASE	Amplified spontaneous emission
BG	Bessel Gaussian
BPP	Beam parameter product
CCD	Charge-coupled device
CV	Cylindrical vector
ETU	Energy transfer upconversion
FPI	Fabry-Perot interferometer
FWHM	Full width at half maximum
HG	Hermite-Gaussian
HR	High reflectivity
HWP	Half-wave plate
LG	Laguerre-Gaussian
MSE	Mode-selection element
NA	Numerical aperture
NPRO	Non-planar ring oscillator
OAM	Orbital angular momentum
PBS	Polarization beam splitter
PER	Polarization extinction ratio
PM	Polarization maintaining
SR	Strehl ratio
SVR	Spatially variant retardation

Chapter 1: Introduction

1.1 Overview

Lasers emitting coherent light at frequencies from ultraviolet to infrared regions have extensively contributed to our modern world since their invention by Schawlow and Townes in 1958 [1]. The unique properties characterised by high intensity, directionality and spectral purity have benefited an extraordinary variety of application areas including the manufacturing industry, optical communications, medicine, military defence and scientific research. Practical laser devices have been developed employing numerous gain materials, resonator configurations and pumping techniques. Among them, diode-pumped solid-state lasers and fibre lasers have attracted much attention.

End-pumped solid-state lasers have been widely applied in relatively low power regimes (less than a few watts) with advantages of flexibility and compactness in resonator design, ease with which excellent beam quality can be obtained, a diverse range of available operating wavelengths, and high efficiency achievable compared to side pumped geometries. The benefits of this technique have incubated many advanced solid-state laser systems ranging from compact monolithic lasers [2] to much more complicated ultra-fast laser devices [3]. However, the requirement for very small pump beam size comparable to laser beam size leads to extremely high thermal loading density within the laser gain medium. As a result, scaling the laser brightness has been hindered due to several deleterious thermal effects within laser crystals including highly aberrated thermal lensing, stress induced birefringence and ultimately catastrophic fracture of laser material [4]. Over the course of last few decades, many novel resonator configurations including side-pumped rod lasers [5], 'zig-zag' slab lasers [6] and thin disk lasers [7] have been developed to mitigate these adverse thermal effects and hence have successfully scaled the laser brightness to much higher levels (greater than a few hundred watts). These methods, however, significantly sacrifice the advantages of the end-pumped geometry. For many applications, end-pumped solid-state lasers which are capable of efficient power scaling and relative simplicity in laser design are preferred.

In addition to requirement for high power and high brightness, some other beam properties including the unique electric field structures, exotic polarization states, and special operating wavelengths may be able to benefit a number of applications as well. Laser beams with an azimuthal phase dependence of $exp(il\varphi)$ in electric field is an example of such a beam. In contrast to ordinary plane waves, this beam has a vortex (helical-structure) phase front that carries orbital angular momentum (OAM) of $l\hbar$ per photon, as recognized by Allen in 1992 [8]. These vortex beams are characterized by an intensity null at the beam centre due to a phase singularity and have proved to offer enormous benefits to a variety of fields ranging from optical manipulation of microscopic particles [9] to laser material processing [10], and from nonlinear and quantum optics to imaging [11] and optical communications [12, 13]. Perhaps, the most familiar optical vortex beam is the higher-order LG beam in free-space, which is difficult to obtain directly from laser devices. The main reason is that a laser cavity usually has rectangular(x, y) symmetry due to tilted surfaces of optical elements resulting in Hermit-Gaussian (HG) modes being excited. In addition, the fundamental Gaussian mode is generally preferentially excited due to best spatial overlap with the population inversion and the lowest intracavity round-trip loss, resulting in it having the lowest threshold. Formulation of a laser design strategy to directly generate a vortex beam inside a laser cavity with high efficiency is essential for the applications mentioned above.

Moreover, polarization is one of most essential properties of a laser beam. Conventional linear, circular and elliptical polarizations, which have a spatially uniform polarization state over the beam cross section, are the most familiar. The vector nature of a laser beam has been comprehensively exploited in numerous applications ranging from optical communications, optical data storage, optical metrology, optical display, biological science and material science. Recently, increasing attention has been paid to laser beams with space-variant polarization state distributions over the beam cross section. This new form of polarization state is expected to induce novel effects during laser-matter interactions that are able to benefit a large number of applications. Radially polarized and azimuthal polarized beams having cylindrical symmetry in polarization state are two particular examples. Specially designed polarization selective elements or particular resonator configurations are always required to generate these cylindrical vector (CV) beams in free space.

It is well known that some eigen modes in fibres also possess these unique polarization and phase properties. For example, the TM_{01} mode has a radial polarization, while TE_{01} mode has an azimuthal polarization. Particular coherent superpositions of higher-order modes in fibres are able to form optical vortex beams as well. Therefore, optical fibres are expected to offer an alternative route to efficiently generate these exotic beams. Fibre laser configurations have already proved to be a robust architecture for scaling output power to very high average power due to excellent heat dissipation properties and thermal loading per unit length resulting from the very large ratio of surface to doped volume. Over the last ten years, near diffraction-limited mode output power of fibre lasers has steadily increased from 1.36kW in 2004 [14] to 10kW in 2009 [15] with very high slope efficiency near to 90%. In contrast, output power for radially polarized fibre lasers is at the watt-level [16, 17]. Lack of effective ways to suppress the oscillation of the fundamental mode is one of most essential factors that has hindered power scaling of radially polarized modes in fibre lasers.

The main objective of this thesis is to develop novel strategies for efficient excitation of these exotic doughnut-shaped beams with either vortex phase fronts or cylindrically symmetric polarizations directly within solid-state lasers and fibre lasers or external to them. In addition, we also explore migration of thermal effects in solid-state lasers using a novel pumping geometry. Solid-state lasers, whilst no longer competitive with fibre lasers for the generation of high-power continuous output, are still very important for the generation of short pulses with high peak powers (greater than a few megawatts) which would catastrophically damage fibre lasers. This thesis will only consider laser operation in continuous wave mode, but the developments of these techniques are readily to transfer to pulsed lasers.

1.2 Thesis structure

Chapter 2 introduces the relevant background information on doughnut-shaped beams with a vortex phase front or CV polarization. It begins with a brief description of end-pumped solid-state lasers, describing pump sources, gain material and key laser performance parameters. Then the spatial electric field characteristics of beams in free space are described through solving the scalar and vector Helmholtz equations in the paraxial approximation. This is followed by introducing the most attractive properties including OAM and tight focusing

capability for doughnut-shaped beams. A brief review of prior work on generation of doughnut-shaped beams from end-pumped solid-state lasers and applications are included in the last two sections of this chapter.

In chapter 3, we investigate the use of a ring-shaped pumping scheme for end-pumped solid-state lasers. A study into thermal lensing effects with this novel pumping geometry is presented. This includes approximate analytical modelling of thermally induced lens strengths and lens aberration induced degradation of beam quality for the two lowest-order of the LG modes (TEM_{00} and LG_{01}). The principles for selective generation of these two modes are briefly discussed as well.

In chapter 4, we experimentally investigate the thermally induced lens strength and degradation in beam quality in an Nd:YVO_4 crystal end-pumped by both traditional fibre-coupled laser diode and the ring-shaped pump beam. The results show a significant reduction in thermally induced lens effects for the latter. Finally, preliminary experimental results for power scaling the TEM_{00} mode are presented, suggesting an advantage is indeed obtained for the ring-shaped pump beam.

In chapter 5, we further explore the benefits of the ring-shaped pump beam focusing on the generation of first higher-order LG scalar and vector modes (LG_{01}) characterized by a phase or polarization singularity in end-pumped solid-state lasers. A doughnut-shaped output beam is first demonstrated in a Nd:YAG solid-state laser. Analysis for each axial-mode-frequency is carried out using a Mach-Zehnder interferometer, together with an astigmatism mode converter. Results show that the handedness of directly generated LG_{01} modes is prone to random switching for each longitudinal frequency mode leading to a degenerate doughnut-shaped mode. This is because LG_{01} modes with right-handed (LG_{01}^{+}) and left-handed (LG_{01}^{-}) helical phase trajectories have the same spatial overlap with the pumped region and hence equal threshold pump power. In order to break this degeneracy, we first investigated the generation of a single-frequency doughnut-shaped mode. Furthermore, we exploit the fact that standing-wave intensity distributions for the LG_{01}^{+} and LG_{01}^{-} modes inside the laser cavity are different. A novel intracavity mode selection element is then employed to control the handedness of the LG_{01} mode. Finally, using the same pumping scheme, we theoretically and experimentally investigate the generation of radially-polarized LG_{01} beams.

Chapter 6 focuses on transformations of a linearly-polarized Gaussian beam and a circularly-polarized doughnut-shaped LG_{01} scalar mode beam into a radially polarized doughnut-shaped beam using external polarization converters based on femtosecond laser writing of nanostructure gratings in silica glass. An overview of the theory of femtosecond laser induced nanogratings is described, followed by a description of the spatially variant half wave-plate and quarter wave-plate fabricated via the femtosecond writing technique. The working principles of both polarization converters are discussed with the aid of the Jones matrix. Finally, the performance of the two polarization converters designed for use in ~1μm and ~2μm are experimentally investigated.

In chapter 7, we focus on the generation of doughnut-shaped beams with radial polarization or a vortex phase front in ytterbium (Yb)-doped fibre lasers. An overview of transverse modes in fibre waveguides and prior work on excitation of doughnut-shaped modes in a fibre is discussed. We then experimentally investigate the propagation of the radially-polarized TM_{01} mode in both non-polarization-maintaining (PM) and PM fibres, and results show that the TM_{01} mode can propagate in these fibres. Then we explore the polarization converter investigated in chapter 6 in an Yb-doped fibre laser system to efficiently excite the doughnut-shaped TM_{01} mode with radial polarization. In the final section of this chapter, a simple approach by exploiting the difference in polarization behaviour of individual transverse modes due to the transverse variation of birefringence is experimentally demonstrated to selectively generate the fundamental LP_{01} and the next higher order doughnut-shaped LP_{11} mode with helical phase front.

Chapter 8 concludes all of the work presented throughout this thesis and discusses the future prospects.

Bibliography

1. A. L. Schawlow and C. H. Townes, "Infrared and Optical Masers," Physical Review **112**, 1940-1949 (1958).

2. T. J. Kane, A. C. Nilsson, and R. L. Byer, "Frequency stability and offset locking of a laser-diode-pumped Nd:YAG monolithic nonplanar ring oscillator," Optics Letters **12**, 175-177 (1987).

3. G. P. A. Malcolm, P. F. Curley, and A. I. Ferguson, "Additive-pulse mode locking of a diode-pumped Nd:YLF Laser," Optics Letters **15**, 1303-1305 (1990).

4. W. A. Clarkson, "Thermal effects and their mitigation in end-pumped solid-state lasers," J Phys D Appl Phys **34**, 2381-2395 (2001).

5. S. Konno, S. Fujikawa, and K. Yasui, "Efficient 153W cw TEM00 mode 1064-nm beam generation by a laser-diode-pumped Nd:YAG rod laser," in *Advanced Solid-State Lasers*, 2001), MA4.

6. T. S. Rutherford, W. M. Tulloch, E. K. Gustafson, and R. L. Byer, "Edge-pumped quasi-three-level slab lasers: Design and power scaling," IEEE J. Quantum Elect. **36**, 205-219 (2000).

7. A. Giesen, H. Hugel, A. Voss, K. Wittig, U. Brauch, and H. Opower, "Scalable concept for diode-pumped high-power solid-state lasers," Appl Phys B-Lasers O **58**, 365-372 (1994).

8. L. Allen, M. W. Beijersbergen, R. J. C. Spreeuw, and J. P. Woerdman, "Orbital angular momentum of light and the transformation of Laguerre-Gaussian laser modes," Phys. Rev. A **45**, 8185-8189 (1992).

9. D. G. Grier, "A revolution in optical manipulation," Nature **424**, 810-816 (2003).

10. J. Hamazaki, R. Morita, K. Chujo, Y. Kobayashi, S. Tanda, and T. Omatsu, "Optical-vortex laser ablation," Optics Express **18**, 2144-2151 (2010).

11. S. W. Hell and J. Wichmann, "Breaking the diffraction resolution limit by stimulated emission: stimulated-emission-depletion fluorescence microscopy," Optics Letters **19**, 780-782 (1994).

12. J. Wang, J. Y. Yang, I. M. Fazal, N. Ahmed, Y. Yan, H. Huang, Y. X. Ren, Y. Yue, S. Dolinar, M. Tur, and A. E. Willner, "Terabit free-space data transmission employing orbital angular momentum multiplexing," Nat. Photonics **6**, 488-496 (2012).

13. N. Bozinovic, Y. Yue, Y. X. Ren, M. Tur, P. Kristensen, H. Huang, A. E. Willner, and S. Ramachandran, "Terabit-scale orbital angular momentum mode division multiplexing in fibers," Science **340**, 1545-1548 (2013).

14. Y. Jeong, J. K. Sahu, D. N. Payne, and J. Nilsson, "Ytterbium-doped large-core fiber laser with 1.36 kW continuous-wave output power," Optics Express **12**, 6088-6092 (2004).

15. E. Stiles, "New developments in IPG fiber laser technology," in *5th International Workshop on Fiber Lasers,* (2009).

16. D. Lin, K. Xia, J. Li, R. Li, K. Ueda, G. Li, and X. Li, "Efficient, high-power, and radially polarized fiber laser," Optics Letters **35**, 2290-2292 (2010).

17. C. Jocher, C. Jauregui, M. Becker, M. Rothhardt, J. Limpert, and A. Tunnermann, "An all-fiber Raman laser for cylindrical vector beam generation," Laser Physics Letters **10**, 125108 (2013).

Chapter 2: Background

2.1 Introduction

Ever demanding and more sophisticated applications ranging from laser processing of materials to scientific research, or from medicine to defence, require laser beams with unique properties. The traditional Gaussian-shaped fundamental transverse mode (TEM_{00}) output beam with homogenous polarization states (linear or circular polarization) is not always the best option for some applications in which the polarization behaviour and electric field distribution of the beam has a pronounced impact. Recently, one type of doughnut-shaped beam with phase or polarization singularity at the beam centre has been attracting attention due to a variety of potential applications.

In this chapter, we will briefly introduce the concept of diode end-pumped solid-state lasers and provide the fundamental theory that allows an estimation of laser performance characteristics including threshold and slope efficiency, in section 2.2. In section 2.3, we will solve both the scalar and vector Helmholtz equations to derive mathematical descriptions of electric field distributions for doughnut-shaped beams discussed throughout this thesis. In section 2.4, we will introduce two important properties, namely, the OAM for doughnut-shaped optical vortex beams and tightly focusing capabilities for radially polarized doughnut-shaped beams. A brief historical overview of methods for generating these beams is then described in section 2.5. Finally, potential applications for doughnut-shaped beams will be discussed in section 2.6.

2.2 Diode end-pumped solid-state lasers

A solid-state laser is a laser that uses a solid-state gain medium consisting of a crystal or glass host material doped with transition metals ions. The first solid-state laser was demonstrated using a chromium-doped sapphire crystal pumped by a flash lamp [1]. Flash lamps are robust, relatively cheap and can provide high peak pump power. As a result, they were widely used as pump sources for the earliest solid-state lasers. However, the broadband spectrum of their output results in a large fraction of energy being converted to heat in the solid-state gain medium,

leading to high thermal loading and low overall electrical efficiency. Nowadays, laser diodes are rapidly replacing flash lamps in solid-state lasers due to their various advantages compared with the latter, including narrow emission bandwidth, long lifetime, compactness, and versatility.

An alternative to the side-pumped configuration is an end-pumped geometry. The distinguishing feature of this architecture is that the laser mode collinearly propagates with the pump beam. The first diode end-pumped solid-state laser was demonstrated by Rosenkrantz [2], in which pump light at 868nm emitted from a single chip GaAs laser diode was launched into a Nd:YAG crystal through its end face to generate laser output at 1.06 μm. Figure 2.1 shows a typical example of a diode end-pumped solid-state laser system. The pump beam emitted from a laser diode is collected and focused to a small spot on the end of the laser gain medium, which is spatially overlapped with the resonator mode. This configuration allows maximum use of energy stored in the laser gain medium as the distribution of inverted ions can be spatially matched to the desired resonator transverse mode (normally the fundamental TEM_{00} mode).

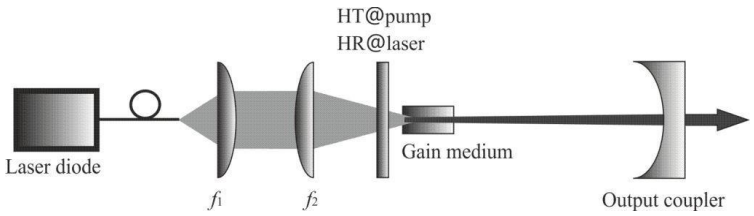

Figure 2.1 Schematic of diode end-pumped solid-state laser.

2.2.1 Laser diodes

Laser diodes have been used as pump sources in commercial solid-state lasers since the mid-1980s when the sophisticated fabrication technique was developed that allowed the development of laser diodes with longer lifetimes (>100000 hours) and high output power at room temperature. The output power of AlGaAs laser diodes in the 900 nm range can now reach >12 W per single emitter thanks to advanced semiconductor chip technology [3]. Moreover, individual emitters are normally integrated to form bars, stacks and bar arrays that are capable of producing multi-kW output powers.

Coupling the output beam of laser diodes into optical fibres for beam delivery has numerous advantageous over free-space delivering of pump light from diode lasers. These include flexibility in design, remote monitoring of pump diodes, circularization and homogenisation of the pump light, and highly repeatable beam quality and pointing stability. Commercially available fibre coupled laser diodes are able to deliver 1.2kW output in a 400 μm fibre with an NA of 0.22 at 976nm. Moreover, it was recently reported that a ~2kW diode laser has been successfully coupled into a 50 μm core fibre with an NA of 0.15 at a single central wavelength. This corresponds to a brightness level of 1468 MW/cm^2-str, with a beam propagation factor (M^2) that is even comparable to fibre, CO_2, and solid-state lasers [4].

2.2.2 Solid-state laser materials

The gain media of a solid-state laser consists of a host material (glass, crystalline or ceramic) doped with active ions. The spectroscopic properties are mainly dependent on the doped ions, whilst the thermal, optical and mechanical properties are primarily determined by the host material. The world's first solid-state laser was demonstrated by using a sapphire crystal doped with chromium (Cr^{3+}:Al_2O_3) as the gain media [1]. Since then laser emission from the visible to the mid-infrared spectrum has been accomplished in various host materials doped with trivalent rare earth ions such as Nd^{3+}, Er^{3+}, Ho^{3+}, Tm^{3+}, Yb^{3+}, etc. [5]. Although numerous solid-state gain materials have been demonstrated, relatively few types are in widespread use today. Probably the most commonly used within the 1μm wavelength range are neodymium doped yttrium aluminium garnet (Nd:YAG), neodymium doped vanadate (Nd:YVO_4), ytterbium doped yttrium aluminium garnet (Yb:YAG), and ytterbium doped silica glass (Yb:glass).

Figure 2.2 depicts the spectroscopic energy level diagram with the standard emission wavelengths for Nd:YAG [6]. The electrons are commonly excited from the $^4I_{9/2}$ ground-state level to the $^4F_{5/2}$ upper level when pumped at 808nm. This is followed by fast non-radiative decay from the pump band into the upper laser level $^4F_{3/2}$. The fluorescence lifetime of the $^4F_{3/2}$ manifold is about 230 μs for a Nd^{3+} doping concentration around 1% [5]. Nd^{3+} ions offer three different transitions from the manifold upper laser level $^4F_{3/2}$ to lower laser levels $^4I_{9/2}$, $^4I_{11/2}$ and $^4I_{13/2}$ corresponding to emission wavelengths of 0.9 μm, 1.06 μm and 1.35 μm,

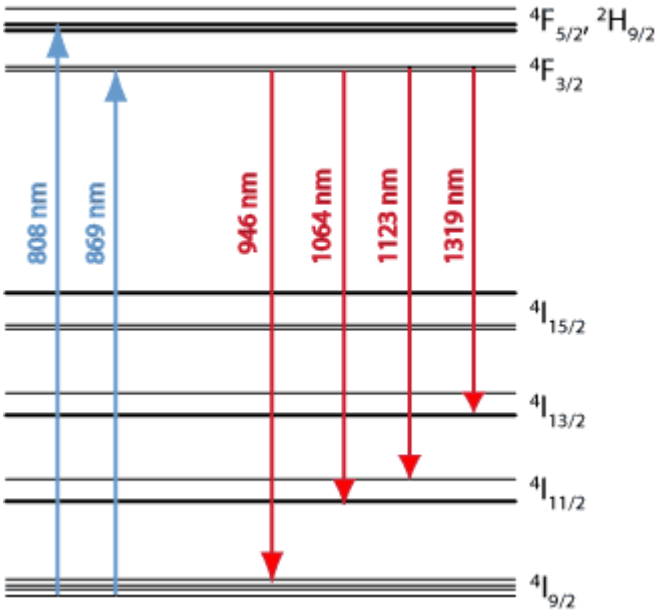

Figure 2.2 Energy level combined with pump and laser transitions in Nd:YAG [6].

respectively. The branching ratios of these transitions at room temperature are as follows: $^4F_{3/2} \rightarrow {}^4I_{9/2}$ =0.3, $^4F_{3/2} \rightarrow {}^4I_{11/2}$ =0.56, $^4F_{3/2} \rightarrow {}^4I_{13/2}$ =0.14, thus the strongest emission occurs at 1.06 μm [7]. The other two low gain transitions at 0.9 μm and 1.35 μm are of particular interest for nonlinear frequency conversion to generate visible light in the blue and red spectral regions.

2.2.3 Performance of solid-state lasers

In this section, we briefly describe several important criteria for the evaluation of laser performance such as the threshold, slope efficiency and beam quality.

2.2.3.1 Threshold and slope efficiency

In a diode end-pumped solid-state laser as shown in Figure 2.1, laser performance can be characterized by determining threshold and slope efficiency. Taking into account the spatial variation of both pump beam and laser mode, the rate equations for a four-level laser system can be written as follows [8, 9]:

$$\frac{dn(x,y,z)}{dt} = r(x,y,z) - \frac{n(x,y,z)}{\tau_f} - c_n \sigma n(x,y,z) \times \sum_{i=1}^{M} s_i(x,y,z) \qquad (2.1)$$

$$\frac{dS_i}{dt} = c_n \sigma \int_{cavity} n(x,y,z) s_i(x,y,z)\,\mathrm{dv} - \gamma_i S_i \tag{2.2}$$

where $n(x,y,z)$ is the population inversion density, σ is the emission cross-section, $r(x,y,z)$ is the pumping rate per unit volume, τ_f is the fluorescence lifetime, c_n is the velocity of light in the laser medium, $s_i(x,y,z)$is the laser photon density of the ith transverse mode, $S_i = \int_{cavity} s_i(x,y,z)\mathrm{dv}$ is the total photon number of the ith mode, $\gamma_i = c\delta_{c,i}/2l$ is the inverse of cavity photon lifetime of the ith mode, $\delta_{c,i}$ is the round-trip cavity loss, and l is the optical length of the cavity.

For steady-state conditions ($dn/dt = dS_i/dt = 0$), the population inversion from Eq. (2.1) is given by:

$$n(x,y,z) = \frac{\tau_f r(x,y,z)}{1 + c_n \sigma \tau_f \sum_{i=1}^{M} s_i(x,y,z)} \tag{2.3}$$

substituting Eq.(2.3) into (2.2) yields the following equation $J_i(S_1, S_2, \ldots)$ describing the steady-state photon number S_i and pumping rate R:

$$J_i(S_1, S_2, \ldots) = \int_{cavity} \frac{r_0(x,y,z) s_{0i}(x,y,z)}{1 + \sum_{j=1}^{M} S_j s_{0j}(x,y,z)/I_0}\mathrm{dv} = I_0 \gamma_i / R \tag{2.4}$$

where

$$I_0 = \frac{1}{c_n \sigma \tau_f} \tag{2.5}$$

$r_0(x,y,z)$ and $s_{0i}(x,y,z)$ are normalized distribution functions defined as:

$$\begin{aligned} s_i(x,y,z) &= S_i s_{0i}(x,y,z) \\ r(x,y,z) &= R r_0(x,y,z) \\ \int_{cavity} s_{0i}(x,y,z)\mathrm{dv} &= \int_{cavity} r_0(x,y,z)\mathrm{dv} = 1 \end{aligned} \tag{2.6}$$

Eq.(2.4) relates the number of ith signal mode photons (S_i) in the presence of other signal modes at a given pumping rate R. As can be seen this relation involves the spatial overlap between the signal and pump photon distributions and the gain saturation effect due to all signal modes above threshold ($S_j \neq 0$). For a laser system with M different output modes, there are M such equations whose solutions describe the number of photons in each mode at a given pumping rate R. Obviously,

it is rather difficult to derive general solutions to the Eq.(2.4) in case of a laser oscillator operating with many different output modes. However, a real laser device usually operate on a single or a few transverse modes as the mode competition due to the gain saturation and different intracavity losses limits the number of excited modes. For a laser oscillator operating with a single transverse mode, the number of photons can be derived by solving Eq.(2.4) by setting $S_2 = S_3 = \cdots S_M = 0$ as follows:

$$R = I_0\gamma_1 / J_1(S_1) \tag{2.7}$$

where

$$J_1(S_1) = J_1(S_1, 0, 0, \ldots, 0) = \int_{cavity} \frac{r_0(x,y,z)s_{01}(x,y,z)}{1 + S_1 s_{01}(x,y,z)/I_0} \mathrm{dv} \tag{2.8}$$

The threshold for the first mode excitation can be obtained by setting $S_1 = 0$ in Eqs.(2.7) and (2.8), and yields:

$$R_{th,1} = I_0\gamma_1 / J_1(0) \tag{2.9}$$

where

$$J_1(0) = \int_{cavity} r_0(x,y,z)s_{01}(x,y,z)\mathrm{dv} \tag{2.10}$$

The number of photons in the first excited mode S_1 and total pumping rate R can be written in terms of laser output power $P_{out,1}$ and absorbed pump power P_{abs} as follows:

$$S_1 = \frac{2lP_{out,1}}{chv_s T_0} \tag{2.11}$$

$$R = P_{abs} / hv_p \tag{2.12}$$

where v_s and v_p are laser and pump frequencies, respectively, T_0 is the transmission of output coupler. Substituting Eq.(2.9) into Eq.(2.12), the threshold absorbed pump power can be derived as:

$$P_{th,1} = \frac{hv_p}{\sigma\tau_f}\frac{\delta_1}{2l}\frac{1}{J_1(0)} = \frac{hv_p}{\sigma\tau_f}\frac{\delta_1}{2}A_{eff} \tag{2.13}$$

where

$$A_{eff} = \frac{1}{lJ_1(0)} \tag{2.14}$$

Here A_{eff} can be considered as the effective pump area which is a function of the pump and signal modes through the simple overlap integral $J_1(0)$. Eq.(2.13) provides a good guide to optimize the laser cavity design. For a given laser device with efficient operation, a low cavity loss and a good spatial overlap between pump beam and laser mode are generally required in order to achieve a low threshold. A small effective pump beam area means that the effective population inversion density is high and hence a low threshold for particular mode can be achieved. Moreover, the slope efficiency is derived as:

$$\begin{aligned}\eta_s &= \frac{dP_{out}}{dP_{abs}} \approx \frac{P_{out}}{P_{abs} - P_{th}} = \frac{Tv_s}{L_1 v_p}\eta_c \\ &= \frac{Tv_s}{L_1 v_p} \frac{\int_{cavity} \frac{r_0(x,y,z)s_{01}(x,y,z)}{1+S_1 s_{01}(x,y,z)/I_0}\mathrm{dv} \int_{cavity} r_0(x,y,z)s_{01}(x,y,z)\mathrm{dv}}{\int_{cavity} \frac{r_0(x,y,z)s_{01}^2(x,y,z)}{1+S_1 s_{01}(x,y,z)/I_0}\mathrm{dv}}\end{aligned} \tag{2.15}$$

where η_c is dependent on the spatial distribution of the pump beam and lasing mode and on the laser output power. However, in the pumping region near the threshold, such that $S_1 s_{01}/I_0 \ll 1$, the approximation can be expressed as:

$$\eta_c \approx \frac{\left(\int_{cavity} r_0(x,y,z)s_{01}(x,y,z)\mathrm{dv}\right)^2}{\int_{cavity} r_0(x,y,z)s_{01}^2(x,y,z)\mathrm{dv}} \tag{2.16}$$

which is only dependent on the spatial distribution of the pump and lasing mode. The η_c can be considered as the coupling efficiency between the pump beam with the lasing mode indicating the fraction of pump power contained in the region of the laser mode which can be a maximum of 1 [8]. From Eqs. (2.13) and (2.16), it can be seen that the spatial overlap of the pump beam and lasing mode is a very important parameter that should be optimized in the design of an end-pumped laser.

When the pump power is far above the threshold, it is worth analysing whether the second transverse mode will be excited or not. If the second transverse mode reaches threshold, Eq.(2.4) becomes:

$$\begin{cases} J_1(S_1,0,\ldots) = \int\limits_{cavity} \dfrac{r_0(x,y,z)s_{01}(x,y,z)}{1+S_1 s_{01}(x,y,z)/I_0}\mathrm{dv} = I_0\gamma_1 h\nu_p / P_p \\ J_2(S_1,0,\ldots) = \int\limits_{cavity} \dfrac{r_0(x,y,z)s_{02}(x,y,z)}{1+S_1 s_{01}(x,y,z)/I_0}\mathrm{dv} = I_0\gamma_2 h\nu_p / P_{th2} \end{cases} \tag{2.17}$$

The second transverse mode can reach threshold only when $P_{th2} \le P_p$, that is:

$$\frac{J_1(S_1,0)}{J_2(S_1,0)} \le \frac{\gamma_1}{\gamma_2} \tag{2.18}$$

It appears that to satisfy the criteria described in Eq.(2.18), the second transverse mode must have a better overlap with the pump beam if the intracavity loss is higher than the first excited mode.

2.2.3.2 Beam quality

The beam parameter product (BPP) and M^2 are the two most popular ways to quantify the laser beam quality. The BPP is defined as the product of beam radius at the waist and the beam divergence half-angle in the far-field. The smallest BPP in theory is equal to λ/π for a diffraction-limited Gaussian beam. According to the ISO standard 11146 [10], the ratio of the BPP for a measured beam to the BPP of a diffraction-limited Gaussian beam is called M^2 having an expression:

$$\mathrm{M}^2 = \frac{\theta \pi w_0}{\lambda} = \frac{\pi w_0^2}{\lambda z_R} \tag{2.19}$$

where θ is the beam divergence half-angle in the far field, w_0 is the beam radius at the waist based on the second moment definition, and z_R is the Rayleigh range which is the distance that a beam must propagate for its beam waist spot size to increase by a factor of $\sqrt{2}$. For a Gaussian-shaped fundamental TEM_{00} mode beam, $M^2=1$. For other higher-order mode beams, $M^2>1$. Laser beam quality is important since the closer a real laser beam is to 1, the more tightly it can be focused, the greater the depth of field, and smaller diameter beam-handling optics are needed to collect the beam. For applications such as directed energy applications, better beam quality translates into better delivery of optical power to the target with smaller beam size in the far field. For material processing, a more tightly focused laser beam results in higher intensities.

From Eq. (2.19), we can see that the M^2 measurement is based on measuring the beam waist spot size and its Rayleigh range. The schematic of the setup for M^2 measurement through this thesis is shown in Figure 2.3. The laser beam is focused by a lens, and the beam spot radius is measured by using a scanning slit beam profiler. A lens with longer focal length is preferable as it affords a more precise Rayleigh range measurement and hence improves the accuracy of the M^2. Therefore, a lens should be selected so that the focused beam diameter on the beam profiler is as large as possible without overfilling the sensor of the beam profiler. One Thorlabs beam profiler (BP104-IR) based on an InGaAs sensor and one Ophir beam profiler (NanoScan 2s Pyro) based on a pyroelectric sensor were utilized in this thesis to measure the M^2 of laser beams at 1μm and 2μm wavelengths, respectively. The first step for measuring M^2 is moving the beam profiler along the axis (z) to find the smallest spot size (w_0) and its position (z_0). Then, measure the beam radius ($w(z)$) in various positions (both within and beyond the Rayleigh range). Theoretically, the beam radius changes with propagation distance in the following form [11]:

$$w(z) = w_0 \left(1 + \left(\frac{z - z_0}{z_R} \right)^2 \right)^{1/2} \tag{2.20}$$

The measured beam spot radius is then fitted to the above equation (Eq.(2.20)) yielding an estimated beam waist radius and Rayleigh range. Finally the M^2 can be calculated by Eq.(2.19).

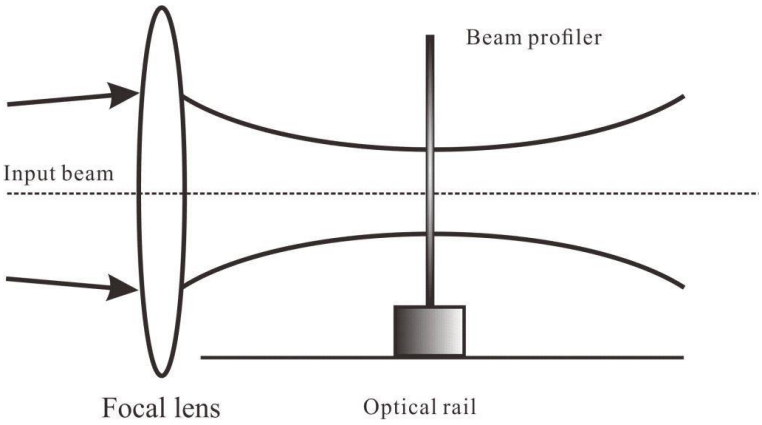

Figure 2.3 Schematic of setup for M^2 measurement.

2.3 Transverse modes in free-space resonator

As far back as 1961, Fox and Li theoretically investigated the diffraction of electromagnetic waves in Fabry-Perot cavities [12]. It was found that the amplitudes and phases of electric fields in an optical resonator are reproduced after many successive round trips. Conventionally, the electric field of laser beams in free space are solutions of the scalar Helmholtz equation in the paraxial approximation described by two familiar families of modes: the HG modes in rectangular coordinates and the LG modes in cylindrical coordinates [11]. These modes have homogeneous polarization state distributions (e.g. linear, circular polarization) over the cross-section of the laser beam. Over the last two decades, another kind of beam with an inhomogeneous polarization state distribution over the beam cross-section known as CV beams have been reported in a series of publications. In contrast, the CV beams can be described by solutions of the vector Helmholtz equation in the paraxial limit [13].

2.3.1 Scalar modes

Most commonly, the electric field of a beam with a homogeneous polarization state distribution across the beam cross-section in free space is derived by solving the scalar Helmholtz equation [14]:

$$(\nabla^2 + k^2)E = 0 \tag{2.21}$$

where ∇^2 is the scalar Laplacian operator, $k = 2\pi / \lambda$ is the wave number, and E is scalar electric field. The paraxial solutions to above scalar Helmholtz equation can either take the form of HG functions in Cartesian coordinates (x, y, z), or of LG functions in cylindrical coordinates (r, φ, z).

For a beam-like paraxial solution in the form of a HG function, the general electric field E can be written as:

$$E(x, y, z, t) = u(x, y, z)\exp[i(kz - \omega t)] \tag{2.22}$$

where z is the propagation axis and $u(x, y, z)$ is the transverse beam profile. Inserting Eq.(2.22) into Eq.(2.21), and applying the slowly varying envelope approximation:

$$\frac{\partial^2 u}{\partial z^2} \ll k^2 u, \qquad \frac{\partial^2 u}{\partial z^2} \ll k \frac{\partial u}{\partial z} \tag{2.23}$$

Eq.(2.21) becomes:

$$\nabla_{\perp}^2 u + 2ik \frac{\partial u}{\partial z} \cong 0 \tag{2.24}$$

where $\nabla_{\perp}^2$ is the transverse Laplacian operator in Cartesian coordinates having the form:

$$\nabla_{\perp}^2 u = \frac{\partial^2 u}{\partial x^2} + \frac{\partial^2 u}{\partial y^2} \tag{2.25}$$

the solution to Eq.(2.24) can be obtained by separation of variables in the x and y directions, which has a mathematical form as follows:

$$\begin{aligned} u_{mn}(x,y,z) = & \left(\frac{2}{\pi}\right)^{1/2} \frac{\exp\left[-j(m+n+1)\phi(z)\right]}{\sqrt{2^{m+n} m! n! w^2(z)}} \\ & \times H_m\left(\frac{\sqrt{2}x}{w(z)}\right) H_n\left(\frac{\sqrt{2}y}{w(z)}\right) \\ & \times \exp\left(-j\frac{k(x^2+y^2)}{2R(z)} - \frac{x^2+y^2}{w^2(z)}\right) \end{aligned} \tag{2.26}$$

where the Hermite polynomials $H_m(x)$ have the form:

$$\begin{aligned} & \frac{d^2 H_m(x)}{dx^2} - 2x\frac{dH_m(x)}{dx} + 2mH_m(x) = 0 \\ & H_m(x) = (-1)^m e^{x^2} \frac{d^m}{dx^m}(e^{-x^2}) \end{aligned} \tag{2.27}$$

and $w(z)$ is the radius of beam size that contains ~86% of the total power in the beam, $R(z)$ is the radius of curvature of the beam wavefront, $(m+n+1)\phi(z)$ is called the Gouy phase shift. All the important parameters of the HG mode beam can be related to the beam waist spot radius (w_0) and the Rayleigh range ($z_R = \pi w_0^2/\lambda$) by the formulas:

$$w(z) = w_0\sqrt{1+\left(\frac{z}{z_R}\right)^2}$$
$$R(z) = z + \frac{z_R^2}{z} \tag{2.28}$$
$$\phi(z) = \tan^{-1}\left(\frac{z}{z_R}\right)$$

Figure 2.4 shows the intensity profiles of several low-order HG modes, starting with the HG_{00} mode and going up to the HG_{22} mode. The HG_{mn} mode has m nodes in the horizontal direction and n nodes in the vertical direction. For $m = n = 0$, the HG mode is a Gaussian beam, which is called the fundamental transverse mode, and it has the lowest beam propagation factor with an $M^2=1$, and other higher-order HG modes with indices m and n have an M^2 factor of $2m + 1$ in the x direction, and $2n + 1$ in the y direction.

An alternative paraxial solution can also be written in cylindrical coordinate (r, φ, z). In this case, the general solution can be written as:

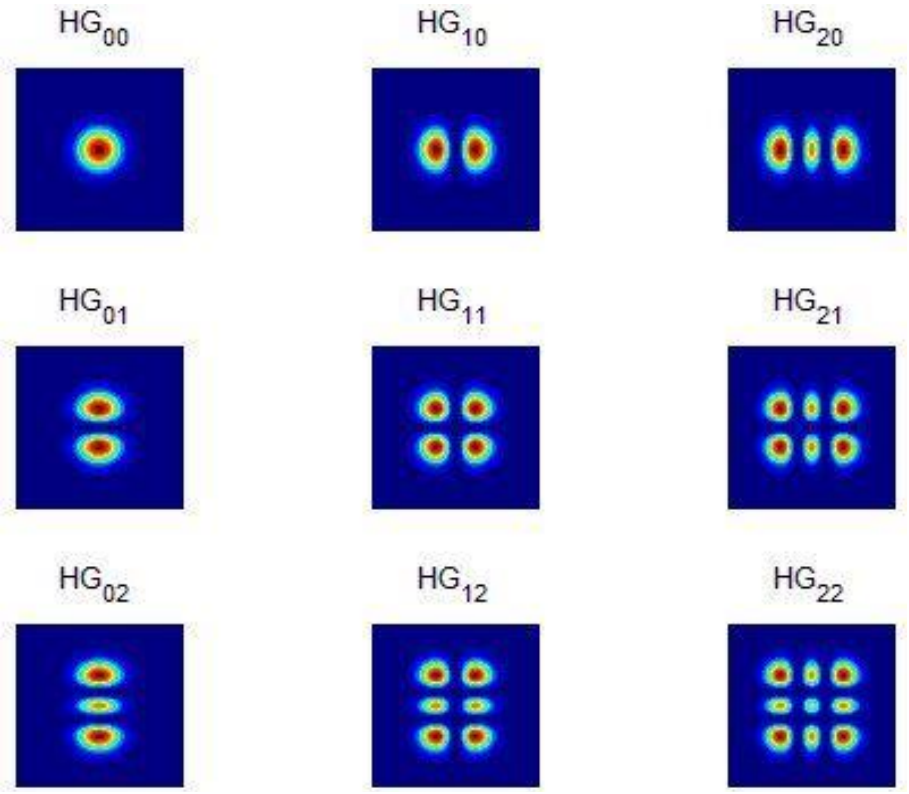

Figure 2.4 Intensity profiles of low-order HG modes, starting with the HG_{00} (upper left-hand side) and growing up to the HG_{22} mode (lower right-hand side).

$$E(r,\varphi,z,t)=u(r,\varphi,z)\exp[i(kz-\omega t)] \tag{2.29}$$

Inserting Eq. (2.29) into Eq. (2.21), and applying the slowly varying envelope approximation, yields:

$$\frac{1}{r}\frac{\partial}{\partial r}(r\frac{\partial u}{\partial r})+\frac{1}{r^2}\frac{\partial^2 u}{\partial \varphi^2}+2ik\frac{\partial u}{\partial z}=0 \tag{2.30}$$

The solutions to Eq. (2.30) are in general the Laguerre-Gaussian solutions having the form [11]:

$$\begin{aligned} u_{pm}(r,\varphi,z)=&\sqrt{\frac{2p!}{(1+\delta_{0m})\pi(|m|+p)!}}\frac{w_0}{w(z)}\exp[j(2p+|m|+1)\phi(z)] \\ &\times\left(\frac{\sqrt{2}r}{w(z)}\right)^{|m|}L_p^{|m|}\left(\frac{2r^2}{w^2(z)}\right)\exp\left(-j\frac{kr^2}{2R(z)}-\frac{r^2}{w^2(z)}+jm\varphi\right) \end{aligned} \tag{2.31}$$

where $L_p^m(x)$ are the Laguerre polynomials having the form:

$$x\frac{d^2L_p^m(x)}{dx^2}-(m+1-x)\frac{dL_p^m(x)}{dx}+pL_p^m(x)=0 \tag{2.32}$$

and

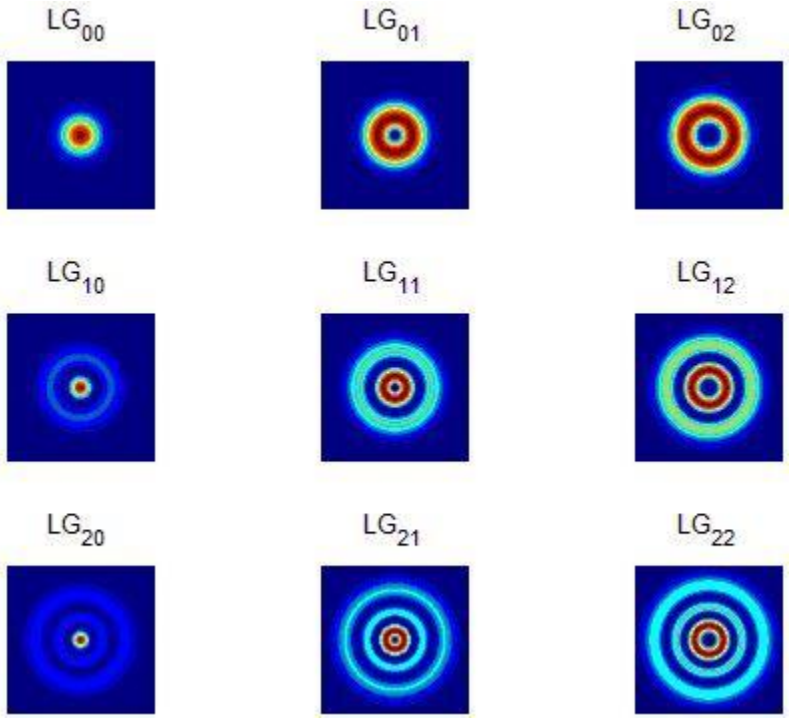

Figure 2.5 Intensity profiles of low-order LG modes, starting with the LG_{00} (upper left-hand side) and growing up to the LG_{22} mode (lower right-hand side).

integer $p \geq 0$ is the radial index and the integer m is the azimuthal index. $(2p + |m| + 1)\phi(z)$ is the Gouy phase shift, and δ_{0m} is the Kronecker delta function. Intensity profiles for several low-order LG modes are shown in Figure 2.5. For $p = m = 0$, the electric field reduces to the fundamental Gaussian mode. For any mode with $m = 0$ (e.g. LG_{p0}), the mode profile contains p dark concentric rings with an on-axis maximum intensity. For any mode with $m \neq 0$, a helical phase term $exp(im\varphi)$ is present in the electric field leading to an intensity null at the beam centre. Modes with the same radial index but opposite azimuthal index have identical intensity distributions but with opposite handedness of helical phase front. They are degenerate and hence tend to oscillate simultaneously in a laser system resulting in LG modes with beam profiles having $cos^2(m\varphi)$ variations in the azimuthal direction appearing as petal-like structures [15].

2.3.2 Vector mode

The solution of the HG and LG modes derived above is referred as scalar beams with spatially homogenous polarization state distributions. In contrast, beams with spatially inhomogeneous polarization state distributions over the beam cross-section are called vector beams, which can always be formed from a coherent superposition of scalar beams with different polarization states. For instance, a coherent superposition of an x-polarized HG_{10} beam with a y-polarized HG_{01} beam leads to a radially polarized doughnut-shaped beam [16]. The electric field of this vector beam is a solution of the vector Helmholtz equation as follows [13, 14, 16]:

$$\nabla \times \nabla \times \vec{E} - k^2 \vec{E} = 0 \tag{2.33}$$

For a particular class of vector beams with axially symmetric polarization, the solution of Eq.(2.33) takes the form:

$$\vec{E}(r,z) = \hat{n}(\varphi) E(r,z) \exp[i(kz - \omega t)] \tag{2.34}$$

where $\hat{n}(\varphi)$ is the unit vector that indicates the orientation of the electric field and satisfies the following criteria [16, 17]:

$$\frac{\partial \hat{n}(\varphi)}{\partial \varphi} = -m\hat{n}^*(\varphi), \quad \frac{\partial^2 \hat{n}(\varphi)}{\partial \varphi^2} = -m^2 \hat{n}(\varphi), \quad \frac{\partial \hat{n}(\varphi)}{\partial r} = 0, \quad \frac{\partial \hat{n}(\varphi)}{\partial z} = 0 \tag{2.35}$$

where $\hat{n}^*(\varphi)$ is orthogonal to $\hat{n}(\varphi)$, m is the integer representing mth-higher order modes. Substituting Eqs. (2.34) and (2.35) into Eq.(2.33), we obtain:

$$\frac{1}{r}\frac{\partial}{\partial r}(r\frac{\partial E}{\partial r})-\frac{m^2}{r^2}E+2ik\frac{\partial E}{\partial z}=0 \tag{2.36}$$

The general solution to Eq.(2.36) can be derived by the method of separation of variables in the following form[16, 17]:

$$E_m(r,z)=A(\beta_s^2)J_m(\beta_s r)\exp(-\frac{i\beta_s^2 z}{2k}) \tag{2.37}$$

where β_S is the separation parameter, J_m is the mth-order Bessel function of the first kind, and $A(\beta_S^2)$ is the arbitrary function of β_S that determines the weight of Bessel beams. Although Eq. (2.37) describes non-diffraction, and self-similar beams that carry infinite energy, almost any beam could be obtained by appropriate superposition of Bessel beams. One of particular interest is Bessel beams with a Gaussian envelope, also called Bessel-Gaussian (BG) beams that can be described as:

$$\begin{aligned}E_m(r,z)&=BG_m(r,z)\\&=E_0\frac{w_0}{w(z)}\exp(i\phi(z))J_m\left(\frac{\beta_s r}{1+iz/z_R}\right)\\&\times\exp\left(-i\frac{\beta_s^2 z/(2k)}{1+iz/z_R}\right)\exp(-\frac{r^2/w_0^2}{1+iz/z_R})\end{aligned} \tag{2.38}$$

For m=0, BG corresponds to uniformly polarized axial symmetrical scalar beams. If m=1, BG is an axially-symmetric polarized vector beam where the polarization distribution depends on unit vector $\hat{n}(\varphi)$. Unlike scalar LG beams, these beams do not have a helical phase term of $exp(im\varphi)$. Particularly, if $\hat{n}(\varphi)$ is aligned in the radial direction or azimuthal direction, the beam is radially-polarized or azimuthally-polarized. Figure 2.6 shows the intensity distributions and electric field distributions for the lowest-order of these beams. Both radially-polarized and azimuthally polarized beams possess the same intensity distribution characterized by a doughnut-shaped profile which is similar to the scalar LG_{01} mode. The intensity null in the centre is due to a polarization singularity at the beam axis rather than the phase singularity. Furthermore, the electric field in Figure 2.6 can always be simplified to [14]:

$$\vec{E}(r,z)=E_0 r\exp(-\frac{r^2}{w^2})\vec{e}_i \qquad i=r,\varphi \tag{2.39}$$

where E_0 is the constant, $\vec{e}_i$ is the unit vector denoting radial or azimuthal direction.

As a result, this unique beam is often called radially or azimuthally polarized LG_{01} beam which was firstly reported in a ruby laser [18]. It can also be formed by a coherent supposition of HG_{10} and HG_{01} modes with orthogonally linear polarization[14]:

$$\vec{E}_r = \vec{e}_x HG_{10} + \vec{e}_y HG_{01} \tag{2.40}$$

$$\vec{E}_\varphi = \vec{e}_y HG_{10} + \vec{e}_x HG_{01} \tag{2.41}$$

where $\vec{E}_r$ and $\vec{E}_\varphi$ represent the electric field of radial and azimuthal polarizations, respectively.

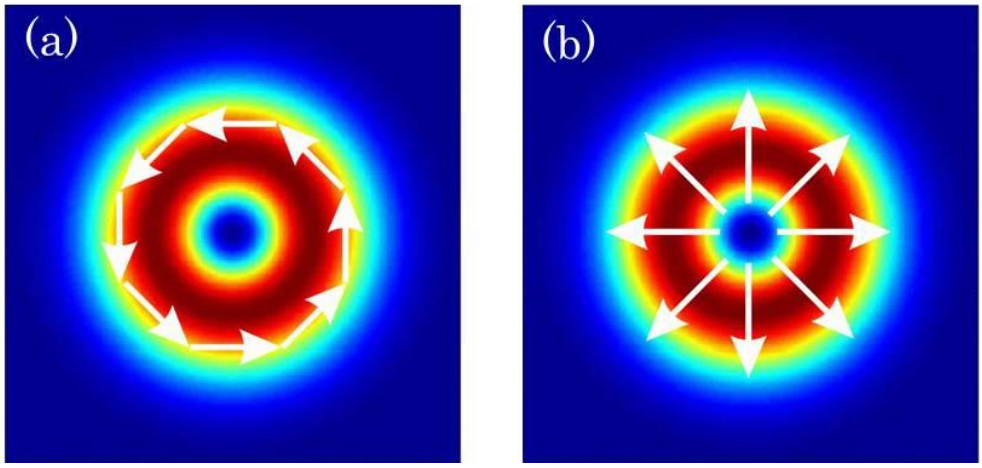

Figure 2.6 Intensity and electric field distributions for the lowest-order (a) azimuthally polarized beam, and (b) radially polarized beam.

2.4 Unique properties of doughnut-shaped LG beams

The intensity null at the centre of beam for both scalar and vector LG modes mentioned in section 2.3 can be attributed to either the phase or polarization singularities. This beam has unique optical properties compared with ordinary Gaussian-shaped beams. For a beam with helical phase front and associated phase singularity at the beam centre, the light carries OAM. While for a beam with a polarization singularity such as a radially-polarized beam, it can be tightly focused to a spot size significantly smaller than for linear polarization, and will have a strong longitudinal electric field component at the focus which is sharp and centered at the optical axis [19, 20]. More details of these characteristics will be discussed in the following section.

2.4.1 Orbital angular momentum

As early as 1909, Poynting had recognized that circularly polarized light carries linear momentum equivalent to $\hbar k$ (where $k = 2\pi/\lambda$, $\hbar = h/2\pi$, and h is Planck's constant) as well as a spin angular momentum of $\pm\hbar$ per photon [21]. The idea that light can carry OAM came much later. It was not until 1992 that Allen and his colleagues had realized that a beam with an azimuthal dependent phase structure of $exp(im\varphi)$ (where φ is the azimuthal angle over the beam cross section, and m is the integer value which can be positive or negative) carries an OAM equivalent to a value of $m\hbar$ for each photon [22].

As is well known, the energy flux density ($\vec{S}$) of an electromagnetic field is represented by the Poynting vector:

$$\vec{S} = \frac{1}{\mu_0}\left\langle \vec{E} \times \vec{B} \right\rangle \tag{2.42}$$

where μ_0 is the permeability of free-space, $\vec{B}$ is the magnetic flux density and $\vec{E}$ is the electric field. Meanwhile the linear momentum density ($\vec{p}$) and the angular momentum density ($\vec{j}$) can be expressed in terms of $\vec{E}$ and $\vec{B}$ as follows [23]:

$$\vec{p} = \varepsilon_0 \left\langle \vec{E} \times \vec{B} \right\rangle \tag{2.43}$$

$$\vec{j} = \varepsilon_0 \left(\vec{r} \times \left\langle \vec{E} \times \vec{B} \right\rangle \right) = \vec{r} \times \vec{p} \tag{2.44}$$

It should be noted that the Eq.(2.44) involves both spin and orbital angular moment density. The linear momentum density of a beam within the paraxial approximation can be written as [22, 24]:

$$\vec{p} = i\omega \frac{\varepsilon_0}{2}\left(u^* \nabla u - u \nabla u^* \right) + \omega k \varepsilon_0 |u|^2 \hat{z} + \omega \xi \frac{\varepsilon_0}{2} \frac{\partial |u|^2}{\partial r} \hat{\varphi} \tag{2.45}$$

where u is the complex amplitude of the field distribution, $\hat{z}$ is the unit vector in the z direction, ξ describes the polarization state (when $\xi = 1$ and $\xi = -1$ represents right- and left-hand circularly polarized light, respectively, and $\xi = 0$ for linearly-polarized light). The first term of Eq. (2.45) is related to the phase gradient and leads to the OAM. The final term of Eq. (2.45) only depends on polarization state and consequently give rise to the spin angular momentum. The cross product of the linear momentum density described in Eq.(2.45) with the radius vector $\vec{r} = (r, 0, z)$

yields an angular momentum density described in Eq. (2.44), from which the z component can be derived from:

$$j_z = rp_\varphi \tag{2.46}$$

For circularly polarized LG modes, Eqs. (2.45) and (2.46) can be evaluated analytically so that the local angular momentum density in the direction of propagation is given by [22]:

$$j_z = \varepsilon_0 \left(\omega m |u|^2 - \frac{1}{2} \omega \xi r \frac{\partial |u|^2}{\partial r} \right) \tag{2.47}$$

Therefore, each photon has an equivalent value of $\sigma\hbar$ for spin angular momentum and $m\hbar$ for the orbital angular momentum, and the total angular momentum is [22]:

$$J_z = (m + \xi)\hbar \tag{2.48}$$

2.4.2 Tightly focusing properties of radially-polarized beams

When a beam is focused by a lens with a high numerical aperture (NA), the classical scalar theory is no longer valid as the vector nature of electric field has to be considered. Richard-Wolf and co-workers [25, 26] have proposed a vectorial diffraction method to describe the electric field in the focal region for this case. In addition, the focusing properties of a cylindrical vector beam has been investigated by Youngworth [27]. The geometry of vector diffraction theory is illustrated in

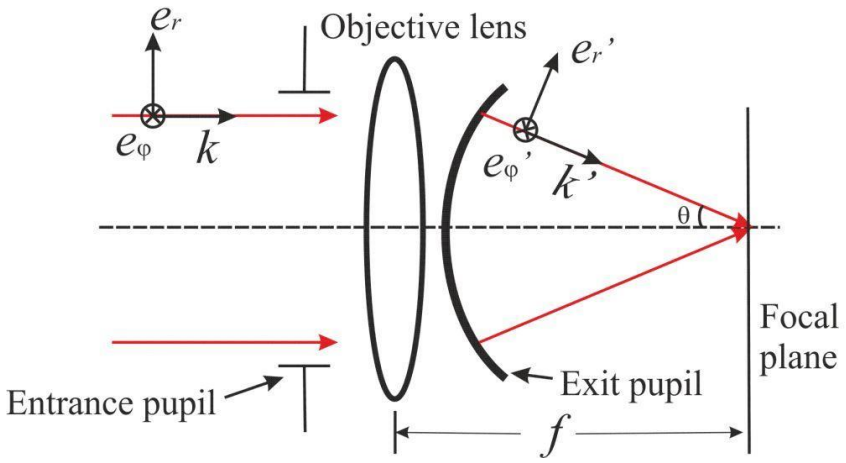

Figure 2.7 Schematic of focused radially and azimuthally polarized beam by an objective lens f [14].

Figure 2.7. For a cylindrical vector incident beam, assuming a plane wavefront, the electric field in the pupil plane can be expressed as:

$$\vec{E}_i(r,\varphi) = E_0(\cos\alpha_0\hat{e}_r + \sin\alpha_0\hat{e}_\varphi) \tag{2.49}$$

in which, E_0 is the peak field amplitude,$\hat{e}_r$ and $\hat{e}_\varphi$ are radial and azimuthal unit vector, respectively, $cos\alpha_0$ and $sin\alpha_0$ denote the normalized amplitude for the components of radial polarization and azimuthal polarization, respectively.

Therefore, in the image plane by employing cylindrical coordinates, the three orthogonal components of electric field near the paraxial focus can be derived as follows [27]:

$$\begin{cases} E_r(r,\varphi,z) = A\cos\alpha_0 \int_0^{\theta_{\max}} \cos^{1/2}\theta \sin 2\theta E_0(\theta) J_1(kr\sin\theta) e^{ikz\cos\theta} d\theta \\ E_\phi(r,\varphi,z) = 2A\sin\alpha_0 \int_0^{\theta_{\max}} \cos^{1/2}\theta \sin\theta E_0(\theta) J_1(kr\sin\theta) e^{ikz\cos\theta} d\theta \\ E_z(r,\varphi,z) = i2A\cos\alpha_0 \int_0^{\theta_{\max}} \cos^{1/2}\theta \sin^2\theta E_0(\theta) J_0(kr\sin\theta) e^{ikz\cos\theta} d\theta \end{cases} \tag{2.50}$$

where A is a constant, $E_0(\theta)$ is the apodization function, θ_{max} is the maximum focused angle determined by the NA of the lens. From Eq. (2.50), it can be seen that for a radially polarized incident beam ($\alpha_0 = 0$), the electric field in the image plane near the focus only has radial and longitudinal components. For an azimuthal polarized incident beam ($\alpha_0 = \pi/2$), however, the electric field only has an azimuthal component.

Figure 2.8(a) shows an example of calculated intensity distributions of the transverse electric field component for a tightly focused radially polarized beam at the focus (*r*-*z* plane). A ring-shaped intensity distribution with a null at the beam axis is observed. Figure 2.8(b) shows the intensity of the longitudinal electric field component in the vicinity of focus. The electric field is along the beam propagation direction and is sharply centred around the optical axis. There is also a halo ring around the beam, but its intensity is much smaller compared to the intensity at the beam centre. Figure 2.8(c) shows the total intensity distribution through the focus and Figure 2.8(d) shows the intensity distribution of each component as a function of radial position in the focal plane. In this case, it is obvious that the maximum

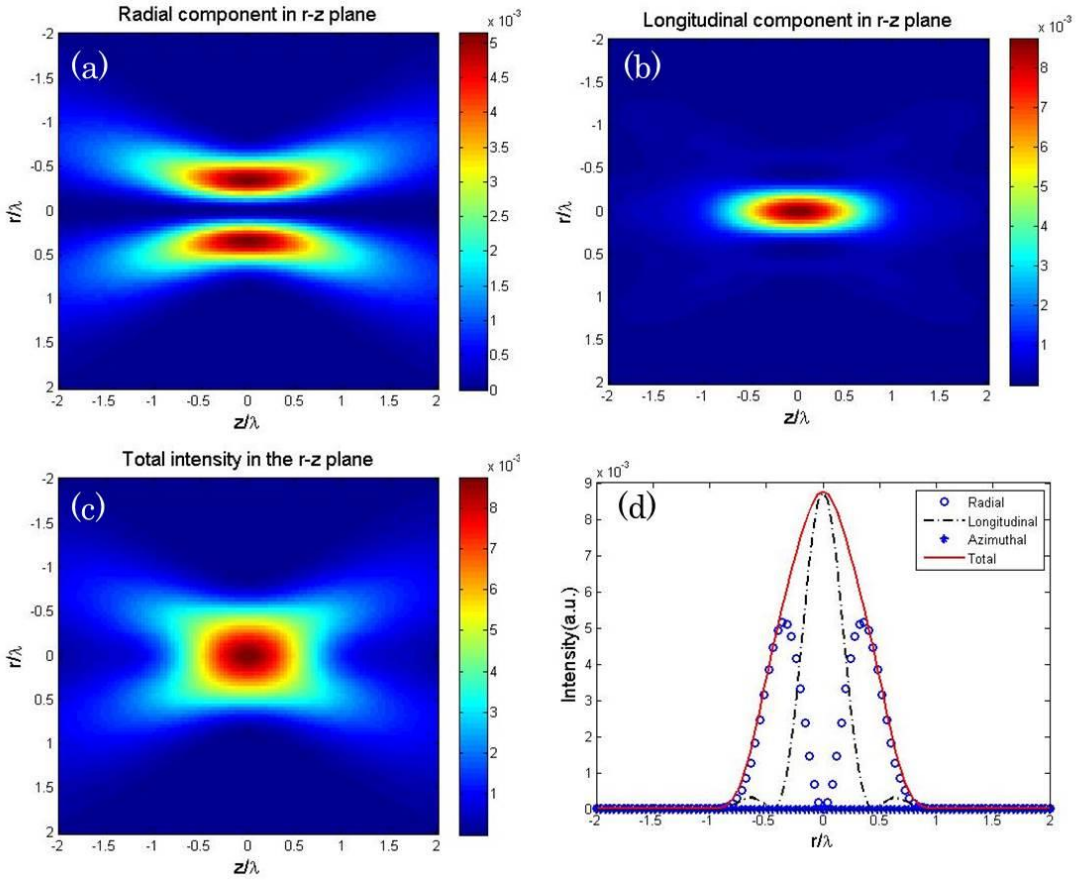

Figure 2.8 Calculated intensity distribution of each component of a high-NA(1.4) radially polarized beam through focus; (a)-(c) the radial component, longitudinal component, and the total intensity distributions in the *r*-*z* plane; (d) the intensity distribution of each component in the r-direction scan across the focus.

intensity of the longitudinal component is much stronger than that of the transverse component.

The ratio of the maximum longitudinal intensity to the transverse intensity is dependent on the focusing angle as shown in Figure 2.9. The longitudinal component is negligible at small focusing angles, and gradually increases to 2.4 at a focusing angle of $\pi/2$ radians. Due to the sharp peak of longitudinal electric field around the beam centre, a spot size as small as $0.16\lambda^2$ has been demonstrated, compared with $0.26\lambda^2$ spot size achieved by a linearly polarized beam under the same focusing condition [19].

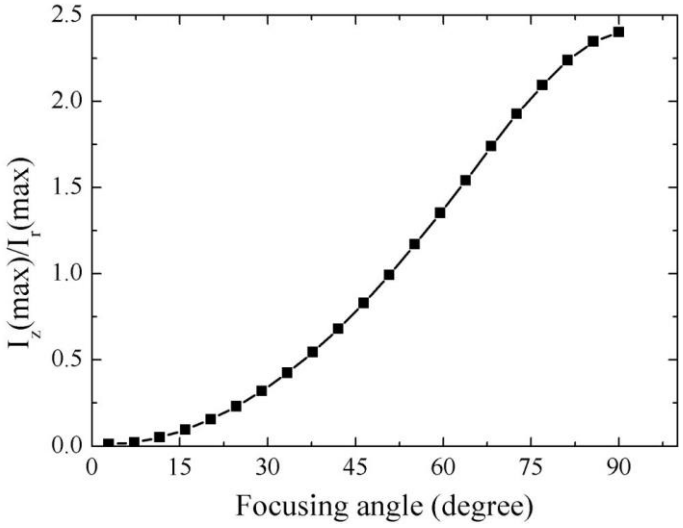

Figure 2.9 The ratio of maximal intensity of longitudinal component to radial component as a function of focusing angle.

2.5 History of doughnut-shaped LG mode generation

A number of techniques have been developed for generating doughnut-shaped beams with an optical vortex phase front or cylindrically symmetric polarization state distribution over the past decades. Depending on whether a laser gain medium is involved or not, these techniques can be categorized as active or passive methods.

2.5.1 Generation of optical vortex beams

2.5.1.1 Passive generation methods

Typically, passive methods exploit an external beam shaping arrangement to transform a plane wave beam to a helical phase front beam as shown in Figure 2.10. This could be achieved by employing an appropriate optical element including an astigmatic mode converter [28], a spiral phase plate [29], a computer-generated hologram [30], a liquid crystal spatial light modulator [31].

The astigmatic mode converter was firstly designed by Allen et al. in 1992 to transform between HG and LG modes [22]. The mode converter is composed of a pair of cylindrical lens. A HG mode orientated 45° to the lens axis can be decomposed into two orthogonal HG modes aligned to the lens axis that will

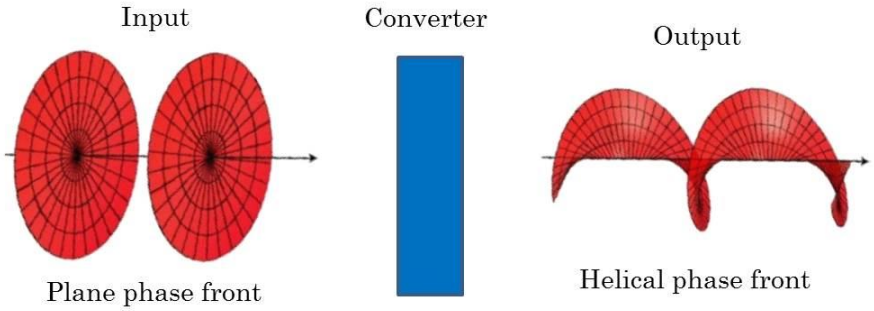

Figure 2.10 Schematic of converting a plane wave to a helically phased beam.

undergo $\pi/2$ different Gouy phase shift due to astigmatism of the cylindrical lens and hence form a pure LG mode. One of advantages of this technique is offering up to ~100% of conversion efficiency in theory and is only limited by the transmission of lenses. A more detailed description on this technique is given in [28].

Spiral phase plate is another popular way to produce optical vortex beams. The surface of such a transparent plate is like a turn of a staircase: the thickness of plate increases proportional to the azimuthal angle around the centre of the plate according to $m\lambda\varphi/2\pi(n-1)$, where m is the integer and n is the refractive index of the plate. As the step height should be of the order of the wavelength, it requires rigorous precision in the step height of the spiral plate. In the original work reported by Beijersbergen, this was achieved by immersing the spiral plate in a liquid for which the refractive index was controlled by adjusting the liquid temperature [29]. When a beam with plane wavefront passes through this plate, a phase term $exp(im\varphi)$ will be added to the input beam to form a helical wavefront. The resulting helically phased beam is no longer a pure mode, but rather a superposition of eigen LG modes. Its intensity distribution varies with propagation distance and appears as a doughnut-shaped profile in the far-field. The conversion efficiency was reported as high as ~89% and this value is limited by the overlap of input and output mode. The overlap integral of the Gaussian mode and LG_{01} mode with optimized waist was calculated to be ~93% in theory [32].

A computer-generated hologram is an alternative approach which has become very popular. The hologram is formed by interfering a reference beam with the objective beam and functions by diffracting the reference beam into the first order. In order to generate the helically phased beam, the hologram can be created either by interfering a tilted planar beam with a helical beam to form the forked diffraction

grating or by interfering a spherical beam with a helical beam to create the spiral Fresnel zone plate [30]. This technique becomes particularly appealing with the help of a liquid crystal spatial light modulator which is able to create any hologram interference pattern. Therefore, any complex beams, not restricted to helical beams, can easily be generated with this method. The mode conversion efficiency of this technique is relatively low (~34%) mainly limited by the diffraction of gratings [33].

2.5.1.2 Active generation methods

Passive methods mentioned in the above section, however, suffer from the drawbacks of relative low conversion efficiency and/or degradation in beam quality, and are generally not suitable for high power operation (greater than a few tens of watts) due to power handling limitations. On the other hand, a variety of techniques for direct generation of doughnut-shaped LG beams with helical phase front from a laser resonator have been developed recently. Figure 2.11 illustrates a typical schematic experimental setup for directly generating LG optical vortex beams in end-pumped solid-state lasers. Mode selection normally relies on special resonator configurations, intracavity mode-selective elements, or shaping the inversion profiles within the laser crystal.

Ito employed a spot defect rear mirror to suppress the oscillation of lower order transverse modes in an end-pumped Nd:YAG laser cavity to generate scalar LG vortex beams with an intensity null on the beam axis [34]. Naidoo explored pumping a monolithic microchip laser with a ring-shaped pump beam profile by using a phase mask to obtain higher modal overlap with the LG_{01} mode allowing for preferential excitation of the desired doughnut-shaped LG_{01} vortex mode[35]. There are also several other observations on LG_{01} vortex beams in side-pumped Nd:YVO_4 and Nd:$GdVO_4$ bounce lasers, in which the laser operates in a stable region such that the LG_{01} mode is stable but the fundamental TM_{00} mode is

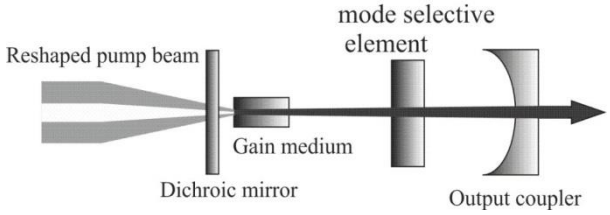

Figure 2.11 Schematic of typical solid-state lasers generating doughnut-shaped laser beams.

unstable resulting from the LG_{01} mode experiencing a weaker thermal lens [36, 37]. However, the handedness of the helical phase front for generated LG vortex beams tends to be random and cannot be controlled. The underlying reason for generating an LG vortex beam with determined handedness of helical phase front is still unknown. One hypothesis is that any intracavity asymmetric factor breaks the degeneracy of $LG_{0\pm m}$ modes. In contrast, often $LG_{0\pm m}$ modes with opposite handedness helical phase fronts tend to oscillate simultaneously inside a laser cavity, and coherent superposition of two equally-weighted modes of opposite handedness leads to an output beam with a petal-like intensity profile, which has been reported in the literature [15, 34, 38, 39]. Bisson explored the diffraction of a beam at a circular aperture to form a pump with a ring-shaped intensity distribution that spatially matched the intensity of the desired LG_{0m} mode. The beam was employed to pump a Nd:YAG laser leading to petal-like LG_{0m} beams with orders ranging from m=1 to more than m=200 [39]. Naidoo successfully demonstrated the intra-cavity generation of a petal-like beam in an Nd:YAG laser cavity by using an intracavity stop to suppress the fundamental mode and to induce equivalent losses for the two opposite handedness $LG_{0\pm m}$ modes. In addition, the fact that the petal-like pattern is the result of coherent superposition of two equally-weighted opposite handedness $LG_{0\pm m}$ modes was verified by an intensity measurement, analysis on propagation and a full modal decomposition using a phase-only spatial light modulator [15]. However, two petal-like beams with different frequencies are also able to form a doughnut-shaped beam as a result of incoherent superposition [40]. This was demonstrated in an end-pumped Nd:YAG laser where a doughnut-shaped output beam was obtained with the aid of an intracavity spatial light modulator. But the results of the modal decomposition revealed that the doughnut-shaped output beam was actually due to incoherent superposition of two petal-like beams.

2.5.2 Vector LG modes generation

2.5.2.1 Passive generation methods

Radially-polarized and azimuthally-polarized LG beams have been paid particular attention among other vector LG beams. Similar to the generation of helically phased beam, passive methods have also been widely used to obtain these beams. Usually, a polarization converter with spatially variant polarization properties is

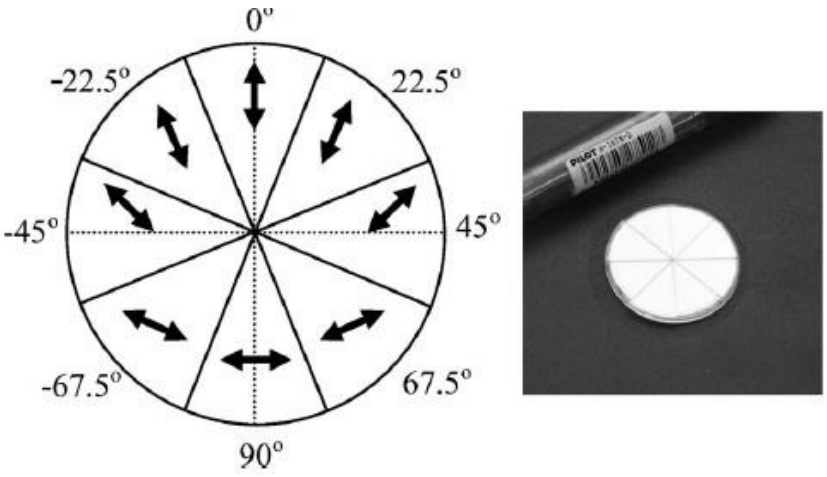

Figure 2.12 Schematic of a spatially variant segmented half-wave plates (left); and its photo image (right) [41].

employed to transform a linearly or circularly-polarized input beam to the beam with desired cylindrical vector polarization. One of most popular polarization converters is a segmented waveplate shown in Figure 2.12 [41]. It consists of eight segments of half-wave plates glued together with the appropriate orientation. When a linearly polarized beam propagates through it, each half-wave plate will rotate the linear polarization by a different amount resulting in a doughnut-shaped intensity distribution with radial polarization in the far-field. The power handling capability of this element is mainly limited by the damage of the bonded interfaces. The intensity of the damage threshold can be up to ~tens of watts/mm^2. Alternatively, a spatially variant waveplate can be fabricated by subwavelength gratings inducing form birefringence [42]. The advantage of this technique is that the orientation of the fast/slow axis of birefringence can be rotated continuously and hence the transformed beam has excellent radial or azimuthal polarization purity. Another popular method is to use a liquid crystal spatial light modulator, which offers flexibility and the capability of producing almost any arbitrary complex beam polarization [43]. In addition, interferometric techniques have also been used to generate cylindrical vector beams in free space. For example, radial or azimuthal polarizations can be formed by a coherent superposition of orthogonally polarized TEM_{01} and TEM_{10} beams [44].

2.5.2.2 Active generation methods

The first direct generation of a vector LG beam was demonstrated in a pulsed ruby laser, in which an intracavity uniaxial c-cut calcite crystal was utilized as a polarization discriminating element allowing only the azimuthally polarized-mode to be within the stability region of the laser resonator [18]. The development of direct methods of generating vector LG beams in solid-state lasers has been revived in last decade. Similar to techniques applied to generate scalar LG beams, techniques with a polarization selective optical element in combination with a special resonator configuration are always employed.

A conical Brewster prism having a high transmission for radial polarization and relative lower transmission for azimuthal polarization shown in Figure 2.13(a) was inserted into the laser resonator to selectively generate a radially polarized beam from a Nd:YAG laser [45]. This element consists of silica glass convex and concave Brewster conical prisms. The lateral surface of the convex prism was coated with multilayers of alternating Ta_2O_5 and SiO_2 thin films to enhance the polarization discrimination, and the concave prism is used to compensate the beam divergence.

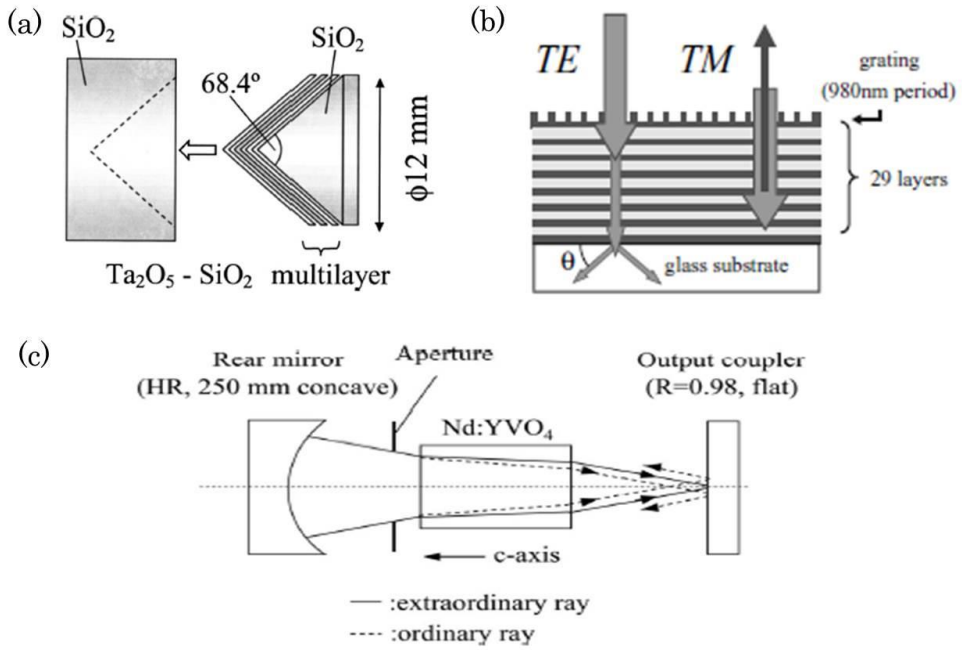

Figure 2.13 (a) A conical Brewster prism [45]; (b) cross-section of the polarization-selective circular grating mirror [46]; (c) schematic of a laser resonator for generating radially polarized beam based on the use of birefringence of crystal [47].

A polarization-selective circular grating mirror as shown in Figure 2.13(b) has been utilized in an Nd:YAG laser to successfully generate over 100W in a radially polarized output beam with a degree of polarization purity exceeding 70% [46]. This mirror is composed of a circular diffraction grating engraved on the top of several alternating high and low index dielectric multilayers. In this case, the electric field parallel to the grating line (azimuthally polarized beam) will be coupled into a guided mode in the multilayer system and experience losses due to leakage into the substrate, whereas the electric field orthogonal to the grating line (radially polarized beam) is not affected by the grating but is totally reflected. As a result, azimuthal polarization experiences substantial loss compared with the radial polarization.

In addition to the above specially designed polarization selective elements, more common uniaxial crystals with axially symmetric birefringence including Nd-doped or undoped c-cut YVO_4 or α-BBO were employed as polarization discrimination elements in several diode-pumped solid state lasers. One example of an experimental setup employing this technique is shown in Figure 2.13(c). These methods employed double refraction within the crystal to make the ordinary rays and extraordinary rays experienced a different optical path within the laser cavity so that a different loss might be introduced to achieve mode selection [47-49]. Another typical technique is to exploit the thermal induced birefringence within the laser gain medium such that the radial and azimuthal polarization components have different focal lengths [50]. One of the advantages of this approach is that no special polarization selective components are needed. The laser resonator should be designed near the resonator stability limit, so that the beam with one polarization is within the resonator stable region, but the orthogonal one is outside the stable region. The performance of this technique was enhanced by using a ring-shaped pump beam. In this case, thermally induced bifocusing makes the two orthogonal modes have a slightly different mode volume, and hence the mode with better spatial overlap with the population inversion will reach the threshold first and be preferentially excited. This technique has been applied to a hybrid Er:YAG laser yielding up to 13.1 W of radially polarized LG_{01} output [51].

2.6 Applications of doughnut-shaped LG beams

In section 2.5 we discussed techniques for generating either LG scalar or vector beams. In this section we will look at some promising applications for these unique beams.

2.6.1 Applications for vortex LG beams

The applications of LG scalar beams arise from their helical phase fronts and associated doughnut-shaped intensity distributions and OAM. These beams have widespread applications in optical manipulation [52], advanced quantum optics [53], optical communications [54], new types of imaging system [55], and material processing [56].

Since the optical vortex beam has a doughnut-shaped intensity distribution in the focal plane as shown in Figure 2.14(a), it is more suitable for trapping metallic particles [57], absorbing [58], low-index or high-index dielectric-constant particles [59] that would be damaged or unstably trapped by conventional optical tweezers using Gaussian-shaped beams. Lack of radiation pressure along the axial direction allows for more efficient trapping for large dielectric particles compared with Gaussian beams [60, 61]. Particles are always drawn to the ring's circumference as shown in Figure 2.14(b). Moreover, OAM transfers to illuminated particles exerting

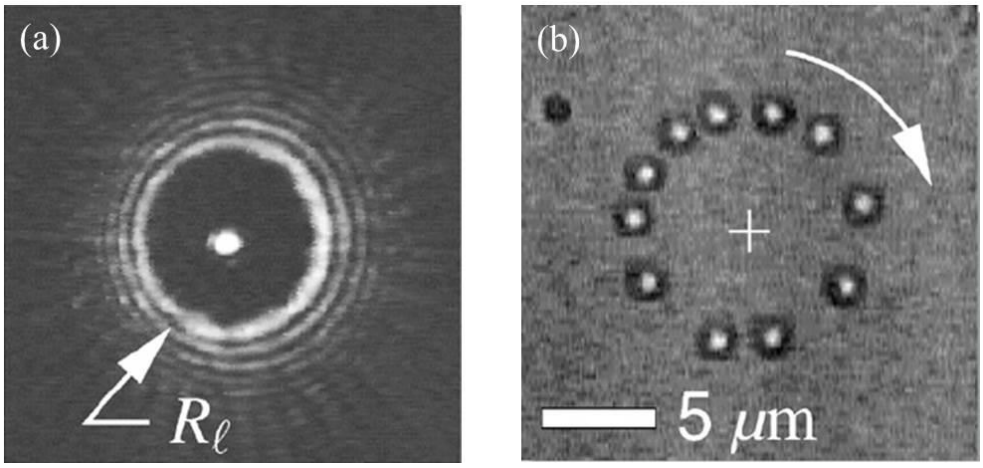

Figure 2.14 (a) Intensity distributions of a helical phased beam with topology *l* in the focal plane; the central bright spot is intensity for a collinear propagated Gaussian beam. (b) 1um diameter colloidal particles circulate when held in a helical beam [57].

forces and torque on them resulting in rotation around the beam axis as shown in Figure 2.14(b) [57].

The fact that each photon carries OAM for doughnut-shaped LG scalar beams indicates a potential application of OAM in the quantum domain in that OAM is a useful description of a spatial degree of freedom of light [53]. Similar to frequency, it exists within the infinite dimensional Hilbert space, and the number of dimensions of the Hilbert space can be controlled as required [62]. The information transfer and communication encoded as OAM states of a beam has been successfully demonstrated in [54]. This provides a potential route to tremendously increase the capacity of communication systems either by encoding information as OAM states or by using OAM beams as information carriers for multiplexing [63]. Recently,terabit free-space data transmission was achieved by employing OAM multiplexing technique [63].

In addition, the utilization of nanosecond optical vortex pulses in laser ablation yielded a fine, clear and smooth processed surface with less ablation threshold in comparison with a non-vortex annular beam with same polarization [56].

2.6.2 Applications for cylindrical vector LG beams

The applications for LG vector beams originate from their unique focusing properties including a much smaller spot size in comparison with a linearly polarized beam and a strong longitudinal electric field component in the vicinity of the focus obtained under tight focusing [19]. The unique vectorial polarization distribution has potential applications in high resolution imaging including confocal microscopy, second-harmonic generation microscopy [64], and dark field imaging [65]. Radially polarized beams offer a more promising configuration for laser driven electron acceleration in a vacuum and they may have the capability to accelerate electrons to the level of GeV energies in a vacuum [66-68] due to a strong longitudinal electric field component playing a dominant role in accelerating electrons. From Eq.(2.50) it can be seen that the transverse and longitudinal electric components are $\pi/2$ out of phase indicating the vanishing of the time averaged Poynting vector along the optical axis. This property offers stable trapping of metallic particles in 3-dimensions [69].

In addition to a variety of applications in the scientific research areas mentioned above, radially and azimuthally polarized LG beams have also widespread applications in laser material processing including cutting, micro-hole drilling and welding [70]. The benefit of these cylindrically symmetric polarization states is that the material surface is processed with the same (i.e. spatially and temporally invariant) polarization state independent of process movement. In addition, the doughnut-shaped intensity profile has a steeper intensity gradient leading to a more flat-top like distribution compared with Gaussian beams.

During material processing, the radiation of the incident laser beam is absorbed by the target material and is converted into the heat to form a cutting kerf, a micro-hole or an ablated surface structure. A typical schematic geometry of laser material processing is shown in Figure 2.15(a). The polarization of the beam parallel with the interaction plane is called p-polarization, and the orthogonal one is called s-polarization. In the case of cutting a thick metal sheet with a large ratio of thickness to the cutting width, the majority of radiation absorption occurs on the front and on the wall of the cleaving channel, which means the beam always interacts with the material at a very large angle (~85°). Figure 2.15(b) shows one example of the calculated absorption coefficient for p-polarized and s-polarized beam at different incident angles according to the Fresnel law. It is evident that the absorption coefficient for p-polarization is significantly greater than that of s-polarization at large incident angles, and hence the beam with p-polarization in the interaction plane is preferred to maximize the absorption efficiency. Niziev calculated the cutting speed for radially poalrized beam can be increased by a

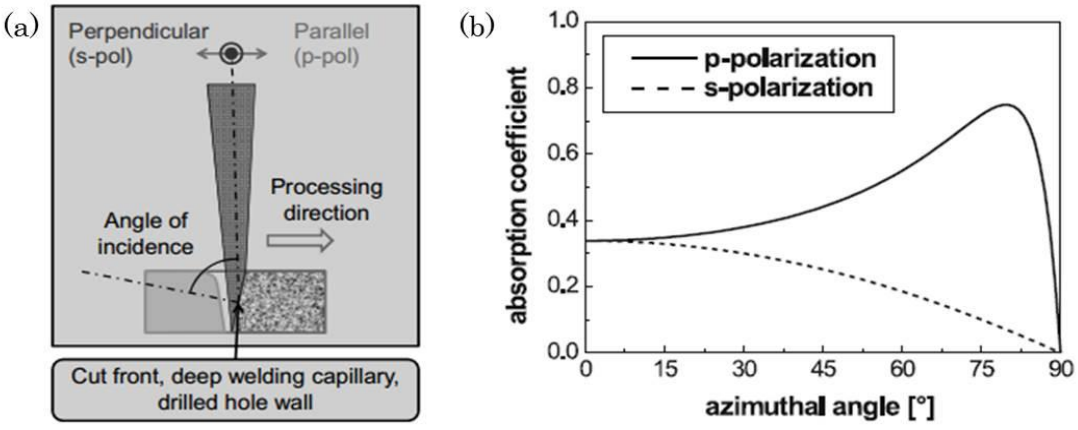

Figure 2.15 (a) Schematic geometry of laser material processing; (b) calculated absorption coefficient for p-polarized and s-polarized beams for mild steel [70].

factor 1.5-2 compared with traditionally p-polarized and circularly polarized beams [71]. The main reason is that a global p-polarized beam with respect to the cutting channel surface leading to an increased absorption coefficient. Experimental results from Institute fur Strahlwerkzeuge shows an increase of up to 40% in cutting velocity for a CO_2 laser with radial polarization in cutting 2mm stainless steel sheet [70].

The application of laser drilling, however, is much different and rather complicated due to multiple reflections at the wall, the waveguiding effect and finally the absorption of radiation at the bottom of the hole are key factors in determining the laser drilling efficiency [72]. Experimental investigations on micro-hole drilling by using radially and azimuthally polarized nanosecond and picosecond pulses were carried out in [72, 73]. The results show that either radially or azimuthally polarized beam have the best efficiency depending on the optical properties of the metal. Figure 2.16 shows a transverse section of two microholes drilled in a 1mm thickness steel sheet with radially and azimuthally polarized pulses. A slender capillary with straight walls was obtained with the azimuthally polarized beam. Moreover, it was found that azimuthal polarization is more suitable for drilling holes with high aspect ratios in >1mm thick sheet or extraordinarily small holes with a diameter less than 50 μm, while the radial polarization can be used in the fabrication of boreholes with relatively large diameters in thin sheets with thickness less than 500 μm.

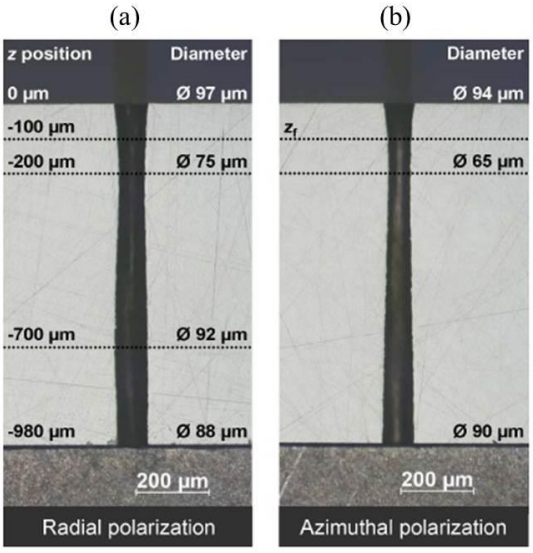

Figure 2.16 Transverse section of microholes in 1mm sheets, drilled with radially (a) and azimuthally (b) polarized beams [73].

Bibliography

1. T. H. Maiman, "Stimulated optical radiation in ruby," Nature **187**, 493-494 (1960).

2. L. J. Rosenkrantz, "GaAs diode-pumped Nd:YAG Laser," Journal of Applied Physics **43**, 4603-4605 (1972).

3. S. Strohmaier, C. Tillkorn, P. Olschowsky, and J. Hostetler, "High-power, high-brightness direct-diode lasers," Opt. Photon. News **21**, 24-29 (2010).

4. R. K. Huang, B. Chann, J. Burgess, M. Kaiman, R. Overman, J. D. Glenn, and P. Tayebati, "Direct diode lasers with comparable beam quality to fiber, CO_2, and solid state lasers," High-Power Diode Laser Technology and Applications X **8241**(2012).

5. W. Koechner, *Solid-State Laser Engineering,* 6th. (Springer, 2005).

6. D. R. Paschotta, "Neodymium-doped gain media" (2014), retrieved http://www.rp-photonics.com/img/ndyag_levels.png.

7. R. C. Powell, *Physics of Solid-State Laser Materials* (Springer, New York, 1998).

8. K. Kubodera and K. Otsuka, "Single-transverse-mode LiNdP4O12 slab waveguide Laser," Journal of Applied Physics **50**, 653-659 (1979).

9. M. J. F. Digonnet and C. J. Gaeta, "Theoretical analysis of optical fiber laser amplifiers and oscillators," Applied Optics **24**, 333-342 (1985).

10. I. S. 11146, "Lasers and laser-related equipment: Test methods for laser beam widths, divergence angles and beam propgataion ratios," (2005).

11. A. E. Siegman, *Lasers* (University Science Books, 1986).

12. A. G. Fox and T. Li, "Resonant modes in a maser interferometer," Bell Syst. Tech. J. **40**, 453-488 (1961).

13. D. G. Hall, "Vector-beam solutions of Maxwell's wave equation," Optics Letters **21**, 9-11 (1996).

14. Q. Zhan, "Cylindrical vector beams: from mathematical concepts to applications," Advances in Optics and Photonics **1**, 1 (2009).

15. D. Naidoo, K. Ait-Ameur, M. Brunel, and A. Forbes, "Intra-cavity generation of superpositions of Laguerre-Gaussian beams," Applied Physics B: Lasers and Optics **106**, 683-690 (2012).

16. A. V. Nesterov and V. G. Niziev, "Laser beam with axially symmetric polarization," J. Phys. D: Appl. Phys **33**(2000).

17. Y. Senatsky, J. Bisson, J. Li, A. Shirakawa, M. Thirugnanasambandam, and K. Ueda, "Laguerre-Gaussian modes selection in diode-pumped solid-state lasers," Optical Review **19**, 201-221 (2012).

18. D. Pohl, "Operation of a ruby laser in the purely transverse electric mode TE01," Applied Physics Letters **20**, 266-267 (1972).

19. R. Dorn, S. Quabis, and G. Leuchs, "Sharper Focus for a Radially Polarized Light Beam," Physical Review Letters **91**,233901 (2003).

20. S. Quabis, S. R. Dorn, M. Eberler, O. Glockl, and G. Leuchs, "Focusing light to a tighter spot," Optics Communications **179**, 1-5 (2000).

21. J. H. Poynting, "The wave motion of a revolving shaft, and a suggestion as to the angular momentum in a beam of circularly polarised light," Proceedings of the Royal Society of London. Series A **82**, 560-567 (1909).

22. L. Allen, M. W. Beijersbergen, R. J. C. Spreeuw, and J. P. Woerdman, "Orbital angular momentum of light and the transformation of Laguerre-Gaussian laser modes," Physical Review A **45**, 8185-8189 (1992).

23. J. D. Jackson, *Classical Electrodynamcis* (Willey, New York, 1962).

24. A. T. O'Neil, I. MacVicar, L. Allen, and M. J. Padgett, "Intrinsic and extrinsic nature of the orbital angular momentum of a light beam," Physical Review Letters **88**, 053601 (2002).

25. E. Wolf, "Electromagnetic diffraction in optical systems. I. An integral representation of the image field," Proceedings of the Royal Society of London. Series A. Mathematical and Physical Sciences **253**, 349-357 (1959).

26. B. Richards and E. Wolf, "Electromagnetic diffraction in optical systems. II. Structure of the image field in an aplanatic system," Proceedings of the Royal Society A: Mathematical, Physical and Engineering Sciences **253**, 358-379 (1959).

27. K. S. Youngworth and T. G. Brown, "Focusing of high numerical aperture cylindrical-vector beams," Optics Express **7**, 77-87 (2000).

28. M. W. Beijersbergen, L. Allen, H. E. L. O. van der Veen, and J. P. Woerdman, "Astigmatic laser mode converters and transfer of orbital angular momentum," Optics Communications **96**, 123-132 (1993).

29. M. W. Beijersbergen, R. P. C. Coerwinkel, M. Kristensen, and J. P. Woerdman, "Helical-wavefront laser beams produced with a spiral phaseplate," Optics Communications **112**, 321-327 (1994).

30. N. R. Heckenberg, R. McDuff, C. P. Smith, and A. G. White, "Generation of optical phase singularities by computer-generated holograms," Optics Letters **17**, 221-223 (1992).

31. V. Garbin, D. Cojoc, E. Ferrari, R. Z. Proietti, S. Cabrini, and E. Di Fabrizio, "Optical micro-manipulation using Laguerre-Gaussian beams," Japanese Journal of Applied Physics Part 1-Regular Papers Brief Communications & Review Papers **44**, 5773-5776 (2005).

32. G. Machavariani, N. Davidson, E. Hasman, S. Blit, A. A. Ishaaya, and A. A. Friesem, "Efficient conversion of a Gaussian beam to a high purity helical beam," Optics Communications **209**, 265-271 (2002).

33. A. Schwarz and W. Rudolph, "Dispersion-compensating beam shaper for femtosecond optical vortex beams," Optics Letters **33**, 2970-2972 (2008).

34. A. Ito, Y. Kozawa, and S. Sato, "Generation of hollow scalar and vector beams using a spot-defect mirror," J. Opt. Soc. Am. A **27**, 2072-2077 (2010).

35. D. Naidoo, T. Godin, M. Fromager, E. Cagniot, N. Passilly, A. Forbes, and K. Ait-Ameur, "Transverse mode selection in a monolithic microchip laser," Optics Communications **284**, 5475-5479 (2011).

36. S. P. Chard, P. C. Shardlow, and M. J. Damzen, "High-power non-astigmatic TEM00 and vortex mode generation in a compact bounce laser design," Applied Physics B: Lasers and Optics **97**, 275-280 (2009).

37. M. Okida and T. Omatsu, "Direct generation of high power Laguerre-Gaussian output from a diode-pumped Nd:YVO4 1.3-μm bounce laser," Optics Express **15**, 7616-7622 (2007).

38. Y. F. Chen, Y. P. Lan, and S. C. Wang, "Generation of Laguerre–Gaussian modes in fiber-coupled laser diode end-pumped lasers," Applied Physics B: Lasers and Optics **72**, 167-170 (2001).

39. J. F. Bisson, Y. Senatsky, and K.-I. Ueda, "Generation of Laguerre-Gaussian modes in Nd:YAG laser using diffractive optical pumping," Laser Physics Letters **2**, 327-333 (2005).

40. I. A. Litvin, S. Ngcobo, D. Naidoo, K. Ait-Ameur, and A. Forbes, "Doughnut laser beam as an incoherent superposition of two petal beams," Optics Letters **39**, 704-707 (2014).

41. G. Machavariani, "Efficient extracavity generation of radially and azimuthally polarized beams," Optics Letters **32**, 1468-1470 (2007).

42. Z. Bomzon, V. Kleiner, and E. Hasman, "Formation of radially and azimuthally polarized light using space-variant subwavelength metal stripe gratings," Applied Physics Letters **79**, 1587 (2001).

43. M. A. A. Neil, F. Massoumian, R. Juskaitis, and T. Wilson, "Method for the generation of arbitrary complex vector wave fronts," Optics Letters **27**, 1929-1931 (2002).

44. S. C. Tidwell, D. H. Ford, and W. D. Kimura, "Generating Radially Polarized Beams Interferometrically," Applied Optics **29**, 2234-2239 (1990).

45. Y. Kozawa and S. Sato, "Generation of a radially polarized laser beam by use of a conical Brewster prism," Optics Letters **30**, 3063-5065 (2005).

46. T. Moser, H. Glur, V. Romano, F. Pigeon, O. Parriaux, M. A. Ahmed, and T. Graf, "Polarization-selective grating mirrors used in the generation of radial polarization," Applied Physics B **80**, 707-713 (2005).

47. K. Yonezawa, "Generation of a radially polarized laser beam by use of the birefringence of a c-cut NdYVO4 crystal," Optics Letters **31**, 2151-2153 (2006).

48. Y. Kozawa, K. Yonezawa, and S. Sato, "Radially polarized laser beam from a Nd:YAG laser cavity with a c-cut YVO4 crystal," Applied Physics B **88**, 43-46 (2007).

49. M. P. Thirugnanasambandam, Y. Senatsky, and K. Ueda, "Generation of radially and azimuthally polarized beams in Yb:YAG laser with intra-cavity lens and birefringent crystal," Optics Express **19**, 1905-1914 (2011).

50. I. Moshe, S. Jackel, and A. Meir, "Production of radially or azimuthally polarized beams in solid-state lasers and the elimination of thermally induced birefringence effects," Optics Letters **28**, 307-309 (2003).

51. J. W. Kim, J. I. Mackenzie, J. R. Hayes, and W. A. Clarkson, "High power Er:YAG laser with radially-polarized Laguerre-Gaussian (LG_{01}) mode output," Optics Express **19**, 14526-14531 (2011).

52. D. G. Grier, "A revolution in optical manipulation," Nature **424**, 810-816 (2003).

53. G. Molina-Terriza, J. P. Torres, and L. Torner, "Twisted photons," Nature Physics **3**, 305-310 (2007).

54. G. Gibson, J. Courtial, M. Padgett, M. Vasnetsov, V. Pas'ko, S. Barnett, and S. Franke-Arnold, "Free-space information transfer using light beams carrying orbital angular momentum," Optics Express **12**, 5448-5456 (2004).

55. S. Furhapter, A. Jesacher, S. Bernet, and M. Ritsch-Marte, "Spiral phase contrast imaging in microscopy," Optics Express **13**, 689-694 (2005).

56. J. Hamazaki, R. Morita, K. Chujo, Y. Kobayashi, S. Tanda, and T. Omatsu, "Optical-vortex laser ablation," Optics Express **18**, 2144-2151 (2010).

57. A. T. O'Neil and M. J. Padgett, "Three-dimensional optical confinement of micron-sized metal particles and the decoupling of the spin and orbital angular momentum within an optical spanner," Optics Communications **185**, 139-143 (2000).

58. H. Rubinsztein-Dunlop, T. A. Nieminen, M. E. J. Friese, and N. R. Heckenberg, "Optical trapping of absorbing particles," Advces in Quantum Chemistry. **30**, 469-492 (1998).

59. K. T. Gahagan and G. A. Swartzlander, "Simultaneous trapping of low-index and high-index microparticles observed with an optical-vortex trap," J. Opt. Soc. Am. B **16**, 533-537 (1999).

60. N. B. Simpson, D. McGloin, K. Dholakia, L. Allen, and M. J. Padgett, "Optical tweezers with increased axial trapping efficiency," Journal of Modern Optics **45**, 1943-1949 (1998).

61. A. T. O'Neil and M. J. Padgett, "Axial and lateral trapping efficiency of Laguerre-Gaussian modes in inverted optical tweezers," Optics Communications **193**, 45-50 (2001).

62. Y. F. Chen, T. M. Huang, C. F. Kao, C. L. Wang, and S. C. Wang, "Optimization in scaling fiber-coupled laser-diode end-pumped lasers to higher power: Influence of thermal effect," IEEE J. Quantum Elect. **33**, 1424-1429 (1997).

63. J. Wang, J. Y. Yang, I. M. Fazal, N. Ahmed, Y. Yan, H. Huang, Y. X. Ren, Y. Yue, S. Dolinar, M. Tur, and A. E. Willner, "Terabit free-space data transmission employing orbital angular momentum multiplexing," Nature Photonics **6**, 488-496 (2012).

64. D. P. Biss and T. G. Brown, "Polarization-vortex-driven second-harmonic generation," Optics Letters **28**, 923-925 (2003).

65. D. P. Biss, K. S. Youngworth, and T. G. Brown, "Dark-field imaging with cylindrical-vector beams," Applied Optics **45**, 470-479 (2006).

66. L. Cicchitelli, H. Hora, and R. Postle, "Longitudinal-Field Components for Laser-Beams in Vacuum," Physical Review A **41**, 3727-3732 (1990).

67. M. O. Scully and M. S. Zubairy, "Simple Laser Accelerator - Optics and Particle Dynamics," Physical Review A **44**, 2656-2663 (1991).

68. Y. I. Salamin, "Electron acceleration from rest in vacuum by an axicon Gaussian laser beam," Physical Review A **73**(2006).

69. Q. Zhan, "Trapping metallic rayleigh particles with radial polarization," Optics Express **12**, 3377-3372 (2004).

70. R. Weber, A. Michalowski, M. Abdou-Ahmed, V. Onuseit, V. Rominger, M. Kraus, and T. Graf, "Effects of Radial and Tangential Polarization in Laser Material Processing," Physics Procedia **12**, 21-30 (2011).

71. V. G. Niziev and A. V. Nesterov, "Influence of beam polarization on laser cutting efficiency," J. Phys. D: Appl. Phys. **32**(1999).

72. M. Meier, V. Romano, and T. Feurer, "Material processing with pulsed radially and azimuthally polarized laser radiation," Applied Physics A **86**, 329-334 (2006).

73. M. Kraus, M. A. Ahmed, A. Michalowski, A. Voss, R. Weber, and T. Graf, "Microdrilling in steel using ultrashort pulsed laser beams with radial and azimuthal polarization," Optics Express **18**, 22305-22313 (2010).

Chapter 3: Theory for end-pumped lasers with ring-shaped pump beams

3.1 Introduction

Scaling of the output power and brightness of diode-pumped solid-state lasers is necessary to meet the needs of many applications in both industrial and scientific regions including material processing, remote sensing, nonlinear frequency conversion to extend operating wavelength, and so on. Typically, solid-state lasers are classified as being either side pumped or end-pumped lasers. The side-pumped configuration is generally utilized in high-power operation due to weaker thermal effects but offers relatively low efficiency. On the other hand, the end-pumped geometry has been dominant at lower powers (a few watts) benefiting from the much higher efficiency achievable, flexibility, compactness in resonator design, and the relative ease with which diffraction-limited fundamental mode operation can be achieved [1]. Scaling end-pumped lasers to higher power, whilst making full use of these advantages, is attractive and in demand for a variety of applications. Since a small focused pump beam size is required for end-pumped solid-state lasers, power scaling has proved to be rather challenging due to the high heat loading density within the laser gain medium, which results in a highly-nonuniform temperature distribution. This consequently causes internal stresses and a deformation of the end faces of the laser material. The net result is degradation in beam quality due to highly aberrated thermal lensing, depolarization loss because of thermally induced birefringence and ultimately fracture of laser material [2].

In this chapter, we present a simple technique to reduce thermal lensing allowing scaling to higher output powers in an end-pumped laser geometry. This was achieved by tailoring the pump beam profile to a ring-shaped intensity distribution leading to a weaker thermal lensing effect in the laser crystal. Section 3.2 introduces a novel fibre-based pump beam re-shaping element to tailor the pump beam emerging from conventional fibre-coupled laser diodes to a beam with a ring-shaped intensity distribution in the near field. Section 3.3 theoretically investigates the thermal lens effects including the thermal lens strength and beam

quality degradation for different transverse modes in a cylindrically symmetric laser crystal under the ring-shaped pumping scheme. In section 3.4, we briefly discuss the basic principles of transverse mode selection using this unique pumping scheme.

3.2 Ring-shaped pumping scheme

Ring-shaped pump beams can be used to generate a doughnut-shaped population inversion within the laser crystal to spatially match to the intensity profile of higher-order LG modes and hence preferentially excite these higher-order modes. The ring-shaped pump beam can be formed by focusing a multi-mode fibre-coupled laser diode away from the focal plane [3], by using a diffractive element [4], and etc.. For the latter case, the beam is transmitted into a circular aperture to form different diffraction ring-shaped patterns depending on the Fresnel number. The doughnut-shaped beam can then be achieved by controlling the Fresnel number to N=2, which requires both a small aperture and long propagation distance. The disadvantages of this approach are obvious, namely that a large fraction of pump power is obstructed and the pumping system is really large and cumbersome. A novel fibre based beam conditioning element was developed in our group in 2011 [5], in which a capillary fibre was used to convert a Gaussian-shaped beam emitting from a Er,Yb fibre laser into a ring-shaped beam to pump an Er:YAG bulk solid-state laser leading to direct generation of radially-polarized LG_{01} mode with high efficiency. In this thesis, we further exploit this technique to investigate its performance on a number of other end-pumped solid-state lasers.

The pump beam tailoring technique used in this thesis involved a novel fibre-based beam conditioning element. A silica capillary fibre with a 105 μm diameter of inner-hole and 200μm diameter of inner-cladding with a NA of ~0.46 was tapered down to a solid-core with a diameter of ~105 μm. The NA of capillary fibre can be estimated through the formula: $NA^2 = 2 \cdot n_{clad} \cdot dn$ (where n_{clad} is the refractive index of inner-cladding and dn is the difference of refractive index between inner-cladding and polymer coating). Figure 3.1(a) shows a typical example of a side view of the tapered capillary fibre fabricated by using a Vytran filament fusion splicer (GPX-3000) by my colleague Dr Jae Daniel. In order to get the full image of the side view of the tapering region, the tapering length was set to be ~1.2mm. It can be seen that the diameter of inner cladding of capillary fibre rapidly reduces to a solid-

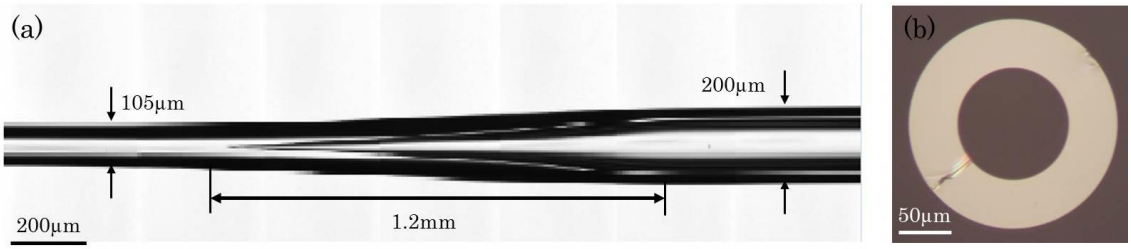

Figure 3.1 (a) The side view of tapered, and (b) end-facet of flat cleaved capillary fibre.

core with a diameter of ~105μm. Consequently, the pump beam emitted from a fibre-coupled laser diode can be easily coupled into the capillary fibre either by a traditional free-space lens-based coupling system or by splicing the two fibres together. For the capillary fibre used in the experiments in this thesis, the tapering length is actually 25mm to achieve a smooth variation of fibre diameter and hence reduce propagation loss. Figure 3.1(b) shows a typical end view of the capillary fibres cleaved by the York FK11 fibre cleaver. A line feature is always present opposite to the scribe location on the cleave plane. This is because the stress is propagated from the scribe location in both clockwise and anti-clockwise directions and meets on the other side of the fibre cleave plane. This line feature cannot be avoided in the experiments by using the York FK11 fibre cleaver, but can be reduced by optimizing the cleaving tension applied to the capillary fibre. Beam propagation in the inner-cladding (annular silica guide) of the capillary fibre results in a ring-shaped beam profile in the near-field. Some degradation of beam propagation quality is introduced by the pump beam conditioning element, which can be attributed to the highly multimode properties of capillary fibre.

Figure 3.2 shows a typical evolution of the beam intensity distribution at a wavelength of 808nm in the near field focused by an aspheric lens after emerging from the capillary fibre. The beam exits with a clear doughnut-shaped intensity profile with an outer diameter of ~800 μm and inner diameter of ~400 μm in the focal plane as shown in the Figure 3.2(d), which is a magnified image of the end-facet of the capillary. Beyond the focal plane, the beam profile varies with the propagation distance as a result of diffraction. The axial separation of each snapshot is equal to 2 mm. From Figure 3.2, we can conclude that the beam nearly maintains a ring-shaped profile for a range of ~10 mm. This range depends on the input beam quality and the beam size radius, that is the longer the Rayleigh range, the longer this range is. Although the brightness of the ring-shaped beam is much

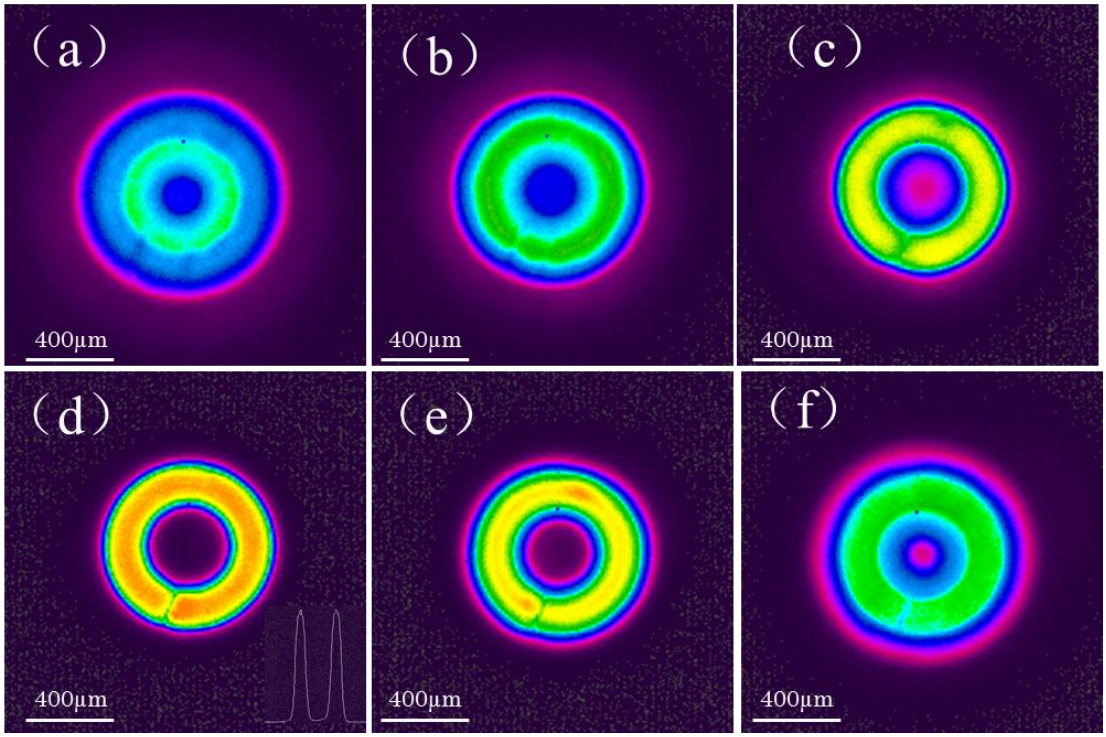

Figure 3.2 The snapshot of evolution of pump beam intensity distribution in the near field. The propagation distance between each snapshot is 2 mm.

lower than that of the original beam, it is still more than sufficient to spatially match the laser mode within the laser gain medium and preferentially excite the doughnut-shaped mode.

3.3 Thermal effects in end-pumped solid-state lasers

In this section, we focus on the adverse effects of heat generation in end-pumped solid-state lasers with a ring-shaped pump beam. We will consider a cylindrically symmetric laser rod with edge-cooling to determine an expression for the spatial temperature profile and thermal lens strength. Then we numerically calculate the effective thermal lens strength and investigate the degradation in beam quality caused by the thermally induced phase aberration.

3.3.1 Heat generation and temperature profiles

As illustrated in Figure 2.2, lasing emission requires ions from the lower energy level to be excited to higher energy levels to obtain a condition of population inversion by an optical pumping process. The laser wavelength is longer than the pump wavelength in most cases. The difference in energy between these two

wavelengths deposits into the crystal by non-radiative decay resulting in heat generation within the crystal, which is also known as quantum defect heating. The fraction of absorbed pump energy converted to heat due to the quantum defect is written as:

$$\eta_q = 1 - \frac{\lambda_p}{\lambda_l} \tag{3.1}$$

where λ_p and λ_l are the pump and laser wavelengths. For Nd:YAG and Nd:YVO_4 crystals, with a pump wavelength of λ_p =808nm and a laser wavelength of λ_l=1064nm, the fraction of pump power converted to the heat via quantum defect heating approaches ~0.24. Quantum defect heating is often considered to be the dominant mechanism for heat generation in the laser gain medium, but there are also other mechanisms that can contribute to heat loading in the crystal such as energy transfer upconversion (ETU) [6], concentration quenching [7], and excited state absorption [8]. The heat deposited in the gain medium must be conducted to the external environment where it can be removed. The net result is a spatial variation in temperature within the laser gain medium.

Here we will discuss an edge-cooled end-pumped laser rod with a cylindrical geometry mounted in a heat-sink with its outer surface maintained at a constant temperature as shown in Figure 3.3. The heat generated per unit volume can be written as:

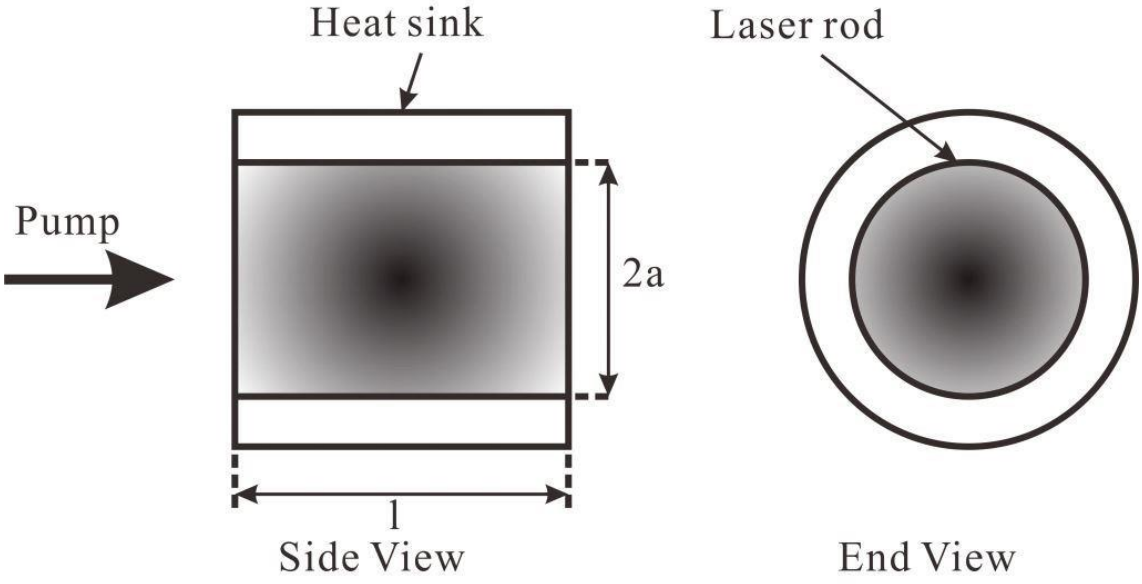

Figure 3.3 Side and end view of a typical edge-cooled, end-pumped solid-state laser.

$$Q(r,z) = \frac{dP_h(r,z)}{dV} = \alpha_p \eta_t I_p(r) \exp(-\alpha_p z) \tag{3.2}$$

where $P_h(r,z)$ is the power dissipated as heat in the laser crystal, α_p is the absorption coefficient of the gain material at the pump wavelength, η_t is the fraction of absorbed pump power converted to heat (we assume this value is independent on the spatial coordinate) and $I_p(r)$ is the pump beam intensity distribution in the laser rod.

Under steady-state conditions, the heat flux $h(r,z)$ must satisfy the equation [9]:

$$\nabla \cdot h(r,z) = Q(r,z) \tag{3.3}$$

The heat flux results in a spatial temperature distribution within the crystal given by:

$$h(r,z) = -K_c \nabla T(r,z) \tag{3.4}$$

where K_c is the thermal conductivity of the laser material.

If we assume that the heat flow is purely along the radial direction and neglect the axial heat flow, the one-dimensional heat conduction equation is determined by substituting Eq.(3.4) into (3.3) as shown in the following expression:

$$\frac{d^2T(r,z)}{dr^2} + \frac{1}{r}\frac{dT(r,z)}{dr} + \frac{Q(r,z)}{K_c} = 0 \tag{3.5}$$

Although the intensity profile of a ring-shaped pump beam as shown in Figure 3.2(d) looks like a Gaussian shape in the ring, we assume that the ring-shaped pump beam has a 'step-like' intensity profile with outer radius r_b and inner intensity null radius r_a as shown in Figure 3.4 in order to derive a simple analytical solution of the temperature distribution in the laser gain medium. This provides a simple way to describe the main differences of temperature distributions for traditional pump beams (Gaussian shape or top-hat shape) and ring-shaped pump beams. Moreover, by comparing with the traditional top-hat pump beams, this approximation provides a good estimation to quantify the advantages of this new type of pump beam in terms of maximum temperature in the crystal, thermal length strength and degradation in beam quality. Therefore, the normalized intensity distribution can be described as:

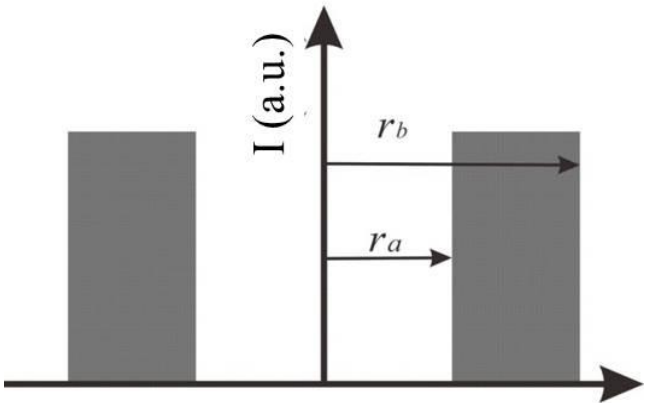

Figure 3.4 Intensity distribution for a ring-shaped beam with outer radius r_b and inner intensity null radius r_a.

$$I(r)=\begin{cases}\dfrac{1}{\pi(r_b^2-r_a^2)}\cdot & r_a<r<r_b \\ 0 & elsewhere\end{cases} \tag{3.6}$$

Substituting Eq. (3.6) into (3.2), the heat generated per unit volume can be expressed as:

$$Q(r,z)=\begin{cases}\dfrac{\eta_t\alpha_p exp(-\alpha_p z)P_{abs}}{\pi(r_b^2-r_a^2)} & r_a<r<r_b \\ 0 & elsewhere\end{cases} \tag{3.7}$$

where P_{abs} is the absorbed pump power. Substituting Eq.(3.7) into (3.5), the analytical solution for the temperature distribution can be derived as:

$$T(r,z)=\begin{cases}D_1 & 0\le r\le r_a \\ -\dfrac{1}{4}Ar^2+C_2\ln(r)+D_2 & r_a\le r\le r_b \\ C_3\ln(r)+D_3 & r_b\le r\le r_{rod}\end{cases} \tag{3.8}$$

where

$$\begin{cases} A = \dfrac{Q(r,z)}{K_c} \\ C_2 = \dfrac{1}{2} A r_a^2 \\ C_3 = \dfrac{1}{2} A (r_a^2 - r_b^2) \\ D_3 = T_F + \dfrac{Q(z)(r_b^2 - r_a^2)}{2h_0 r_{rod}} - C_3 \ln(r_{rod}) \\ D_2 = (C_3 - C_2)\ln(r_b) + \dfrac{1}{4} A r_b^2 + D_3 \\ D_1 = -\dfrac{1}{4} A r_a^2 + C_2 \ln(r_a) + D_2 \end{cases} \tag{3.9}$$

where T_F is the coolant temperature, r_{rod} is the radius of laser crystal, and h_0 is the convective heat transfer coefficient, which is a function of the coolant flow rate, the physical properties of the coolant and the laser rod. For a thermally insulated rod, $h_0 = 0$, and $h_0 = \infty$ for unrestricted heat flow from the rod surface to the heat sink. The heat transfer coefficient is typically around h_0 =0.5-2Wcm^{-2}K^{-1} for practical cases [10].

If the inner radius r_a is decreased to zero (i.e. corresponding to a top-hat shaped pump scenario), the temperature distribution can be written as:

$$T(r,z) = T_F + \frac{Q(z) r_b^2}{2h_0 r_{rod}} + \frac{Q(z) r_b^2}{4K} \cdot \begin{cases} -2\ln\left(\dfrac{r_b}{r_{rod}}\right) + 1 - \left(\dfrac{r}{r_b}\right)^2 & r \le r_b \\ -2\ln\left(\dfrac{r}{r_{rod}}\right) & r > r_b \end{cases} \tag{3.10}$$

Figure 3.5 shows the predicted temperature distributions for a Nd:YAG rod (Φ3×10mm) under conditions of ring-shaped pumping and top-hat shaped pumping beams. The following parameters were used for calculation: incident pump power P_p= 50 W, α_p =0.3 mm^{-1}, crystal length l_0=10mm, K_c=14Wm^{-1}K^{-1}, η_t =0.3; the ring-shaped pump beam had an outer radius of r_b = 0.4 mm and inner radius of r_a =0.21 mm. For comparison, the beam radius of top-hat shaped pump was set at r = 0.4 mm as well. It can be seen that the crystal has a maximum temperature on the surface face adjacent to the input pump beam, and the temperature rapidly decreases with the beam propagation distance. The difference between the two pumping schems is that the termparutre is more unifrom in the case of ring-shaped pumping scheme as shown in Figure 3.5(a).

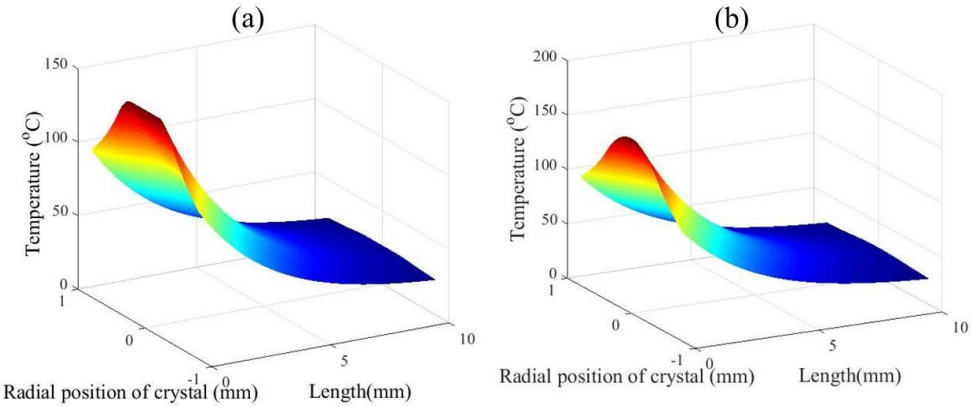

Figure 3.5 Calculated temperature distributions for a Nd:YAG crystal end pumped with 50 W of (a) ring-shaped pump beam and (b) top-hat pump profile.

Figure 3.6 shows radial temperature distributions on the front entrance of the laser crystal as a function of radius for both pump schemes. For the top-hat pump beam, the temperature has a parabolic funciton within the pump beam region and a logarithm function outside the pumped region. However, it can be seen that the temperature is constant within the region of $r < r_a$ for a ring-shaped pump beam due to no net heat flow within this region. Outside the pumped region ($r > r_b$), the temperature distribution is equivalent for both scenarios. It is worth noting that

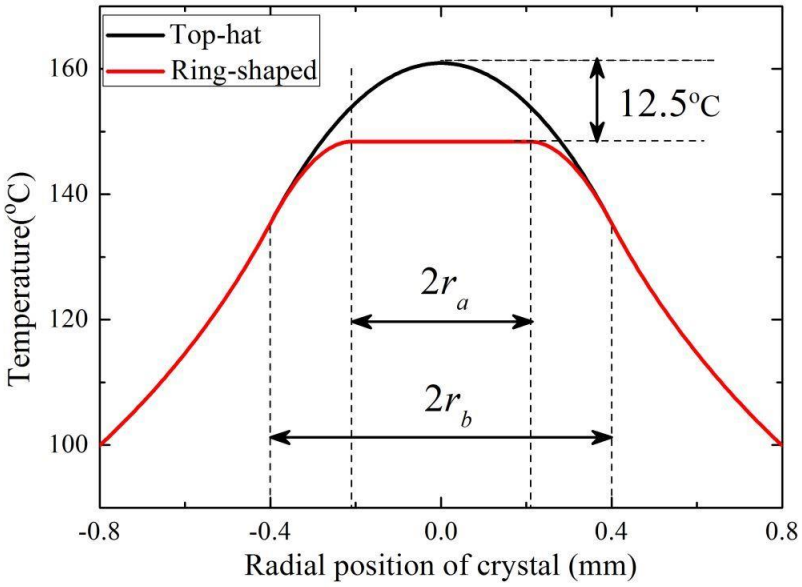

Figure 3.6 Radial temperature distributions on the pump input end-face of the crystal as a function of radius under conditions of top-hat pumping and ring-shaped pumping.

the maximum temperature is ~12.5℃ lower over the pumped region for the ring-shaped pump beam.

3.3.2 Thermal lensing

The non-uniform temperature distribution within the crystal leads to a significant thermal lens through three mechanisms [10]. Firstly, the temperature of the crystal is higher in the centre of the transverse mode compared with the outer regions, resulting in a transverse variation of refractive index due to the thermo-optic effect. Secondly, thermally induced stress causes changes in the refractive index due to the photo-elastic effect. Finally, thermal expansion of the crystal can cause bulging of the crystal end-faces, leading to different optical paths over the cross-section of the crystal. Among these three factors, the temperature dependence of the refractive index often plays a dominant contribution to thermal lensing, but the relative importance of the other two contributions depends on the thermo-optical and thermo-mechanical properties of the laser material.

According to [2], substituting Eq.(3.2) into (3.3) yields the following expression for the radial heat flux $h(r,z)$:

$$h(r,z)=\frac{\alpha_P \gamma \exp(-\alpha_P z)}{r}\int_0^r r' I_p(r')dr' \tag{3.11}$$

The temperature difference $\Delta T(r,z)$ from the centre of laser rod to any radial position r can be determined by substituting Eq.(3.11) into (3.4) described as:

$$\Delta T(r,z)=T(0,z)-T(r,z)=\frac{1}{K_c}\int_0^r h(r',z)dr' \tag{3.12}$$

Considering the variation of refractive index with temperature, the bulging end-faces, and stress-induced birefringence, the phase difference can be expressed as:

$$\Delta\phi(r)=\phi(0)-\phi(r)=\frac{2\pi}{\lambda}\int_0^l \Delta T(r,z)\left[\frac{dn}{dT}+(n-1)(1+\nu)\alpha_T+2C_{r,\varphi}n^3\alpha_T\right]dz \tag{3.13}$$

where dn/dT is the change of refractive index with temperature, v is Poisson's ratio, α_T is the thermal expansion coefficient, $C_{r,\varphi}$ are functions of the elasto-optical coefficient of the crystal. If we define:

$$s(r) = \frac{2\pi}{P_p}\int_0^r r' I_p(r')dr' \tag{3.14}$$

as the fraction of the total incident pump power P_p contained within a disc of radius r, then Eq. (3.13) can be rewritten as:

$$\Delta\phi(r) = \frac{P_p\eta_t\eta_{abs}\left[dn/dT + (n-1)(1+\nu)\alpha_T + 2C_{r,\varphi}n^3\alpha_T\right]}{K_c\lambda}\int_0^r \frac{s(r')}{r'}dr' \tag{3.15}$$

where $\eta_{abs} = 1 - exp(\alpha_p l)$ is the fraction of pump power absorbed in the laser rod. From Eq.(3.15), it can be seen that the transverse phase distortion $\Delta\phi(r)$ strongly depends on the transverse intensity profile $I_p(r)$ of the pump beam. Generally, the transverse phase distortion $\Delta\phi(r)$ does not only have a simple parabolic dependence, but also has higher-order aberrations. In this case, the thermal lens can be considered as one whose focal length varies radially. Thus, the focal length $f_t(r)$ of a thin thermal lens can be derived as [9]:

$$f_t(r) \approx \frac{2\pi r}{\lambda\dfrac{d\Delta\phi(r)}{dr}} \tag{3.16}$$

substituting Eq. (3.15) into (3.16), an approximation of thermal lens focal length can be written as:

$$f_t(r) = \frac{2\pi K_c r^2}{P_p\eta_{abs}\eta_t(dn/dT + (n-1)(1+\nu)\alpha_T + 2C_{r,\varphi}n^3\alpha_T)s(r)} \tag{3.17}$$

For a pump beam with the ring-shaped intensity profile described above, *s(r)* has the following expression:

$$s(r) = \begin{cases} 0 & r < r_a \\ \dfrac{r^2 - r_a^2}{r_b^2 - r_a^2} & r_a \le r \le r_b \\ 1 & r > r_b \end{cases} \tag{3.18}$$

Substituting Eq.(3.18) into (3.15) and (3.16), the thermal lens focal length can be derived as:

$$f_t(r)=\frac{2\pi K_c}{P\eta_{abs}\eta_t(dn/dT+(n-1)(1+\nu)\alpha_T+2C_{r,\varphi}n^3\alpha_T)}\begin{cases}\infty & r<r_a\\ (r_b^2-r_a^2)\dfrac{r^2}{r^2-r_a^2} & r_a\le r\le r_b\\ r^2 & r\ge r_b\end{cases} \quad (3.19)$$

In a laser material such as Nd:YAG, the temperature dependence of refractive index is the major contribution to thermal lensing. The stress dependence of refractive index and end-face bulging provide relatively weak contributions to thermal lensing.

From the expression for the thermal lens focal length described in Eq.(3.19), we can compare the thermal lens strength for top-hat and ring-shaped pump beams for otherwise identical operation conditions. The results of this comparison are shown in Figure 3.7, in which it can be seen that the advantage of the top-hat pump beam is in producing a lens which is essentially unaberrated over the pumped region $(r<r_b)$ due to a constant focal length. In theory, the ring-shaped pump beam produces a much weaker lens strength over the pump region, and the lens power even decreases to zero within the region of $r<r_a$, corresponding to an infinite focal length. Within the region of $r_a<r<r_b$, the lens power rapidly increases from zero to the value equal to the top-hat shaped pump beam at the radius of $r=r_b$. Beyond the pump region, the focal length strength varies in the same fashion for both

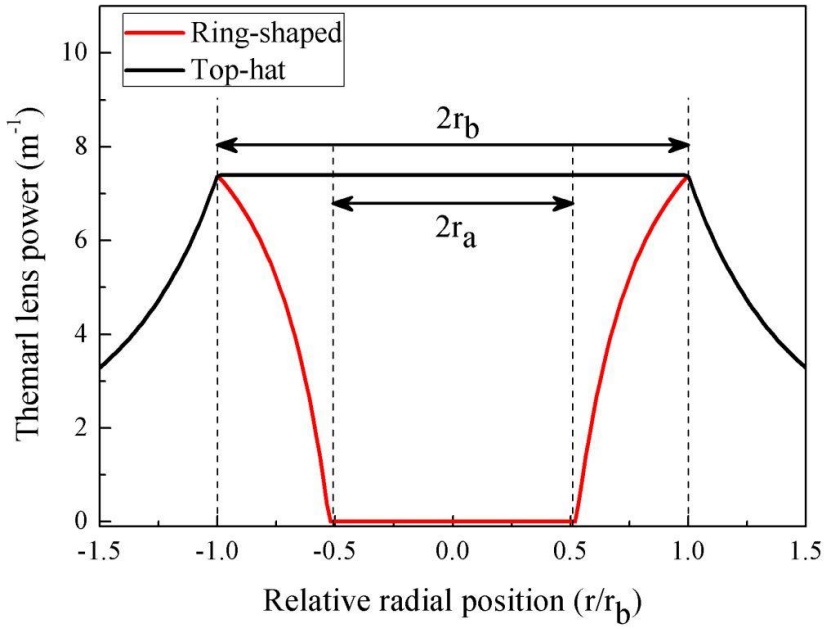

Figure 3.7 Calculated thermal lens power versus relative radial position for top-hat and ring-shaped pump beams.

pump beams. The rapid variation of focal length within the pump region leads to a wave aberration $\delta\phi(r)$ referred to a reference sphere:

$$\delta\phi(r)=\Delta\phi(r)-\frac{2\pi}{\lambda}\frac{r^2}{2f_e} \tag{3.20}$$

where f_e is the effective focal length. According to diffraction theory of the aberration, the fraction of intensity at the centre of the reference sphere can be described by the Strehl ratio (SR) in the presence of aberrations [11]. The effective focal length f gives the best quadratic approximation in Eq.(3.20) resulting in the maximum value for the SR weighted by the electric field amplitude ($u(r)$) of the beam [12]:

$$SR=\frac{\left|\int_0^{r_0}\exp(i\delta\phi(r))u(r)rdr\right|^2}{\left|\int_0^{\infty}u(r)rdr\right|^2} \tag{3.21}$$

where r_0 is the radius of the laser rod. The amplitude is $u(r)=\exp(-r^2/w^2)$ for the TEM_{00} mode and $u(r)=r\exp(-r^2/w^2)$ for the LG_{01} mode. Note, that the effective focal length f_e is dependent not only on the phase distortion $\Delta\phi(r)$ but also on the laser mode electric field distribution. For a spherical lens with no aberration, SR is equal to a maximum value of 1, and the value is always less than 1 for lens with a phase aberration. Since there is no analytical solution for Eq.(3.21), a numerical calculation has been performed to estimate the effective thermal lens focal length.

Figure 3.8 shows one example of the calculated effective thermal lens power for the TEM_{00} and LG_{01} modes as a function of pump power in an end-pumped Nd:YAG rod crystal for top-hat and ring-shaped pumping schemes. The beam waist radius for the TEM_{00} mode was set to $w=0.8r_b$. The other parameters for the laser crystal are the same as described in section 3.3.1. The blue dot represents the calculated thermal lens power at the centre of the pumped region in the case of a top-hat shaped pump beam according to Eq.(3.19). The effective thermal lens strengths for the TEM_{00} and LG_{01} modes with the top-hat shaped pump beam were also estimated by SR according to Eq.(3.21). The results are represented by the yellow line and purple dashed lines, respectively, showing a slightly weaker thermal lens strength than that of the value calculated from Eq.(3.19). This is due to a fraction of the laser beam power being beyond the pumped region which will experience a

longer thermal lens focal length, and hence the averaged effective thermal lens power is less than the value calculated from Eq.(3.19). It is obvious that the difference between these two methods is a function of relative beam size with respect to the pump beam size. The difference increases with the increase of relative laser beam size. When $w = r_b$, the thermal lens focal lengths for the TEM_{00} and LG_{01} modes estimated by SR are around 10% and 20% longer than results obtained from Eq.(3.19). Therefore, Eq. (3.19) still provides an effective and simple way to estimate the thermal lens power for lower-order modes with a beam size $w < r_b$. From Figure 3.8, we can see that the thermal lens strength in the case of a ring-shaped pump beam is less than that of a top-hat shaped pump beam. At a fixed pump power, the thermal lens focal length for the TEM_{00} mode in the case of a ring-shaped pump beam is 47% longer than that of top-hat shaped pump beam, this value becomes 31% for the LG_{01} mode. In contrast to the top-hat shaped pump beam, the thermal lens strength is slightly stronger for the LG_{01} mode than the TEM_{00} mode in case of a ring-shaped pump beam. The main reason is that the TEM_{00} mode benefits more from the central part of the pump region that has less thermal lens strength as its intensity is a maximum at the beam centre while the intensity is a null at the centre for LG_{01} mode.

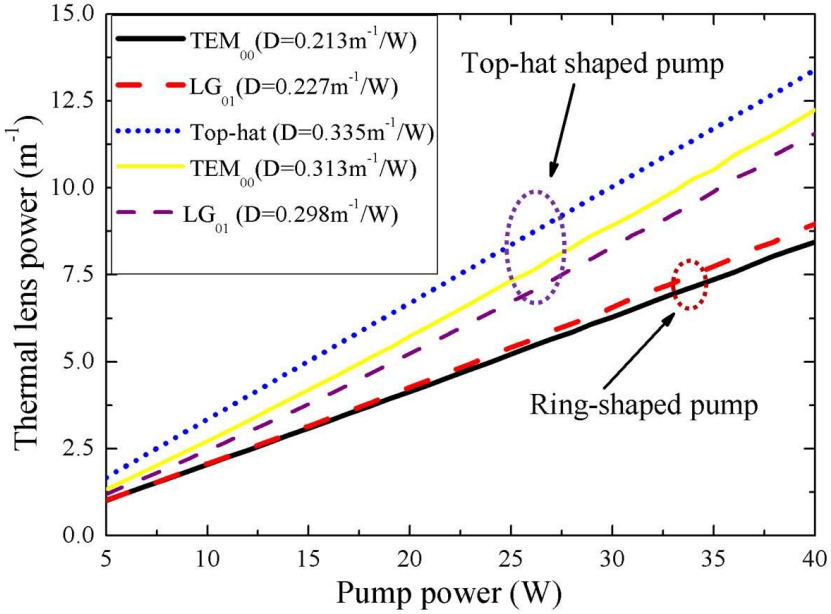

Figure 3.8 Calculated effective thermal lens power for TEM_{00} and LG_{01} modes as a function of pump power for top-hat shaped pumping and ring-shaped pumping schemes.

3.3.3 Effect of thermal lensing on beam quality

The variation of focal length with radial position described in Eq. (3.19) suggests that the phase difference created by thermal lensing is not simply parabolic with radial position, hence the effect of non-parabolic phase aberration should be considered. Since the phase aberration in the central portion of pumped region is relatively small, we restrict our consideration to situations where $w_s < w_p$, so that higher order terms than the quartic phase aberration can be neglected. The degradation in beam quality caused by a quartic phase aberration in a spherical lens or in a thermal lens generated by a pump beam with arbitrary transverse intensity profile has been theoretically analysed by Siegman [13] and Clarkson [2]. In this section, we apply the results of this analysis to numerically estimate the effect of a quartic phase aberration on beam quality degradation for a TEM_{00} and LG_{01} mode after passing through a thermal lens produced by a ring-shaped pump beam.

According to analysis in [13], a laser beam with arbitrary beam profile and beam quality M_i^2, after passing through a spherically aberrated lens with focal length f, will experience a phase distortion as follows:

$$\Delta\phi(r) = \frac{2\pi}{\lambda}\left(\frac{r^2}{2f} - C_4 r^4\right) \tag{3.22}$$

where C_4 is the quartic phase aberration coefficient, and the beam will suffer a degradation in beam quality with resultant M_f^2 given by:

$$M_f^2 = \left[(M_i^2)^2 + (M_q^2)^2\right]^{1/2} \tag{3.23}$$

where M_q^2 is the added contribution to beam quality due to the quartic phase aberration, which has a formula:

$$M_q^2 = \frac{8\pi\beta_r}{\lambda} C_4 \overline{r^4} \tag{3.24}$$

in which $\overline{r^4}$ is the averaged fourth power of radial moment evaluated on the beam intensity profile, and β_r is a dimensionless parameter given by:

$$\beta_r^2 = \frac{\overline{r^2}\,\overline{r^6} - \left(\overline{r^4}\right)^2}{\left(\overline{r^4}\right)^2} \tag{3.25}$$

The value of β_r is only dependent on the beam intensity profile and is calculated to be $1/\sqrt{2}$ and $1/\sqrt{3}$ for TEM_{00} and LG_{01} modes, respectively. It can be seen from Eq.(3.24) that the quartic phase aberration coefficient C_4 is the only parameter that should be determined to obtain M_q^2. The analytical solution for C_4 and resultant M_q^2 is derived in [2], which is a good approximation for the situation where $w_s < w_p$. Here we will numerically calculate C_4 in order to obtain a more accurate estimate for M_q^2 and the resultant M_f^2 in case of top-hat and ring-shaped pump beams. The process of numerical analysis is as follows: first the phase distortion is calculated according to Eqs. (3.15) and (3.18), then the effective thermal lens is estimated through Eqs.(3.20) and (3.21), and finally C_4 is estimated by the best approximation of Eq. (3.22). The resultant C_4 is then substituted to Eq.(3.24) to calculate the beam degradation factor M_q^2 and hence to obtain M_f^2 by Eq. (3.23).

Figure 3.9(a) and (b) show an example of variation of beam quality factor M^2 as a function of pump power for TEM_{00} and LG_{01} modes with two specific ratios of w_s/w_p after making a single pass of a Nd:YAG rod crystal end-pumped by top-hat and ring-shaped pump beams. In both figures, the red line and dark dashed-line represent the degraded beam quality for modes with two specific beam sizes ($w_s = 0.8w_p$ and $w_s = w_p$) induced by a pump beam with a ring-shaped intensity profile, and the blue circle and green square represent the values induced by a top-hat shaped pump beam. Obviously, both TEM_{00} and LG_{01} modes have significantly less degradation in the situation of ring-shaped pump beam especially when the

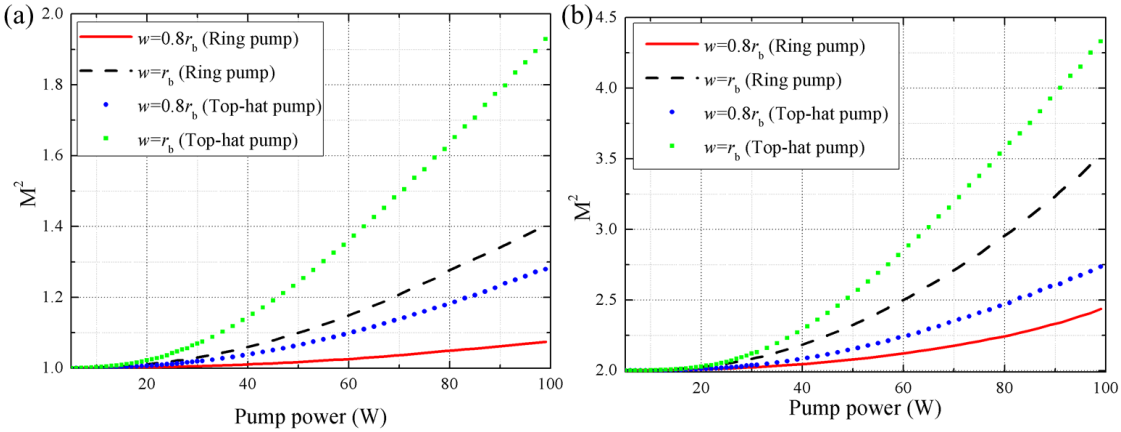

Figure 3.9 Beam quality factor M^2 versus the pump power for (a) TEM_{00} mode and (b) LG_{01} mode with two specific ratio of laser beam to pump spot size under pump beams with top-hat and ring-shaped intensity profiles.

pump power is greater than 20W. This can be attributed to a longer effective focal length as shown in Figure 3.8 under ring-shaped pumping resulting in a smaller quartic aberration coefficient, which is related to $C_4 \propto 1/f^3$ for a thin lens [13]. In addition, in both pumping schemes, a smaller ratio of w_s/w_p yields reduced beam deterioration as the beam occupies the central portion of pumped region where the non-parabolic distortion is much smaller than outside the pumped region. Furthermore, we can estimate the upper limit on pump power (P_{max}) before the degradation in beam quality becomes significantly. For example, if we have an initial beam quality $M_i^2 = 1$ for a diffraction-limited TEM_{00} mode and $M_i^2 = 2$ for a LG_{01} mode, and we can tolerate a degraded beam that the brightness decreases by 13.5%, then it is desirable that $M_f^2 = 1.08$ for the TEM_{00} mode and $M_f^2 = 2.15$ for the LG_{01} mode. For both modes with $w_s = 0.8w_p$ under the ring-shaped pump beam, we estimate P_{max}=100W and P_{max}=65W for TEM_{00} and LG_{01} modes, respectively; these values drop to 54W and 51W under a top-hat shaped pump beam. For modes with $w_s = w_p$ in the case of a ring-shaped pump beam, we estimate P_{max}=46W and P_{max}=37W for TEM_{00} and LG_{01} modes, respectively; and these values are estimated to be P_{max}=32W and P_{max}=32W under a top-hat shaped pump beam.

3.4 Transverse mode selection

3.4.1 Principle of mode selection

In this section, we will discuss the basic theory on transverse mode selection in solid-state lasers under the condition of ring-shaped pumping. According to Eq. (2.13) in Chapter 2, the threshold pump power for the first excited laser mode is dependent on the intracavity loss and effective pump area. Therefore, the mode which has the minimum value of $\delta_1 \cdot A_{eff}$ reaches threshold first, and hence will be preferentially excited.

Assuming a pump beam has a ring-shaped profile as shown in Figure 3.10, and the beam radius is constant within the laser crystal, the normalized pumping rate ($\int_{crystal} r_p(r, \varphi, z) = 1$) can be described as:

$$r_p(r,\varphi,z)=\begin{cases}\dfrac{1}{\pi(r_b^2-r_a^2)}\cdot\dfrac{\alpha e^{-\alpha z}}{1-e^{-\alpha l_0}} & r_a<r<r_b \\ 0 & elsewhere\end{cases} \tag{3.26}$$

where, α is the absorption coefficient at the pump wavelength, l_0 is the length of gain medium, r_a and r_b are the inner and outer radius of pump beam, respectively. The ring-shaped pump beam becomes to a top-hat shaped beam when r_a decreases to 0.

The normalized photon density for the LG_{0n} mode with negligible diffraction over the length of gain medium can be expressed as:

$$s_n(r,\varphi,z)=\frac{2}{n!\pi w^2 l_0}\left(\frac{2r^2}{w^2}\right)^n \exp(-\frac{2r^2}{w^2}) \tag{3.27}$$

where w is the beam waist radius for the fundamental TEM_{00} mode. Substituting Eqs.(3.26) and (3.27) to Eqs. (2.10) and (2.14), the analytical formula for the effective pump beam area for the LG_{0n} mode is derived as:

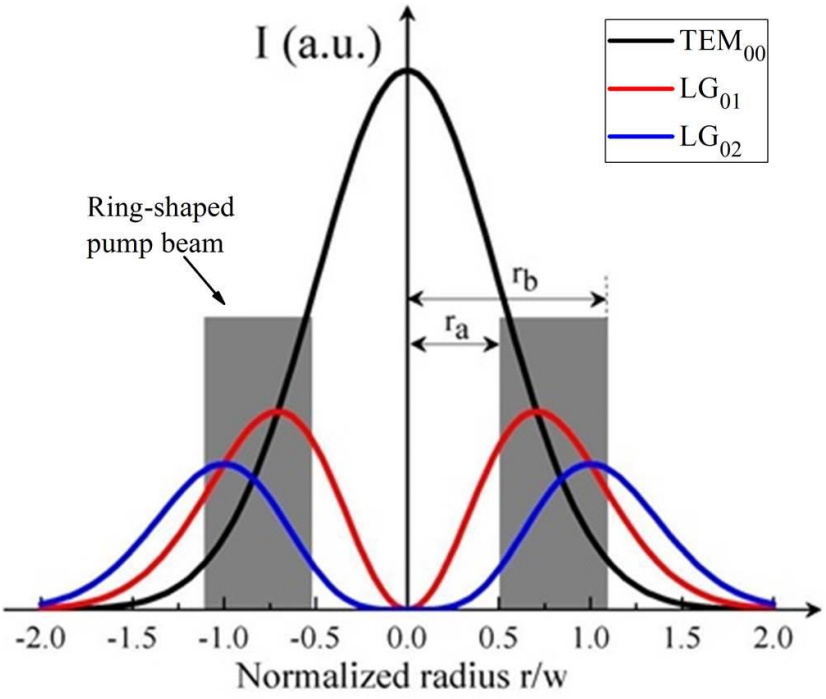

Figure 3.10 Radial intensity distribution for TEM_{00}, LG_{01}, and LG_{02} modes. The radius are normalized to the beam radius w of the fundamental TEM_{00} mode.

$$A_{eff}^{0n} = \pi(r_b^2 - r_a^2)\left\{\sum_{m=0}^{n}\frac{1}{(n-m)!}\cdot \left[\left(\frac{2r_a^2}{w^2}\right)^{n-m}\exp\left(-\frac{2r_a^2}{w^2}\right) - \left(\frac{2r_b^2}{w^2}\right)^{n-m}\exp\left(-\frac{2r_b^2}{w^2}\right)\right]\right\}^{-1} \tag{3.28}$$

For the three lowest order LG modes (TEM_{00}, LG_{01} and LG_{02}), Eq.(3.28) can be derived as follows:

$$A_{eff}^{00} = \pi(r_b^2 - r_a^2)\left[\exp(-\frac{2r_a^2}{w^2}) - \exp(-\frac{2r_b^2}{w^2})\right]^{-1} \tag{3.29}$$

$$A_{eff}^{01} = \pi(r_b^2 - r_a^2)\left[(\frac{2r_a^2}{w^2}+1)\cdot\exp(-\frac{2r_a^2}{w^2}) - (\frac{2r_b^2}{w^2}+1)\cdot\exp(-\frac{2r_b^2}{w^2})\right]^{-1} \tag{3.30}$$

$$A_{eff}^{02} = \pi(r_b^2 - r_a^2)\left[(\frac{2r_a^4}{w^4}+\frac{2r_a^2}{w^2}+1)\cdot\exp(-\frac{2r_a^2}{w^2}) - (\frac{2r_b^4}{w^4}+\frac{2r_b^2}{w^2}+1)\cdot\exp(-\frac{2r_b^2}{w^2})\right]^{-1} \tag{3.31}$$

Figure 3.10 shows a schematic of radial intensity distributions for the three lowest order LG modes and the ring-shaped pump beam intensity profiles. Intuitively, the ring-shaped pump beam has a better spatial overlap with the doughnut-shaped LG modes and hence a smaller effective pump area is obtained compared with the fundamental TEM_{00} mode. Actually, it can also have a better spatial overlap with the fundamental TEM_{00} mode in the following two cases: (a) The value of r_a/r_b is very small such that the ring-shaped beam is more like a top-hat shaped beam; (b) the r_b is much smaller than the beam radius of TEM_{00} mode (w). In general, the ring-shaped pump beam can have a better spatial overlap with any transverse LG mode depending on parameters including the ratio of r_a/r_b and its relative beam size (r_b/w). Therefore by controlling these parameters appropriately, the desired LG_{0n} mode can have the best overlap with the ring-shaped pump beam compared to the other LG modes leading to the smallest effective pump beam area, and hence it will reach threshold first and be preferentially excited. In the following sections, we will discuss how these parameters determine the LG mode selection criterion and impact on laser efficiency.

3.4.2 Threshold

We assume the ratio of the inner radius to the outer radius for the ring-shaped pump beam is $a = r_a/r_b$, which is a constant within the range of $0 \ll a < 1$; and the ratio of the outer radius (r_b) to the beam radius of the TEM_{00} mode is: $b = r_b/w$. From Eq.(3.28), it can be seen that the A_{eff} is only a function of b for a given value of a.

Figure 3.11 illustrates two examples of A_{eff} for the three lowest order LG modes as a function of relative pump beam radius b in the case where $a = 0.25$ and $a = 0.525$, respectively. It is evident that there are always three different regions where each LG mode will have the smallest A_{eff} compared with the other two modes and hence it will have the lowest threshold pump power ignoring any difference of intracavity loss for each mode. Within region I, in which $A_{eff}^{00} < A_{eff}^{01} < A_{eff}^{02}$, the fundamental TEM_{00} mode should have the lowest threshold pump power. With an increase of b, the effective pump area for the LG_{01} becomes smaller than the TEM_{00} mode ($A_{eff}^{01} < A_{eff}^{00}$) at a particular pump beam size b_1, which is equal to $1.21w^2$ and $0.93w^2$ in the case of Figure 3.11(a) and (b), respectively. Thus in region II, the LG_{01} mode has the smallest effective pump area, and hence is expected to have the lowest threshold pump power. With further increase in the pump beam size to region III, the LG_{02} mode will finally have the smallest effective pump area resulting in the lowest threshold pump power for the LG_{02} mode. Based on this simple calculation of the overlap integral parameter and hence the effective pump

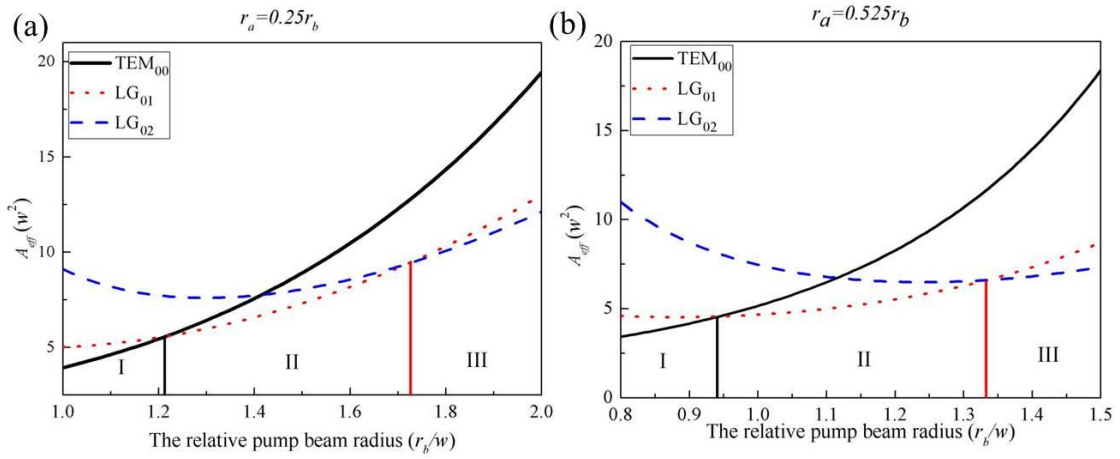

Figure 3.11 The calculated effective pump area for three lowest order of LG mode as a function of relative pump beam radius.

area for each mode, it is easy to design a particular resonator to allow the desired transverse mode to reach threshold first.

Furthermore, it is necessary to show that no other transverse mode breaks into oscillation when laser operates far above the threshold. From Eq.(2.18), we can see that it requires that the second mode has much less spatial overlap with the pump beam or the loss for the second mode is much higher than that of the first mode. Only in this way, the oscillation of the first mode can significantly saturate the gain to suppress the oscillation of other modes.

3.4.3 Slope efficiency

Slope efficiency is one of most important parameters to evaluate the performance of a laser. Furthermore, a prerequisite for this mode selection is that the lowest threshold mode should also have a high slope efficiency, so that it efficiently saturates the gain, and hence prevent adjacent modes from lasing. The slope efficiency has a formula given by Eq.(2.15), which is a function of several variables including the transmission efficiency of the output coupler, the total intracavity loss, pumping efficiency and coupling efficiency between pump beam and laser beam. Among them, coupling efficiency between pump and laser beams is one of the factors that must be optimized during the laser design.

In order to derive the analytical solution for the coupling efficiency η_c, we define:

$$V_1 = \iiint s(x,y,z) r_p(x,y,z) dv \tag{3.32}$$

$$V_2 = \iiint s^2(x,y,z) r_p(x,y,z) dv \tag{3.33}$$

Then, Eq.(2.16) can then be written as:

$$\eta_c = \frac{\left(\iiint s(x,y,z) r_p(x,y,z) dv\right)^2}{\iiint s^2(x,y,z) r_p(x,y,z) dv} = \frac{V_1^2}{V_2} \tag{3.34}$$

Substituting Eqs. (3.26) and (3.27) to Eqs. (3.32) and (3.33), V_1 and V_2 have the formulas as follows:

$$V_1 = \frac{1}{\pi(r_b^2 - r_a^2) l_0 n!}\left\{\sum_{m=0}^{n}\frac{n!}{(n-m)!}\cdot \left[\left(\frac{2r_a^2}{w^2}\right)^{n-m}\exp\left(-\frac{2r_a^2}{w^2}\right) - \left(\frac{2r_b^2}{w^2}\right)^{n-m}\exp\left(-\frac{2r_b^2}{w^2}\right)\right]\right\} \tag{3.35}$$

$$V_2 = \frac{1}{(r_b^2 - r_a^2)\cdot(n!\pi l_0 w)^2 4^n}\left\{\sum_{m=0}^{2n}\frac{2n!}{(2n-m)!}\cdot \left[\left(\frac{4r_a^2}{w^2}\right)^{2n-m}\exp\left(-\frac{4r_a^2}{w^2}\right) - \left(\frac{4r_b^2}{w^2}\right)^{2n-m}\exp\left(-\frac{4r_b^2}{w^2}\right)\right]\right\} \tag{3.36}$$

Therefore, η_c is derived by dividing V_1^2 by V_2 having an expression:

$$\eta_c = \frac{4^n w^2}{r_b^2 - r_a^2}\frac{\left\{\sum_{m=0}^{n}\frac{n!}{(n-m)!}\left[\left(\frac{2r_a^2}{w^2}\right)^{n-m}\exp\left(-\frac{2r_a^2}{w^2}\right) - \left(\frac{2r_b^2}{w^2}\right)^{n-m}\exp\left(-\frac{2r_b^2}{w^2}\right)\right]\right\}^2}{\sum_{m=0}^{2n}\frac{2n!}{(2n-m)!}\left[\left(\frac{4r_a^2}{w^2}\right)^{2n-m}\exp\left(-\frac{4r_a^2}{w^2}\right) - \left(\frac{4r_b^2}{w^2}\right)^{2n-m}\exp\left(-\frac{4r_b^2}{w^2}\right)\right]} \tag{3.37}$$

Figure 3.12 depicts the two examples of calculated coupling efficiency for the TEM_{00} and the LG_{01} mode as a function of relative pump beam size in the case of $a = 0.25$ and $a = 0.525$, respectively. For the TEM_{00} mode, η_c monotonically decreases with the increase of relative pump beam size. This is apparent as the intensity of the TEM_{00} mode is maximum at the beam centre and monotonically decreases with the increase of radial position. The increase of relative pump beam

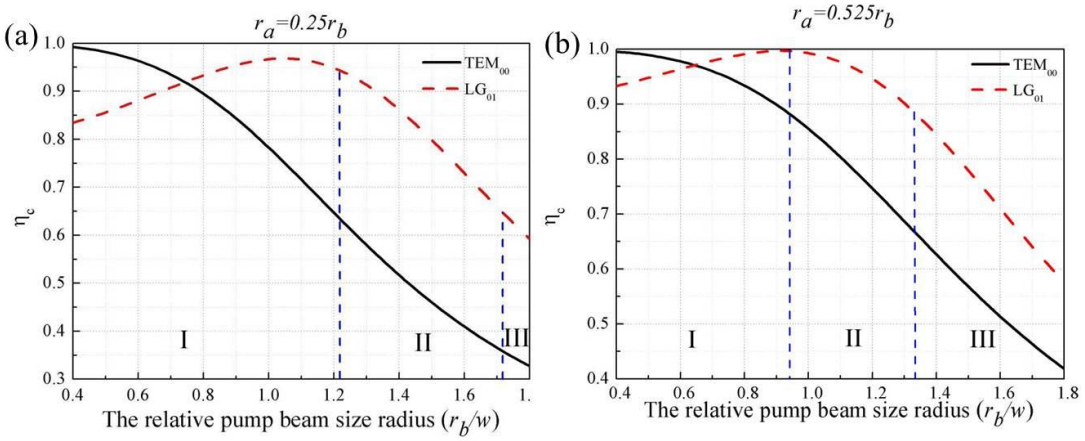

Figure 3.12 The calculated coupling efficiency as a function of normalized pump beam radius for LG_{01} mode.

size induces a decrease of spatial overlap between pump beam and laser mode. The population inversion moves towards the wings of the TEM_{00} mode and leads to an increased unpopulated inversion region in the centre of beam and hence the coupling efficiency decreases. In addition, for pump beams with the same relative spot size, the one with a larger value of a has a higher value of η_c. This is because the larger a is, the thinner the ring-shaped pump beam is, and hence the intensity of the TEM_{00} mode within the pump region is more uniform leading to a higher coupling efficiency.

For the LG_{01} mode, the story is a slightly different as the intensity maximum is no longer at the beam centre and the intensity profile is no longer a monotonic function of radius. From Figure 3.12, it is evident that $\eta_c$increases with r_b/w when the relative pump beam size is relative small, and after reaching a maximum value, it decreases with further increase of the relative pump beam. The coupling efficiency for the LG_{01} mode is much higher than that of the TEM_{00} mode especially when $r_b/w > 1$, which confirms that the ring-shaped beam is more favourable for exciting a LG_{01} mode.

3.5 Conclusion

In this chapter, we first introduced a ring-shaped pumping scheme in an end-pumped solid-state laser. This was achieved by using an all-fibre based pump beam conditioning element based on using a capillary silica fibre. One end of the capillary fibre was gradually tapered down to a solid-core, in which the pump beam emitted from the laser diode was launched. As the pump beam can only propagate in the annular silica guide of the capillary fibre, it is transformed to a ring-shaped intensity distribution after passing through the fibre.

We then theoretically investigated thermal lensing effects including thermal lens strength and its effect on degradation in beam quality in an edge-cooled laser rod crystal end-pumped by top-hat and ring-shaped pump beams. An analytical formula to express the transverse temperature distribution was derived by solving the one-dimensional heat transfer equation. The results show a more uniform temperature distribution within the pump region in case of a ring-shaped pump beam, and in particular a constant temperature distribution within the inner ring of pump beam with an intensity null. The analytical form of the thermal lens focal

length as a function of radial position was then derived and the averaged effective thermal lens focal length was estimated by SR. The numerical simulation results show an approximate 32% and 24% reduction in thermal lens power for the TEM_{00} and LG_{01} modes when $w_s = 0.8r_b$ in the situation of a ring-shaped pump beam, respectively. Moreover, the degradation in beam quality caused by the quartic phase aberration was numerically investigated as well. The results suggest that the laser beam experiences much less degradation under a ring-shaped pumping scheme.

We briefly discussed the principle of transverse mode selection with the use of a ring-shaped pumping scheme. The underlying mechanism is based on tailoring the ring-shaped pump beam to achieve a better spatial overlap for the desired transverse mode. The calculation results show that by adjusting the relative signal/pump beam sizes(w_s/r_b), different order LG modes can have the best spatial overlap with the pump beam and hence have the minimum threshold. Meanwhile the slope efficiency factor was calculated to provide a guidance for optimizing the laser efficiency.

Bibliography

1. J. Berger, D. F. Welch, D. R. Scifres, W. Streifer, and P. S. Cross, "High power, high efficient neodymium:yttrium aluminum garnet laser end pumped by a laser diode-array," Applied Physics Letters **51**, 1212-1214 (1987).

2. W. A. Clarkson, "Thermal effects and their mitigation in end-pumped solid-state lasers," J. Phys. D: App.l Phys. **34**, 2381-2395 (2001).

3. Y. F. Chen, Y. P. Lan, and S. C. Wang, "Generation of Laguerre–Gaussian modes in fiber-coupled laser diode end-pumped lasers," Applied Physics B: Lasers and Optics **72**, 167-170 (2001).

4. J. F. Bisson, Y. Senatsky, and K.-I. Ueda, "Generation of Laguerre-Gaussian modes in Nd:YAG laser using diffractive optical pumping," Laser Physics Letters **2**, 327-333 (2005).

5. J. W. Kim, J. I. Mackenzie, J. R. Hayes, and W. A. Clarkson, "High power Er:YAG laser with radially-polarized Laguerre-Gaussian (LG_{01}) mode output," Optics Express **19**, 14526-14531 (2011).

6. S. Guy, C. L. Bonner, D. P. Shepherd, D. C. Hanna, and A. C. Tropper, "High-inversion densities in Nd:YAG: upconversion and bleaching," IEEE J. Quantum Elect. **34**, 900-909 (1998).

7. D. C. Brown, "Heat, fluorescence, and stimulated-emission power densities and fractions in Nd:YAG," IEEE J. Quantum Elect. **34**, 560-572 (1998).

8. T. Y. Fan, "Heat generation in Nd:YAG and Yb:YAG," IEEE J. Quantum Elect. **29**, 1457-1459 (1993).

9. M. E. Innocenzi, H. T. Yura, C. L. Fincher, and R. A. Fields, "Thermal modeling of continuous-wave end-pumped solid-state lasers," Applied Physics Letters **56**, 1831-1833 (1990).

10. W. Koechner, *Solid-State Laser Engineering,* 6th. (Springer, 2005).

11. M. Born and E. Wolf, *Principles of Optics: Electromagnetic Theory of Propagation, Interference and Diffraction of Light,* 7th. (Cambridge University, 1999).

12. Y. F. Chen, T. M. Huang, C. F. Kao, C. L. Wang, and S. C. Wang, "Optimization in scaling fiber-coupled laser-diode end-pumped lasers to higher power: Influence of thermal effect," IEEE J. Quantum Elect. **33**, 1424-1429 (1997).

13. A. E. Siegman, "Analysis of laser beam quality degradation caused by quartic phase aberrations," Applied Optics **32**, 5893-5901 (1993).

Chapter 4: Fundamental mode operation using a ring-shaped pump beam

4.1 Introduction

As we discussed in the Chapter 3, the ring-shaped pumping scheme will provide advantages including a weaker thermal lens and less phase distortion compared with the traditional Gaussian-shaped and top-hat shaped pumping schemes. The net result is that the laser resonator can operate in a stable region with increased pump power leading to the prospect of higher output power. Moreover, the desired transverse mode can be selected by appropriately tailoring the ring-shaped pump beam for better spatial overlap for the desired transverse mode. Therefore, it is expected that the ring-shaped pumping scheme can provide a route to power scaling of the fundamental TEM_{00} mode.

In this chapter, we present the TEM_{00} mode operation in a Nd:YVO_4 laser end-pumped by a ring-shaped pump beam while conserving the benefits of high efficiency, but reducing the thermal lensing effect compared with the traditional pumping scheme provided by fibre-coupled laser diode. We first discuss the principles of TEM_{00} selection in detail. Experimental validation of this technique is then presented in the section 4.3, confirming enhanced power scaling capability compared with traditional fibre-coupled laser diode pumping schemes.

4.2 TEM_{00} mode selection

In section 3.4.1, we briefly discussed the principle of transverse mode selection with the use of a ring-shaped pumping scheme. The underlying mechanism is based on tailoring the ring-shaped pump beam for a better spatial overlap of the desired transverse mode. From Figure 3.11, it is obvious that the ring-shaped pump beam has a better spatial overlap with the fundamental TEM_{00} mode when the relative pump beam size is within region I, and hence results in the lowest threshold pump power for the TEM_{00} mode. However, a small pump beam size (normally $r_b/w < 1$) causes another detrimental problem that the laser beam suffers from the pronounced beam distortion and degradation in beam quality due

to a non-parabolic phase aberration beyond the pump region as we discussed in section 3.3. Therefore, it is necessary to restrict the laser mode within the pump beam region to reduce the aberrated phase induced beam distortion. The larger pump beam size naturally leads to a better spatial overlap for the LG_{01} mode. In order to allow the fundamental TEM_{00} mode to have minimum threshold, an extra intracavity loss for the LG_{01} mode is required. This can be achieved by simply inserting an appropriate circular aperture in the cavity to suppress lasing on higher order LG modes.

4.2.1 Laser performance comparison for different shaped pump beam

In practice, a Gaussian-shaped pump beam is always used to provide better spatial overlap with the fundamental TEM_{00} mode and hence leads to a lower threshold and higher slope efficiency than a top-hat pump beam in traditional end-pumped solid-state lasers at low output powers. For a Gaussian-shaped pump beam with constant beam radius w_p within the laser material, the normalized pumping rate can be written as:

$$r_p(r,z) = \frac{\alpha e^{-\alpha z}}{1-e^{-\alpha L_0}} \frac{2}{\pi w_p^2} \exp\left(-\frac{r^2}{w_p^2}\right) \tag{4.1}$$

substituting the Eq.(4.1) into Eq.(2.7) and (2.12), the effective pump beam area A_{eff} and coupling efficiency η_c have expressions as follows:

$$A_{eff} = \frac{\pi}{2}(w_p^2 + w_s^2) \tag{4.2}$$

$$\eta_c = \frac{w_s^2(w_s^2 + 2w_p^2)}{(w_p^2 + w_s^2)^2} \tag{4.3}$$

Meanwhile, these values can be derived from Eq.(3.28) and (3.37) for the top-hat shaped and ring-shaped pump beams. Figure 4.1 shows the calculated effective pump beam area and coupling efficiency for the TEM_{00} mode with three different pumping schemes: Gaussian, top-hat and ring-shaped pump beams. From Figure 4.1(a), it can be seen that the TEM_{00} mode has the smallest pump beam area in the case of Gaussian-shaped pump beam compared with other pump beams. The differences between A_{eff} tend to reduce as the relative TEM_{00} mode beam radius

(w_s/w_p) increases. Here, we will focus on our analysis within the region of w_s/w_p<1, where the laser beam suffers from less aberrated phase induced beam distortion.

Within the range of w_s/w_p<1, the TEM$_{00}$ mode has much less overlap with the ring-shaped pump beam. The calculated A_{eff} dramatically increases as w_s/w_p decreases, which means that an increase of threshold pump power is required with the decrease of relative laser beam size, although the laser beam benefits from less phase distortion. Therefore, designing such a resonator is a compromise between reduced beam distortion and increased threshold pump power. The small beam size is required to reduce beam distortion, but decreasing the beam size significantly lifts the threshold pump power. From Figure 4.1(a), we can see that for the ring-shaped pump beam with r_a/r_b =0.525, A_{eff} only slightly varies from $5.97\,w_p^2$ to $5.14\,w_p^2$ when $0.8<w_s/w_p<1$, which is about two times larger than that of a Gaussian-shaped pump beam. In addition, the difference for A_{eff} between the Gaussian-shaped pump beam and the ring-shaped pump beam significantly increases with an increase of r_a/r_b. The dark cyan curve in Figure 4.1(a) depicts the A_{eff} as a function of relative laser beam size for a particular r_a/r_b=0.9. It can be seen that the A_{eff} varies from $9.335w_p^2$ to $16.46w_p^2$ when $0.8<w_s/w_p<1$, which is 7 times that of a Gaussian-shaped pump beam at the point w_s/w_p=0.8, and this ratio dramatically increases when w_s/w_p<0.8. It suggests that the TEM$_{00}$ mode can only have a comparable threshold pump power compared with a traditional Gaussian-shaped pump beam when the ratio of r_a/r_b is relatively small. Moreover, the ring-shaped pump beam provides a better coupling efficiency allowing a higher slope

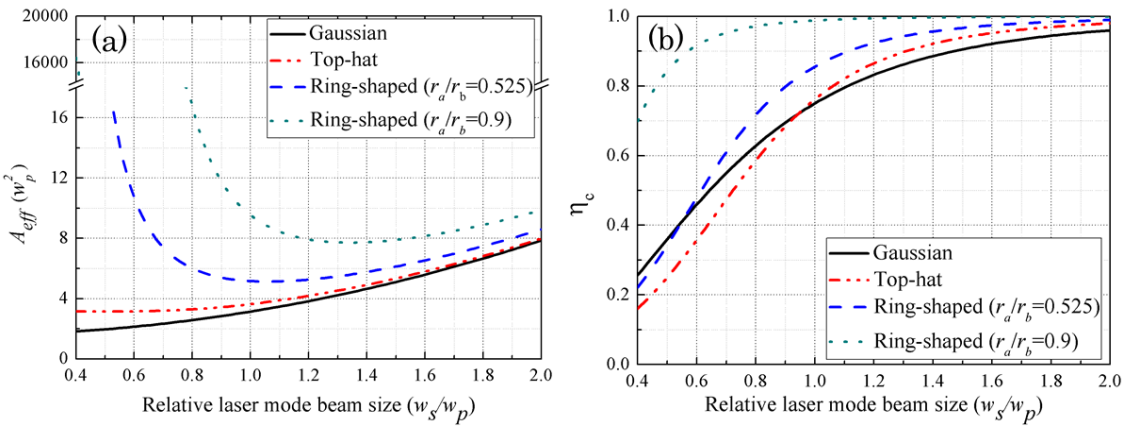

Figure 4.1 The effective pump areas and coupling efficiencies for TEM$_{00}$ mode in case of different pumping schemes.

efficiency for TEM_{00} mode operation as shown in Figure 4.1(b), which can compensate its drawback of relative higher threshold. For a ring-shaped pump beam with a parameter of r_a/r_b=0.525, the η_c is 15% higher than that of a Gaussian-shaped pump beam when $0.8<w_s/w_p<1$. Although the value of η_c is much higher (near to 1) for a ring-shaped pump beam with a parameter of r_a/r_b=0.9 within the same mode size region, it is still difficult to compensate for its significantly higher threshold to achieve a high output power. Based on these considerations, we will further investigate the performance of the ring-shaped pump beam with a parameter of r_a/r_b=0.525 on fundamental TEM_{00} mode operation in comparison with a quasi-Gaussian shaped pump beam provided by a traditional fibre-coupled laser diode.

4.2.2 Higher order mode suppression

As we discussed in the last section, the ring-shaped pump beam with a parameter of r_a/r_b=0.525 should have a better performance compared with a traditional Gaussian or top-hat shaped pump beam when the laser mode size is within the range of $0.8<w_s/w_p<1$. However, when the laser beam size is within this range, the LG_{01} mode has the best spatial overlap with the pump beam and hence the smallest effective pump beam area as can be seen from Figure 3.11, and is expected to have the lowest threshold. However, the threshold is also dependent on the mode's intracavity loss as shown in Eq.(2.13). Therefore, the TEM_{00} mode can also reach the threshold first if the intracavity loss for LG_{01} mode is much higher. From Eq.(2.9) and (2.13), we can see that the mode selection for TEM_{00} mode must satisfy the following criteria:

$$\frac{\gamma_{00}}{J_{00}(0)} < \frac{\gamma_{01}}{J_{01}(0)} \tag{4.4}$$

substituting Eq.(3.28) into (2.13), yields the following expression:

$$\frac{\gamma_{01}}{\gamma_{00}} = \frac{T_0+\delta_{01}}{T_0+\delta_{00}} > 1 + \frac{\frac{2r_a^2}{w^2}\exp\left(-\frac{2r_a^2}{w^2}\right) - \frac{2r_b^2}{w^2}\exp\left(-\frac{2r_b^2}{w^2}\right)}{\exp\left(-\frac{2r_a^2}{w^2}\right) - \exp\left(-\frac{2r_b^2}{w^2}\right)} \tag{4.5}$$

When $0.8<w_s/w_p<1$, the maximum value of γ_{00}/γ_{01} varies from 0.63 to 0.91 to satisfy Eq. (4.5), which means that the total cavity loss for TEM_{00} mode must be

less than 0.63 times the LG_{01} mode cavity loss in order to have the lowest threshold for the TEM_{00} mode in the case of w_s/w_p=0.8. Increasing laser mode size, the TEM_{00} mode has an improved spatial overlap with the ring-shaped pump beam, and thus the minimum value of γ_{00}/γ_{01} to satisfy the Eq. (4.5) decreases. When w_s/w_p=1, the value of γ_{00}/γ_{01}increases to 0.91.

Furthermore, it is necessary to consider that no other transverse mode breaks into oscillation when the laser operates on TEM_{00} mode far above the threshold. This could be achieved when the threshold pump power for the second mode (LG_{01}) is higher than the pump power. According to Eq. (2.18), it requires:

$$\frac{J_{00}(S\ ,0)}{J_{01}(S\ ,0)} > \frac{\gamma_{00}}{\gamma_{01}} \tag{4.6}$$

which suggests that the LG_{01} mode should have small overlap integral factor with the pump beam or the loss for the LG_{01} mode is much higher than that of the TEM_{00} mode. Only in this way, the oscillation of the first mode can significantly saturate the gain to suppress the oscillation of other modes. As the value of $J_{00}(S,0)\ /J_{01}(S,0)$ in the left part of Eq. (4.6) is dependent on the intensity distributions of the pump and laser modes in the cavity, it is difficult to change this value for a particular resonator. However controlling the loss ratio of γ_{00}/γ_{01} is much easier and is always done to suppress the oscillation of the second transverse mode.

Figure 4.2(a) shows some calculated maximum ratios of intracavity loss of the TEM_{00} mode to the LG_{01} mode for preventing the LG_{01} mode from oscillation as a function of relative laser mode beam size for particular pump powers. This value increases with the increase of TEM_{00} mode beam size as a result of an improved spatial overlap with the ring-shaped pump beam compared with the LG_{01} mode. At a fixed TEM_{00} mode beam size, the ratio decreases with the increased output power. The reason is that it becomes more difficult to saturate the gain of the LG_{01} mode with the increase of pump power resulting from an increased undepleted population inversion within the crystal that has a better spatial overlap with the LG_{01} mode. As a result, an increased round-trip cavity loss is required to prevent the LG_{01} mode from lasing. Figure 4.2(b) shows the dependence of the maximum value of γ_{00}/γ_{01} on the absorbed pump power for a particular TEM_{00} mode beam size, manifesting an increased intracavity loss is always required for the LG_{01} mode

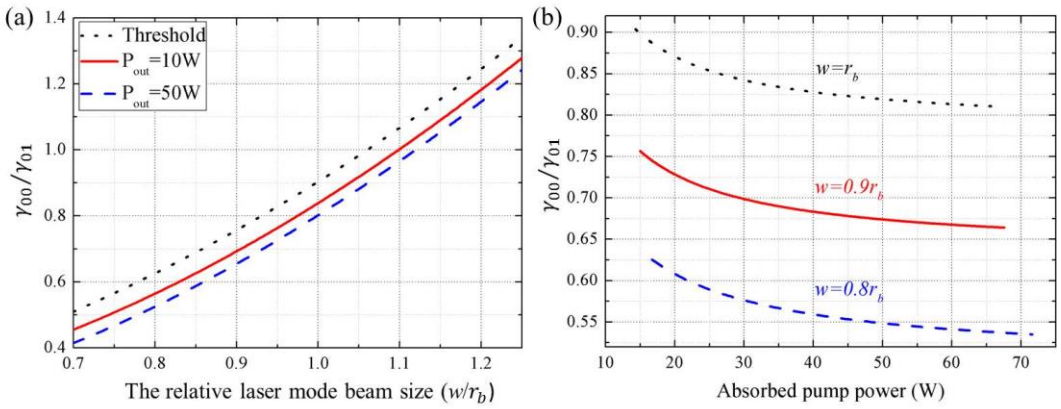

Figure 4.2 Calculated examples of maximum ratio of intracavity losses between TEM_{00} and LG_{01} modes for preventing LG_{01} mode from lasing (a) as a function of relative laser mode size at particular pump powers; (b) as a function of pump power at particular relative laser mode size.

in order to exclusively oscillate the TEM_{00} mode. For instance, the maximum value of γ_{00}/γ_{01} decreases from 0.76 at the threshold pump power to 0.67 at 50W of absorbed pump power for $w_s/w_p = 0.9$.

In a real laser cavity, the diffraction loss always exists for any transverse mode due to the limited lateral boundaries of intracavity components such as the resonator mirrors, laser material or limiting apertures, which depends on the ratio of the radius of the laser beam size to the aperture radius. This loss only depends on the Fresnel number ($N = a^2/\lambda l$, where a is the smallest aperture of an intracavity optical element, and l is the cavity length). Since the higher order modes have a much larger mode size than that of fundamental TEM_{00} mode, they must experience much higher diffraction loss. Therefore, an aperture with appropriate size is usually applied in the cavity to suppress the higher order modes and hence enforce the laser to preferentially operate on the fundamental TEM_{00} mode. The ratio of diffraction losses for the first higher order TEM_{01} mode to the TEM_{00} mode with a given Fresnel number is illustrated in Figure 4.3 [1]. It shows that the mode selectivity is strongly dependent on the cavity geometry for a given Fresnel number. The mode selectivity improves with a decrease of $|g|$ ($g = 1 - l/R$, where R is the curvature of the mirror), which is strongest in a confocal resonator and weakest in a plane-plane or a concentric resonator. Moreover, this figure suggests that the operation of the TEM_{00} mode in a laser resonator requires that the Fresnel number

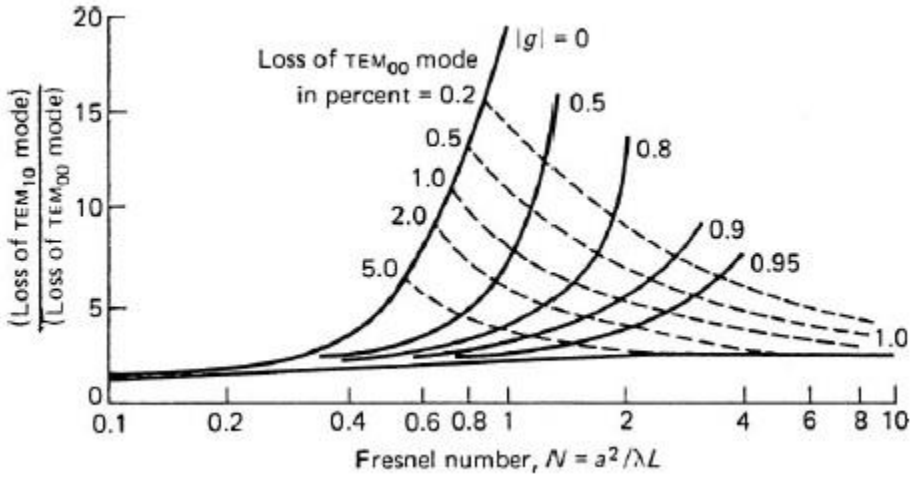

Figure 4.3 Ratio of the losses per transit of the two lowest order modes for the symmetrical resonator taken from [1]. The dashed curves are contours of constant loss for the TEM_{00} mode.

is on the order of around 0.5-2. Otherwise a large N results in insufficient mode discrimination, while a small N causes severe loss for the desired TEM_{00} mode [2].

4.3 Experimental work on TEM_{00} mode operation

In this section, we will experimentally investigate power scaling of the fundamental TEM_{00} mode with the use of a ring-shaped pumping scheme in an end-pumped solid-state laser.

4.3.1 Laser material selection

From the large number of neodymium doped materials, yttrium aluminium garnet (YAG) and yttrium orthovanadate (YVO_4) are two of the most popular host materials used in diode end-pumped solid-state lasers in the 1μm wavelength region. The good thermal and structural properties of YAG mean it can be pumped harder and is a good choice for very high power oscillators. However, it suffers from the drawback of stress-induced birefringence as pump power is increased.

It is well known that the threshold of a continuous-wave laser is determined by two parameters, that is the upper-state lifetime (τ) and the stimulated emission cross-section (σ_e). Nd:YAG has a longer upper-state lifetime, but a much smaller stimulated emission cross-section than Nd:YVO_4, and thus the product of $\tau\sigma_e$ is much smaller than for the latter. This suggests that for similar cavities, Nd:YVO_4

will have the lower threshold and with its higher gain, allow the use of higher transmission output couplers leading to a greater slope efficiency. Since the threshold is higher in case of ring-shaped pumping, the choice of Nd:YVO_4 with its larger $\tau\sigma_e$ product will benefit performance before thermal effects become pronounced

4.3.2 Measurement of thermal lensing in Nd:YVO_4

Knowledge of how the thermal lens strength changes with variation in absorbed pump power is essential for the design of laser cavities. General techniques for measuring thermal lensing can be classified into two categories: interferometric and non-interferometric. For the former method, the optical path length difference as a function of transverse position is measured by interferogram [3, 4]. For non-interferometric techniques, the change of a probe beam passing through the thermal lens is measured to calculate the averaged focal length of thermal lens [5-7]. The non-interferometric method benefits from no requirement for precise alignment of highly sensitive interferometers and thus allows simple measurements of the thermal lens focal length. In our experiment, the thermal lens was measured under non-lasing conditions by measuring the effect of the lens on a known probe beam.

The schematic for measuring the thermal lens focal length is illustrated in Figure 4.4. A 3×3×10mm a-cut with low doping level (0.1 at.%-doped) Nd:YVO_4 crystal was used in order to reduce the influence of ETU on the thermal loading under non-lasing conditions. Both end-faces of the Nd:YVO_4 were anti-reflection coated at

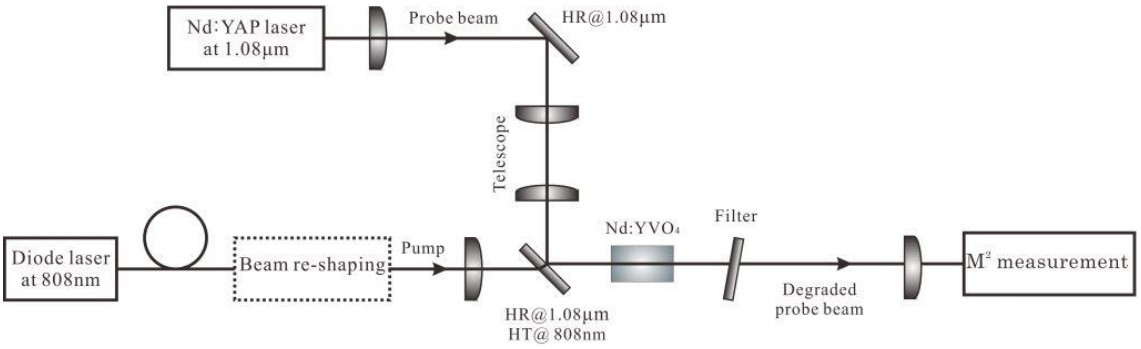

Figure 4.4 Experimental setup for measuring degradation in beam quality after a single pass through a diode-end-pumped Nd:YVO_4 crystal under non-lasing condition.

1064nm and 808nm. The crystal was wrapped with 125 μm thick indium foil and was mounted in a water-cooled aluminium heat sink. The temperature of the heat sink was maintained at 18℃ to maximize the heat elimination and keep the crystal from any condensation on its end facets. Pump power was provided by a fibre-coupled diode laser at 808 nm with a 200 μm diameter and 0.22 NA delivery fibre yielding a maximum pump power of 60 W. The pump power was measured by a Gentec-eo power detector (UP55N-100H-H9) which can measure a maximum average power of 100W and has a calibration uncertainty of ±2.5% and repeatability of ±0.5% with noise power of 5mW. Note, all optical powers above 30W were measured by this power detector during the experiments throughout this thesis. In the case of a traditional fibre-coupled pumping scheme, the pump beam was imaged into the laser rod and magnified by a factor of 4 to get a beam size with a radius of ~400 μm using an arrangement of lenses. For ring-shaped pumping, the pump beam was coupled to a capillary fibre to produce a beam with a ring-shaped intensity distribution in the near-field. In this case, one end of the capillary fibre was heated up and was gradually tapered to form a solid core with a diameter of ~105 μm, in which the pump beam was directly launched by using two aspheric lenses (f_1=11mm with NA=0.25 and f_2=4mm with NA=0.62) to reimage the output from the fibre-coupled laser diode. The free-space coupling configuration yielded a maximum pump power of 48W corresponding to a launching efficiency of 80%. The coupling loss could be attributed to mismatch of focal lengths of the aspherical lens in the coupling system. The re-shaped pump beam M^2 was degraded from ~56 to ~115 as the capillary fibre was non-optimized. The re-shaped pump beam was then imaged into the laser rod and magnified by a factor of 4 to achieve a ring-shaped beam with an outer radius of ~400 μm and an inner radius of ~210 μm. A Nd:YAP laser with a diffraction-limited Gaussian beam and an output power of ~100 mW at 1.08 μm provided the probe beam with M^2~1.05±0.05 for the measurement as it experiences negligible gain on passing through the Nd:YVO_4. The probe beam emerging from the Nd:YAP laser was firstly collimated, and then a telescope lens system was utilized to produce a beam with variable beam waist radius from 300 μm to 900 μm on the input front surface of the Nd:YVO_4. The beam waist was also adjusted to be located on the front surface of crystal. The probe beam was carefully aligned to propagate collinearly with the pump beam and hence along the axis of the thermally induced lens, and was finally focused by a lens of focal length f=200 mm. The degraded beam quality, beam waist and its location could then be

determined by an M^2 measurement. Based on this information, the focal length of the thermal lens could be derived by using the ABCD matrix formalism [8].

We firstly measured the M^2 for a range of different probe beam sizes w_s by using a Thorlabs fully automated M^2 measurement system which is configured with a scanning slit beam profiler (BP104-IR) and a motorized linear translation stage. The typical M^2 measurement accuracy of this system is ±5%. Note, the M^2 measurements for laser beams at wavelengths around ~1μm were carried out by using this system throughout this thesis. Figure 4.5 shows the increase in M^2 versus w_s/w_p at the maximum absorbed pump power for different pump shape configurations. It can be seen that there is a dramatic increase in M^2 for $w_s/w_p>1$. The M^2 in both the horizontal (x) and vertical (y) directions increased up to $M^2>3.9$ when $w_s/w_p=2.25$ in both cases, although the beam had a more severe degradation under the condition of a quasi-top-hat pump beam. From Figure 4.5(b), it can be seen that probe beam has nearly negligible degradation in beam quality ($M^2<1.1$) when the relative beam size is $w_s/w_p=0.75$ under ring-shaped pumping, which is much better than for quasi-top-hat pumping for which M^2 is ~1.5 as seen in Figure 4.5(a). This confirms that the ring-shaped pump beam yields weaker phase distortion, as expected.

As we discussed in section 4.2, the laser beam size must be smaller compared with the pump beam size in order to reduce beam distortion, and the beam size should be within the range of $0.8<w_s/w_p<1$ to efficiently excite the fundamental TEM_{00} mode under the condition of a ring-shaped pump beam. A probe beam with beam

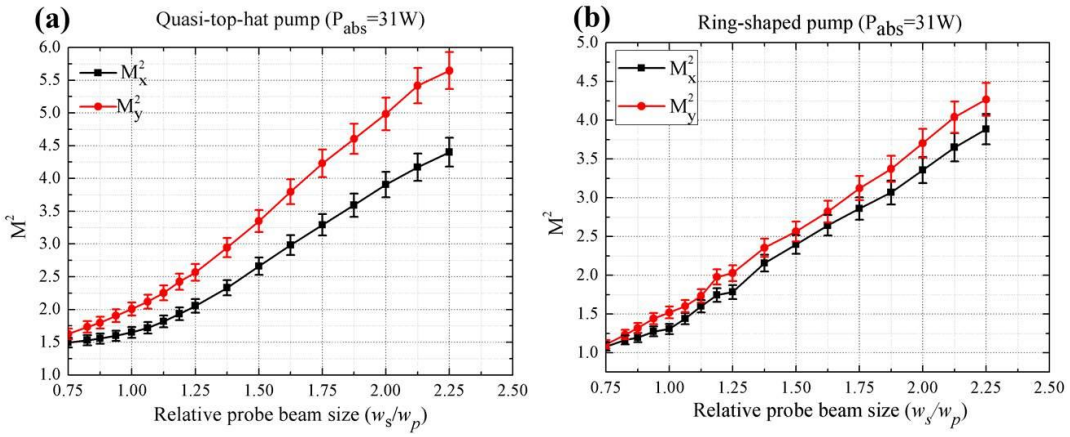

Figure 4.5 Probe beam quality factor M^2 versus the ratio of probe beam size (w_s) to pump beam size (w_p) for 31 W of absorbed pump power.

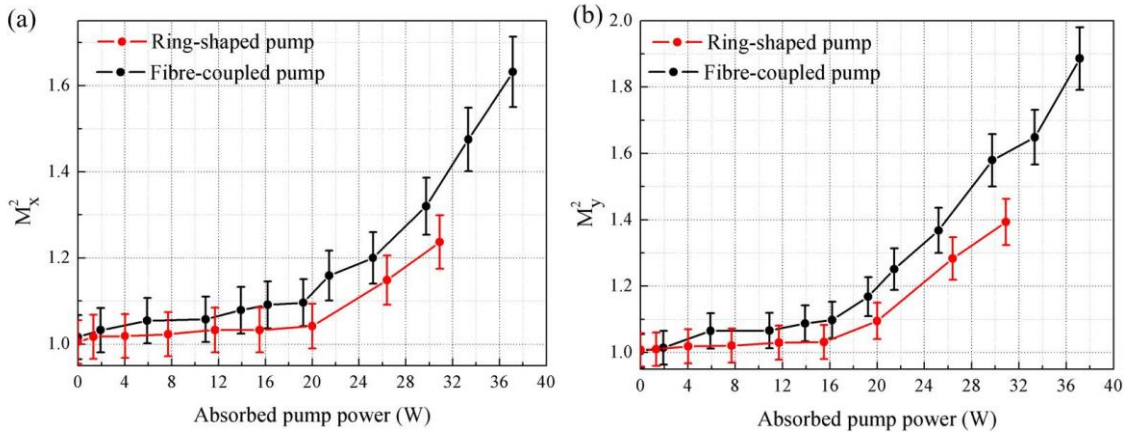

Figure 4.6 Probe beam quality factor M^2 versus absorbed pump power when the ratio of w_s/w_p=0.94 in case of fibre-coupled and ring-shaped pump beams.

radius of ~375 μm (w_s/w_p=0.94) was launched to pass through the crystal to measure the thermal lens strength and its effect on beam quality. Figure 4.6 shows the measured beam quality factor M^2 versus the absorbed pump power in both pump configurations. It can be seen that the probe beam has a lower value of M^2 for ring-shaped pumping. Note that there is a negligible beam degradation (M^2<1.1) when the absorbed pump power is less than 20 W for ring-shaped pumping. Above this power, the M^2 increased to M_x^2=1.24±0.06 and M_y^2=1.39±0.08 at the maximum absorbed pump power (31W). In comparison, the beam quality factor rapidly increased to M_x^2=1.47±0.07 and M_y^2=1.65±0.08 at 33W of absorbed pump power in the case of the conventional fibre-coupled pump scheme, showing that the ring-shaped pump beam offers less phase distortion for the TEM_{00} mode.

Figure 4.7 shows the measured thermal lens strength versus absorbed pump power under conditions of both pumping schemes. By fitting the measured thermal lens focal length by the formula $f_t = a/P_{abs}$ (a is a constant), it can be seen that the thermal lens focal length under the condition of ring-shaped pumping is around 40% longer than the traditional fibre-coupled pumping scheme, indicating that thermal lens strength is much weaker. In addition, the dioptric power of the thermal lens is plotted against absorbed pump power in Figure 4.7(b). We can see that the dioptric power was found to be 0.237 m^{-1}/W in the case of a traditional fibre-coupled pumping and 0.167 m^{-1}/W for ring-shaped pumping. The measured thermal lens strength provides a guideline for designing a laser resonator to operate on the TEM_{00} mode in the stable region with the available pump power.

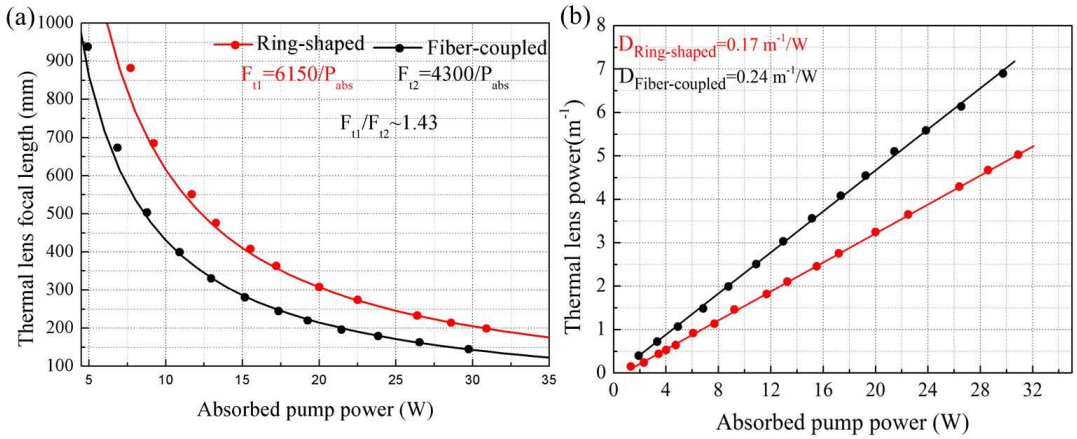

Figure 4.7 (a) Measured thermal lens focal length and (b) the corresponding thermal lens power versus absorbed pump power at the centre of pump region for a probe beam with relative beam radius w_s/w_p=0.94.

4.3.3 TEM$_{00}$ mode generation

The experimental proof of the principle was carried out in an end-pumped Nd:YVO_4 laser. The schematic of the experimental set-up is illustrated in Figure 4.8. The pump beam and laser crystal are the same as used in section 4.3.2 for measuring the thermal lensing effects. The crystal was wrapped with 125 μm thick indium foil and mounted in a water-cooled aluminium heat-sink maintained at 18℃ and was placed ~5 mm from the input coupling mirror. As we discussed in section 3.4, the laser performance of the output mode is strongly dependent on the relative beam size (w_s/w_p). A Z-fold cavity was employed to reduce the thermal lens induced beam size variation within the gain medium to ensure that only one transverse

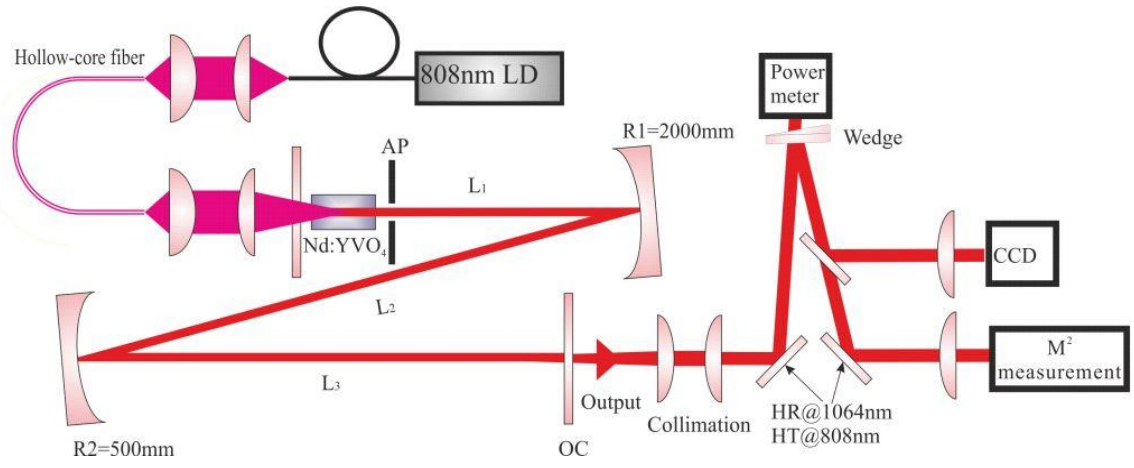

Figure 4.8 Schematic configuration of the diode-end-pumped Nd:YVO_4 laser with a ring-shaped pump beam.

mode would be excited over the range of pump power. The resonator consisted of two curved mirrors with radius of curvature R_1=2000 mm and R_2=500 mm respectively; both with high reflectively (>99.8%) at 1064 nm, a plane input coupling mirror with high transmission (>95%) at 808 nm and high reflectivity at 1064 nm, and a plane output coupler with a transmission of 20% at 1064nm. The cavity length could be adjusted appropriately to achieve different beam sizes within the crystal to allow the resonator to operate on either the TEM_{00} or LG_{01} modes as predicted in Figure 3.11.

In the last section, the averaged thermal lens focal length (f_t) was measured to be ~200 mm under the maximum 31 W of absorbed pump power for a probe beam with a beam radius of ~375 μm. Therefore, the cavity was designed to be stable when the f_t is greater than 200 mm. Based on this consideration, two cavities supporting laser modes with different beam waists within the crystal were designed to verify the feasibility of the principle.

First, the cavity was designed to operate in region II ($0.75< w_s/w_p <1.06$) in which the LG_{01} mode would normally be preferentially excited. When the cavity length was designed to be ~L_1=153 mm, L_2=285 mm, and L_3=210mm, the calculated TEM_{00} mode beam size within the crystal is plotted as a function of absorbed pump power in the blue curve in Figure 4.9(a). It can be seen that the beam size w_s gradually decreases with the increase of therml lens strength. The minimum beam size is w_s~330 μm at f_t=350 mm, and then the beam size rapidly increases to w_s=360 μm at f_t=218mm. Note that the variation of beam size is still small and is

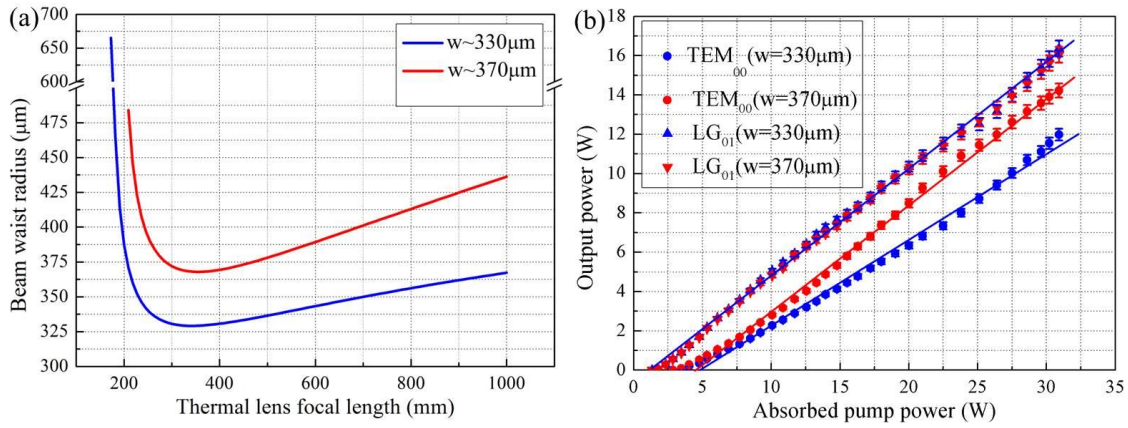

Figure 4.9 The calculated beam waist within the laser crystal versus the thermal lens focal length for different cavity designs. (b) Output power of TEM_{00} and LG_{01} modes versus absorbed pump power for different cavity designs.

less than 10% within this region. After careful alignment of the cavity, the laser initially started lasing on the doughnut-shaped LG_{01} mode at ~2.1 W of absorbed pump power (P_{abs}) and increased linearly to 16.4 W at P_{abs}=31 W with a slope efficiency of 55%. The output power was measrued by using a Gentec-eo power detector (UP19K-30H-H5) which has a measurment repeatablity of ±0.5% and calibration uncertaintity of ±2.5%. The output characteristic was plotted by the blue trianguluar in Figure 4.9(b). The LG_{01} mode oscillation was successfully suppressed by inserting an aperture with a diameter of 0.9 mm placed 25 mm behind the laser crystal, and hence the fundamental TEM_{00} mode was preferentially excited. Figure 4.9(b) (blue circle) shows the output power of the TEM_{00} mode as a function of absorbed pump power. It reached threshold at P_{abs}=3.5 W, and the output power increased linearly to 12 W at P_{abs}=31 W, corresponding to a slope efficency of 43%. It is worth mentioning that the size of aperture was optimised, and an aperture with larger diameter could not sufficiently suppress the higher LG_{01} mode, while a smaller aperture would introduce much more loss for the TEM_{00} ocillation resulting in a relatively low efficiency. The aperture was made of a copper plate drilled to form a sequence of ring-holes with diamters from 0.5 mm to 1.5 mm with a step-variation of 0.1 mm.

To investigate the effect of the mode size on the TEM_{00} mode performance, the cavity length was then adjusted to be ~L_1=153 mm, L_2=305 mm, and L_3= 170 mm, corresponding to a total cavity length L=628 mm. The red line in Figure 4.9(a) shows the calculated TEM_{00} mode beam size within the crystal as a function of thermal lens focal length. In this case, the minimum beam size is w_s=370 μm and occurs at f_t=372 mm, and the beam size increases to w_s=460 μm at f_t=220 mm. Further increase in the thermal lens strength results in a rapid increase of beam size and finally goes beyond the resonator stability region. In this case, the laser had a LG_{01} mode output without an aperture. Moreover, it had the similar output power performance as for the case with the beam radius of w_s=330 μm. When an aperture with a diameter of 1.1 mm was inserted 50 mm after the crystal, the fundamental TEM_{00} mode could be exclusively excited. It reached threshold at a pump power P_{abs}=2.9 W, and the output power increased linearly to 14.2 W at the maximum available of P_{abs}=31W, corresponding to a slope efficiency of 54%. A significant improvement of the laser performance could be attributed to better spatial overlap of the laser mode with the pump beam. The calculated coupling efficiency (η_c) is equal to 0.82 for the laser mode size w_s =370 μm, which is 14%

higher than the former situation in which η_c is calculated as 0.72 at w_s =330 μm. Another reason could be the different losses induced by the aperture as different sized apertures were used. Figure 4.10(a) shows the beam size radius of the fundamental TEM_{00} mode on the aperture as a function of thermal lens strength. The round-trip diffraction loss caused by the aperture can be written as:

$$\delta = 1 - \left(2\pi \int_0^{d/2} I(r) r dr\right)^2 \tag{4.7}$$

where $I(r)$ is the intensity distribution of the laser mode at the aperture plane, and d is the diameter of the aperture. The calculated loss for each mode is illustrated in Figure 4.10(b). It is obvious that the LG_{01} mode has a much higher loss than the TEM_{00} mode in both cavity configurations resulting in sufficient suppression of the LG_{01} mode. The loss for the TEM_{00} mode in both resonator configurations gradually decreases with the increase of thermal lens strength when f_t is greater than ~250 mm. Moreover, the loss difference for the TEM_{00} mode for the two resonator configurations is less than 2% when f_t >210 mm. Taking into account 20% transmission efficiency for the output coupler, the slightly different diffraction loss caused by the aperture should have a negligible effect on the variation of slope efficiency, especially when the thermal lens is strong. Therefore, the increased slope efficiency is due to the improved effective spatial overlap efficiency in the latter case. The slope efficiency increased by 12.6% which is consistent with the estimated 14% increased value for η_c.

Figure 4.11(a) shows the intensity distribution of output mode when the laser

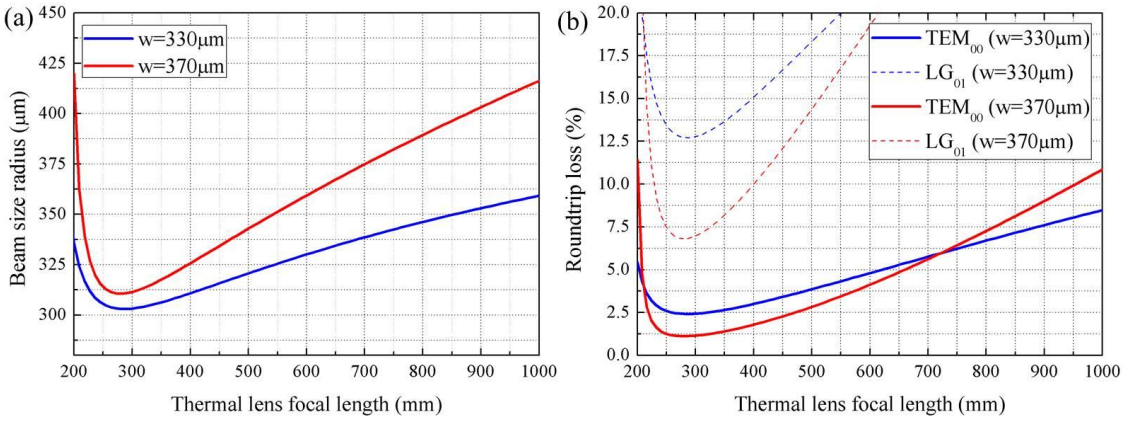

Figure 4.10 The calculated beam size radius of TEM_{00} mode on the aperture as a function of thermal lens focal length and (b) the roundtrip loss caused by the aperture for the TEM_{00} and LG_{01} modes versus the thermal lens focal length.

operated on the LG_{01} mode at the maximum output power of 16 W in the second resonator configuration. The beam profile was measured by a Spiricon CCD camera (LBA-FW-SCOR20). As the laser beam size is comparable to the pump beam size within the gain crystal, an aperture with a diameter of 1.3 mm was inserted in the cavity to filter the distorted intensity in the wings. Figure 4.11(b) shows the beam size radius in the horizontal and vertical directions after passing through a focal lens. Fitting to the M^2 functions of Eqs. (2.19) and ((2.20)) showed a beam quality of 2.04±0.10 in the horizontal and 2.14±0.11 in the vertical direction, which are in close agreement with the theoretical value of 2 for a LG_{01} mode. Without inserting the aperture, the doughnut-shaped LG_{01} mode was also excited, but with a distorted beam profile, and the M^2 was degraded to be ~2.27±0.11 in the horizontal and ~2.39±0.12 in the vertical. The beam degradation is attributed to the aberrated nature of thermal lensing that the beam wings experience more severe distortion than the centre of beam. Therefore, an aperture was inserted in the cavity to filter the distorted beam and hence improve the beam quality.

After adjusting the aperture size to be 1.1mm, the output mode switched to the TEM_{00} mode. Figure 4.12(a) shows the beam profile of the TEM_{00} mode at the maximum output power of 14.2W. The M^2 was measured as 1.08±0.05 in the horizontal and 1.03±0.05 in the vertical direction verifying that the diffraction-limited Gaussian mode was obtained. The results suggest that the LG_{01} mode could be sufficiently suppressed with an appropriately sized aperture resulting in preferential oscillation of the TEM_{00} mode.

To compare the performance of output of the TEM_{00} mode under the condition of

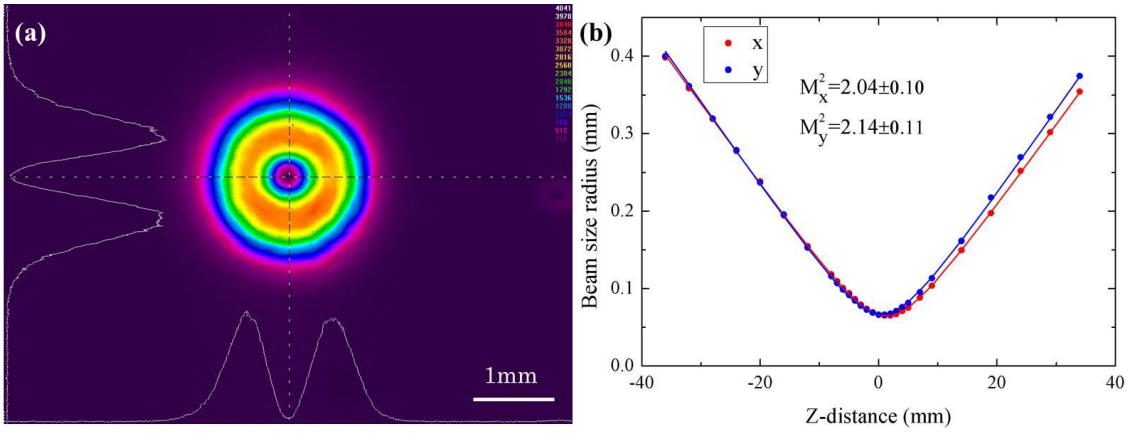

Figure 4.11 (a) Experimental intensity distribution of LG_{01} mode at maximum output power of 16W; and (b) the M^2 data measurement.

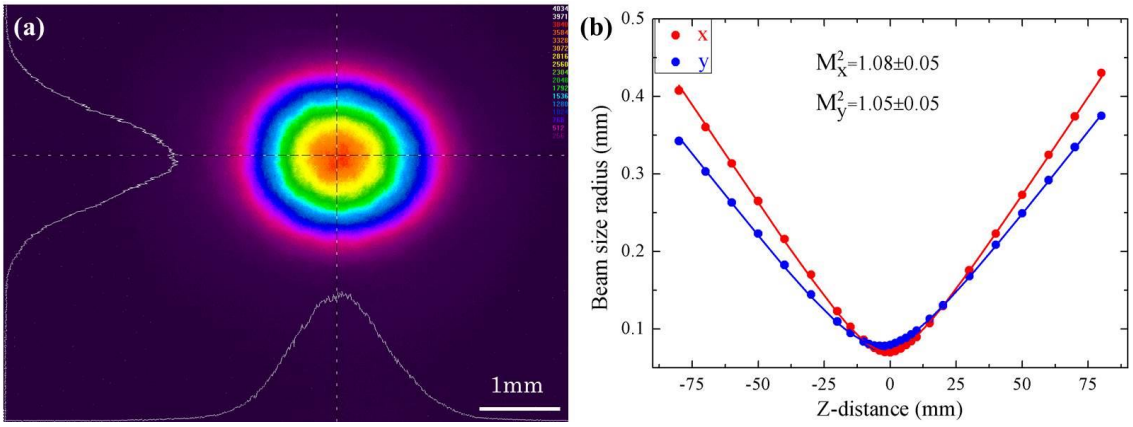

Figure 4.12 (a) Experimental intensity distribution of TEM_{00} mode at maximum output power of 14.2W; and (b) the M^2 data measurement.

ring-shaped pumping and the traditional fibre-coupled 'top-hat' like pumping, the capillary fibre in the experiment set-up (as shown in Figure 4.8) was then removed, and the pump beam was directly provided by the fibre-coupled laser diode. The focused beam yielded a more uniform intensity distribution compared with a Gaussian-shaped pump beam. The beam M^2 was measured to be ~50 in both the vertical and horizontal directions, resulting in a Rayleigh range of z_r =12.4 mm when focused down to a beam waist of 400 μm, which was two times longer than that of a ring-shaped pump beam. For comparison, a resonator configuration the same as the second one was employed.

Initially, the laser was operated without inserting the aperture. Figure 4.13 shows the output power and optical to optical efficiency versus the absorbed pump power. It reached the threshold at P_{abs}= 2.5 W, and then increased linearly to 10.3 W at P_{abs}=20.5 W with a slope efficiency of 56%. Between ~20-28W of absorbed pump

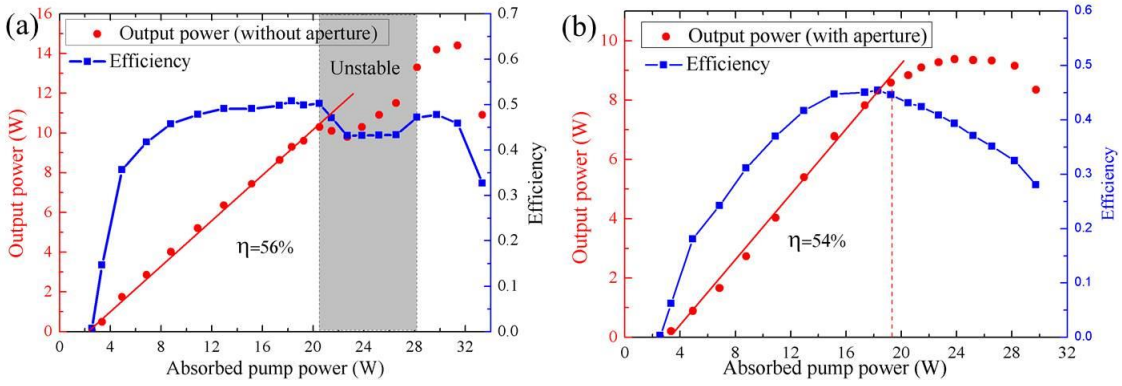

Figure 4.13 Output power and the optical-to-optical efficiency (a) without inserting aperture; and (b) after inserting an aperture with diameter of d=1.1 mm.

power, the cavity becomes unstable as seen by a drop in efficiency and output power, and degradation in the beam quality of the output beam. At higher pump power, the cavity enters the stability zone again, regaining efficiency and output power. The maximum output power increased to 14.4 W at P_{abs}=31.4 W, and then the cavity enters the unstable zone again resulting in a dramatic drop in output power and optical efficiency. Figure 4.14 shows some typical output beam profiles when P_{abs}>15 W. It can be seen that the output beam had a Gaussian-shaped intensity profile in the first stability zone. The M^2 was measured to be 1.21±0.06 in the horizontal and 1.06±0.05 in the vertical direction at an output power of 9.3 W. Within the unstable region, the beam profiles deteriorates to a two-lobed structure with a decrease of output power. Once the cavity enters the stability zone again, the beam profile becomes a little elliptical in shape, and the M^2 was measured to be 1.54±0.08 in the horizontal and 1.40±0.07 in the vertical direction at an output power of 14.2 W, which suffers from serious deterioration in beam quality compared with the maximum output power of the TEM_{00} mode from the same cavity under the condition of the ring-shaped pump scheme.

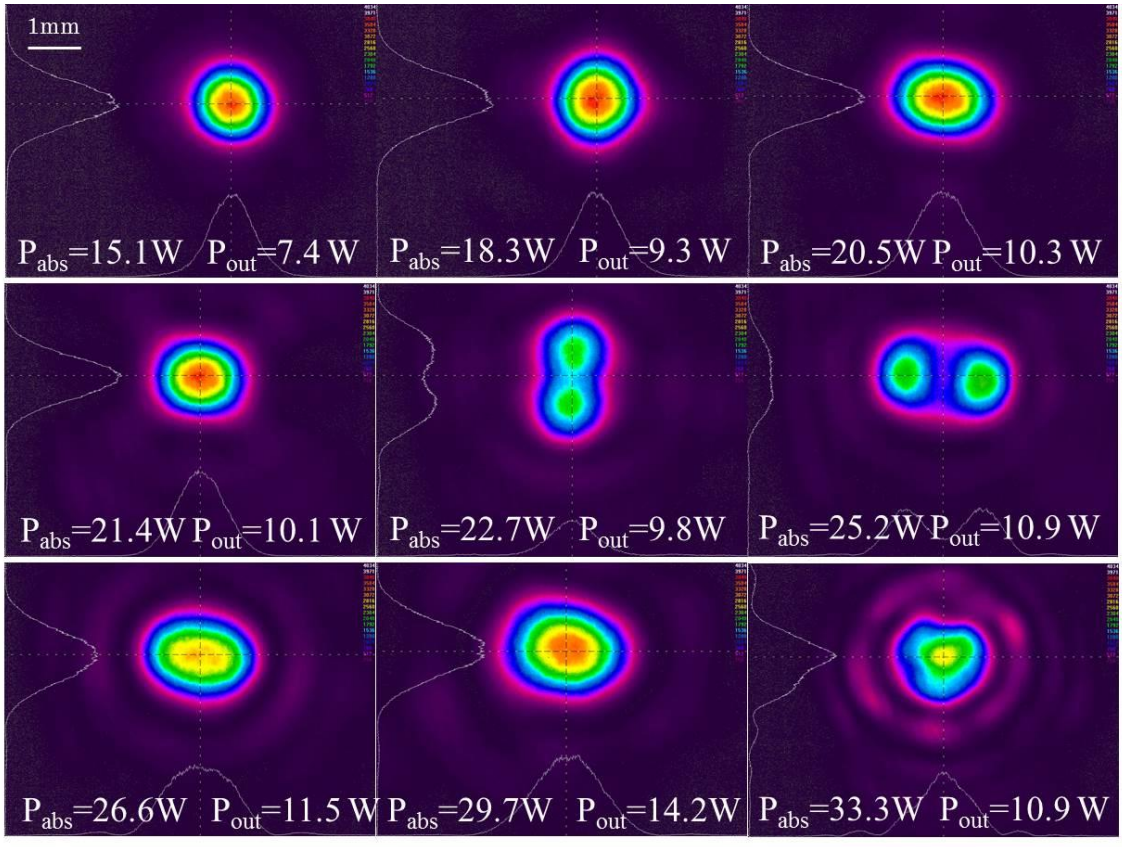

Figure 4.14 Dynamic output beam profiles at different pump powers.

In order to obtain the diffraction-limited TEM_{00} mode at high power, an aperture with diameter of d=1.1mm was then inserted in the cavity at the same position as in the ring-shaped pumping scheme cavity. The laser output power and optical to optical efficiency as a function of absorbed pump power are shown in Figure 4.13(b). It reached threshold around P_{abs}=2.5 W and the output power increased linearly to 8.6W at P_{abs}=19.3W with a slope efficiency of 54%. At higher absorbed pump power, the phenomenon of roll-over occurred, resulting in a rapid decrease in optical-to-optical efficiency. The maximum output power reached 9.4 W at P_{abs}=23.8 W. In addition, the diameter of the aperture was adjusted from 1.0 mm to 1.4 mm in steps of 0.1 mm at P_{abs}=19.3 W to investigate the influence of aperture size on the laser performance. When the aperture diameter was set to 1.0mm, the output power decreased to 7.5W due to increased diffraction loss. When the aperture diameter was adjust to 1.4mm, the output power decreased to 8.2W as well. This is because when the aperture is too large compared with the beam size, the function of cleaning up the distorted beam was undermined, and hence resulted in more loss induced by the aberrated phase front. Figure 4.15 shows the output beam intensity distribution at an output power of 8.6 W appearing as a Gaussian-shaped profile and the corresponding beam radius in the horizontal and vertical directions after passing through a focal length, showing an improvement in the beam quality to M^2<1.1 in both directions. It is worth noting that the beam quality is maintained even up to the point of roll-over, where a maximum output power of 9.4W was obtained at P_{abs}=23.8 W. Although the maximum output power is much lower than without the aperture, the brightness is still higher.

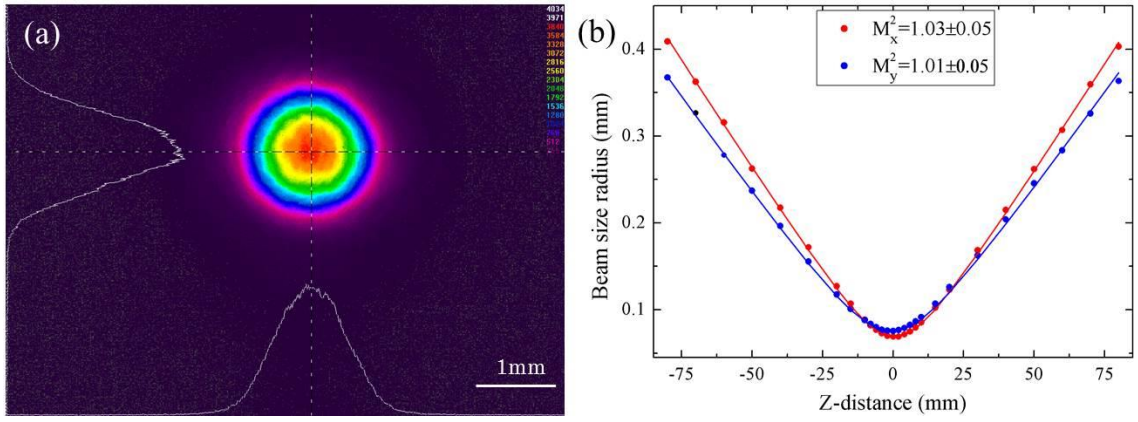

Figure 4.15 Experimental intensity distribution of TEM_{00} mode at output power of 8.6W; and (b) the M^2 data measurement.

According to the results we obtained above in both pumping schemes, it suggests that the ring-shaped pump beam yields an improved performance for generating the fundamental TEM_{00} mode compared with a traditional fibre-coupled pump source. In our experiment, the maximum output power for a diffraction-limited TEM_{00} mode from the same cavity configuration is 53% higher than the latter due to a much reduced phase distortion and reduced thermal lens strength.

4.4 Conclusion

In this chapter, we have successfully demonstrated an attractive route for power scaling of the fundamental TEM_{00} mode in a diode end-pumped Nd:YVO_4 solid-state laser. This has been accomplished by using a novel ring-shaped pump beam to reduce thermal lens strength and alleviate the thermally induced non-parabolic phase aberration in the laser crystal. This technique offers flexibility in end-pumped solid-state lasers, and hence in combination with other techniques is able to provide a strategy for further power scaling of TEM_{00} mode operation.

The principle of the TEM_{00} mode selection in case of a ring-shaped pumping scheme was first discussed. The underlying mechanism is to control the spatial overlap of cavity modes with the pump beam as well as the intracavity round-trip loss for cavity modes. The numerical calculation shows that the ring-shaped pump beam will lead to a higher threshold pump power compared with both Gaussian-shaped and top-hat shaped pump beams, but its higher effective overlap efficiency allows the laser to have a higher slope efficiency so that it yields a higher output power. The critical value of γ_{00}/γ_{01} for suppression of the LG_{01} mode was analysed numerically. The results shows that the critical value increases with the increase of relative cavity mode beam size, which means that less intracavity loss is required to suppress the higher order LG modes to deliberately excite the fundamental TEM_{00} mode. Particularly for the TEM_{00} mode with beam size radius $w = 0.8r_b$, controlling $\gamma_{00}/\gamma_{01} < 0.55$ is sufficient to suppress the oscillation of the LG_{01} mode at $P_{abs} = 50$ W. A circular aperture was used to induce differential losses for each mode and hence to suppress the higher order modes.

In the final section of this chapter, the technique was then implemented in a proof-of-principle experiment in an end-pumped Nd:YVO_4 laser. First the thermal lens strength and degradation in laser beam quality was investigated with the aid of a

probe beam. Experimental results indicate that the thermal lens was in fact 30% weaker than the traditional fibre-coupled diode pump beam. The beam degradation was also less severe with the M^2 degrading from 1.05±0.05 to 1.24±0.06 in the horizontal and 1.39±0.07 in the vertical direction under 31 W of absorbed pump power compared to a rapidly degraded M^2 value of 1.47±0.07 in the horizontal and 1.65±0.08 in the vertical direction for the top-hat fibre-coupled diode pump beam. A simple Z-folded cavity design was designed to achieve 14.2 W of diffraction-limited TEM_{00} mode (M^2<1.1) limited only by the available pump power, compared with a maximum of 9.4 W of diffraction-limited TEM_{00} power obtained with the traditional pumping scheme. This verifies the advantages of a ring-shaped pump beam in end-pumped solid-state laser architectures for power scaling of TEM_{00} mode operation.

Bibliography

1. T. Li, "Diffraction Loss and Selection of Modes in Maser Resonators with Circular Mirrors," Bell System Technical Journal **44**, 917-932 (1965).

2. A. E. Siegman, "Analysis of laser beam quality degradation caused by quartic phase aberrations," Applied Optics **32**, 5893-5901 (1993).

3. J. L. Blows, J. M. Dawes, and T. Omatsu, "Thermal lensing measurements in line-focus end-pumped neodymium yttrium aluminium garnet using holographic lateral shearing interferometry," Journal of Applied Physics **83**, 2901-2906 (1998).

4. J. L. Blows, T. Omatsu, J. Dawes, H. Pask, and M. Tateda, "Heat generation in Nd:YVO4 with and without laser action," IEEE Photonics Technology Letters **10**, 1727-1729 (1998).

5. P. K. Mukhopadhyay, J. George, K. Ranganathan, S. K. Sharma, and T. P. S. Nathan, "An alternative approach to determine the fractional heat load in solid state laser materials: application to diode-pumped Nd:YVO4 laser," Opt Laser Technol **34**, 253-258 (2002).

6. B. Neuenschwander, R. Weber, and H. P. Weber, "Determination of the thermal lens in solid-state lasers with stable cavities," IEEE Journal of Quantum Electronics **31**, 1082-1087 (1995).

7. J. Zheng, S. Z. Zhao, and L. Chen, "Thermal lens determination of LD end-pumped solid-state laser with stable resonator by slit scanning method," Opt Laser Technol. **34**, 439-443 (2002).

8. A. E. Siegman, *Lasers* (University Science Books, 1986).

Chapter 5: Doughnut-shaped beam generation in solid-state laser

5.1 Introduction

Chapter 3 introduced a unique ring-shaped pumping scheme for end-pumped solid-state lasers and discussed its advantages of reduced adverse thermal lensing effects and flexibility in transverse modes selection. It explained how each LG_{0n} mode could be selectively generated by simple adjustment of pump beam dimensions to spatially-match the intensity of the desired LG_{0n} mode. In Chapter 4, selectively exciting and power scaling of the fundamental TEM_{00} mode beam was also successfully demonstrated exploiting the weaker thermal lens of the ring-shaped pump beam. In this chapter, we will further explore this technique to generate the first higher order LG_{01} beam characterized by a doughnut-shaped intensity profile with either an optical vortex phase front or with cylindrically symmetric polarization distribution. First, we will demonstrate generation of degenerate doughnut-shaped LG_{01} modes in a Nd:YAG solid-state laser end-pumped by the ring-shaped pump beam, followed by analysing the mode composition of the excited mode. We will then investigate a method to break the degeneracy to excite an LG_{01} mode with a well-determined handedness of helical phase front. Finally, we will present an experiment for generating a radially polarized LG_{01} mode.

5.2 Degenerate LG_{01} modes

As discussed in section 3.4, any transverse mode having the 'best' spatial overlap with the population inversion is likely to be preferentially excited. By adjusting the ring-shaped pump beam dimension appropriately to yield an inversion distribution that is spatially matched to the intensity distribution for the first higher order LG_{01} mode in the laser crystal, lasing will occur preferentially on this doughnut-shaped mode with a phase front that advances with a helical trajectory described by $exp(\pm i\varphi - ikz)$. Theoretically, LG_{01} modes with right-handed (LG_{01}^{+}) and left-handed (LG_{01}^{-}) helical phase trajectories have the same spatial overlap with the pumped

region and hence should have equal threshold pump powers resulting in a beam with petal-like pattern due to coherent superposition of modes with opposite handedness. Coherent superposition of LG_{0n} modes with opposite handedness has been experimentally demonstrated inside a laser cavity by inserting a circular stop to suppress the Gaussian beam oscillation [1] or by using a ring-shaped pump beam obtained from defocusing a misaligned fibre-coupled diode [2]. However, direct generation of the LG_{01} mode with a single well-determined handedness of helical phase front from a laser resonator was reported in the literature [3-5], but the handedness tends to be random and could not be controlled as the underlying mode selection mechanism was not fully understood. One possible reason for oscillating only one handedness rather than both could be due to small imperfections on the cavity mirrors and intracavity components. Another possibility is that the doughnut-shaped output beam is an incoherent superposition of two petal-pattern beams as reported in [6].

5.2.1 Generation of degenerate LG_{01} modes in a Nd:YAG laser

It was reported that a doughnut-shaped LG_{01} mode could be directly generated inside a laser resonator by using a spot-defect mirror [4] or an intra-cavity circular absorber [5] to suppress the fundamental TEM_{00} mode. However, these techniques suffer from a relatively low efficiency due to poor spatial overlap between the pump beam and the LG_{01} mode. Here we further explore the use of the ring-shaped pumping technique to directly generate a doughnut-shaped LG_{01} mode in an end-pumped Nd:YAG laser.

The schematic diagram of experimental set-up is shown in Figure 5.1. The pump light was provided by a fibre-coupled diode laser at 808nm with a 105μm diameter and 0.22 NA delivery fibre yielding a maximum pump power of 4W. The output from the pump laser was reformatted by using the pump beam conditioning

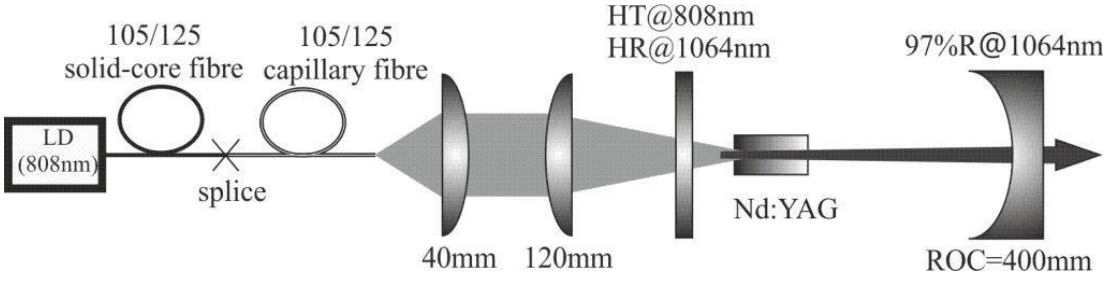

Figure 5.1 The schematic experimental setup of LG_{01} mode generation.

element described in Chapter 3. In this case, the capillary silica fibre was directly spliced to the fibre coupled laser diode, yielding ~3.5W of output power in a beam with a ring-shaped near-field intensity profile as shown in Figure 3.2. A simple two-mirror resonator configuration (Figure 5.1) was employed for the Nd:YAG laser comprising a plane pump input coupling mirror with high transmission (>95%) at the pump wavelength, high reflectivity (>99.8%) at the lasing wavelength (1.064μm), and a concave output coupler with a radius of curvature of 300 mm and a transmission of 3% at 1.064 μm. A 10mm long Nd:YAG rod crystal with 0.8 at.% was used as the gain medium with both end faces antireflection coated at the pump and lasing wavelengths. The latter was mounted in a water-cooled copper heat-sink maintained at 18℃ and was placed ~2 mm from the input coupling mirror. The cavity length was adjusted to ~130mm to yield a calculated mode waist radius for the LG_{01} mode of ~315 μm in the Nd:YAG rod. The pump beam was imaged into the laser rod and magnified by a factor of 3 using an arrangement of lenses to achieve preferential lasing on the LG_{01} mode.

After careful alignment of the laser resonator to ensure cylindrical symmetry of the optical system, the doughnut-shaped LG_{01} mode reached threshold at 0.5W of incident pump power. Figure 5.2 plots the laser output power as a function of incident pump power. The LG_{01} mode output power increased linearly up to 1.7W at the maximum incident pump power of 3.5W. The corresponding slope efficiency

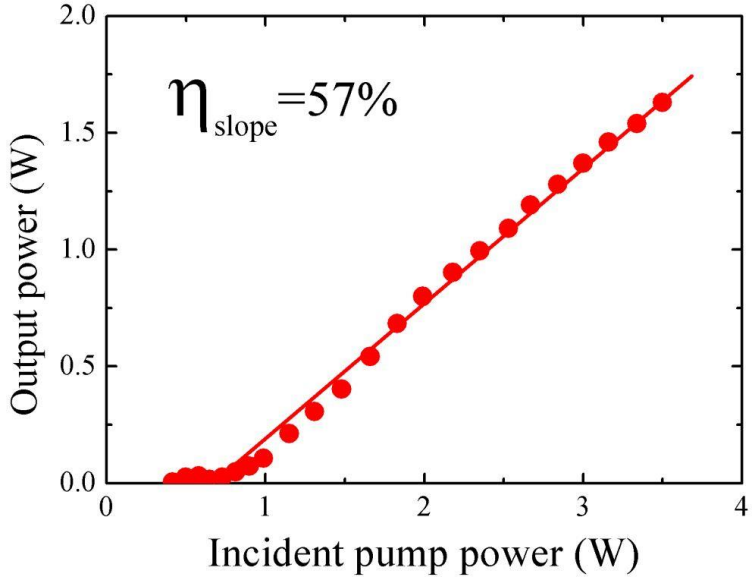

Figure 5.2 LG_{01} mode output power as a function of incident pump power.

is 57% with respect to the incident pump power.

One of typical LG_{01} mode profiles measured at 1.7W of output power is shown in Figure 5.3(a). The beam profile was well maintained above the threshold power as monitored by a Spiricon CCD Camera (LBA-FW-SCOR20). Figure 5.3(b) illustrated the measured transverse intensity distribution as a function of radius which is in close agreement with the theoretical transverse intensity profile of the LG_{01} mode. The intensity at the beam centre is near to zero indicating sufficient suppression of the lower order TEM_{00} mode owing to less spatial overlap with the pump beam. It is worth mentioning that the doughnut-shaped beam intensity profile observed in the experiment was stable against the mechanical vibration and thermal fluctuation occurring in the laboratory. Without deliberately misalignment the cavity, the doughnut-shaped beam profile could be maintained during the experiment.

The polarization state of observed doughnut-shaped modes were non-polarized over the full range of pump power, in contrast to the results described in [7] where the generated doughnut-shaped mode had radial polarization due to thermally-induced bifocussing and hence slightly different mode sizes for radial and azimuthal polarization states. The net result is that the mode (radial polarization in this case [7]) with a better spatial overlap with the ring-shaped population inversion reaches the threshold first, and prevents the other mode (azimuthal polarization) from oscillating due to gain saturating. However, in our case, the modes with radial and azimuthal polarization had nearly the same mode size within the laser crystal due to very weak thermally-induced bifocussing and a plan-concave resonator used.

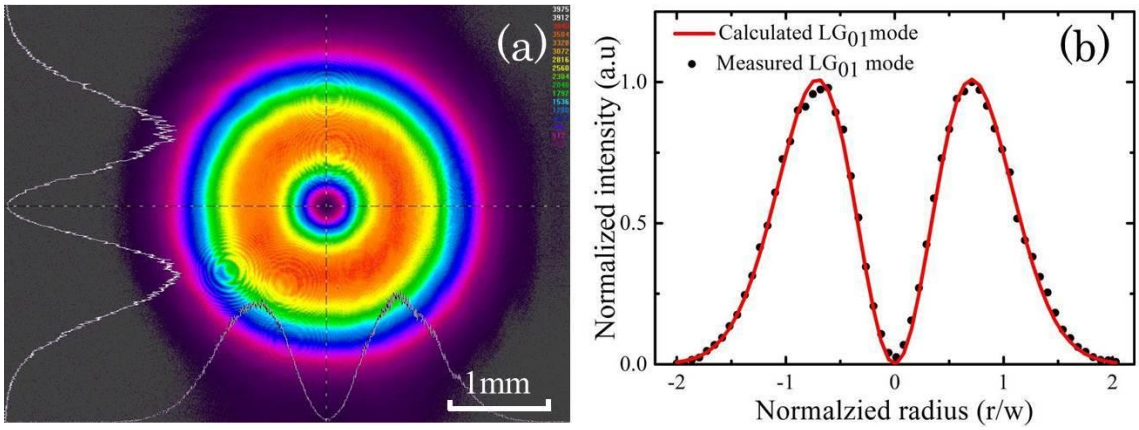

Figure 5.3 (a) LG_{01} mode beam profile, and (b) calculated and measured intensity distributions.

Therefore, they had nearly the same threshold and reached the threshold simultaneously, and hence the output had a non-polarized state.

The beam propagation parameters (M_x^2 and M_y^2) were measured to be 2.07±0.06 and 2.04±0.04 at 1.7 W output power respectively as shown in Figure 5.4, which are in excellent agreement with the theoretical value of 2 confirming that a high beam

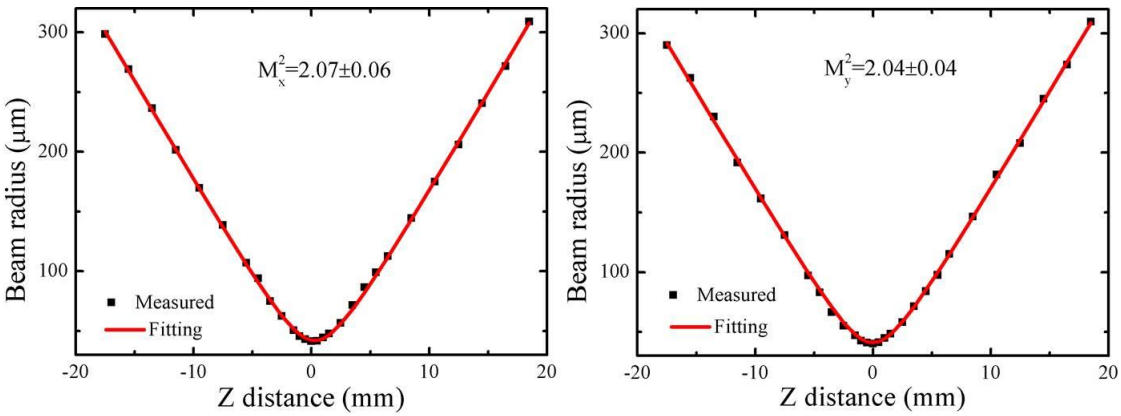

Figure 5.4 M^2 measurement at 1.7 W output power.

quality LG_{01} mode was generated.

5.2.2 Beam phase front measurement

In order to measure the phase front shape of the generated doughnut-shaped LG_{01} mode, a Mach-Zehnder interferometer was built as shown in Figure 5.5. The output

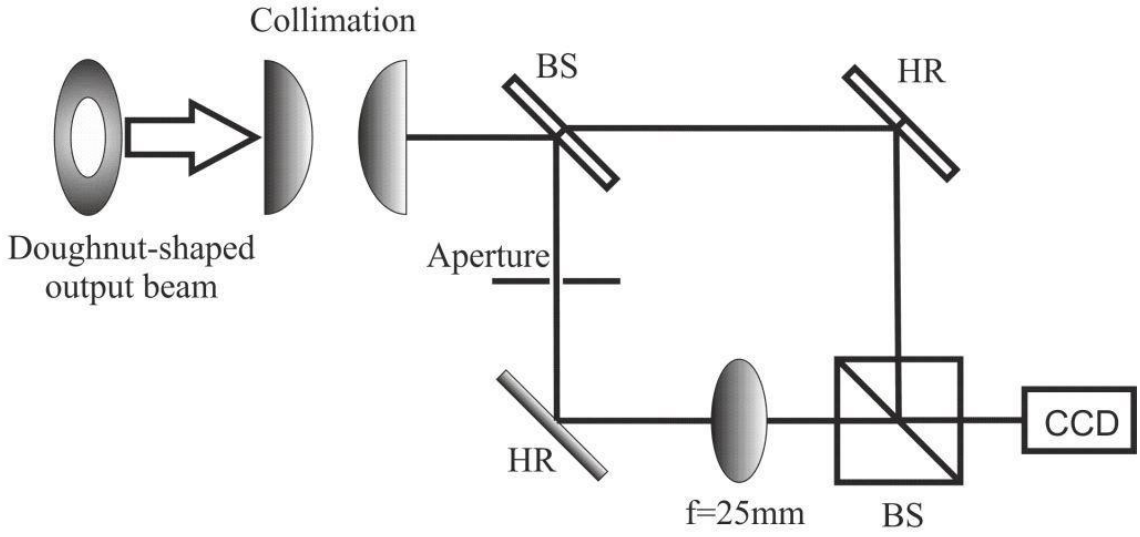

Figure 5.5 Mach-Zehnder interferometer for measuring the beam phase front shape.

laser beam was collimated and then was split into a signal and reference beam. In the reference arm, a spherical wavefront was obtained by using a very small aperture followed by a spherical lens. Finally the reference beam was superimposed with the signal beam and generated an interference pattern on the CCD camera.

As is well known, for a beam with spherical wave front, the phase front can be described as:

$$\Phi_1(r) = -\frac{kr^2}{2R_1} \tag{5.1}$$

where R_1 is the radius of curvature of wavefront. For the LG_{01} mode with a determined helical phase front, the phase shape can be written as:

$$\Phi_2(r,\varphi) = \pm\varphi - \frac{kr^2}{2R_2} \tag{5.2}$$

where R_2 is the radius of curvature of the LG_{01} mode. From Eq.(5.1) and (5.2), the interference maxima fringes of these two beams on any plane have the formula:

$$\pm\varphi + kr^2 \frac{R_1 - R_2}{2R_1R_2} = 2n\pi\ , \quad (n = 0, \pm1, \pm2, \ldots) \tag{5.3}$$

Figure 5.6 shows two examples of calculated interference patterns for spherical waves with LG_{01} modes with opposite handedness helical phase front according to Eq.(5.3). It can be seen that the interference pattern has either a clockwise or anti-clockwise spiral pattern determined by the sense of azimuthal phase front in

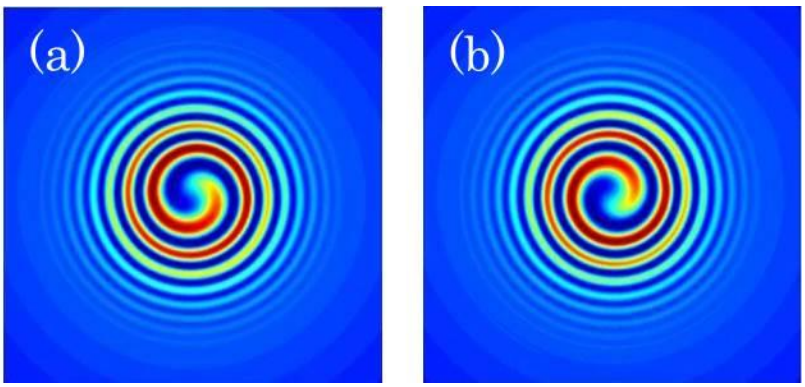

Figure 5.6 Interference patterns of optical vortex modes with a spherical reference wave (a) LG_{01}^{-} mode, and (b) LG_{01}^{+} mode.

Eq.(5.3).

One typical measured interference pattern for the doughnut-shaped output beam is shown in Figure 5.7. It appears that neither a clockwise nor anti-clockwise spiral pattern was obtained suggesting that the generated doughnut-shaped mode did not have a helical phase front. One of main reasons is that the multi axial-mode doughnut-shaped output tends to be a 'hybrid' mode consisting of TEM_{01} mode with different orientations and LG_{01} modes with either the same or opposite handedness of helical phase front at different frequencies. Therefore, the output did not have a pure helical phase front and hence the obtained interference did not have a clear spiral fringe as shown in Figure 5.6. The composition of the obtained doughnut-shaped LG_{01} mode will be further investigated in the following section.

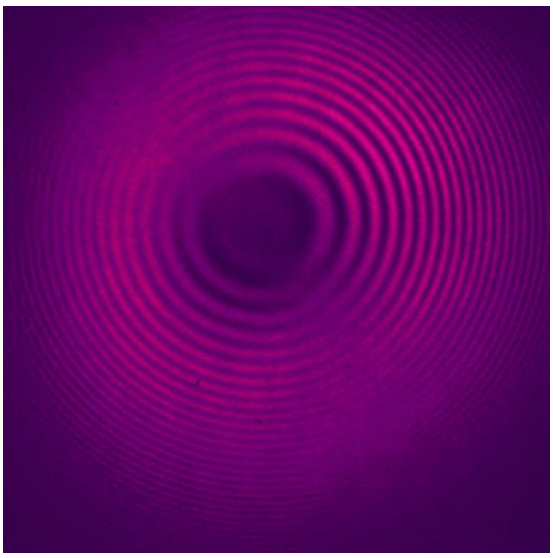

Figure 5.7 Typical interference pattern of doughnut-shaped LG_{01} output mode with a spherical wavefront reference beam.

5.3 Characterization of the doughnut-shaped LG_{01} mode

Measuring the interference pattern of a doughnut-shaped beam with a beam with a spherical wavefront in section 5.2.2 revealed that the doughnut-shaped output beam did not have a well-defined sense of helical phase front. One reason might be that the mode of opposite handedness was excited simultaneously with different frequencies, or the doughnut-shaped beam was a result of incoherent superposition of petal-like patterned LG modes with orthogonal orientations. To verify this

hypothesis, we employed both Mach-Zehnder interferometer and an astigmatic mode-converter to analyse each axial mode of the output beam.

5.3.1 Astigmatic mode-conversion

According to [8], the electric field amplitude of the HG_{nm} and LG_{nm} modes which propagate along the z axis can be expressed as:

$$\begin{aligned} u_{nm}^{HG}(x,y,z) = C_{nm}^{HG}(1/w(z))\exp[-ik(x^2+y^2)/2R(z)]\exp[-(x^2+y^2)/w(z)^2] \\ \times\exp[-i(n+m+1)\cdot\psi(z)]H_n(x\sqrt{2}/w(z))H_n(y\sqrt{2}/w(z)) \end{aligned} \tag{5.4}$$

and

$$\begin{aligned} u_{nm}^{LG}(r,\phi,z) = C_{nm}^{LG}(1/w(z))\exp[-ikr^2/2R(z)]\exp[-r^2/w(z)^2] \\ \times\exp[-i(n+m+1)\cdot\psi(z)]\exp(-i(n-m)\phi) \\ \times(-1)^{\min(n,m)}(r\sqrt{2}/w(z))^{|n-m|} \\ \times L_{\min(n,m)}^{|n-m|}(2r^2/w(z)^2) \end{aligned} \tag{5.5}$$

with

$$R(z) = (z_R^2 + z^2)/z \tag{5.6}$$

$$\frac{1}{2}kw^2(z) = (z_R^2 + z^2)/z_R \tag{5.7}$$

$$\psi(z) = \arctan(z/z_R) \tag{5.8}$$

where $H_n(x)$ is the Hermite Polynomial of order n, $L_p^l(x)$ is the generalized Laguerre Polynomial, k is the wave number, and z_R is the Rayleigh range. The order of the mode is defined by $N=n+m$. For LG modes, the radial index p is defined as $min(n, m)$ and the azimuthal index is $l=|n-m|$.

A HG mode with its principal axis at 45° with respect to (x, y) axes can be decomposed into a set of HG modes constituents with the following relationship[8]:

$$u_{nm}^{HG}\left(\frac{x+y}{\sqrt{2}},\frac{x-y}{\sqrt{2}},z\right) = \sum_{k=0}^{N} b(n,m,k)\,u_{N-k,k}^{HG}(x,y,z) \tag{5.9}$$

where the real coefficient b is defined as:

$$b(n,m,k) = \left(\frac{(N-k)!k!}{2^N n!m!}\right)^{1/2} \times \frac{1}{k!}\frac{d^k}{dt^k}[(1-t)^n(1+t)^m]_{t=0} \tag{5.10}$$

Moreover, the relationship between LG_{nm} and HG_{nm} modes is given by:

$$u_{nm}^{LG}(x,y,z)=\sum_{k=0}^{N} i^{k} b(n,m,k)\, u_{N-k,k}^{HG}(x,y,z) \tag{5.11}$$

which has the same real coefficient *b(n,m,k)* as in Eq. (5.9). The factor i^k corresponds to a π/2 relative phase shift between the successive components. Some examples of a mode decomposition are depicted in the Figure 5.8.

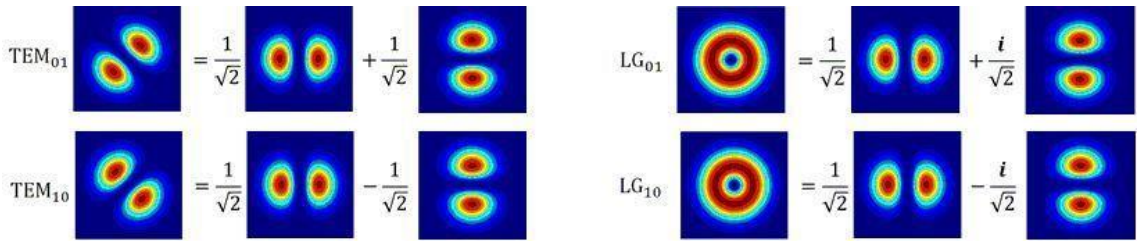

Figure 5.8 Examples of the decomposition of HG_{nm} and LG_{nm} modes of order 1.

From Eqs. (5.9) and (5.11), it is obvious that a HG mode can be converted to a LG mode if we introduce a relative π/2 phase in the successive decomposition components. This could be easily done by exploiting the Gouy phase of a HG mode using an astigmatic π/2 phase mode converter as illustrated in Figure 5.9. The mode converter is composed of two identical cylindrical lenses with specific separation in the optical axis.

To achieve π/2 Gouy phase difference between *x*-component and *y*-component and confine the astigmatic within the region of the pair of cylindrical lens, it requires that the focal length of cylindrical lenses and the distance to satisfy [8]:

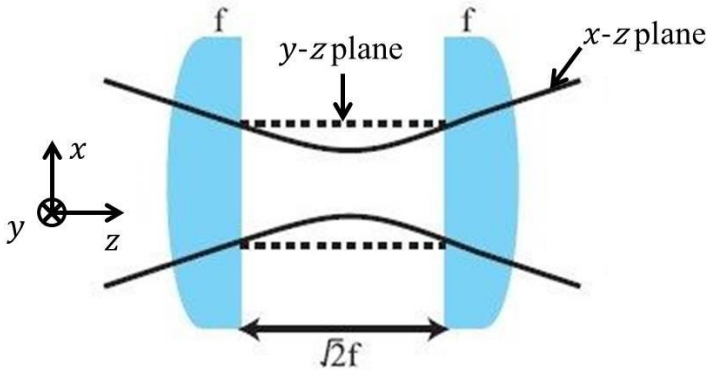

Figure 5.9 π/2 phase mode converter.

$$f = (1+\frac{1}{\sqrt{2}})^{-1} z_x \tag{5.12}$$

$$d = \frac{f}{\sqrt{2}} \tag{5.13}$$

In the experiment, a π/2 mode converter was built consisting of two identical cylindrical lenses with focal length 50mm in the plane parallel to Figure 5.9. The separation distance between two cylindrical lenses was adjusted to be 35.4mm to satisfy the criteria of Eq.(5.13).

A linearly-polarized TEM_{01} mode with its nodal line oriented to 45° with respected to the vertical direction (shown in Figure 5.10(a)) was investigated firstly to confirm the effectiveness of the mode converter. The diagonal TEM_{01} mode was formed by passing a radially-polarized LG_{01} mode through a linear polarizer whose transmission axis was oriented at 45° with respect to vertical direction. When the diagonal TEM_{01} mode with a Rayleigh range of 42.7mm passed through the mode converter, a doughnut-shaped mode could be observed as shown in Figure 5.10(b), confirming that the mode converter functioned perfectly.

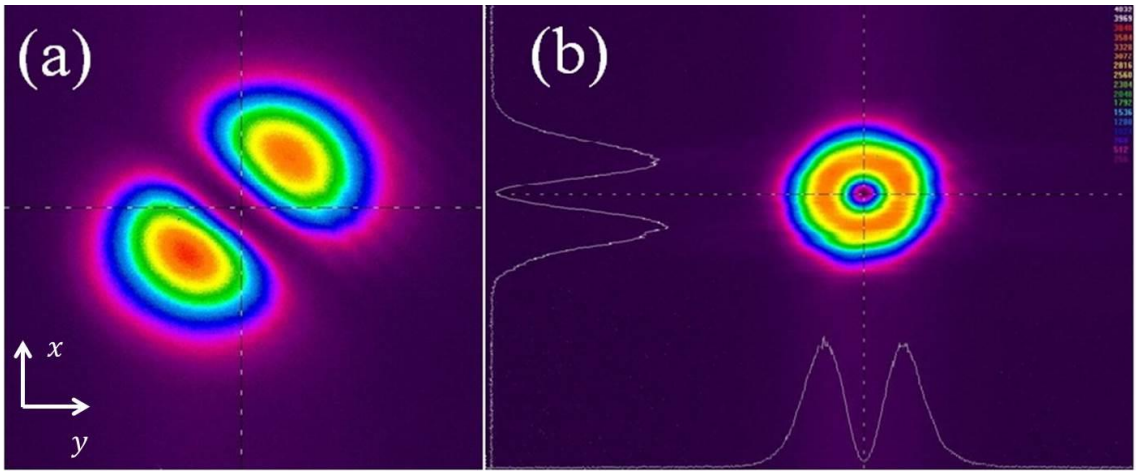

Figure 5.10 (a) A diagonal TEM_{01} mode beam profile; (b) the beam profile of diagonal TEM_{01} mode after passage through the mode converter.

5.3.2 Mode analysis

In this section, we will apply the Mach-Zehnder interferometer together with π/2 mode converter to analyse the composition of each axial mode of the doughnut-shaped mode generated in section 5.2.

Figure 5.11 shows the schematic experiment setup for analysing the axial modes of the doughnut-shaped LG_{01}. The output beam (shown in Figure 5.12(a)) was split into two beams. One beam was analysed by the π/2 mode converter, the other one was simultaneously investigated using the Mach-Zehnder interferometer. Initially, the multi-axial frequency output beam was checked without inserting the Fabry-Perot interferometer (FPI) to separate axial modes. The Rayleigh range of the doughnut-shaped output beam was carefully adjusted using a telescope before the mode converter to satisfy the criteria of Eqs. (5.12) and (5.13). After passing through the π/2 mode converter, the beam still showed a nearly doughnut-shaped intensity profile rather than a two-lobed structure as shown in Figure 5.12(b). Meanwhile the interference pattern measured by the Mach-Zehnder interferometer was similar as shown in Figure 5.7. Both measurements suggested that the doughnut-shaped LG_{01} output mode did not have a pre-determined helical phase front.

A scanning FPI with free spectra range of 3.75 GHz was placed behind the collimation lenses as depicted in Figure 5.11. About six axial-modes with frequency spacing of ~1.08GHz were usually observed by using a fast silicon photodiode to detect the resonated mode of scanning FPI. Then, manually tuning the voltage applied on the piezoelectric transducer to adjust the separation of two etalons, each axial mode could be deliberately selected. A CCD camera was placed before the π/2 mode converter to monitor the beam intensity profile for each axial mode showing either a two-lobe structured profile or a doughnut shape. For each axial-mode with doughnut-shaped intensity profile, the phase front was checked by the π/2 mode

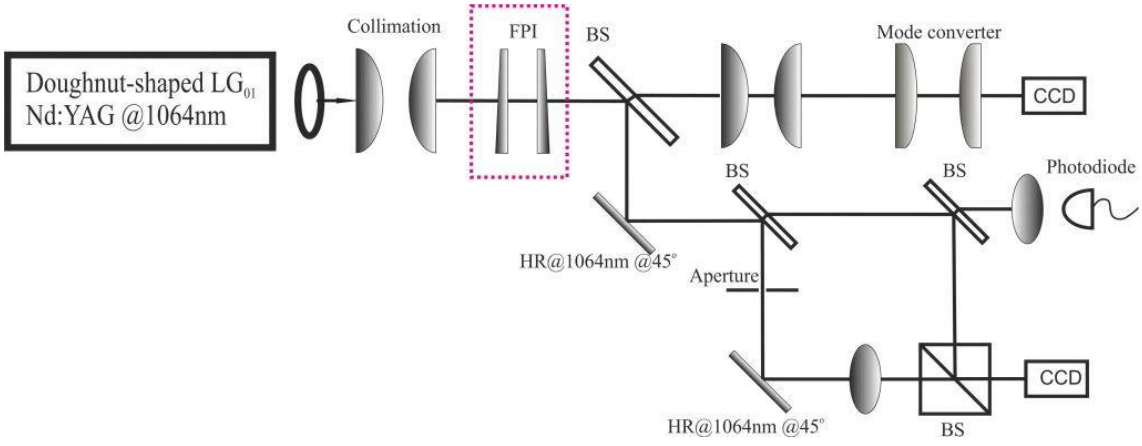

Figure 5.11 Schematic diagram for measuring the helical phase front of doughnut-shaped LG_{01} mode.

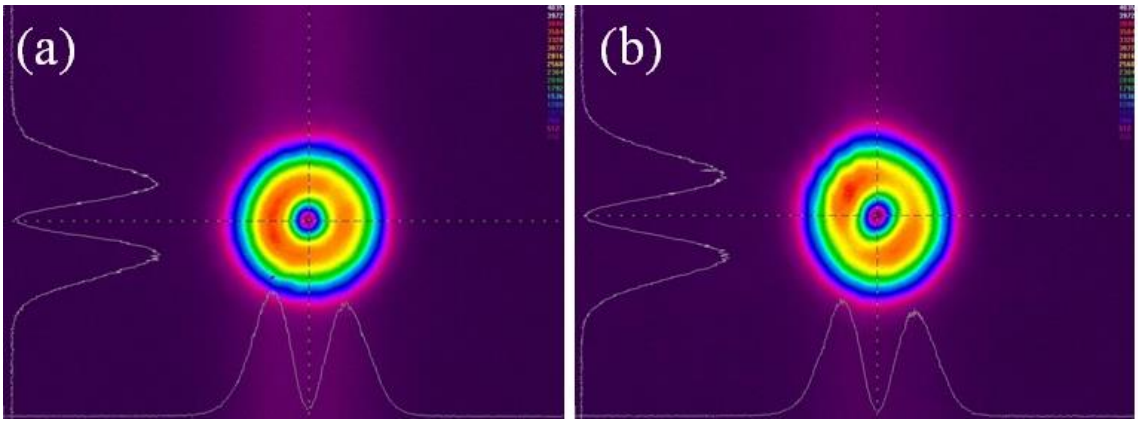

Figure 5.12 (a) doughnut-shaped LG_{01} mode output, and (b) the corresponding beam profile behind the π/2 mode converter.

converter and the Mach-Zehnder interferometer simultaneously as illustrated in Figure 5.11. The resultant interference patterns show clear spiral fringes with either anti-clockwise or clockwise handedness, and the beam intensity profiles show a two-lobe structure TEM_{01} mode with nodal line oriented at 45° or −45° as shown in Figure 5.13, confirming that each axial-mode with doughnut-shaped profile had a determined sense of helical phase front.

Based on this measurement, we can conclude that the doughnut-shaped LG_{01} beam with multi-axial frequencies generated from a solid-state laser resonator tends to

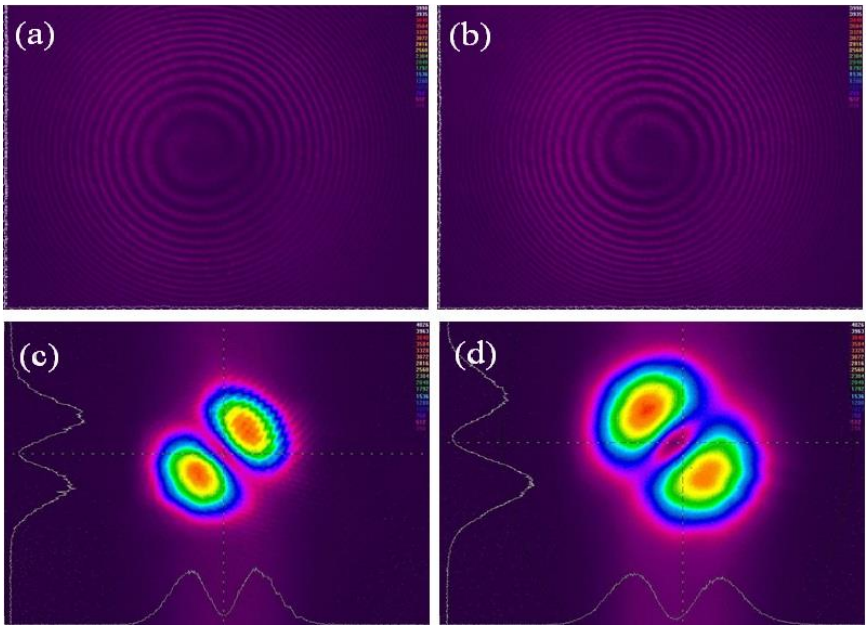

Figure 5.13 Interferometer patterns and outputs of mode converter. (a) and (c) represent LG_{01} mode with anti-clockwise handedness of helical phase front; (b) and (d) represent clockwise handedness.

be a result of incoherent superposition of degenerate TEM_{01} and LG_{01} modes with opposite handedness of helical phase front. This is because TEM_{01} and doughnut-shaped LG_{01} modes have nearly the same spatial overlap with the population inversions and hence they are tend to reach the threshold simultaneously.

5.4 Improving LG_{01} mode selection

The doughnut-shaped LG_{01} beam with a well-determined handedness of helical phase front offering OAM of $\pm\hbar$ for each photon is more desirable in a wealth of promising applications in areas such as optical manipulation of particles [9], free-space communication [10], optical memory [11], quantum information [12] and laser processing of materials [13]. A number of different techniques for generating LG beams with a helical phase front have been devised over the years. The most popular techniques exploit external beam-shaping arrangements to transform a Gaussian mode into the LG_{01} mode in the far-field (e.g. in homogenous anisotropic media [14], spiral phase plate [15], computer-generated hologram [16]). These methods, however, suffer from the drawbacks of relatively low conversion efficiency (varies from 20% to 90%) and/or degradation in beam quality, and are generally not suitable for high power operation due to power handling limitations. A variety of techniques aimed at directly generating higher order LG doughnut modes have also been reported [17]. However, many are prone to yielding an output beam with a petal-pattern structure that is a coherent superposition of LG modes of opposite handedness [1]. Further confusion can also arise if the doughnut-shaped beam directly generated from the lasers is an incoherent superposition of two petal-pattern beams [6] giving the false impression that an LG doughnut mode with a particular handedness of helical phase has been generated. Hence, robust, efficient and power scalable direct generation of LG doughnut beams with well-determined handedness is desirable for a wide range of applications.

5.4.1 Single frequency LG_{01} mode

As we presented in section 5.3, each axial mode with doughnut-shaped intensity profile has a well determined helicity. It suggests that the doughnut-shaped beam generated from a single frequency laser resonator must have a well-determined helical phase front. In this section, we construct and test a single-frequency laser system to verify our hypothesis.

A large number of techniques have been employed to achieve single-frequency lasers, such as monolithic non-planar ring oscillators (NPRO) [18], microchip lasers [19], the twisted-mode technique[19] and inserting etalons in the laser cavity. Although the technique of a traveling-wave unidirectional ring cavity has been widely used to achieve single-frequency mode in solid-state lasers, the optical alignment of the cavity is difficult for generating LG_{01} mode with good beam quality as it is vulnerable to astigmatism caused by the folded curved mirrors in the cavity. Another approach is the NPRO, but it is difficult to control the reshaped pump beam to match the LG_{01} mode within the crystal and this system is also expensive. The twisted-mode technique, however, is a relative simple technique to implement for generating single-frequency LG_{01} mode as it only requires two quarter waveplates and a Brewster-angled plate in a linear cavity. For these reasons, we chose the twisted-mode technique to investigate single-frequency LG_{01} mode operation.

5.4.1.1 Twisted-mode technique

Figure 5.14 shows a schematic diagram of the twisted-mode technique consisting of two cavity mirrors M1 and M2, a laser crystal placed between two λ/4 wave-plates (Q1 and Q2), and a Brewster-angled plate (Bs) placed between M1 and Q1. The fast axes of Q1 and Q2 are orthogonal to each other and are oriented to 45° with respect to the transmission axis of the Brewster's plate. The principle of the twisted-mode technique is described as following:

The electric field of a linearly polarized beam travelling towards the right before

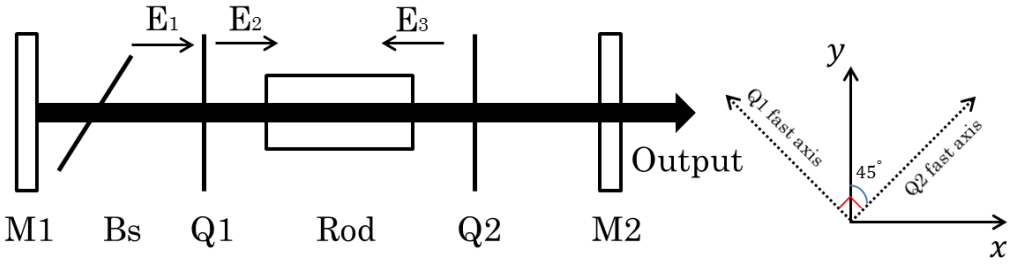

Figure 5.14 A typical example of schematic of laser resonator with twisted-mode technique.

Q1 can be expressed as

$$\begin{aligned} E_{x1} &\sim \sin(\omega t - kz) \\ E_{y1} &\sim \sin(\omega t - kz) \end{aligned} \tag{5.14}$$

when the wave passes through the Q1, the electric field becomes:

$$\begin{aligned} E_{x1} &\sim \sin(\omega t - kz + \pi/2) \\ E_{y1} &\sim \sin(\omega t - kz) \end{aligned} \tag{5.15}$$

which becomes a circularly polarized wave. After reflecting from M2 and double passing through the Q2, the electric field of the wave becomes:

$$\begin{aligned} E_{x1} &\sim \sin(\omega t + kz - 2kL + \pi/2) \\ E_{y1} &\sim \sin(\omega t + kz - 2kL + \pi) \end{aligned} \tag{5.16}$$

where L is the optical length of the laser cavity. Within the laser rod, the sum of two circularly polarized waves travelling in opposite directions yields two orthogonal linear standing waves which are spatially displaced with respect to each other by λ/4, which can be expressed as:

$$\begin{aligned} E_x &\sim \cos(kL - kz)\cos(\omega t - kL) \\ E_y &\sim \sin(kL - kz)\cos(\omega t - kL) \end{aligned} \tag{5.17}$$

therefore, the total intensity distribution is:

$$E_x^2 + E_y^2 \sim 4\cos^2(\omega t - kL) \tag{5.18}$$

which is independent on the z-axis position. Hence, the problem of spatial hole burning is avoided and spatially homogeneous population inversion is formed within the laser crystal.

5.4.1.2 Experiment and results

The schematic diagram of the twisted mode Nd:YAG laser for single-frequency LG_{01} mode generation is illustrated in Figure 5.15, in which the same pump source, beam re-shaping technique and cavity design were employed as in Figure 5.1. An un-coated silica window with 200 μm thickness was placed in the cavity and was rotated to Brewster's angle (~55°) to ensure the output beam had the p polarization. The key element of the twisted-mode technique consists of two zero-order λ/4 wave-plates, which were anti-reflection coated on both sides at 1.064 μm and 0.808 μm and were placed at the both ends of the Nd:YAG. The fast axes of the

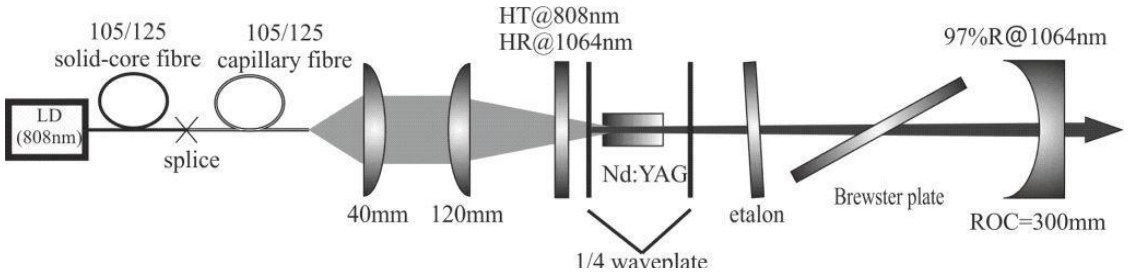

Figure 5.15 The schematic experimental setup of single-frequency LG_{01} mode.

λ/4 wave-plates were set to be 90^0 with respect to each other and 45^0 with respect to the polarization direction of beam. The cavity length was set to be approximately 130 mm enabling the LG_{01} mode waist to be 315μm which has a good spatial overlap with the pump beam. The resonator had a longitudinal mode spacing of 1.08 GHz.

Without inserting the λ/4 waveplates, etalon and Brewster plate, the laser operated on multiple longitudinal modes as described in the last section. Single-frequency operation was achieved by inserting λ/4 waveplates at both ends of the Nd:YAG rod to suppress spatial-hole-burning together with an intracavity etalon. It is worth mentioning that the laser operated at a few longitudinal modes when only inserting the pair of λ/4 waveplates because of the residual spatial-hole-burning due to imperfect anti-reflection coatings. An uncoated fused silica etalon with 1mm thickness mounted in a mirror mount was perpendicularly inserted to the cavity. The single-frequency operation on the doughnut-shaped LG_{01} mode was realized

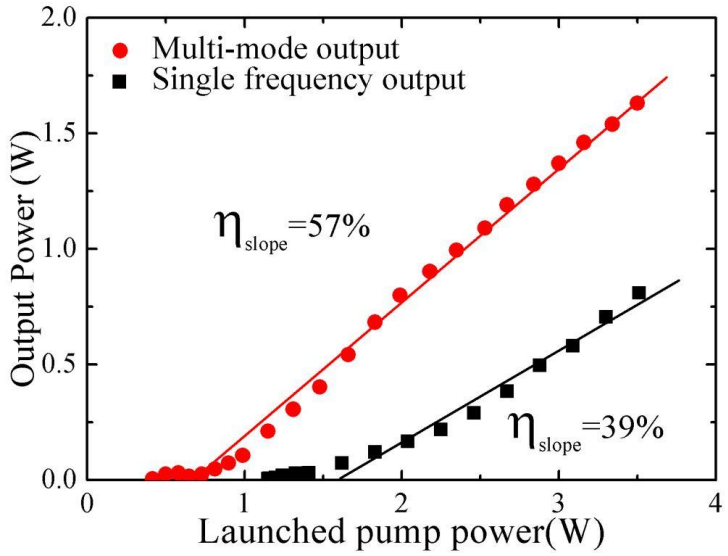

Figure 5.16 The multi-axial mode and sing-axial-mode doughnut-shaped LG_{01} mode output power as a function of the launched pump power.

only when the etalon was carefully adjusted to specific angles. These angles slightly varied with the output power and cavity alignment. Figure 5.16 plots the output power of both multi-axial mode and single-axial-mode operation on the doughnut-shaped LG_{01} mode as a function of launched pump power. The single-axial-mode operation reached threshold at ~1.5 W of launched pump power. The output power increased linearly with the launched pump power with a slope efficiency of 39.6% and reached 0.81 W at the maximum available pump power. The lower output power and slope efficiency for single-frequency operation compared to multi-axial-mode operation could be attributed to the much higher intracavity loss associated with the insertion of additional uncoated components.

The digital traces of the scanning FPI at the maximum output power of 0.81 W are illustrated in Figure 5.17. The measured full width at half maximum (FWHM) linewidth was ~135 MHz limited by the resolution of the FPI. Note, that single-frequency operation was only realized by tilting the etalon to several specific angles.

The phase front shape was measured by the same Mach-Zehnder interferometer as described in the last section. The resulting interference pattern had a clear spiral fringe with either clockwise or anti-clockwise handedness as illustrated in Figure 5.18 verifying that the doughnut-shaped output beam had a helical phase front with determined handedness. The handedness tended to be random but was stable once the laser oscillation was established. Flipping the handedness between the

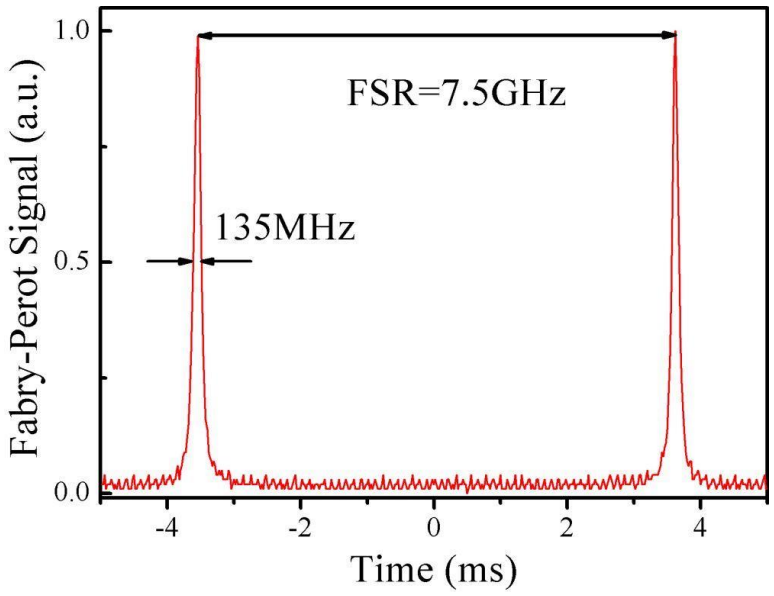

Figure 5.17 Oscillator trace from a scanning FPI with 7.5GHz free spectra range.

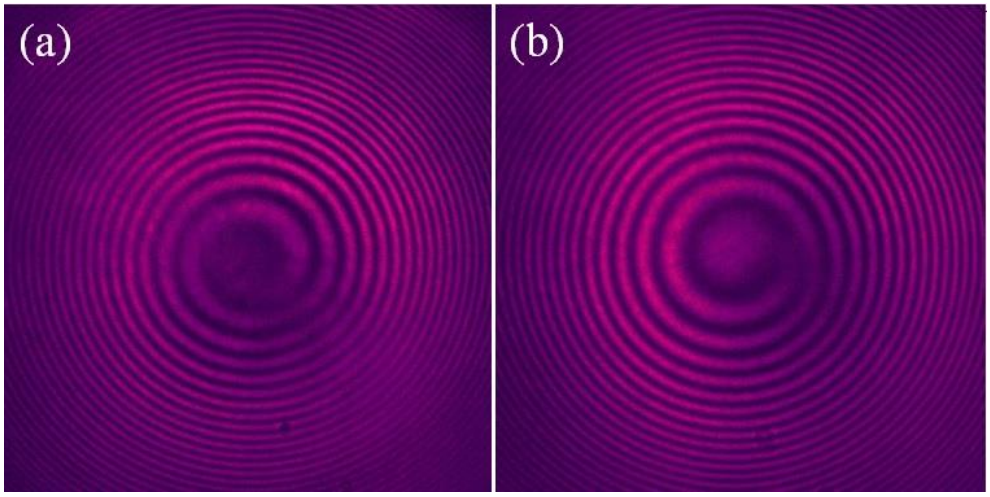

Figure 5.18 Interference patterns of doughnut-shaped LG_{01} beams for single-frequency operation: (a) anti-clockwise, and (b) clockwise helical phase front.

opposite sense could also be achieved by tilting the cavity mirror together with adjustment of the etalon.

5.4.2 Controlling the handedness of the LG_{01} mode

Although the single-frequency operation presented in previous section allows the LG_{01} beam to have a well-determined helical phase front, the handedness of helical phase front could not be pre-selected or controlled as in most other techniques. In this section we demonstrate a very simple scheme for directly generating doughnut-shaped LG_{01} modes with controllable handedness of helical phase in an end-pumped solid-state laser.

5.4.2.1 Principle of mode selection

Our approach makes use of a fibre-based pump beam conditioning element described in section 3.2 in combination with a novel intracavity mode-selection element (MSE). The pump beam conditioning element is used to re-format the pump beam into a beam with an annular intensity distribution in the near-field. In this way, the pump beam profile can be tailored to yield an inversion distribution that is spatially-matched to the intensity distribution for the LG_{01} mode in the laser crystal, so that lasing occurs preferentially on the LG_{01} mode since it has the lowest threshold. However, LG_{01} modes with right-handed (LG_{01}^{+}) and left-handed (LG_{01}^{-}) helical phase trajectories have the same spatial overlap with the pumped

region and hence equal threshold pump powers. In order to break this degeneracy, we exploit the fact that the standing-wave intensity distributions for the LG_{01}^{+} and LG_{01}^{-} modes inside the laser resonator are different. This can be shown as follows: The scalar instantaneous electric field for a $LG_{01}^{\pm}$ mode propagating in the forward (+z) direction can be expressed in the form:

$$E_f = u(r)\cos(\omega t - kz \pm \varphi) \tag{5.19}$$

where $k = 2\pi/\lambda$ is the wavenumber, ω is angular frequency, φ is azimuthal angle and $u(r)$ is a complex function describing the amplitude of the electric field. Whereas, the electric field for the $LG_{01}^{\pm}$ mode propagating in the backward (−z) direction after reflection by a high reflectivity resonator mirror can be written as:

$$E_b = u(r)cos(\omega t + kz \mp \varphi) \tag{5.20}$$

This assumes that the loss at the mirror is negligible. The resulting standing-wave electric-field distribution for the $LG_{01}^{\pm}$ mode is:

$$E^{\pm} = 2u(r)\cos(\omega t)\cos(-kz \pm \varphi) \tag{5.21}$$

Hence, the time-averaged standing-wave intensity distribution can be written as:

$$I^{\pm} = |u(r)|^2 \cos^2(\omega t)\cos^2(-kz \pm \varphi) \tag{5.22}$$

Thus inside a laser resonator both LG_{01}^{+} or LG_{01}^{-} modes have a two-lobed transverse intensity distribution that rotates by 2π radians for every wavelength increment in the distance along the cavity axis, but they rotate in opposite directions. Hence by strategically positioning structures with nanoscale thickness it is possible to generate a differential loss and hence selectively excite the LG_{01}^{+} or LG_{01}^{-} mode. The underlying principle of operation of the MSE is illustrated in Figure 5.19. Two nanoscale thickness wires oriented to 45° with respect to each other are positioned in the centre of beam. The first wire defines the orientation of the standing wave pattern at a fixed position in the cavity as shown in Figure 5.19(a). As the two-lobe structure of standing wave pattern of LG_{01}^{+} and LG_{01}^{-} modes counter-rotate with the same pitch along resonator axis, the two-lobe pattern of LG_{01}^{-} mode rotates clockwise by angle $(n+1/4)\pi$ after propagating a distance $(n/2+1/8)\lambda$, where n is an integer. The second wire can then be strategically positioned so that it is perpendicular to the two-lobed intensity pattern (see Figure 5.19(b)) and, as a

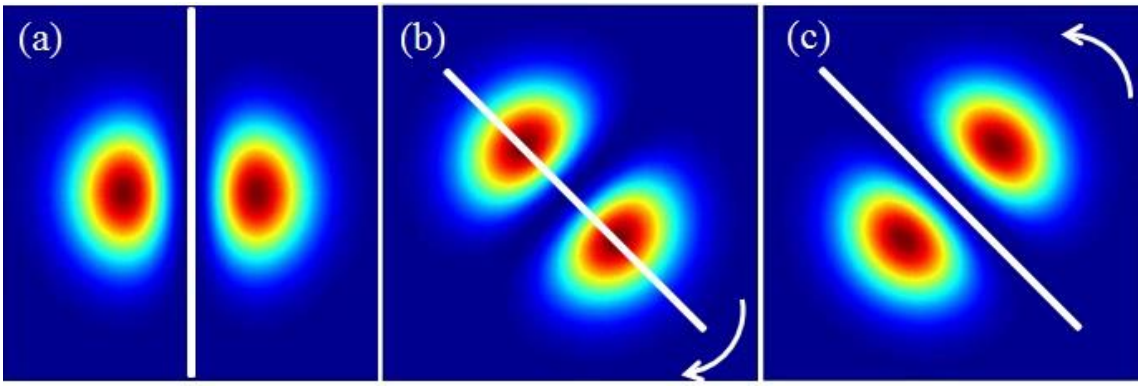

Figure 5.19 (a) The instantaneous intracavity intensity pattern for the LG_{01}^{+} and LG_{01}^{-} modes at a fixed position; (b)-(c) the respective intensity patterns for the LG_{01}^{-} and LG_{01}^{+} modes after propagating a distance of (n/2+1/8)λ. The white lines represent the line-shaped loss region introduced by the first wire (a) and second wire (b)-(c).

consequence, causes negligible and minimum loss for the LG_{01}^{-} mode. In contrast, the intensity pattern for the LG_{01}^{+} mode rotates anti-clockwise by angle (n+1/4)π and hence is parallel to the second wire (Figure 5.19 (c)) resulting in maximum loss for the LG_{01}^{+} mode. The net result is that the loss introduced by the wire is much higher than for the LG_{01}^{-} and hence lasing on the LG_{01}^{+} mode is suppressed. The opposite situation can be achieved simply by adjusting the spacing of the two wires to be (n/2+3/8)λ. It should be noted that a differential loss sufficient for preferential lasing on LG_{01}^{-} or LG_{01}^{+} modes can also be achieved using a different angle between the wires providing their spacing is adjusted accordingly.

5.4.2.2 Loss calculation for MSE

Here, we will calculate the loss of a rectangular obstacle to the TEM_{10} mode. Without taking the effect of diffraction into account, the loss can be derived just by calculating the overlap of an obstacle with the beam. Considering a rectangle with a width of 2R and height of 2d rotated by an azimuthal φ as shown in Figure 5.20, the integration area can be decomposed to region I and II. For a TEM_{10} mode with normalized intensity distribution:

$$I(r,\ \theta)=\frac{4}{\pi w^2}\cdot\frac{2r^2}{w^2}\exp(-\frac{2r^2}{w^2})\cos^2\theta \tag{5.23}$$

the beam power within the rectangular obstacle can be express as:

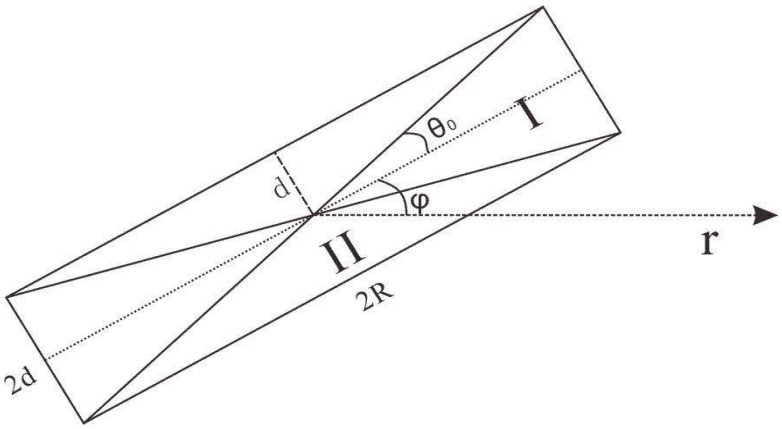

Figure 5.20 Schematic diagram of rectangular obstacle.

$$P_{loss} = P_I + P_{II} = 2\int_I I(r,\theta)ds + 2\int_{II} I(r,\theta)ds \tag{5.24}$$

Since d ≪ R, substituting Eq.(5.23) into Eq. (5.24), we have:

$$P_I = \frac{2}{\pi}\left\{\frac{1}{4}\left[\sin 2(\varphi+\theta_0) - \sin 2(\varphi-\theta_0)\right]\cdot\left[1-(\frac{2R^2}{w^2}+1)\exp(-\frac{2R^2}{w^2})\right]\right\} \tag{5.25}$$

$$P_{II} = \frac{2}{\pi}\int_{\varphi+\theta_0}^{\varphi+\pi-\theta_0}\cos^2\theta\left[1-\left(\frac{2d^2}{w^2\sin^2(\theta-\varphi)}+1\right)\exp\left(\frac{-2d^2}{w^2\sin^2(\theta-\varphi)}\right)\right]d\theta \tag{5.26}$$

where θ_0 = atan(d/R). From Eqs. (5.25) and (5.26), it can be seen that P_I has an explicit solution, but P_{II} has an implicit formula which can be calculated numerically. The losses for a TEM_{10} mode induced by several rotated rectangular obstacles are depicted in Figure 5.21, in which the beam waist is assumed to be w=400 μm, and the rectangular obstacles have the same width of 25mm but different heights of 20 μm, 50 μm and 100 μm, respectively. It is obvious that the minimum loss occurs when the rectangular obstacle is parallel to the two-lobed intensity pattern, while the maximum loss occurs when the rectangular obstacle is perpendicular to the two-lobed intensity pattern.

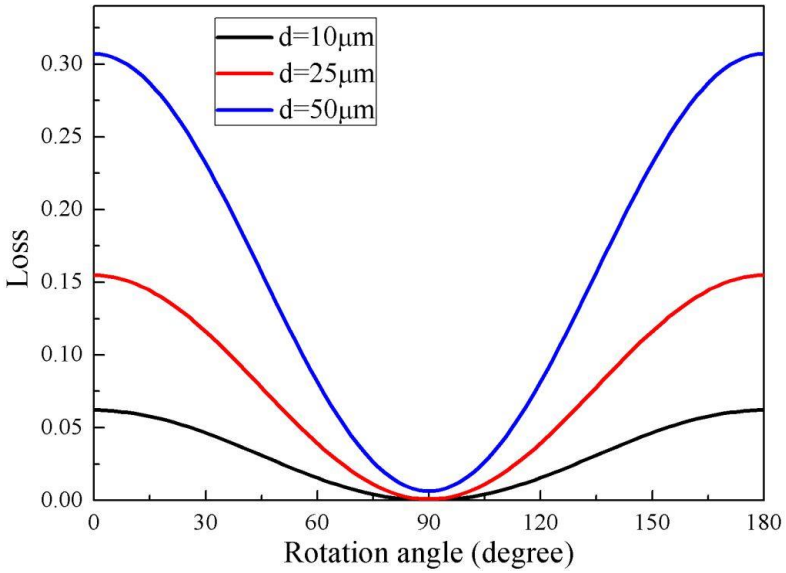

Figure 5.21 Calculated loss of three rotated rectangular obstacles for TEM_{10} mode.

5.4.2.3 Experimental set-up and results

Figure 5.22 shows a schematic diagram of the diode-end-pumped Nd:YAG laser used in our experiments to demonstrate LG_{01} mode operation with controllable handedness of helical phase. The laser system including the pump scheme and cavity design is similar to the one described in the last section. The cavity length was adjusted to 220 mm to yield a calculated mode waist radius for the LG_{01} mode of ~370 μm in the Nd:YAG rod. The pump beam was imaged into the laser rod and

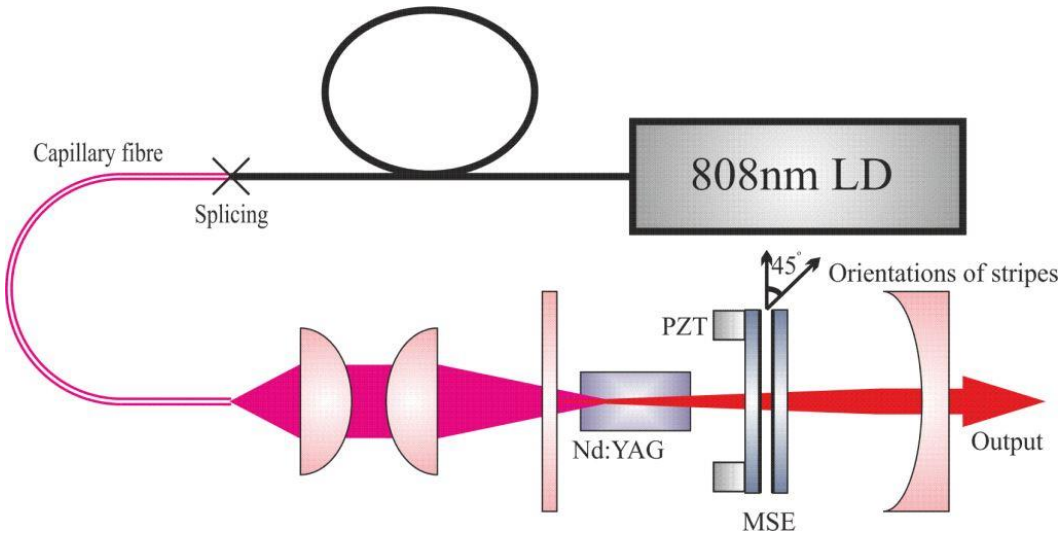

Figure 5.22 Schematic of experimental laser set-up for controlling the handedness of the LG_{01} mode.

magnified by a factor of 3 using an arrangement of lenses to achieve preferential lasing on the LG_{01}^{+} and LG_{01}^{-} modes. Discrimination between these modes was achieved using a MSE consisting of two thin aluminium stripes (20 μm wide and 10 nm thick) deposited on antireflection coated fused silica windows. The windows were placed in the resonator between the laser rod and output coupler with the aluminium stripes rotated with respect to each other by 45° and separated by a distance of ~100 μm. One of the windows was mounted on a piezoelectric transducer (PZT) so that the spacing of two windows could be precisely controlled.

Figure 5.23 illustrates the calculated single-pass loss for the relevant transverse modes caused by the two aluminium stripes as a function of spacing between them. The red and dark lines in Figure 5.23 represent the loss of LG_{01}^{-} and LG_{01}^{+} modes periodically modulated by the variation of spacing between the two stripes. Due to the characteristic counter-rotating nature of the standing wave patterns for the LG_{01}^{+} and LG_{01}^{-} modes with distance along the cavity axis, both modes generally have a different spatial overlap with the two stripes resulting in different loss. The minimum loss of LG_{01}^{-} mode and LG_{01}^{+} mode always occurs when the spacing of two stripes is (n/2+1/8)λ and (n/2+3/8)λ respectivley. The blue line represents the minimum loss for the TEM_{01} mode, which occurs when its two-lobed intensity profile is orientated at an angle ~21.7° (in the clockwise sense with respect to

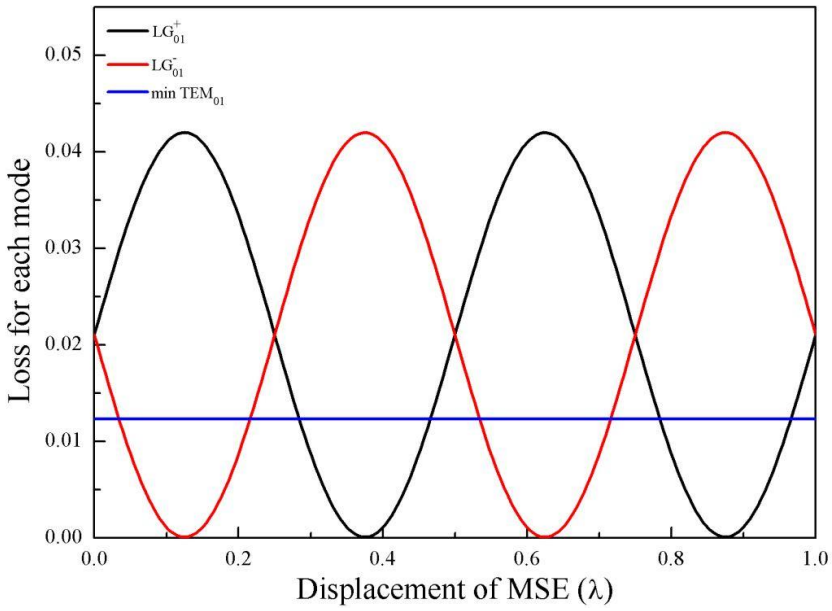

Figure 5.23 Calculated single-pass loss for different modes induced by the MSE as a function of spacing between the two stripes of the MSE.

Figure 5.19(a)) such that there is minimum overlap with the two stripes.

From Figure 5.23, it can be seen that the loss for the $LG_{01}^{\pm}$ mode is lower than for the TEM_{01} mode when the displacement of the two stripes is within a particular range. Outside this range, it is reasonable to expect that only the TEM_{01} mode with minimum loss will lase. Hence, by adjusting the spacing of the two stripes in the range of a wavelength, it should be possible to select the LG_{01}^{-}, TEM_{01} or LG_{01}^{+} modes.

When the laser cavity was carefully aligned without inserting the MSE into the cavity, the laser tended to operate on both LG_{01}^{+} and LG_{01}^{-} modes for different longitudinal modes due to the inhomogeneous axial gain distribution within the crystal caused by spatial hole burning. In order to enforce lasing on an LG_{01} mode with the same handedness for all longitudinal modes, the MSE was positioned at the centre of the intracavity beam and aligned to be perpendicular to the beam for either the LG_{01}^{-} or LG_{01}^{+} modes.

Figure 5.24(a)-(c) shows different output beam profiles at the maximum available pump power whilst continuously varying the distance between the two silica windows. The sequence of beam profiles is agreement with the calculated loss for different transverse modes as a function of stripe separation. As expected, there is a range of stripe separation where the TEM_{01} mode lases due it having a lower loss than both LG_{01} modes. The handedness of the helical phase front of the LG_{01} mode

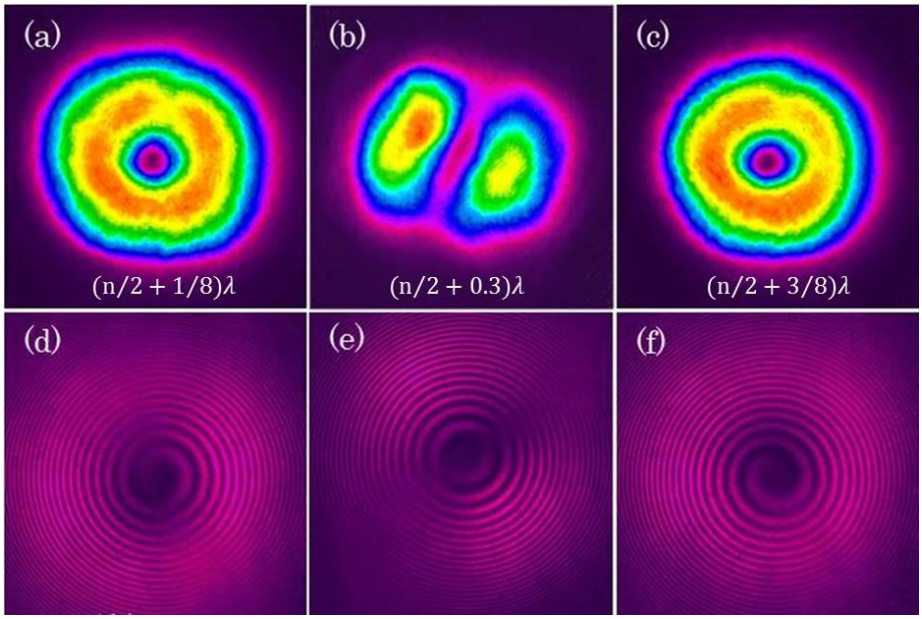

Figure 5.24 (a)-(c) Intensity profiles for LG_{01}^{-} TEM_{01} and LG_{01}^{+} modes. (d)-(f) interference patterns of corresponding modes.

was checked using the Mach-Zehnder interferometer. The resultant interference pattern shows a spiral fringe pattern with either a clockwise or anti-clockwise direction, which indicates the handedness of the helical phase front. Figure 5.24(d)-(f) show the interference pattern for the lasing modes selected in Figure 5.24(a)-(c) respectively. The opposite rotational direction of the spiral fringes in Figure 5.24(d) and Figure 5.24(f) indicates that the LG_{01} modes generated had opposite handedness of helical phase front. It is worth mentioning that switching the handedness of LG_{01} mode is controllable and repeatable. The PZT used in the experiment produces a linear displacement of approximately 2λ for the maximum applied voltage of 1kV. The mean applied voltage between the maximum output powers for the LG_{01}^{-} and LG_{01}^{+} modes was measured to be 121± 14V, which corresponds to a displacement of ~λ/4 as expected from theory. Moreover, the mean voltage range over which LG_{01}^{-} (or LG_{01}^{+}) mode operation is maintained was measured to be 88 ± 8V which corresponds to a displacement tolerance of ~0.18λ.

The laser output power the for LG_{01}^{-} and LG_{01}^{+} mode operation as a function of absorbed pump power is plotted in Figure 5.25. The threshold pump power (absorbed) was measured to be 0.65 W and the laser yielded a maximum output power of 1.13 W for the LG_{01}^{+} mode at the maximum available pump power of 3.29 W (absorbed). The corresponding slope efficiency with respect to absorbed power was 43%. A slightly lower maximum output power of 0.99 W was obtained for LG_{01}^{-} operation at the maximum pump power with corresponding slope efficiency ~37%.

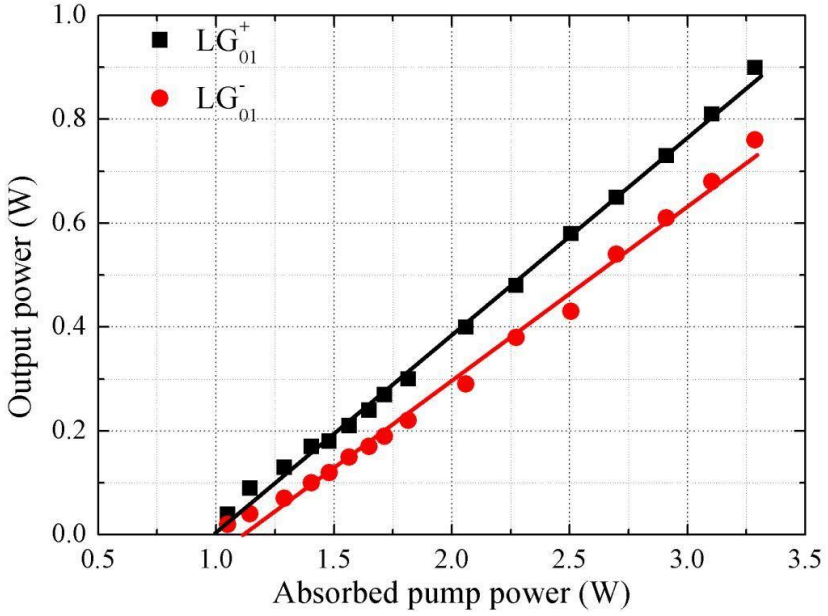

Figure 5.25 Laser output power versus absorbed pump power.

The small difference in maximum output power for LG_{01}^{+} and LG_{01}^{-} operation is attributed to etalon effects between imperfect antireflection coatings on the surfaces of the fused silica windows. Better antireflection coatings are desirable to yield equivalent power for both LG_{01}^{-} and LG_{01}^{+} operation. Meanwhile precisely tuning the cavity length to choose specific axial modes to compensate the etalon effects might be also helpful. The polarization state of the output beam was checked using a Glan-Taylor polarizer verifying that both LG_{01}^{+} and LG_{01}^{-} modes were unpolarised.

5.5 Radially-polarized LG_{01} mode generation

A variety of techniques for generation of radially-polarized LG_{01} modes in laser resonators have been demonstrated in the last two decades, which mainly rely on inserting polarization discrimination elements in the cavity such as a Brewster window [20], conical prisms [21], and polarization discriminations diffractive mirrors [22]. Making use of thermally-induced bi-focusing is another simple route. The previous work using this method is to design a specific resonator that allows the resonator to operate in the vicinity of the stability boundary allowing only one polarization to be stable while the orthogonal one is unstable [23]. One of main disadvantages it suffers is that high pump power is normally required to achieve significant bi-focusing to achieve enough mode discrimination, and the other is that the laser can only operate at a particular output power for radial or azimuthal polarization. An improvement of this technique was achieved in an Er:YAG laser by implementing a ring-shaped pump beam.[7] In this section, we will further discuss the utilization of a ring-shaped pump beam for generation of a radially-polarized output beam from an end-pumped Nd:YAG laser.

5.5.1 Effect of thermal lens on mode discrimination

For a cubic crystal such as an Nd:YAG crystal, there are three independent elasto-optical coefficients. Therefore, its indicatrix becomes an ellipsoid under transverse stress oriented in the radial and azimuthal directions, and hence the refractive index changes differently in radial and azimuthal directions. This leads to birefringence in the radial and azimuthal directions. In the section 3.3, we theoretically investigated the thermal lensing effect in an edge-cooled end-pumped rod crystal. We derived an analytical formula to described the thermal lens focal

length taking into account the effect of end-face bulging and the stress dependence of refractive index. From Eq (3.19), it can be seen that the ratio of f_ϕ/f_r is invariant with respect to radial position r. For a Nd:YAG rod crystal with parameters: $dn/dT = 7.3 \times 10^{-6}\ K^{-1}$, n=1.82, $\nu = 0.25$, $\alpha_T = 7.5 \times 10^{-6} K^{-1}$, $C_r = 0.017$, and $C_\phi = -0.0025$, the ratio of f_ϕ/f_r is calculated to be 1.12, which means that the thermal lens focal length in the azimuthal direction is 12% longer than that of the radial direction. Figure 5.26 shows one example of the calculated thermal lens power in the radial and azimuthal directions as a function of radial position under a 4W pump beam for the Nd:YAG used in section 5.2.

In section 5.2, we successfully demonstrated generation of a doughnut-shaped LG_{01} beam from an end-pumped Nd:YAG laser. However, the polarization state of the output beam tended to be non-polarized, which is totally different from the results described in [7] where a radially polarized LG_{01} beam was excited by using the ring-shaped pumping scheme. One of main reasons is that the thermally-induced birefringence was too weak in our previous experiment as the heat load is less than 1 W. The thermal lens focal length in the azimuthal direction was roughly measured to be f_ϕ~960mm, and the value in radial position was estimated to be f_r~857mm. Based on the measured thermal lens focal length, the mode radius for both radial and azimuthal polarization within the gain medium can be calculated using the ABCD matrix formula.

The radius of the beam size for the LG_{01} mode with radial- and azimuthal-

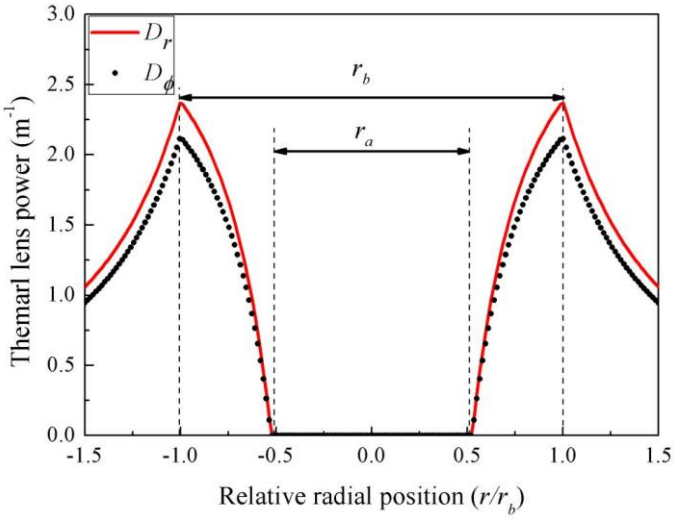

Figure 5.26 Calculated thermal lens power in the radial and tangential direction versus relative radial position for 4 W of pump power.

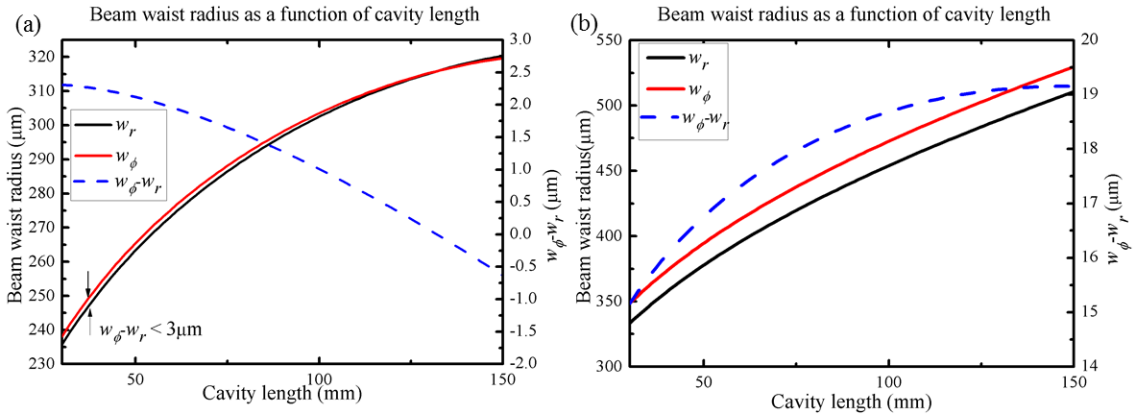

Figure 5.27 Calculated beam waist radius and corresponding difference for radial and azimuthal polarization as a function of cavity length in (a) plane-concave cavity; and(b) plane-plane cavity.

polarization in a plano-concave cavity and a plane-plane cavity as a function of cavity length were calculated as shown in Figure 5.27. The radius curvature of the concave mirror is 300mm. It is evident that the difference in beam waist radius between the orthogonal polarizations is always less than 3 μm despite variations of cavity length in the plano-concave configuration. This difference, however, is always greater than 15 μm in plane-plane cavity configuration as illustrated in Figure 5.27(b). The different mode sizes within the crystal result in different spatial overlaps with the population inversion and hence a slightly different threshold pump power. According to Eqs.(2.13) and (3.28), the overlap integral factors can be calculated and hence the threshold pump power for radial and azimuthal polarization can be estimated. Figure 5.28 shows the calculated overlap integral factors and the estimated ratio of threshold pump power for radially and azimuthally polarized modes in the plane-plane cavity configuration as illustrated in Figure 5.27(b). It can be seen that the threshold pump power for azimuthal polarization is approximately 2%~9% higher than that of radial polarization in the plane-plane configuration. Therefore, the radially-polarized mode should reach the threshold first and be preferentially excited with the azimuthally-polarized mode suppressed due to the gain saturation. Based on this analysis, a ring-shaped pump beam in combination with a plane-plane resonator configuration is proposed to generate radially polarized beam even under condition of a rather weak birefringence effect.

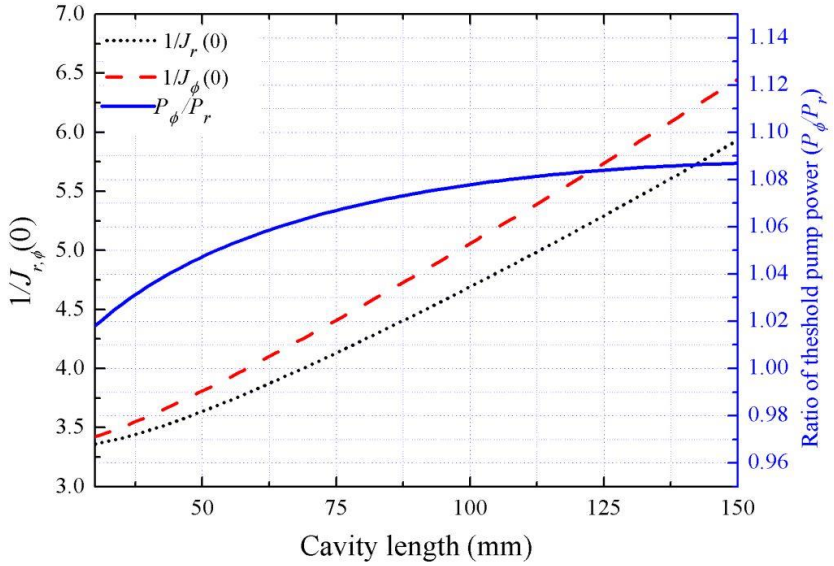

Figure 5.28 Calculated spatial overlap integral for ring-shaped pump beam with orthogonal polarization beams, and the calculated ratio of threshold pump power for azimuthal/radial modes.

5.5.2 Experimental results

The schematic diagram of the experimental set-up is shown in Figure 5.29, in which the same pump source and beam re-shaping technique were employed as in Figure 5.1. A simple two-mirror resonator configuration was employed for the Nd:YAG laser comprising a plane pump input coupling mirror with a high transmission (>95%) at the pump wavelength, a high reflectivity (>99.8%) at the lasing wavelength (1.064μm), and a plane output coupler with transmission of 10% at 1.064 μm. A 10mm long Nd:YAG rod crystal was used as the gain medium with both end faces antireflection coated at the pump and lasing wavelengths. The latter

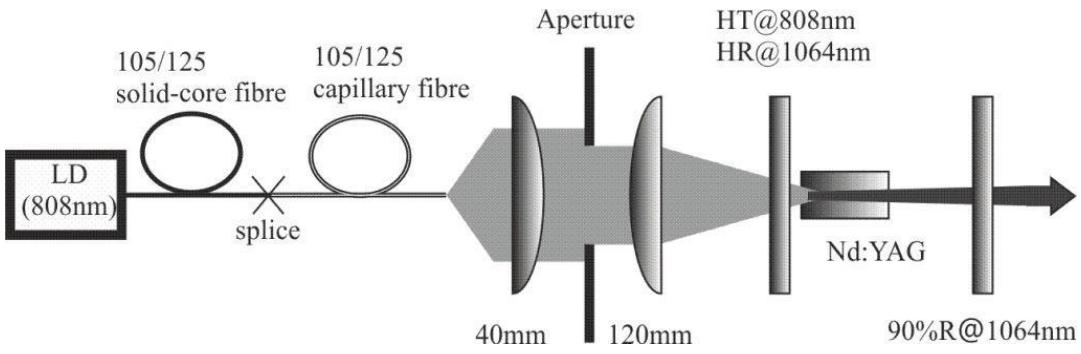

Figure 5.29 Schematic diagram of Nd:YAG resonator configuration used for radially-polarized mode operation.

was mounted in a water-cooled copper heat-sink maintained at 18℃ and was placed ~2 mm from the incoupling mirror. The cavity length was adjusted to ~50mm to yield a calculated mode waist radius for the radially-polarized LG_{01} mode of ~375 μm in the Nd:YAG rod. The pump beam was imaged into the laser rod and magnified by a factor of 3 to achieve preferential lasing on the designed mode.

Initially, there was no aperture between the pump coupling lenses. After carefully aligning the resonator and adjusting the length of cavity to be within a particular range, a doughnut-shaped beam was generated as shown in Figure 5.30(a). Above the threshold power, the doughnut-shaped beam was maintained well up to the maximum output power of 1.3W. Figure 5.30(b)-(e) shows the output beam profiles after passing through a Glan-Taylor calcite polarizer rotated at different angles. The imperfect two-lobe structure of intensity distribution along the orientation of polarizer confirms that the beam is only partially radially polarized. Despite precise alignment during the experiment, the imperfect two-lobe structures rather than clean two-lobe structures were observed at all times, confirming that the output beam was a 'hybrid' polarization state, but with the radial polarization still dominant. Partial radial polarization could be due to the similar overlap of both radial and azimuthal polarizations with the population inversion, therefore, both modes could be generated simultaneously.

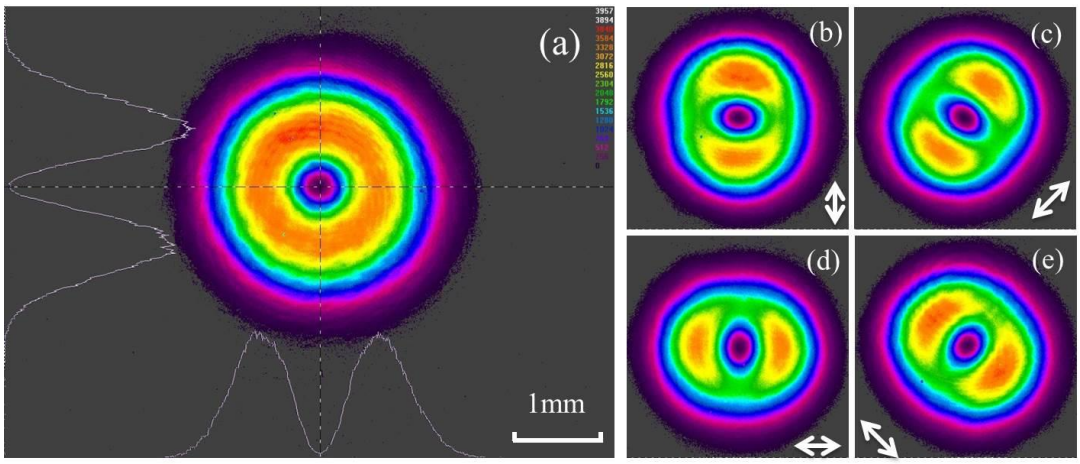

Figure 5.30 Partially radially-polarized beam. (a) Intensity distribution of the full beam profile; (b)-(c) intensity distributions of beam through after passage through a rotated calcite polarizer. The white arrows indicate the orientation of the polarizer.

One essential prerequisite for mode discrimination is that there should be enough of a difference in mode overlap between the orthogonal polarization states, and hence the invariant doughnut-shaped pump beam profile is required to maintain the discrepancy of spatial-mode-matching between orthogonal polarization states. Since the Rayleigh range of the pump beam was measured to be approximately only 4mm long, much less than the length of laser rod, an aperture was placed between the pair of collimating and focusing lenses to increase the Rayleigh range of pump beam by adjusting the diameter of aperture. The Rayleigh range of the pump beam could be increased when the diameter of aperture was decreased as the part of beam with higher divergence angles was blocked by the aperture and hence the M^2 was improved. When 30% of the pump beam was blocked by the aperture through decreasing the diameter of the aperture, radially-polarized output with high polarization purity was generated directly from the laser resonator as shown in Figure 5.31. As a large fraction of pump power was blocked, the maximum output power was only 700mW, thus the power dropped by ~46% compared with the case of a partially radially-polarized beam. This is mainly due to the significantly lower available pump power and less spatial overlap between pump beam and laser mode in the latter. This method is capable of generating a pure radially-polarized beam at the cost of laser operating efficiency.

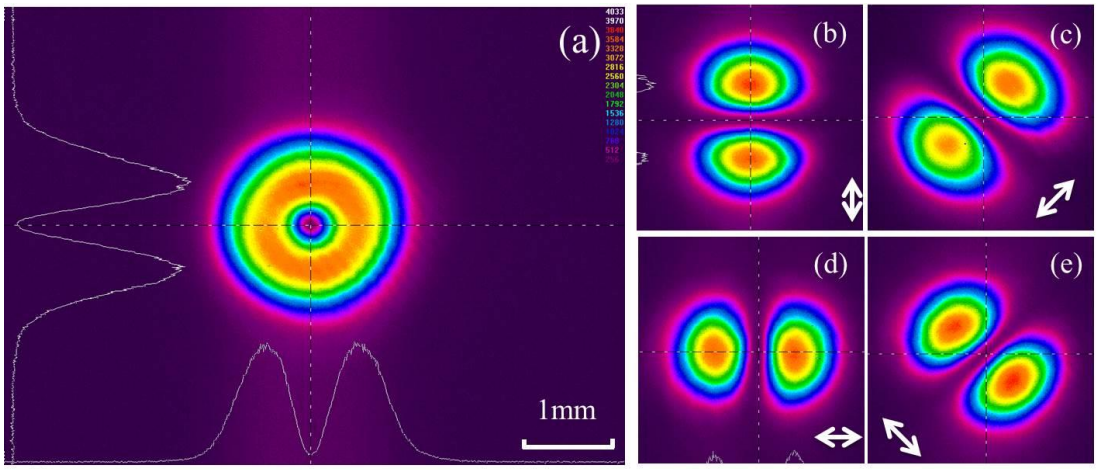

Figure 5.31 Pure radially-polarized beam. (a) Intensity distribution of the full beam profile; (b)-(c) intensity distributions of beam after passing through a rotated calcite polarizer. The white arrows indicate the orientation of the polarizer.

5.6 Conclusion

In this chapter we have successfully demonstrated the use of a ring-shaped pumping scheme for directly generating the doughnut-shaped LG_{01} beam with helical phase front and radially-polarized LG_{01} beam inside an end-pumped Nd:YAG laser. Demonstrating for the first time, to the best of our knowledge, control of the handedness of the helical phase front of the LG_{01} mode inside a laser resonator.

We first demonstrated the validity of an LG_{01} mode selection technique developed in Chapter 3 inside an end-pumped Nd:YAG laser cavity. The doughnut-shaped LG_{01} beam was excited with a maximum output power of 1.7 W and with corresponding slope efficiency of 57% with respected to the launched pump power. The M^2=2.1 was in close agreement with the theoretical value of 2 for a doughnut-shaped LG_{01} mode.

We then measured the phase front of the doughnut-shaped mode by using a Mach-Zehnder interferometer. The non-spiral interference pattern obtained showed that the doughnut-shaped mode did not have a well-defined helical phase front. Furthermore, an investigation of the mode composition was carried out by measuring the phase front and intensity profile for each longitudinal mode component of the generated beam, selected by a FPI outside the cavity. The intensity profiles showed a two-lobe structure or a doughnut-shape for different longitudinal modes suggesting that the TEM_{01} mode and LG_{01} mode tended to coexist in the output beam. Moreover, the phase front of each doughnut-shaped axial-mode was measured by an astigmatic $\pi/2$ mode converter and a Mach-Zehnder interferometer simultaneously. The resultant interference pattern had a clear spiral fringes with either clockwise or anti-clockwise rotation direction verifying that each longitudinal doughnut-shaped mode had a well-determined helical phase front. The measurements discussed above suggest that the generated doughnut-shaped beam tends to be a hybrid mode with the presence of TEM_{01}, LG_{01}^{+} and LG_{01}^{-} modes for different longitudinal modes.

In order to generate an LG_{01} mode with a well-determined handedness, the twisted-mode technique was applied to enforce lasing on a single-frequency doughnut-shaped LG_{01} mode. Furthermore, we have successfully demonstrated, for the first time to our best knowledge, achieving lasing on the LG_{01} mode with

controllable handedness of the helical phase front in an end-pumped solid-state laser. Our approach is based on the use of a novel mode selection element consisting of two nanoscale thickness aluminium strips to provide discrimination between LG_{01} modes with opposite handedness by exploiting the fact that the standing wave intensity distribution for the LG_{01}^{+} and LG_{01}^{-} modes inside the laser resonator are different. This scheme has been applied to a diode-pumped Nd:YAG laser to generate LG_{01} modes with controllable handedness at output powers ~1 W. Moreover, this approach also allows repeatable switching between LG_{01}^{+} and LG_{01}^{-} modes.

In the final section of this chapter we looked into the generation of a radially-polarized LG_{01} beam in a Nd:YAG laser by using the ring-shaped pump beam scheme. The method is exploiting the difference of spatial overlap between pump beam and modes with orthogonal polarization states resulting from even weak thermally induced birefringence. The net result is that a slightly different threshold is obtained for each mode. A plane-plane cavity configuration was used in the experiment to maximize the difference of spatial overlap for orthogonally polarized modes leading to a pure radially-polarized output beam.

Bibliography

1. D. Naidoo, K. Ait-Ameur, M. Brunel, and A. Forbes, "Intra-cavity generation of superpositions of Laguerre-Gaussian beams," Applied Physics B: Lasers and Optics **106**, 683-690 (2012).

2. Y. F. Chen, Y. P. Lan, and S. C. Wang, "Generation of Laguerre–Gaussian modes in fiber-coupled laser diode end-pumped lasers," Applied Physics B: Lasers and Optics **72**, 167-170 (2001).

3. S. P. Chard, P. C. Shardlow, and M. J. Damzen, "High-power non-astigmatic TEM00 and vortex mode generation in a compact bounce laser design," Applied Physics B: Lasers and Optics **97**, 275-280 (2009).

4. A. Ito, Y. Kozawa, and S. Sato, "Generation of hollow scalar and vector beams using a spot-defect mirror," J. Opt. Soc. Am. A **27**, 2072-2077 (2010).

5. M. Harris, C. A. Hill, P. R. Tapster, and J. M. Vaughan, "Laser modes with helical wave fronts," Physical Review A **49**, 3119-3122 (1994).

6. I. A. Litvin, S. Ngcobo, D. Naidoo, K. Ait-Ameur, and A. Forbes, "Doughnut laser beam as an incoherent superposition of two petal beams," Optics Letters **39**, 704-707 (2014).

7. J. W. Kim, J. I. Mackenzie, J. R. Hayes, and W. A. Clarkson, "High power Er:YAG laser with radially-polarized Laguerre-Gaussian (LG_{01}) mode output," Optics Express **19**, 14526-14531 (2011).

8. M. W. Beijersbergen, L. Allen, H. E. L. O. van der Veen, and J. P. Woerdman, "Astigmatic laser mode converters and transfer of orbital angular momentum," Optics Communications **96**, 123-132 (1993).

9. D. G. Grier, "A revolution in optical manipulation," Nature **424**, 810-816 (2003).

10. G. Gibson, J. Courtial, M. Padgett, M. Vasnetsov, V. Pas'ko, S. Barnett, and S. Franke-Arnold, "Free-space information transfer using light beams carrying orbital angular momentum," Optics Express **12**, 5448-5456 (2004).

11. L. Veissier, A. Nicolas, L. Giner, D. Maxein, A. S. Sheremet, E. Giacobino, and J. Laurat, "Reversible optical memory for twisted photons," Optics Letters **38**, 712-714 (2013).

12. G. Molina-Terriza, J. P. Torres, and L. Torner, "Twisted photons," Nature Physics **3**, 305-310 (2007).

13. J. Hamazaki, R. Morita, K. Chujo, Y. Kobayashi, S. Tanda, and T. Omatsu, "Optical-vortex laser ablation," Optics Express **18**, 2144-2151 (2010).

14. L. Marrucci, C. Manzo, and D. Paparo, "Optical spin-to-orbital angular momentum conversion in inhomogeneous anisotropic media," Physical Review Letters **96**, 163905 (2006).

15. M. W. Beijersbergen, R. P. C. Coerwinkel, M. Kristensen, and J. P. Woerdman, "Helical-wavefront laser beams produced with a spiral phaseplate," Optics Communications **112**, 321-327 (1994).

16. N. R. Heckenberg, R. McDuff, C. P. Smith, and A. G. White, "Generation of optical phase singularities by computer-generated holograms," Optics Letters **17**, 221-223 (1992).

17. Y. Senatsky, J. Bisson, J. Li, A. Shirakawa, M. Thirugnanasambandam, and K. Ueda, "Laguerre-Gaussian modes selection in diode-pumped solid-state lasers," Optical Review **19**, 201-221 (2012).

18. J. J. Zayhowski and A. Mooradian, "Single-frequency microchip Nd lasers," Optics Letters **14**, 24-26 (1989).

19. V. Evtuhov and A. Siegman, "A "twisted-mode" technique for obtaining axially uniform energy density in a laser cavity," Applied Optics **4**, 142-143 (1965).

20. A. A. Tovar, "Production and propagation of cylindrically polarized Laguerre Gaussian laser beams.pdf," J. Opt. Soc. Am. A **15**, 2705-2711 (1998).

21. J. Li, K. Ueda, M. Musha, A. Shirakawa, and L. Zhong, "Generation of radially polarized mode in Yb fiber laser by using a dual conical prism," Optics Letters **31**, 2969-2971 (2005).

22. A. V. Nesterov, V. G. Niziev, and V. P. Yakunin, "Generation of high-power radially polarized beam," J.Phys. D: Appl. Phys **32**, 2871-2875 (1999).

23. I. Moshe, S. Jackel, and A. Meir, "Production of radially or azimuthally polarized beams in solid-state lasers and the elimination of thermally induced birefringence effects," Optics Letters **28**, 307-309 (2003).

Chapter 6: Extracavity conversion to radial polarization

6.1 Introduction

Radially and azimuthally polarized beams have attracted growing interest for use in a variety of applications due to unique optical properties. These beams can be directly excited inside a laser resonator using specially designed polarization selective elements or particular resonator configurations [1-4]. Alternatively, the most popular way to obtain these beams at relatively low power levels is to transform a linearly-polarized TEM_{00} beam into a radially or azimuthally polarized beam using an external polarization mode converter. Traditionally, these converters were constructed from liquid crystals [5] or from an arrangement of half-wave plates bonded together to form a segmented spatially variant retardation plate (SVR) [6] and, as a consequence, they generally suffered from low polarisation purity, degraded beam quality and low transformation efficiency. However, recent work on femtosecond laser writing of nanostructure gratings in silica glass has allowed the realization of a new type of radial polarization converter with improved performance [7]. In this chapter, we will introduce this new type of radial polarization converter and demonstrate efficient conversion to radial polarization in both the one-micron and two-micron band.

6.2 Polarization converter

6.2.1 Femtosecond laser induced nanogratings

Laser induced periodic patterns on a material surface were first observed by Birnbaum. He noted that a regular structure of parallel straight lines was formed on the surface of semiconductor when irradiated by a focused beam of intense ruby laser light [8]. Afterwards, this phenomenon was observed to be rather universal on any material surface such as polymers, metals, and dielectrics. There are several explanations for this periodic structure formation, but the most widely accepted one is that the interference of the incident beam and the surface scattered wave generates a sinusoidal modulated intensity distribution on the material

surface [9, 10]. For a p-polarized incident beam, the induced periodic pattern is perpendicular to the polarization direction with one of two possible periods [9]:

$$\Lambda_{gr} = \frac{\lambda}{1 \pm \sin\theta} \tag{6.1}$$

where Λ_{gr} is the structure period, θ is the angle of the incident beam and λ is the incident beam wavelength. For an s-polarized incident beam, Λ_{gr} is close to λ.

Recently, self-assembled sub-wavelength periodic structures (nanogratings) were observed within silica glass when irradiated by a tightly focused ultrafast pulsed laser. Normally two types of periodic structures are simultaneously formed, with one period (Λ_k) in the direction of the light propagation and the other one (Λ_E) parallel with the beam polarization direction (as shown in Figure 6.1) [11, 12]. It can be seen from the Figure 6.1 that the first period (Λ_k) is approximately the light's wavelength in the material, but the second period (Λ_E) is smaller than the wavelength, in the range of 100-300 nm, and is strongly dependent on the laser wavelength, pulse energy and writing speed [12].

Unlike induced surface regular patterns, the sub-wavelength structures can only be formed inside particular materials including fused silica, sapphire and others. Since the interference of incident and scattered waves cannot form sub-wavelength structures, other mechanisms are responsible for these sub-wavelength structures.

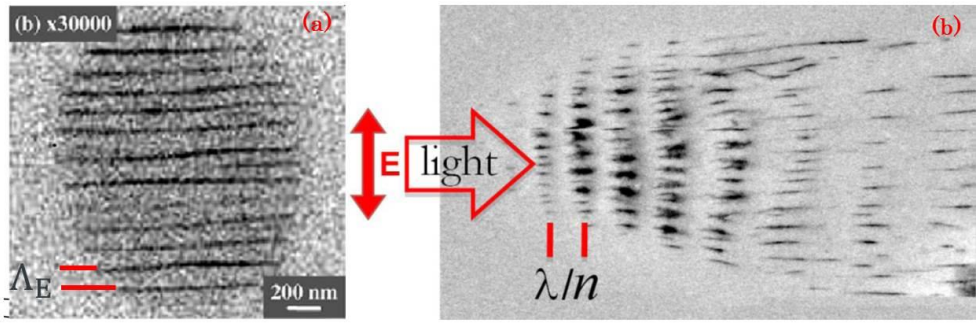

Figure 6.1 Examples of backscattering electron images of a self-assembled nanograting induced by femtosecond pulse. (a) Structure along the polarization direction with a period less than wavelength can be clearly seen on the top view image. (b) structures along the light propagation direction with a period close to the wavelength in the material can be seen from the side view [4, 5].

Indeed, there are several theories that attempt to explain the self-assembled effect including plasma interference [11], nanoplasma formation [13] and self-organization of exciton-polaritons [14].

Since the homogeneous periodic dielectric layered media behaves as a uniaxial birefringent material when the optical wavelength is much larger than the layer period [15], it is evident that the femtosecond induced nanogratings also exhibit a birefringence effect. For a grating consist of two layers with thickness a (refractive index n_1) and b (refractive index n_2) and the period $\Lambda = a + b \ll \lambda$ (as shown in Figure 6.2), the ordinary (n_o) and extraordinary (n_e) refractive indices can be approximately expressed as [16]:

$$n_o^2 = \frac{a}{\Lambda} n_1^2 + \frac{b}{\Lambda} n_2^2 \tag{6.2}$$

$$\frac{1}{n_e^2} = \frac{a}{\Lambda}\frac{1}{n_1^2} + \frac{b}{\Lambda}\frac{1}{n_2^2} \tag{6.3}$$

Femtosecond induced nanogratings in fused silica always exhibit a negative uniaxial birefringence with a typical value of $n_e - n_o \sim -(2\sim4\times10^{-3})$ [17]. However, the retardance defined as the product of refractive index difference and the length of the structure, varies with the writing laser parameters including the averaged power, wavelength, writing speed as well as focusing depth. In [18], The

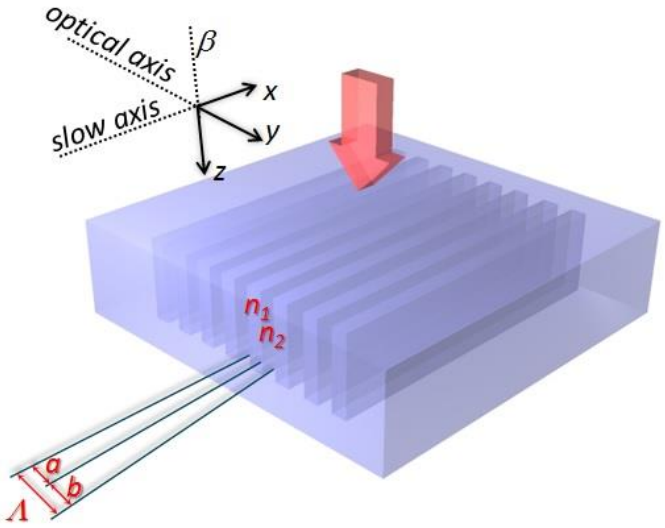

Figure 6.2 Schematic of light with wave number β propagating along the plane of the nanogratings. The gratings consist of two layers with thickness a (refractive index n_1) and b (refractive index n_2).

strong retardance only occurs above a threshold pulse energy and quickly reaches a saturation value with increase of pulse energy. Meanwhile the value of retardance is inversely proportional to the writing speed. Another critical parameter is depth of focus. On the one hand, the depth of focus can be increased by using a spherical lens with high NA such that a strong spherical aberration extends the focus in the light propagation direction resulting in a longer induced structure and hence increases the retardance. On the other hand, the longer focus length can be easily achieved by using an aspheric lens with a low NA in that the lower the NA is the longer the induced structure. With a 0.16 NA aspheric lens, more than 350nm retardance was achieved in a single scan that allows writing of a half-wave plate for 700nm wavelength [18].

6.2.2 Spatially variant waveplate

Traditionally, a quasi-continuous spatially variant waveplate can be achieved with liquid crystal [5], but with several disadvantages in that this cannot be used for high power, as well as temporal instability of the orientation of the liquid-crystal molecules [19]. In addition, a step-variant waveplate can be fabricated by adhering small segments of waveplate with different orientation of crystal's optical axis together [6]. This device has a high optical quality that is able to deal with high power. However, the transformed beam is surrounded by a star-patterned halo due to the diffraction at the interfaces of adjacent segments. Thus a spatial filter is always required to improve the beam quality. Alternatively, computer-generated spatial variant subwavelength metal strip gratings induce form birefringence that is equivalent to a continuous spatially variant waveplate [20]. This device is usually fabricated by method of photolithography with a limited resolution that can only be used for longer wavelengths such as 10.6 μm.

Recent work on femtosecond laser writing of nanostructure gratings in silica glass has allowed the realization of spatially variant waveplates (also called S-waveplate) from visible to near-infrared regions. Typically, two types of spatially variant waveplate are fabricated depending on the induced retardance. The first type is a half-waveplate that normally transforms a linearly polarized beam into radially or azimuthally polarized beam. Figure 6.3(a) illustrates the schematic drawing of the nanograting distributions in this waveplate; the grating structures induce birefringence with slow and fast axes aligned parallel and perpendicular to the

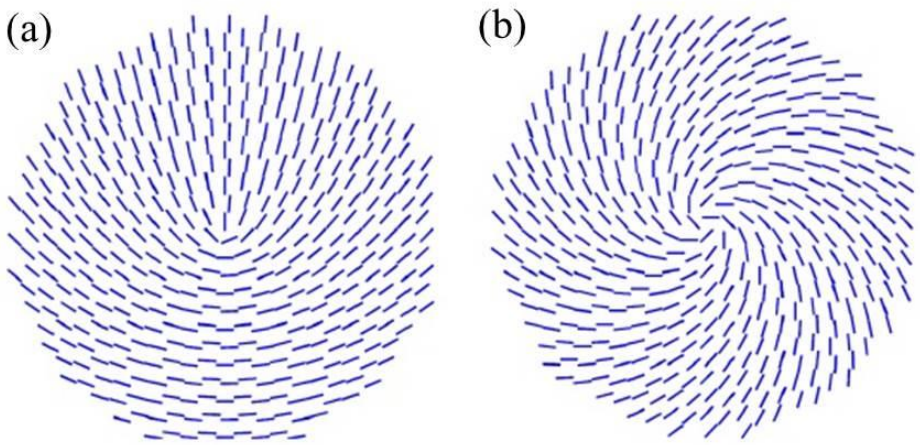

Figure 6.3 Schematic drawings of nanograting distributions in spatially variant half-waveplate(a) and quarter-waveplate(b) [18].

grating direction respectively, which is aligned at an angle $\varphi/2$ from the azimuthal angle φ to form a continuously spatially variant half-waveplate [21]. The second type is a quarter-waveplate as shown in Figure 6.3(b); the directions of the grating structures are aligned at an angle of $\varphi - \pi/4$. It is able to convert a linearly polarized beam into a beam with a helical phase front or convert circular polarization to radial or azimuthal polarization.

The fabrication process is described in detail in [18, 22]. The S-waveplate was fabricated using a mode-locked femtosecond laser operated at a wavelength of 1030nm with a pulse duration of 270fs. The main challenge during the fabrication is continuously varying the slow axis direction of the induced birefringence. This was done by fully synchronising a rotation stage where a half-waveplate was rotated to continuous vary the orientation of slow axis, with a 3-axis translation stage moving in a spiral trajectory. By controlling the writing beam parameters including averaged irradiation power, focus depth, writing speed, spatially variant waveplates designed from the visible wavelength to 2μm range can be fabricated. The optimum values for the pulse energy, repetition rate, numerical aperture, and writing speed required to achieve S-waveplates at 1μm wavelength were found to be 2μJ, 200kHz, 0.16NA, and 1mm/s, respectively. The damage threshold for S-waveplates were measured to be ~22.8J/cm^2 at 1064nm with a 3.5ns pulse duration and repetition rate of 10Hz [18].

6.2.3 Working principle

The polarization behaviour of such converter can be analysed with the aid of the Jones matrix formalism [23]. In the Jones calculus, the polarization state of the incident beam is represented by a Jones vector $\vec{E}_{\text{in}}$ resolved into *x* and *y* component, and the effect of an optical device is described by a 2×2 matrix *M*. Thus the polarization state of a transmitted beam ($\vec{E}_{\text{out}}$) can be expressed as:

$$\vec{E}_{\text{out}} = M\vec{E}_{in} \tag{6.4}$$

The Jones matrix for a quarter-waveplate has the formalism as:

$$M\left(\lambda/4\right)=e^{i\pi/4}\begin{pmatrix}1 & 0\\ 0 & -i\end{pmatrix} \tag{6.5}$$

and a half-waveplate has a Jones matrix:

$$M(\lambda/2)=i\begin{pmatrix}1 & 0\\ 0 & -1\end{pmatrix} \tag{6.6}$$

The spatially variant waveplate can be considered as a waveplate rotated by an angle of θ, and the Jones matrix for a rotator can be expressed as:

$$R_{rot}=\begin{pmatrix}\cos(\theta) & \sin(\theta)\\ -\sin(\theta) & \cos(\theta)\end{pmatrix} \tag{6.7}$$

Therefore, the Jones matrix for a spatially variant half-waveplate with fast axis tilted by an angle of $\varphi/2$ at azimuthal angle φ can be expressed as:

$$\begin{aligned}M(\lambda/2,\varphi/2) &= R_{rot}(-\varphi/2)M(\lambda/2)R_{rot}(\varphi/2)\\ &=\begin{pmatrix}\cos(\varphi) & \sin(\varphi)\\ \sin(\varphi) & -\cos(\varphi)\end{pmatrix}\end{aligned} \tag{6.8}$$

Similarly, the Jones matrix for a rotated quarter-waveplate can be written as:

$$M\left(\lambda/4,\theta\right)=\begin{pmatrix}i\cos^2(\theta)+\sin^2(\theta) & (i-1)\sin(\theta)\cos(\theta)\\ (i-1)\sin(\theta)\cos(\theta) & i\sin^2(\theta)+\cos^2(\theta)\end{pmatrix} \tag{6.9}$$

For the spatially variant quarter-waveplate described in Figure 6.3(b), the rotated angle is equal to $\theta = \varphi - \pi/4$.

Then an incident *x*-polarized beam after passing through the $\lambda/2$ S-waveplate is transformed to radial polarization:

$$\vec{E}_{out,1} = \begin{pmatrix} \cos(\varphi) & \sin(\varphi) \\ \sin(\varphi) & -\cos(\varphi) \end{pmatrix} \begin{pmatrix} 1 \\ 0 \end{pmatrix} = \begin{pmatrix} \cos(\varphi) \\ \sin(\varphi) \end{pmatrix} E_{in} \tag{6.10}$$

While by multiplying Eq.(6.9) with a right-handed circularly polarized beam, the polarization state distribution is derived as:

$$\vec{E}_{out,2} = \begin{pmatrix} \cos(\varphi) \\ \sin(\varphi) \end{pmatrix} e^{i\varphi} e^{i\pi/4} E_{in} \tag{6.11}$$

The output beam then becomes a radially polarized optical vortex beam that not only has a pure radial polarization state distribution represented in the first tem of Eq.(6.11), but also has a helical phase front as indicated in the second term. This beam has a bright centred intensity distribution in the far-field rather than a doughnut-shaped beam as for pure radial polarization with flat phase front. In order to obtain the latter, a spiral phase plate with opposite helicity is always required to compensate for this added phase term.

Figure 6.4 shows an example of the working principle for $\lambda/2$ S-waveplate where a linearly-polarized Gaussian beam is transformed to a radially-polarized beam with doughnut-shaped intensity distribution in the far-field.

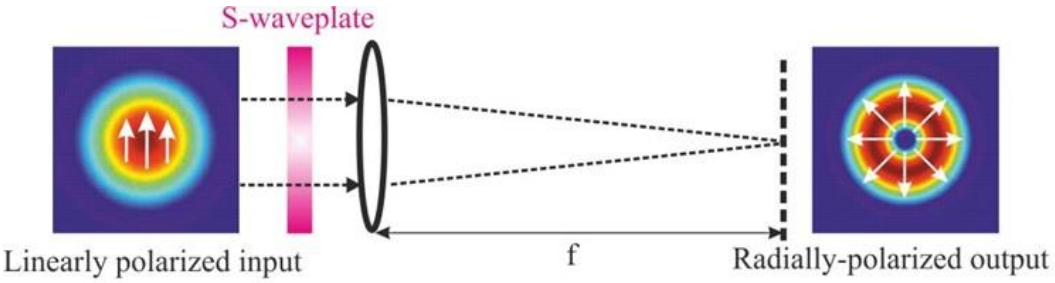

Figure 6.4 Principle of S-waveplate: Incident linearly-polarized beam is converted into radially-polarized beam in the far-field.

6.3 Experimental performance

In this section, we will investigate the performance of S-waveplates designed for 1 μm and 2 μm wavelengths.

6.3.1 1 μm S-waveplate

According to Eq.(6.10), we first tested the performance of a $\lambda/2$ S-waveplate for transformation of a linearly-polarized Gaussian beam into a radially-polarized beam. The basic arrangement of the experimental set-up is shown in Figure 6.5. A linearly-polarized Gaussian-shaped TEM_{00} beam at a wavelength of $\lambda = 1.064\mu m$ with a beam quality factor of $M^2=1.2$ emerging from a home-made Nd:YVO_4 laser was used as the probe beam. The linear polarization of the output beam had a PER>20dB with the electric-field polarized parallel to the plane of Figure 6.5. The output beam was collimated before being incident on the S-waveplate. A non-polarization-independent beam splitter was placed behind the S-waveplate to split the beam into two beams. A 4*f*-imaging system was used in one arm to measure the near-field beam intensity distributions on the S-waveplate, and a spherical lens with a focal length of 1m was placed in the other arm to measure the beam intensity in the far field.

Figure 6.6(a) shows the measured near-field beam intensity distribution on the S-waveplate. The two lobe structured beam intensity distributions in Figure 6.6(b)-(e) verified that the linear polarization was converted to radial polarization after the beam had passed through the S-waveplate. The Gaussian-shaped beam then evolved into a doughnut-shaped intensity distribution with radial polarization in the far-field as shown in Figure 6.6(f), which had an intensity distribution close to

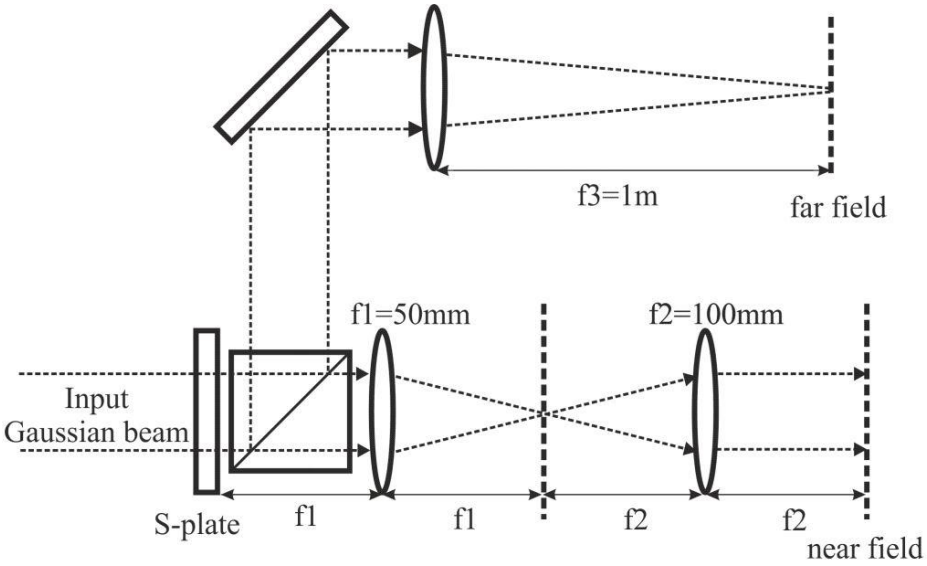

Figure 6.5 Schematic of experiment set-up for transformation of a linearly-polarized Gaussian beam into a radially-polarized doughnut-shaped beam.

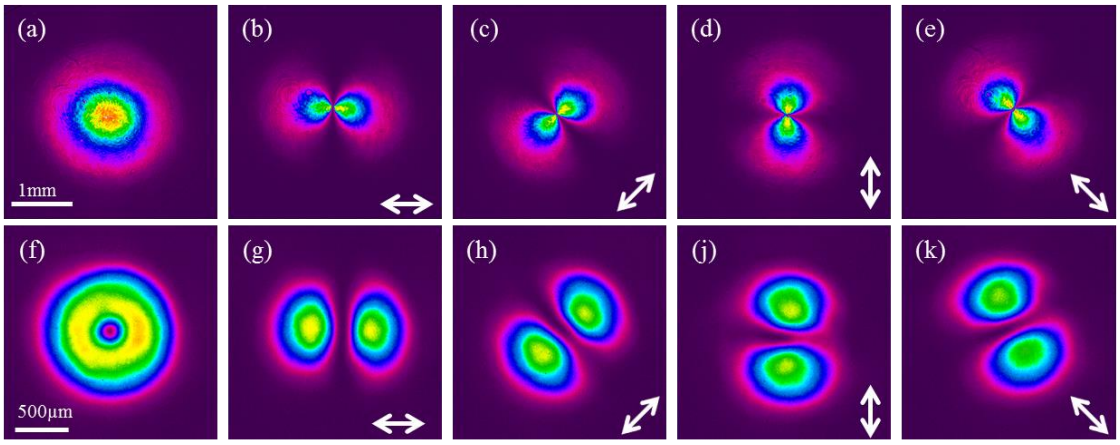

Figure 6.6 (a) Near-field and (f) far-field intensity distributions after a Gaussian-shaped beam was passed through a $\lambda/2$ S-waveplate; (b)-(e) and (g)-(j) the corresponding beam intensity distributions after passing through a rotated linear polarizer.

the ideal LG_{01} beam. However, the electric field distribution of the resultant doughnut-shaped beam is not an eigen LG_{01} mode, but a weighted superposition of a different order of LG modes. The relative amplitude of specific LG modes in the resultant beam can be calculated by a simple overlap integral of the Gaussian mode with the specific LG mode. This value is calculated to be 93% for transforming a TEM_{00} mode to a LG_{01} [24]. The total conversion efficiency was measured to be ~75±1% in the far-field which is around ~18% lower than the theoretical value. The main reason can be attributed to the strong Rayleigh scattering by microscopic inhomogeneities of the nanogratings and induced defect absorption that could be reduced by optimizing the writing parameters [22]. Taking into account the Fresnel reflection losses (~6.9%) on both uncoated surfaces, this suggests that the single-pass loss due to scattering is at least ~11.1±1%. The beam quality factor M^2 was measured to be ~2.7 which was showed a degradation compared to a doughnut-shaped LG_{01} mode (which has a theoretical value of $M^2=2$). The degradation in beam quality could be attributed to the scattering of microscopic inhomogeneities of nanogratings.

The polarization purity was investigated by measuring the intensity of the two-lobed beam at a specific radius r as a function of azimuthal angle θ (as illustrated in the insert of Figure 6.7). Ideally for a pure radially-polarized beam, the intensity at a specific radius r and azimuthal angle θ is equal to

$$I(r,\theta) = I_{\max}(r)\cos^2(\Delta\theta) \tag{6.12}$$

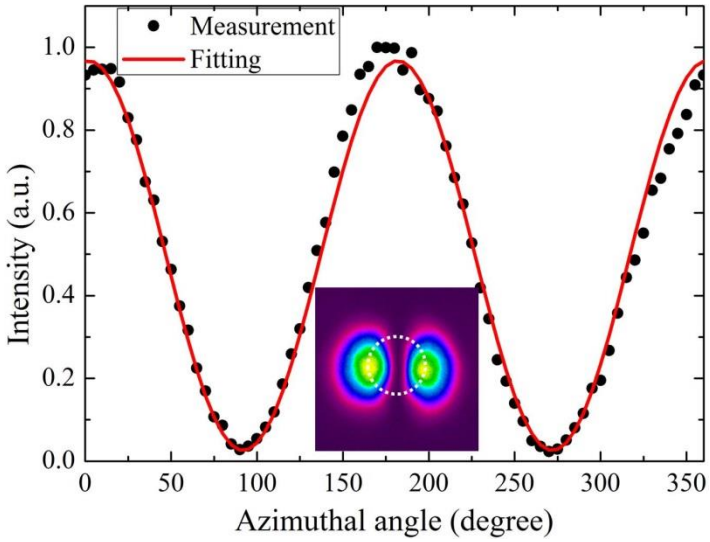

Figure 6.7 The normalized azimuthal intensity profile for radius r after beam passage through a linear polarizer.

where $\Delta\theta$ is the angle between the azimuthal angle and the orientation of the transmission axis of the linear polarizer. The PER is defined as the averaged ratio of I_{max}/I_{min} for the four two-lobed beams in Figure 6.6(g)-(j). With this method, the PER was calculated to be ~14dB confirming that the transformed radially polarized beam had a high polarization purity.

The scattering loss is extremely detrimental for high power applications. For one thing, a large fraction of power would be wasted leading to the requirement of more output power from the laser system. For another, the absorbed energy by the S-waveplate would induce serious thermal effects that deteriorate the polarization purity and beam quality. Therefore, improving the total transmission efficiency is really desirable for practical use. In order to obtain a radial polarization with improved efficiency, we proposed to employ the $\lambda/4$ S-waveplate as it has only one layer of nanograting structures rather than two layers in $\lambda/2$ S-waveplate leading to a much less scattering loss. According to Eq.(6.11), a helically phased LG_{01} beam with opposite helicity to the second term of Eq.(6.11) is necessary to compensate for a spiral phase front indicating a maximum conversion efficiency would be achieved as both incident and output beams have the same intensity distribution.

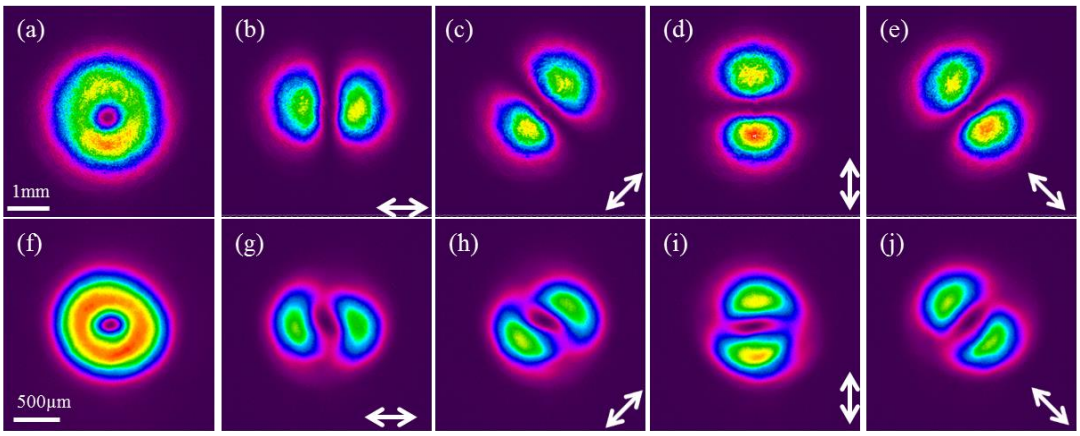

Figure 6.8 (a) Near-field and (f) far-field intensity distributions after a circularly polarized doughnut-shaped LG_{01} optical vortex beam was passed through the $\lambda/4$ S-waveplate. (b)-(e) and (g)-(j) The corresponding beam intensity distributions after passing through a rotated linear polarizer.

In this case, the basic arrangement of experiment setup is the same as shown in Figure 6.5. A linearly polarized doughnut-shaped LG_{01} beam with beam quality M^2=2.1 emitting from a house-made Nd:YVO_4 laser was used as the probe beam. A quarter-waveplate aligned to 45° with respect to the linear polarization direction of the LG_{01} beam was placed before the S-waveplate to form a circularly polarized LG_{01} input beam. Figure 6.8(a) shows the measured near-field beam intensity distribution on the S-waveplate. The two lobe structured beam intensity distributions in Figure 6.8(b)-(e) verified that circularly polarized LG_{01} beam was successfully transformed to the radial polarization after the beam passed through the S-waveplate. The beam profile maintained a doughnut-shaped intensity distribution in the far-field as well as shown in Figure 6.8(f). However, the two lobe structured beam profiles are slightly different from Figure 6.8(b)-(e) indicating a slight degradation in PER in the far-field. The PER was measured to be ~8dB which was significantly lower than that of the $\lambda/2$ S-waveplate. This might be due to the presence of degenerate LG_{01} modes in the input doughnut-shaped beam leading to an incomplete compensation for the spiral phase front. Unlike a Gaussian-shaped input beam, the doughnut-shaped intensity distribution was maintained well over a range of propagation distances. This would benefit specific applications where both polarization and intensity distribution are of particular interest. The total conversion efficiency in the far-field was measured to be ~86±1%, which is ~11% higher than $\lambda/2$ S-waveplate. Assuming 100% overlap for the input and output beams as well as allowing for the Fresenl reflections from both surfaces

of the window, the scatting loss is estimated to be ~7.1% which is approximately half of the $\lambda/2$ S-waveplate. The beam quality factor of M^2 was measured to be ~2.9, which is slightly higher than that of $\lambda/2$ S-waveplate.

Comparing results we have obtained with both the $\lambda/2$ and $\lambda/4$ S-waveplates, it can be seen that although the total conversion efficiency for $\lambda/4$ S-waveplate is 10% higher than that $\lambda/2$ S-waveplate, the requirement for the input beam is much more rigorous. The helical phase front term in Eq.(6.11) must be absolutely compensated, otherwise a degraded PER will result.

6.3.2 2 μm S-waveplate

The 1μm S-waveplate discussed in the previous has the shortcoming of relatively low transmission efficiency due to a rather high Rayleigh scattering loss, which is strongly dependent on wavelength. This means that a beam with longer wavelength should experience much less scattering loss and hence has higher transmission efficiency. In this section, we will investigate a $\lambda/2$ S-waveplate designed for use in ~2μm wavelength band. The $\lambda/2$ S-waveplate had a diameter of 1 mm and was fabricated with the same technique as the 1μm S-waveplate but with different parameters. The nanogratings were written by a femtosecond pulse with 600fs duration, 200kHz repetition and an averaged power of 1.5W and with a 0.13 NA aspheric lens. The higher energy and longer focus depth extended the retardance of each layer to be ~ 500nm. Thus by the stacking of two layers, ~1μm retardance was achieved corresponding to a half-wavelength in ~2μm region.

The experimental set-up is shown in Figure 6.9. The S-waveplate was tested with the aid of a probe beam from a widely-tunable Tm-doped silica fibre laser. The

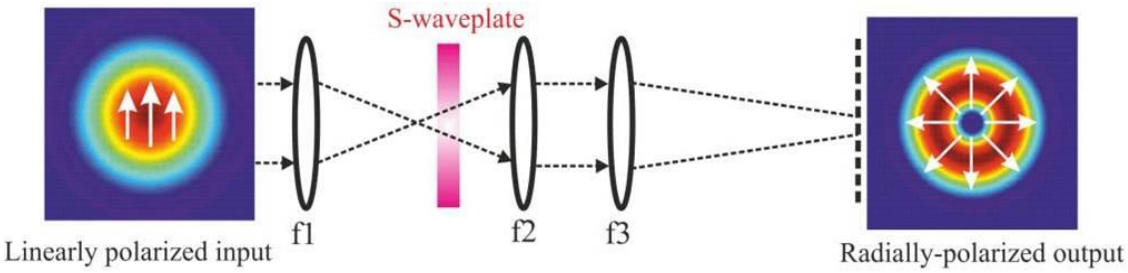

Figure 6.9 Experiment set-up for transformation of a linearly-polarized Gaussian beam into a radially polarized doughnut-shaped beam in ~ 2μm wavelength band.

latter produced a nearly diffraction-limited (Gaussian-shaped) beam with a beam propagation factor of 1.2 and could be tuned over the wavelength range from 1950nm to 2100nm with an output power of 1.5W. The output from the fibre laser was collimated and was polarised using an external polariser to yield a linearly-polarised beam with a PER ~22dB. As the collimated probe beam size was much larger than the diameter of S-waveplate, it was focused down by a spherical lens to achieve a beam size much smaller than the S-waveplate diameter. The S-waveleplate was aligned with respect to the incident beam polarisation direction to yield a radially-polarised output beam.

The resulting doughnut-shaped far-field beam profile was observed with the aid of a Pyrocam III camera (see Figure 6.10(a)). The far-field beam profile after passage through a rotated polarizer is illustrated in Figure 6.10(b)-(e) verifying that the polarization was indeed radial. The transmission efficiency was measured to be ~86%±1% across the wavelength tuning range. Taking into account the Fresnel reflection losses on both uncoated surfaces (~7%) and the spatial overlap integral of the input Gaussian-shaped beam with the doughnut-shaped output beam (~93%), this suggests a single-pass scattering loss should be less than 1%, which is considerably smaller than the scattering loss of ~11.1% measured for an $\lambda/2$ S-waveplate intended for use as a radial polarisation converter in the ~1μm wavelength band. It is expected that the total conversion efficiency could be further improved when a circularly polarized LG_{01} optical vortex beam is utilized to convert to radial polarization by using an appropriate $\lambda/4$ S-waveplate with anti-reflection

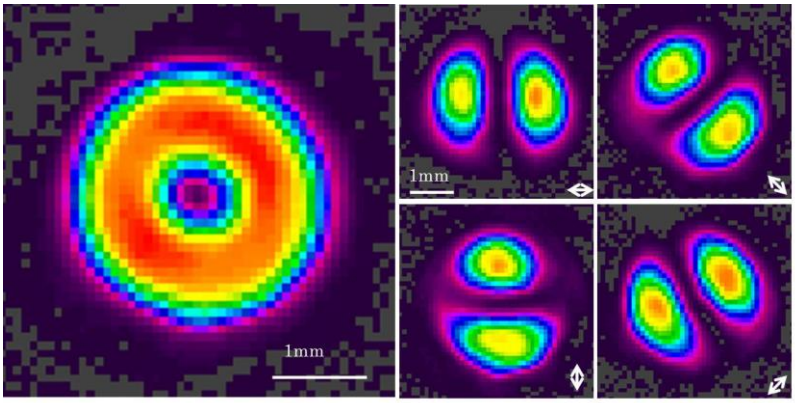

Figure 6.10 Experimental far-field intensity distribution; (b)-(e) beam profiles after passage through a rotated linear polarizer. The white arrows indicate the transmission direction of polarizer.

coatings on both surfaces.

The M^2 factor was measured to be ~2.1 and hence in close agreement with the theory confirming the high quality of the radially-polarized doughnut-shaped beam generated by the S-waveplate. The improvement of beam quality compared with 1μm performance verified that the scattering of inhomogeneities of nanogratings is the main reason for degradation in beam quality. The PER of beam was investigated with the same method described in the previous section. With this method, the PER was calculated to be ~15.5dB. It is worth mentioning that the value of PER varies by less than 3dB from 1950nm to 2100nm with a maximum PER of 17.5dB at 2050nm. This shows that the S-waveplate is a very effective radial polarisation converter across a wide wavelength band. These results for performance of the S-waveplate suggest that it would be suitable for use with high average power lasers at 2μm.

6.4 Conclusion

In this chapter, we have introduced and successfully demonstrated efficient generation of radially-polarized doughnut-shaped beams using a continuously space-variant half-waveplate or quarter-waveplate fabricated by femtosecond writing of sub-wavelength gratings in silica glass.

We first demonstrated femtosecond writing of nanogratigns technique and the fabrication process for these polarization converters which were fabricated by Dr. Martynas Beresna in ORC. The working principles of polarization converters were also discussed with the help of Jones Matrix altogether.

We then experimentally tested the performance of both the $\lambda/2$ and $\lambda/4$ S-waveplate. With the $\lambda/2$ S-waveplate, a linearly-polarized Gaussian-shaped beam was converted to a radially-polarized doughnut-shaped beam in the far-field with a total conversion efficiency of 75%. The loss could be attributed to Fresnel reflection loss on both uncoated surfaces of silica glass(~7%), the mode mismatch between input and output beams (~7%) and strong Rayleigh scattering loss (~11%). The resultant radial polarization had a PER of 14dB and a beam quality factor of M^2=2.7.

The $\lambda/4$ S-waveplate, however, transformed a circularly-polarized LG_{01} optical vortex beam into a radially polarized doughnut-shaped beam with total conversion efficiency of 86%. The improvement of conversion efficiency is due to better mode match between input and output beam as well as the reduced scattering loss because of a single layer of nanogratings. Assuming an identical mode intensity distribution for input and output beams, the scattering loss was estimated to be ~7.6%, almost half that of the $\lambda/2$ S-waveplate. The resultant beam had a PER of 8dB, and a beam quality factor of M^2=2.9. Significant deterioration in the PER might be attributed to a resultant spiral phase front in the radially polarized beam. In order to improve the PER, a highly pure circularly-polarized helically phased LG_{01} beam is required.

Finally, we successfully demonstrated highly efficient conversion to radial polarization in the 2μm band with wavelength tuning from 1950nm to 2100nm by using a newly-designed 2μm $\lambda/2$ S-waveplate. The resultant radially-polarized beam had a maximum PER of 17.5dB at 2050nm with a variation of less than 3dB from 1950nm to 2100nm. The total conversion efficiency was measured to be~86% across the wavelength tuning range. Taking into account the losses due to Fresnel reflection and mode mismatch, the scattering loss was estimated to less than 1%. Moreover, the M^2 ~2.1 confirmed that high quality of the radially-polarized doughnut beam was generated by the S-waveplate. These results suggest that it would be very suitable for use with a high average power laser at 2μm, and an $\lambda/4$ S-waveplate might be suitable for even higher average power as the total conversion efficiency will be close to 100%.

Bibliography

1. D. Pohl, "Operation of a ruby laser in the purely transverse electric mode TE_{01}," Applied Physics Letters **20**, 266-267 (1972).

2. I. Moshe, S. Jackel, and A. Meir, "Production of radially or azimuthally polarized beams in solid-state lasers and the elimination of thermally induced birefringence effects," Optics Letters **28**, 307-309 (2003).

3. Y. Kozawa and S. Sato, "Generation of a radially polarized laser beam by use of a conical Brewster prism," Optics Letters **30**, 3063-5065 (2005).

4. T. Moser, H. Glur, V. Romano, F. Pigeon, O. Parriaux, M. A. Ahmed, and T. Graf, "Polarization-selective grating mirrors used in the generation of radial polarization," Applied Physics B **80**, 707-713 (2005).

5. M. Stalder and M. Schadt, "Linearly polarized light with axial symmetry generated by liquid-crystal polarization converters," Optics Letters **21**, 1943-1945 (1996).

6. G. Machavariani, Y. Lumer, I. Moshe, A. Meir, and S. Jacket, "Efficient extracavity generation of radially and azimuthally polarized beams," Optics Letters **32**, 1468-1470 (2007).

7. M. Beresna, M. Gecevicius, and P. G. Kazansky, "Ultrafast laser direct writing and nanostructuring in transparent materials," Advances in Optics and Photonics **6**, 293-339 (2014).

8. M. Birnbaum, "Semiconductor surface damage produced by ruby lasers," J. Appl. Phys. **36**, 3688-3689 (1965).

9. Z. Guosheng, P. M. Fauchet, and A. E. Siegman, "Growth of spontaneous periodic surface structures on solids during laser illumination," Physical Review B **26**, 5366-5381 (1982).

10. J. E. Sipe, J. F. Young, J. S. Preston, and H. M. Vandriel, "Laser-induced periodic surface structure . I. Theory," Physical Review B **27**, 1141-1154 (1983).

11. Y. Shimotsuma, P. G. Kazansky, J. R. Qiu, and K. Hirao, "Self-organized nanogratings in glass irradiated by ultrashort light pulses," Physical Review Letters **91**, 247405(2003).

12. W. J. Yang, E. Bricchi, P. G. Kazansky, J. Bovatsek, and A. Y. Arai, "Self-assembled periodic sub-wavelength structures by femtosecond laser direct writing," Optics Express **14**, 10117-10124 (2006).

13. V. R. Bhardwaj, E. Simova, P. P. Rajeev, C. Hnatovsky, R. S. Taylor, D. M. Rayner, and P. B. Corkum, "Optically produced arrays of planar nanostructures inside fused silica," Physical Review Letters **96**, 057404(2006).

14. G. Malpuech, A. Kavokin, and G. Panzarini, "Propagation of exciton polaritons in inhomogeneous semiconductor films," Physical Review B **60**, 16788-16798 (1999).

15. M. Born and E. Wolf, *Principles of Optics: Electromagnetic Theory of Propagation, Interference and Diffraction of Light,* 7th. (Cambridge University, 1999).

16. C. Gu and P. C. Yeh, "Form birefringence dispersion in periodic layered media," Optics Letters **21**, 504-506 (1996).

17. E. Bricchi and P. G. Kazansky, "Extraordinary stability of anisotropic femtosecond direct-written structures embedded in silica glass," Applied Physics Letters **88**, 111119(2006).

18. M. Beresna, "Polarization engineering with ultrafast laser writing in transparent media," (Phd Thesis, 2012).

19. S. Quabis, R. Dorn, and G. Leuchs, "Generation of a radially polarized doughnut mode of high quality," Applied Physics B **81**, 597-600 (2005).

20. Z. Bomzon, V. Kleiner, and E. Hasman, "Formation of radially and azimuthally polarized light using space-variant subwavelength metal stripe gratings," Applied Physics Letters **79**, 1587 (2001).

21. M. Beresna, M. Gecevicius, and P. G. Kazansky, "Polarization sensitive elements fabricated by femtosecond laser nanostructuring of glass [Invited]," Optical Materials Express **1**, 783-795 (2011).

22. M. Beresna, M. Gecevicius, P. G. Kazansky, and T. Gertus, "Radially polarized optical vortex converter created by femtosecond laser nanostructuring of glass," Applied Physics Letters **98**, 201101 (2011).

23. D. H. Goldstein, *Polarized light,* 2nd. (2003).

24. G. Machavariani, N. Davidson, E. Hasman, S. Blit, A. A. Ishaaya, and A. A. Friesem, "Efficient conversion of a Gaussian beam to a high purity helical beam," Optics Communications **209**, 265-271 (2002).

Chapter 7: Doughnut-shaped beam generation in Yb-doped fibre lasers

7.1 Introduction

Rare-earth-doped fibre lasers offering power scalability, excellent beam quality and ultra-high optical conversion efficiency in a compact format [1], have seen rapid development over the last decade owing to a range of applications. To date, much of the effort has focused on the development of robust fundamental transverse mode lasers using techniques such as bend-loss filtering [2, 3] or specially designed fibres (e.g. with a photonic crystal geometry [4] or tailored gain dopant distribution in the fibre core [5]) to facilitate scaling of mode area whilst providing suppression of unwanted higher order modes. Recently, operation on individual higher-order modes has attracted growing interest due to the potential for larger mode area, which, in turn, raises the threshold for damage and deleterious nonlinear loss processes allowing further scaling of output power and pulse energy. Further benefits in terms of potential applications in micro-particle manipulation [6], quantum information [7] and laser processing of materials [8] can be derived from the unique properties (i.e. intensity profile, polarization and phase distribution) of some of these higher order modes.

In this chapter we present simple strategies for achieving lasing on the first higher-order doughnut-shaped mode (LP_{11} family of modes) in few-moded ytterbium (Yb)-doped fibre lasers. Firstly we demonstrate a cladding-pumped Yb-doped fibre laser, with a few-moded core and an external cavity containing an S-waveplate. With this arrangement we successfully demonstrate the direct generation of a radially polarized beam from an Yb-doped fibre laser. Secondly, we demonstrate a simple technique for selecting different transverse modes from a few-moded Yb-doped fibre laser using an intracavity polarization filter to exploiting the difference in polarization behaviour believed to be due to different effective birefringence and orientation of fast and slow axes for each mode. Using this approach, we have successfully operated a cladding-pumped Yb-doped fibre laser on the doughnut-shaped LP_{11} mode with high mode purity and controllable handedness of the helical phase front.

7.2 Background

7.2.1 Transverse modes in optical fibres

According to the optical waveguide theory, the exact vector electric field $\vec{e}_t$ in an optical fibre obeying the vector wave equation is given by [9]:

$$\left(\nabla_t^2 + n^2k^2 - \beta^2\right)\vec{e}_t = -\nabla_t\left[\vec{e}_t \bullet \nabla_t \ln(n^2)\right] \quad (7.1)$$

where ∇_t is the transverse gradient vector, ∇_t^2 is the transverse vector Laplacian, n is the refractive index of fibre, k is the free-space wavenumber (given by $2\pi/\lambda$), and β is the propagation constant of individual vector mode. In addition, in a weakly guiding optical fibre (refractive index profile height $\Delta \rightarrow 0$), the scalar wave equation can be derived by neglecting the index gradient (e.g. setting the right-hand side of Eq.(7.1) to zero). The neglect of the index gradient in the right-hand side of Eq.(7.1) leads to a polarization-independent propagation, thus we can choose linearly polarized (LP) modes, or circularly polarized modes as well as arbitrary linear combinations as solutions to Eq.(7.1) [10]. However, if we take account of finite Δ, coupling between the orthogonally polarized LP modes will be introduced, and there is an increasing coupling between polarization components as the increase of Δ leading to a transit to the TE, TM, HE and EH modes. The electric field distributions of these 'true' vector modes are listed in Table 7.1.

Table 7.1 The transverse electric field in the weakly guiding regime are grouped into three families of modes having the same azimuthal order l [9].

Mode		Field $\vec{e}_t$
l=0	HE_{1m}	$\begin{cases}\hat{x}\Psi_{0,m}(r)\\ \hat{y}\Psi_{0,m}(r)\end{cases}$
l=1	TE_{0m}	$(\hat{x}sin\varphi - \hat{y}cos\varphi)\,\Psi_{1,m}(r)$
	TM_{0m}	$(\hat{x}cos\varphi + \hat{y}sin\varphi)\,\Psi_{1,m}(r)$
	HE_{2m}	$\begin{cases}(\hat{x}cos\varphi - \hat{y}sin\varphi)\,\Psi_{1,m}(r)\\ (\hat{x}sin\varphi + \hat{y}cos\varphi)\,\Psi_{1,m}(r)\end{cases}$
l>1	$HE_{(l+1)m}$	$\begin{cases}(\hat{x}cos(l\varphi) - \hat{y}sin(l\varphi))\,\Psi_{l,m}(r)\\ (\hat{x}sin(l\varphi) + \hat{y}cos(l\varphi))\,\Psi_{l,m}(r)\end{cases}$
	$EH_{(l-1)m}$	$\begin{cases}(\hat{x}\,cos(l\varphi) + \hat{y}sin(l\varphi))\,\Psi_{l,m}(r)\\ (\hat{x}si\,n(l\varphi) - \hat{y}cos(l\varphi))\,\Psi_{l,m}(r)\end{cases}$

Where $\Psi_{l,m}(r)$ is the radial field distribution of the corresponding scalar mode, φ is the azimuthal coordinate, and m is the radial index. Figure 7.1 shows the corresponding intensity distributions for the two lowest-order vector modes, along with schematic representations of polarization orientations and effective refractive index (n_{eff}). For modes with azimuthal order l=0, designated as LP_{0m} modes in the scalar approximation and HE_{1m} in the vector solutions, there exist two-fold degeneracies due to the fact that the modes with the orthogonal linear polarization orientations share exact the same value for n_{eff}. For l=1, designated as LP_{1m} modes in the scalar approximation, there exist four vector solutions – TE_{0m}(transverse electric field), TM_{0m} (transverse magnetic field), HE_{2m}^{even} , and HE_{2m}^{odd} modes. The four modes have the same intensity distribution but with different polarization orientations. The lowest-order of LP_{1m} modes is designated as the LP_{11} mode which consists of four vector modes – TE_{01}, TM_{01} HE_{21}^{even} , and HE_{21}^{odd} modes, as depicted in the bottom row of Figure 7.1. The HE_{21}^{even} and HE_{21}^{odd} modes are exactly degenerate due to the same n_{eff}, but the TE_{01} and TM_{01} modes have a slightly different value for n_{eff}. The TM_{01} mode has a radial polarization distribution and the TE_{01} mode has an azimuthal polarization distribution. These two modes are of the most interest from an application perspective. For the other higher order modes (l>1), there are two different vector solutions designated as $HE_{l+1,m}$ and $EH_{l-1,m}$ modes

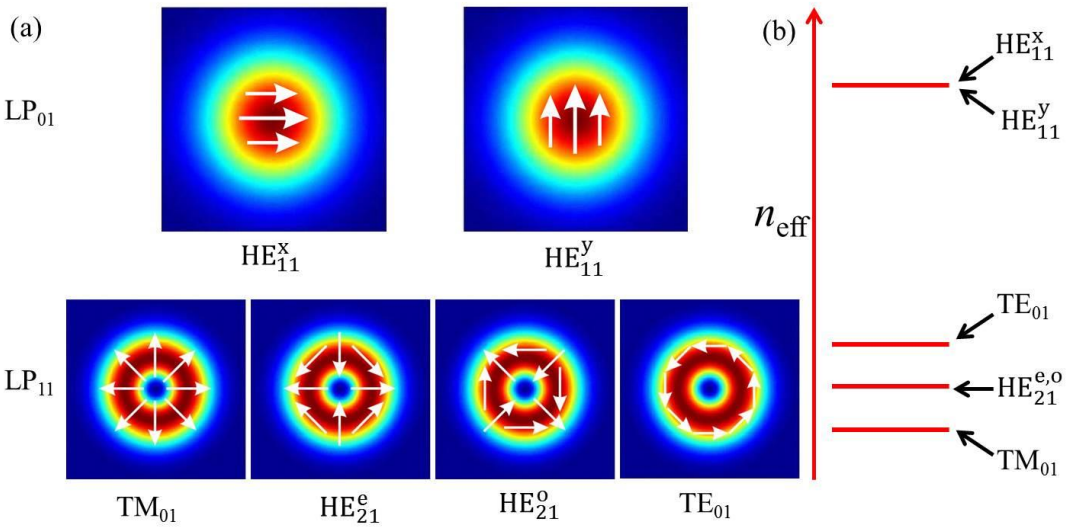

Figure 7.1 (a) Intensity profiles for the fundamental (LP_{01}) and the first higher-order (LP_{11}) mode groups in a step-index fibre. White arrows show the orientation of the electric field in each mode; (b) relative n_{eff} for each vector mode.

which are doubly degenerate. In general, the vector modes with the similar n_{eff} have the similar group velocities and comprise a single mode group in the scalar approximation.

The difference in n_{eff} (i.e. Δn_{eff}) for the TM_{01}, TE_{01} and HE_{21} modes in a weakly guided circular step-index fibre for the example of a fibre where the NA is 0.14 and the core diameter varies from 8 to 30μm at a wavelength of 1060nm is numerically calculated in Figure 7.2. The black dashed line represents the Δn_{eff} between the TE_{01} and HE_{21} modes. The n_{eff} for the TE_{01} mode is always greater than the HE_{21} mode, but Δn_{eff} significantly decreases and tends to zero with the increase of fibre core diameter. The red line indicates the Δn_{eff} between the TM_{01} and HE_{21} modes. It is apparent that the TM_{01} and HE_{21} modes have exact the same n_{eff} when the core diameter is equal to a particular value (~9μm). Below this value, the TM_{01} mode has a higher n_{eff} than the HE_{21} mode, and it has a lower n_{eff} than the HE_{21} mode above this value. It is apparent that the Δn_{eff} becomes larger when the first-higher order mode tends to the fibre cut-off region, where the mode is loosely confined within the fibre core. Indeed, the Δn_{eff} is very small ($<10^{-5}$) in weakly guiding fibres leading to a mode beat length greater than 0.1m. Consequently,

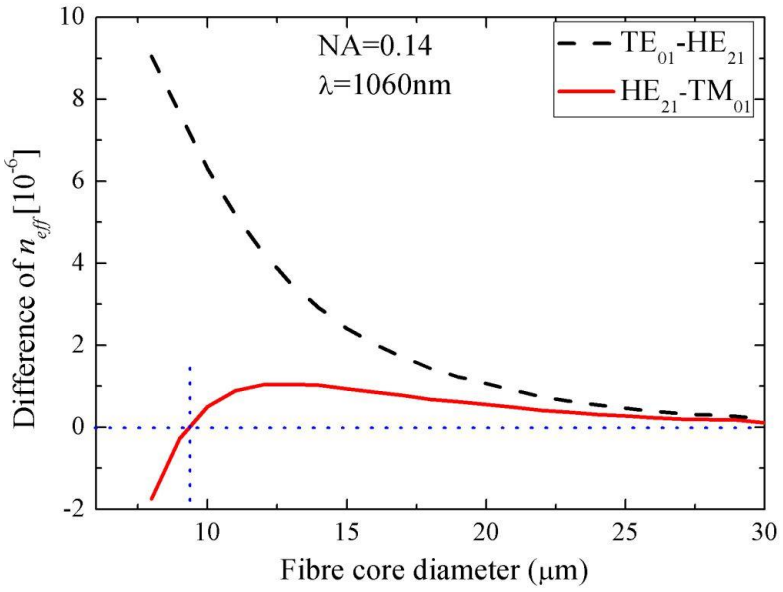

Figure 7.2 The difference between the effective refractive indices of TM_{01} (red) and TE_{01} (black) modes with respect to the HE_{21} modes as a function of fibre core diameter in a circular core step-index fibre with NA=0.14.

these vector modes are likely to be coupled with each other during co-propagating in fibres because of intrinsic and external perturbations, resulting in mostly observed LP_{11} modes with two lobed structure beam profiles, and the mode coupling increases as the Δn_{eff} decreases.

Some examples of the resultant linear combinations of pairs of eigen modes in LP_{11} group are illustrated in Figure 7.3. The top row shows the intensity distributions and polarization states for the four eigen vector modes, and the bottom row shows linear combinations of these eigen modes. As the polarization orientations are orthogonal for the pair of the TE_{01} and TM_{01} modes as well as for the pair of the HE_{21}^{even} and HE_{21}^{odd} modes, the combinations of these two pairs of modes result in a stable doughnut-shaped intensity distribution with varying polarization states depending on their relative phase. In contrast, the combinations of other pairs of eigen modes form two-lobe structure intensity patterns. As these patterns are formed by interference of two eigen modes with slight different n_{eff}, these patterns periodically vary with a beat length of $\lambda/\Delta n_{eff}$ within a fibre. The net result is that these patterns are unstable and the orientation rotates when the fibre is perturbed.

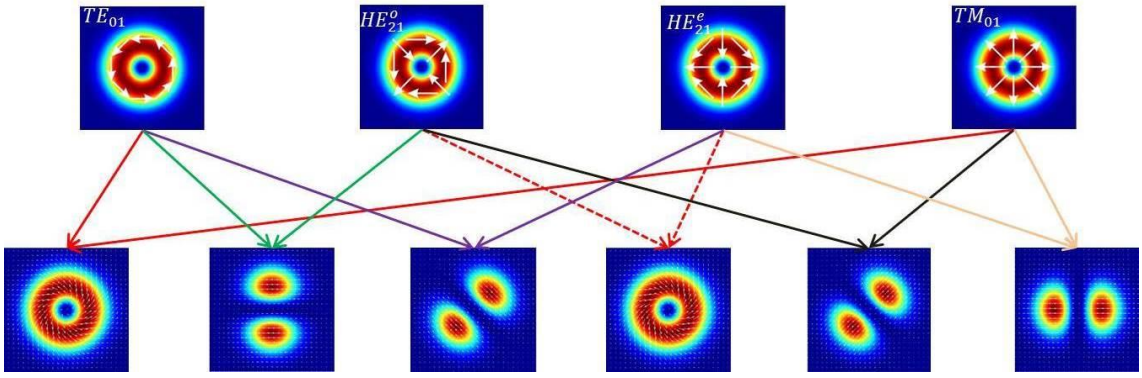

Figure 7.3 Intensity distributions of the first higher-order mode group in a weakly guiding cylindrical fibre. The top row shows four eigen modes of fibre, while the bottom row shows specific combinations of pairs of eigen modes, resulting in LP_{11} modes or doughnut-shaped beams which are likely to be observed at the fibre output. White arrows show the orientation of the electric field in each beam.

7.2.2 Linear birefringence induced LP mode transition

As we discussed in the last section that the four vector modes in LP_{11} family have doughnut-shaped intensity profile in a perfect circular-core step index fibre, and each mode exhibits a unique spatially inhomogeneous polarization state. In reality, it is rather difficult to fabricate a perfect circular core fibre with a uniform refractive index profile. The doughnut-shaped beam profile and its polarization state are strongly influenced by the fibre parameters such as the fibre core geometry and core refractive index profile. Jocher [11] numerically analysed the influence of core ellipticity in a strongly guiding fibre (NA=0.41 and core diameter of 3.2μm) on the first higher order vector modes (LP_{11} family mode). The results show that only 1% of core ellipticity is enough to strongly distort the ideal doughnut-shaped beam profile and its corresponding polarization state. In addition, an optical fibre always exhibits slight birefringence due to imperfection of manufacturing process [12]. Therefore, it is necessary to look at the behaviour of the vector modes in the presence of residual birefringence.

Here we simply quantify the impact of linear birefringence on these four vector modes by introducing the TE fraction value which describes the fraction of power in the *x*-polarization defined as follows [11]:

$$\eta_x = \frac{\int |E_x|^2 \, dxdy}{\int (|E_x|^2 + |E_y|^2) dxdy} \tag{7.2}$$

in which E_x and E_y are amplitude of electric field in the x and y directions, respectively. We calculate these values directly from the vector mode solver in COMSOL Multiphysics 4.1. From Table 7.1, we can see that all four vector modes have equivalent energy in the *x* and *y* directions, and hence these modes have the same TE fraction value of 0.5. However, in fibres with a slight linear birefringence, the intensity profiles for these four vector modes are no longer doughnut-shape, and their polarization states change as well. This is because the birefringence also leads to a polarization correction as index gradient. When the impact of the birefringence is dominant, each polarization field component is uncoupled and thus the modes remain exactly LP modes [10]. Figure 7.4 shows an example of numerically calculated TE fraction values for these four vector modes as a function of linear birefringence of fibre core in a circular core fibre with core diameter of 20μm, 0.08 of NA and wavelength of 1060nm. The TE fraction value rapidly

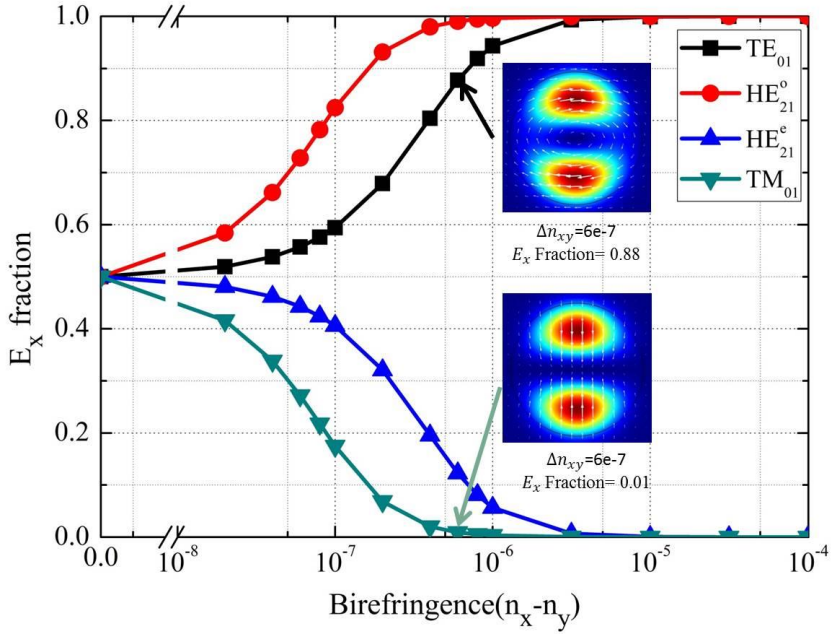

Figure 7.4 Evolution of the intensity fraction of x-polarization for the LP_{11} family modes as a function of fibre core birefringence. The inserts depict intensity profiles and polarization distributions of TE_{01} and TM_{01} modes in case of 6×10^{-7} birefringence.

deviates from 0.5 in the presence of a slight linear birefringence. It is apparent that this value gets close to 1 for TE_{01} and HE_{21}^{o} modes and to 0 for TM_{01} and HE_{21}^{e} mode when the birefringence is greater than $\sim 10^{-5}$, indicating that the polarization of the four vector modes transiting to linear polarization. In addition, the TE fraction value varies more strongly for the TM_{01} mode than the TE_{01} mode indicating that the latter is more sensitive to the linear birefringence for a weakly guiding fibre. The inserts show the beam profiles for the transiting TE_{01} and TM_{01} modes when the fibre birefringence is 6×10^{-7}, which have TE fraction value of 0.88 and 0.01, respectively. The beam profiles for both modes become similar to the LP_{11} modes.

As we discussed above, it seems that the doughnut-shaped LP_{11} family modes cannot exist in a real circular-core fibre due to the residual birefringence. However, the real situation is more complicated than we discussed above as the residual birefringence probably not be a pure linear birefringence. It can also contain some other birefringence such as radial birefringence (principle of the fast or slow axes aligned with the radial or azimuthal orientations) which is favour for supporting the doughnut-shaped TM and TE modes [13, 14]. Indeed, observing the dynamics of mode propagation in the few-mode fibre has been demonstrated in a 50cm length of

Corning HI1060 fibre using high-spatial-resolution imaging of the Rayleigh scattered light. The results showed that the vector modes (such as the TM_{01} and TE_{01} modes) in the LP_{11} family modes successfully propagated with a modal purity of >95% [15].

7.2.3 Historic doughnut-shaped beam generation in optical fibres

From Figure 7.1, it appears feasible to generate the doughnut-shaped modes in few-moded fibres, particularly for cylindrical vector beam, such as azimuthally or radially polarized beams corresponding to the TE_{01} and TM_{01} modes respectively. However, the near-degeneracy of the four vector modes in the LP_{11} group means that the generation of cylindrical vector beams in fibres requires a robust mode discrimination approach to break the degeneracy.

Indeed, a number of sophisticated doughnut-shaped mode selection techniques in few-moded fibres have been developed in recent years. Depending on whether a gain fibre is involved or not, these methods can be categorized as active or passive. Active methods rely on the laser oscillator or amplifier to directly generate doughnut-shaped modes. Alternatively, passive methods involve the use of a mode control technique to force a launched beam to the desired doughnut-shaped mode. G. Volpe successfully demonstrated conversion of LG beams to cylindrical vector beams in a short few-moded fibre. Through controlling the input polarization state, the fibre yielded doughnut-shaped cylindrical vector beams from the LP_{11} group [16]. Another method to generate cylindrical vector beams is to use a fibre grating in combination with a free space etalon to provide cavity feedback only to the desired mode [17]. Moreover, the cylindrical vector modes can be generated and propagated over greater than tens of meters in a specially designed fibre which the refractive index profile is similar to the cylindrical vector modes and hence the difference of effective index of each mode are significantly lifted [18]. In addition to the aforementioned passive methods to generate doughnut-shaped mode in fibres, there is strong motivation to generate the doughnut-shaped modes directly in fibre lasers given the potential advantages for scaling average power. A fibre Bragg grating in conjunction with an acousto-optic tunable-filters allows electronically controllable selection of doughnut-shaped modes as a result of incoherent superposition of two orthogonal LP_{11} modes within a multi-mode Tm-doped fibre laser [19]. Furthermore, several recent investigations were conducted in Yb-doped

and erbium(Er)-doped fibre lasers to produce doughnut-shaped cylindrical vector beams by employing either a dual conical prism [20], birefringent crystal aligned for propagation along the optic axis [21], a segmented wave plate [22] or a photonic crystal grating [23]. The highest laser output power and slope efficiency reported to date in a fibre laser with a radially-polarized output beam is 2.5 W and 46% respectively [23],which is far below the performance reported for bulk solid-state lasers.

7.3 Yb-doped fibre laser with radially polarized output

In this section, we firstly experimentally investigate vector mode propagation in polarization maintaining (PM) and non-PM circular core optical fibres, and then we present an alternative approach for efficiently generating a radially-polarized beam directly in a cladding-pumped Yb-doped fibre laser by employing an S-waveplate as an intracavity polarization-controlling element in an external feedback-cavity arrangement.

7.3.1 Fibre propagation of vector modes

As we mentioned above, generation of radially-polarized beam (TM_{01} mode) in fibres is rather challenging due to near degeneracy of the four vector modes in the LP_{11} group and hence the strong intermodal coupling which is usually caused by inner fibre imperfections such as index inhomogeneities, core ellipticity and eccentricity, as well as external perturbations such as bends or strains [24]. Despite of these challenges, generation of radially-polarized beams in standard fibres has been successfully demonstrated in several earlier reports. Before we investigating an approach for directly generating a radially-polarized beam in an Yb-fibre laser, an experimental investigation of the propagation properties of this vector mode in standard step-index circular core fibres was conducted.

7.3.1.1 Vector mode propagation in non-PM fibres

The experimental set-up used to investigate the propagation properties of a radially-polarized beam in a non-PM fibre is shown in Figure 7.5. The probe beam was from a home-made fibre amplifier which produced ~50mW linearly-polarized Gaussian-shaped output beam (the LP_{01} mode) with a M^2 of 1.1 and a wavelength of 1060nm with 0.2nm 3dB-bandwidth. The PER of the output beam was measured

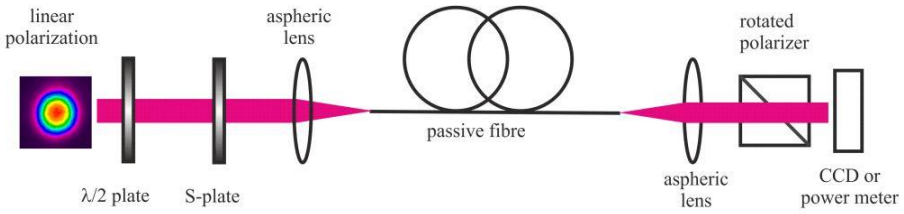

Figure 7.5 Experimental set-up for characterizing the output from a few-moded non-PM fibre with a TM_{01} seed input beam.

to be ~25dB. The incident beam polarization direction was aligned with respect to the $\lambda/2$ S-waveplate with the aid of a $\lambda/2$ waveplate to yield a radially polarized output beam. Based on the waveguide theory [9], the number of transverse modes capable of propagating in the fibre is dependent on the V-number. When the V-number is <2.405, the fibre will only allow the fundamental LP_{01} mode to propagate through the fibre, while the fibre with V-number ranging from 2.405 to 3.832 can only support LP_{01} and LP_{11} modes. Therefore, the resulted radially polarized beam was coupled into a 10m length of Corning SMF-28 fibre, which has a V-number of ~3.6 at 1μm wavelength and consequently can only support LP_{01} and LP_{11} modes. The coupling system consisted of two aspheric lenses with equal focal length of 8mm. The radially-polarized beam was carefully aligned to ensure being incident on the centre of the fibre core. Slight misalignment (lateral offset launching condition) in ~microns would significantly distort the output beam from a doughnut-shaped intensity profile. The total loss including the S-waveplate loss and the coupling loss was measured ~3dB. The output beam from the opposite end of the fibre was collimated by an aspheric lens, and a Spiricon CCD camera was used to detect the emerged beam intensity profile. A linear polarizer on a rotation stage was placed in front of the CCD camera to characterize the polarization state of the output beam.

Figure 7.6 shows some examples of typical measured intensity distributions of the output beam when the radially-polarized beam was launched into the SMF-28 fibre. It is clear that the doughnut-shaped beam was distorted to radially asymmetric beam profiles as shown in Figure 7.6(a)-(d) due to significant inter-modal coupling caused by the intrinsic fibre perturbations such as elliptical core, residual birefringence as well as external perturbation such as residual stress introduced by spooling the fibre with a diameter of ~10cm. The orientation of resulted asymmetric beam was rotated as shown in the images when deliberately bending

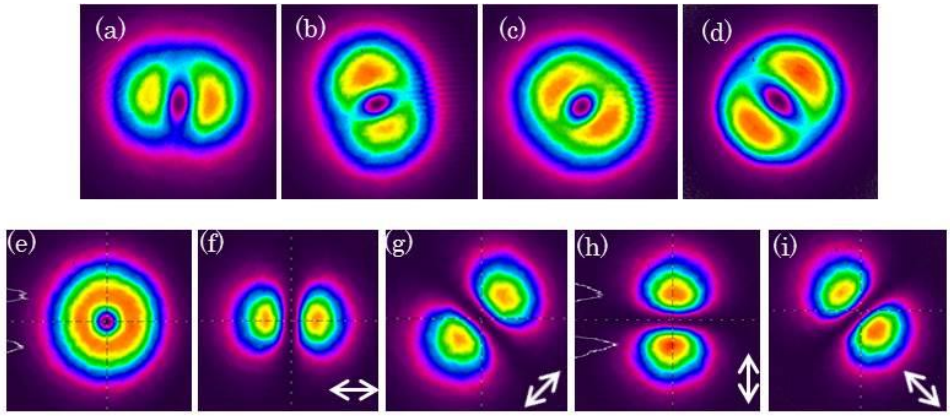

Figure 7.6 Typical output beam profiles when a radially polarized beam propagated through a 10m length SMF-28 fibre. The first row ((a)-(d)): typical output beams with radially asymmetric intensity distributions resulting from strong mode coupling. The second row: (e) doughnut-shaped output beam with radial polarization; (f)-(i) beam profiles after passage through a linear polarizer oriented in the direction indicated by white rows.

and twisting fibre, indicating that the external perturbation can lead to a strong impact on the mode coupling between the four vector modes in LP_{11} family mode. However, the doughnut-shaped beam could be achieved in some particular cases when the fibre was applied appropriate force and was properly macro-bended in the input section of fibre during the experiment. Figure 7.6(e) shows one example of obtained doughnut-shaped beam, and the beam profiles after passage through a rotated linear polarizer are illustrated in Figure 7.6(f)-(i) verifying that the polarization is indeed radial. The results indicate that the impacts of slight core ellipticity and residual weak birefringence on fibre modes can be compensated by deliberate external perturbations including macro-bending and lateral force applied to the fibre. These external perturbations, if properly applied, can lead to a change of the effective refractive index of modes and reduce the mode coupling between the nearly degenerate modes. Consequently, the doughnut-shaped beam with radial polarization can be produced from the fibre end facet. However, this mode is sensitive to external perturbations including the stress and temperature. Slight variation of stress and temperature on fibre will distort the beam profile. During the experiment, the fibre was put on a hot plate which the temperature could be precisely controlled in the accuracy of 1℃. We found that the doughnut-shaped beam profile would experience a significant distortion becoming two-lobed

structure similar to Figure 7.6(a)-(d) even when the variation of temperature was 2℃.

7.3.1.2 Vector mode propagation in PM fibres

We further investigated the propagation of a radially polarized beam in a 2m length of commercially available PM fibre (Nufern PM1550-XP: 0.125 of NA, 8.5μm core diameter, cut-off wavelength around ~1380nm) which can support the first higher order LP_{11} mode at wavelength of 1μm. The experimental set-up is shown in Figure 7.7 which is similar to the experimental setup for non-PM fibre (as shown in Figure 7.6).

In weakly guiding fibre with strong linear birefringence, the modes remain exactly LP modes. Particularly, LP_{11} group mode is split into two nondegenerate group that is $\hat{x}$-$LP_{11e,o}$ and $\hat{y}$-$LP_{11e,o}$. The Δn_{eff} between two groups is significantly lifted due to the birefringence, and thus the modes with two orthogonal polarizations are immune to coupling to each other during the propagation. However, the same linearly polarized even and odd modes are nearly degenerate and hence can couple to each other. As it is well known that the radially polarized TM_{01} mode can be considered as a coherent superposition of $\hat{x}$-LP_{11e} and $\hat{y}$-LP_{11o} modes. When a radially polarized beam is properly launched into the fibre, it mainly excites $\hat{x}$-LP_{11e} and $\hat{y}$-LP_{11o} modes simultaneously. Without considering mode coupling, the two orthogonal LP_{11} modes propagate with different propagation constants resulting in a doughnut-shaped beam profile with varied polarization states on the output facet dependent on the relative phase between the two modes.

During the experiment, a polarization controller (Newport F-POL-IL as shown in Figure 7.7) was placed in the input section of the fibre to apply pressure and twist on the fibre to control the beam profile and polarization state of the output beam.

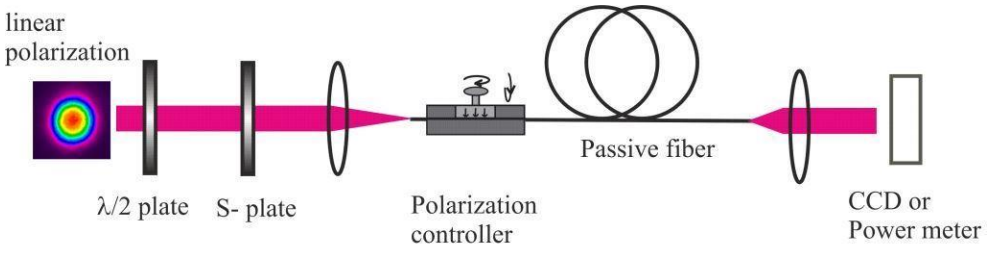

Figure 7.7 Experimental setup for generating and measuring vector modes after propagating through a few-mode PM fibre.

Through rotating and screwing the knob on the fibre squeezer in the centre section, a linear birefringence was introduced in the squeezed fibre and thus the relative phase between the two LP_{11} modes could be precisely controlled. The intensity weights of each LP_{11} mode could also be effectively controlled in this way as the pressure and twist change the mode coupling between the even and odd modes. Figure 7.8 shows several typical doughnut-shaped output beams that were easily produced by this method. The first row represents the radially polarized beam for which the relative phase between the $\hat{x}$-LP_{11e} and $\hat{y}$-LP_{11o} modes is 0 or multiple of $2\,\pi$, the second row represents the situation where the relative phase between these two LP_{11} modes is $\pi/2$, and the third row represents that the case where the relative phase is π corresponding to the hybrid HE_{21}^{e} mode. It is worth mentioning that the coherent superposition of a pair of $\hat{x}$-LP_{11e} and $\hat{y}$-LP_{11o} modes or a pair of $\hat{x}$-LP_{11o} and $\hat{y}$-LP_{11e} modes results in a doughnut-shaped beam profile independent on their relative phase.

Though a radially-polarized beam can be generated in a PM fibre, the polarization state is rather sensitive to external perturbations compared with the case in a non-PM fibre. This is because the mode splitting Δn_{eff} between $\hat{x}$-LP_{11e} and $\hat{y}$-LP_{11o} modes is normally greater than ~10^{-4}, which is much larger than that of non-PM

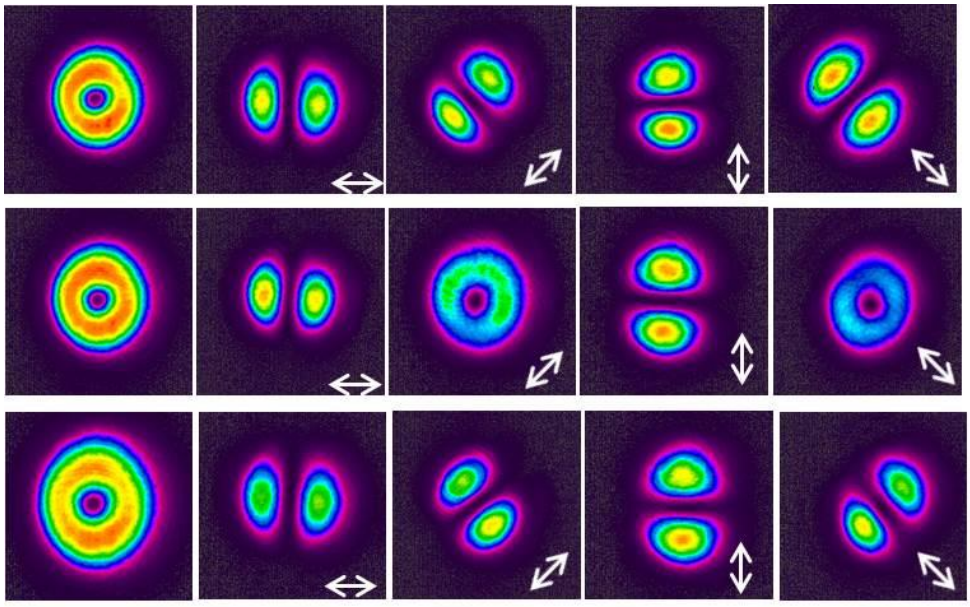

Figure 7.8 Typical doughnut-shaped beams emerging from the fibre under appropriate pressure and twist. The first row: radially-polarized beam output . The second and third row: hybrid polarization state output beams.

fibre (Δn_{eff}~10^{-6}). As a result, the same percentage of variation of Δn_{eff} for the former will induce much more phase shift than the latter, and thus the polarization state varies much faster. Therefore, a non-PM fibre is more suitable for maintaining the polarization state of a radially-polarized beam.

7.3.2 Generating a radially-polarized beam in an Yb-fibre laser

The experimental set-up for directly generating a radially-polarized beam in an Yb-fibre laser is shown in Figure 7.9. It comprised a 1.5m length of non-PM Yb-doped double-clad silica fibre (LIEKKI Yb1200-20/125DC) with feedback for lasing provided by a perpendicularly-cleaved fibre facet at the output coupler end of the fibre and at the opposite end by an external feedback cavity. The Yb-doped fibre had a core diameter of 20 μm, NA of 0.08 and an inner-cladding diameter of 125 μm. The V-number for the fibre is calculated to be 4.83 for 1040 nm guaranteeing that only the fundamental LP_{01} mode, its neighboring higher order LP_{11}, LP_{21} and LP_{02} modes could be guided within the fibre core, while the other higher-order modes have a very high propagation loss. The end of fibre adjacent to the external cavity was cleaved at an angle of 8° to suppress the broadband feedback and hence parasitic lasing between the fibre end facets. Pump light was provided by a fibre-

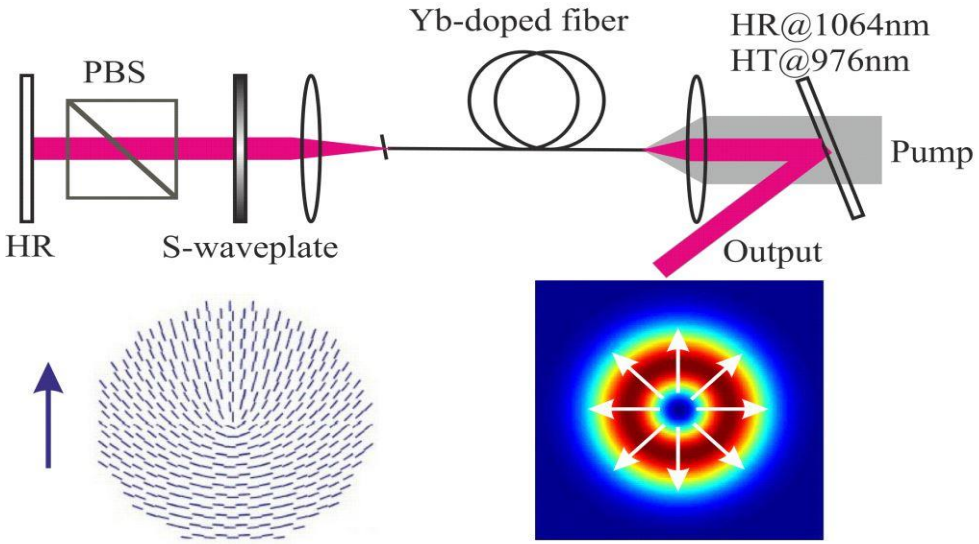

Figure 7.9 Experimental setup for generating a radially polarized beam. The lower-left inset shows the schematic of the nanograting orientation in the S-waveplate; the lower-right insert shows the schematic representation of the intensity and polarization distribution of the TM_{01} mode in the fibre.

coupled 976 nm laser diode with a 105 μm core diameter and 0.12NA, which was free-space coupled into the output end of the fibre via a dichroic mirror. The effective absorption coefficient for pump light at 976 nm launched into the inner-cladding was roughly measured to be ~10 dB/m via cutback technique: 1W of pump light was coupled to 1.75m of fibre and the residual pump power was measured at the output. Subsequently, we cut 0.25m off the fibre from the output-end and measure the residual pump power again. The light emerging from the angle-cleaved end of the fibre was collimated by an aspheric lens with a focal length of 18.4 mm and feedback for lasing was provided by a plane high reflectivity mirror (>99.8% at 1.04 μm). An S-waveplate and a polarization beam splitter (PBS) were placed in the external cavity between high reflectivity mirror and the collimating lens. The PBS allowed only p-polarized light to pass through it and be transmitted to the S-waveplate. When the orientation of the S-waveplate, shown by the arrow in the lower-left insert of Figure 7.9 is aligned parallel to the p-polarization, it converts the p-polarized beam into a radially-polarized beam, which is then coupled into the fibre to excite the radially-polarized TM_{01} mode as shown in the lower-right insert of Figure 7.9. The net result is that the radially-polarized TM_{01} mode has the lowest round-trip loss and hence lasing occurs preferentially on this mode.

The laser beam profile and output power were monitored with the aid of a Spiricon CCD camera and a power meter, respectively. Figure 7.10 shows the output power plotted as a function of the launched pump power. The doughnut-shaped TM_{01}

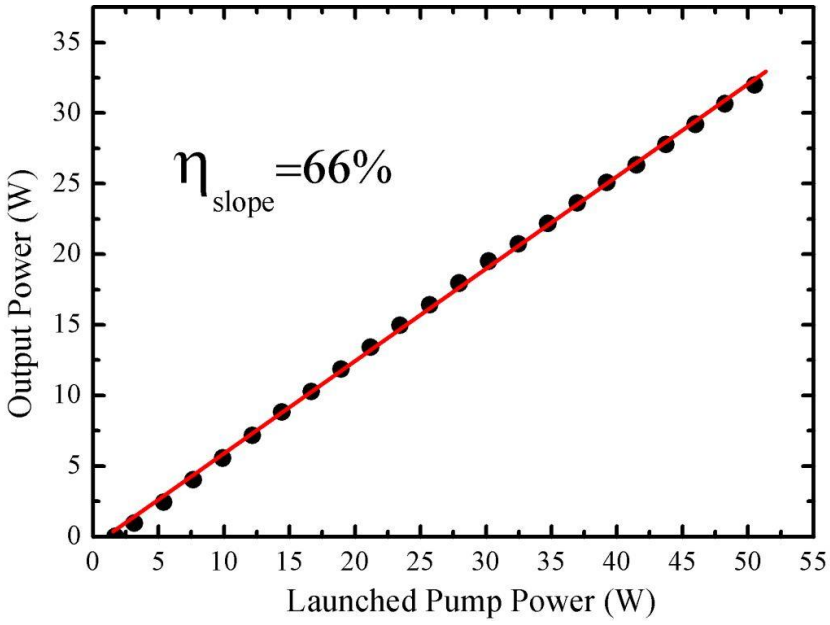

Figure 7.10 Output power versus launched pump power.

mode reached threshold at a pump power of 1.7 W (launched). The output power increased linearly with pump power with a slope efficiency with respect to launched pump power of ~66%, and reached a maximum of 32W at maximum 50W of launched pump power. The slope-efficiency is only slightly below that of the 70-80% value that is typical for conventional Yb-doped fibre lasers. This difference is attributed mainly to the mismatch of spatial overlap between the inversion distribution in the fibre core and doughnut-shaped intensity profile for the TM_{01} mode as well as the additional cavity loss associated with the external feedback arrangement. It is worth noting that the single-pass far-field transmission of the S-waveplate was measured to be ~75%, which corresponds to approximately 2.5dB of round-trip insertion loss at the lasing wavelength due to scattering introduced by microscopic inhomogeneities and induced defect absorption [25] and the lack of antireflection coatings on the S-waveplate faces. The absence of a roll-over in output power suggests that further scaling of the laser power should be achievable with a higher power pump source and with further optimization of the cavity configuration and fibre design.

Figure 7.11(a) and (b) show the intensity distributions of output beams. Figure 7.11(a) is a typical intensity profile measured near the threshold for an output power of 1.1 W, and Figure 7.11(b) is a typical intensity distribution measured at the maximum output power of 32 W. There is a clear intensity null at the beam's centre in Figure 7.11(a), but some residual intensity at the centre of the beam in Figure 7.11(b). Both beams show a pronounced doughnut-shaped pattern confirming the TM_{01} mode was dominant even at the highest power. The intensity distributions at low and high output power after passing through a rotated Glan-Taylor calcite polarizer are shown in Figure 7.11(c)-(j). The white arrow indicates the orientation of transmission axis of polarizer. The symmetric two-lobe-structured intensity distributions parallel to the transmission axis of the polarizer confirm that the output beams corresponded to the radially-polarized TM_{01} mode. The polarization purity was measured to be >95%, confirming the high radial polarization purity for the output beam.

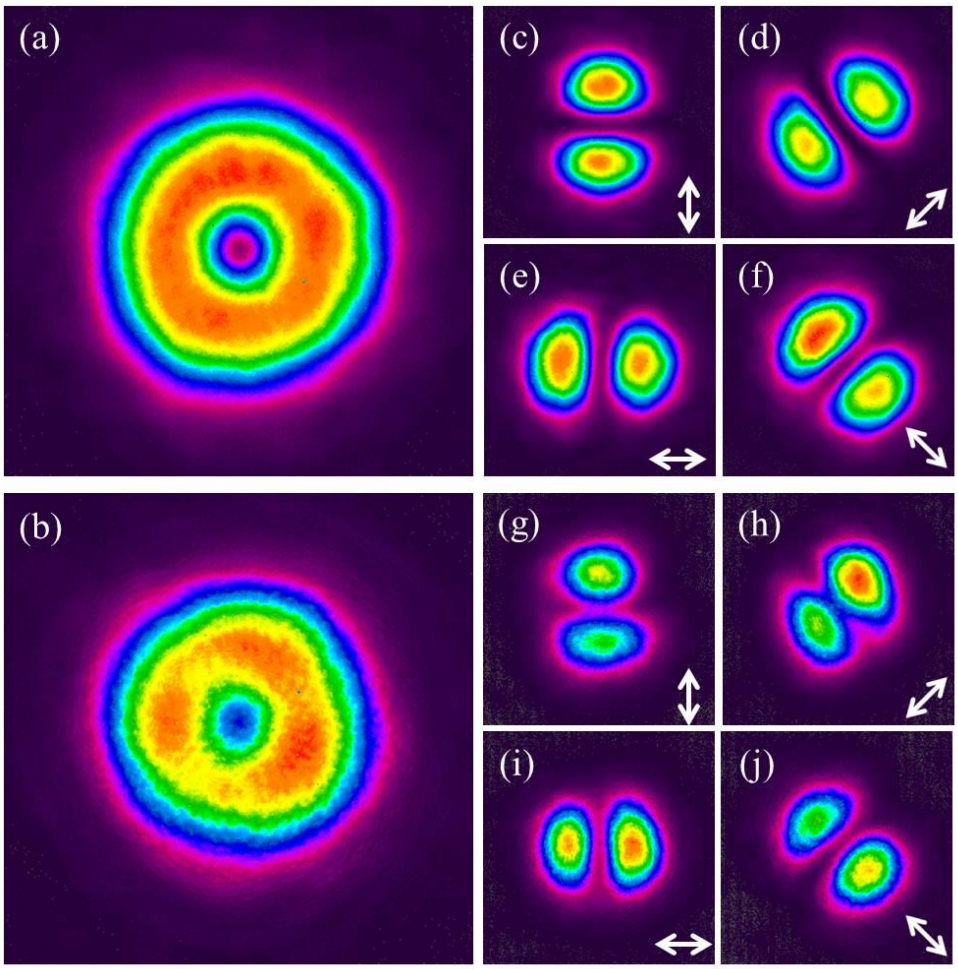

Figure 7.11 Experimental intensity distributions at (a) Pout=1.1W and (b) Pout=32W. (c)-(f) and (g)-(j) show beam profiles after passage through a rotated linear polarizer. The white arrows indicate the axis of polarizer.

The M^2 was also measured at low power and at the maximum output power. At low powers the value for M^2 was found to be approximately 2.1 in close agreement with the theoretical value of 2 for a radially-polarized TM_{01} mode. At higher powers the value for M^2 decreased slightly to ~1.9 indicating the presence of parasitic lasing at relatively low power on the fundamental (LP_{01}) as well as the dominant TM_{01} doughnut-shaped mode.

To estimate the mode purity (i.e. fractional content of TM_{01} versus LP_{01} mode), one-dimensional intensity distributions across the centre of beam were measured as shown in Figure 7.12(a) and (b), corresponding to the beam profiles in Figure 7.11(a) and (b), respectively. The measured intensity distributions plotted by the dark dots were fitted by a linear superposition of the LP_{01} and TM_{01} modes,

represented by the red solid curves. It is clear that there is some residual intensity at the centre of the beam at both low and high output power indicating that the fundamental LP_{01} mode was also excited. The power ratio of the TM_{01} to LP_{01} mode is approximately ~33:1 in Figure 7.12(a) at low power (i.e. the TM_{01} mode purity is ~97%); while this ratio reduces to ~8.5:1 in Figure 7.12(b) at maximum power, corresponding to a mode purity of ~89.5%. Thus, the LP_{01} mode content increases with pump power, but remains relatively low for the operating conditions used in our experiment. The presence of parasitic laser oscillation on the LP_{01} mode is attributed to residual feedback for the fundamental mode from the external cavity due to imperfections in the S-waveplate and Fresnel reflection from its uncoated faces in conjunction with undepleted inversion at the centre of the core due to the null in intensity for the TM_{01} doughnut mode. Thus, by modifying the fibre design to reduce the Yb concentration at the centre of the core and using antireflection coatings to minimize unwanted feedback from the S-waveplate surfaces it should be possible to avoid parasitic lasing on the fundamental mode and improve radial polarization purity and overall efficiency.

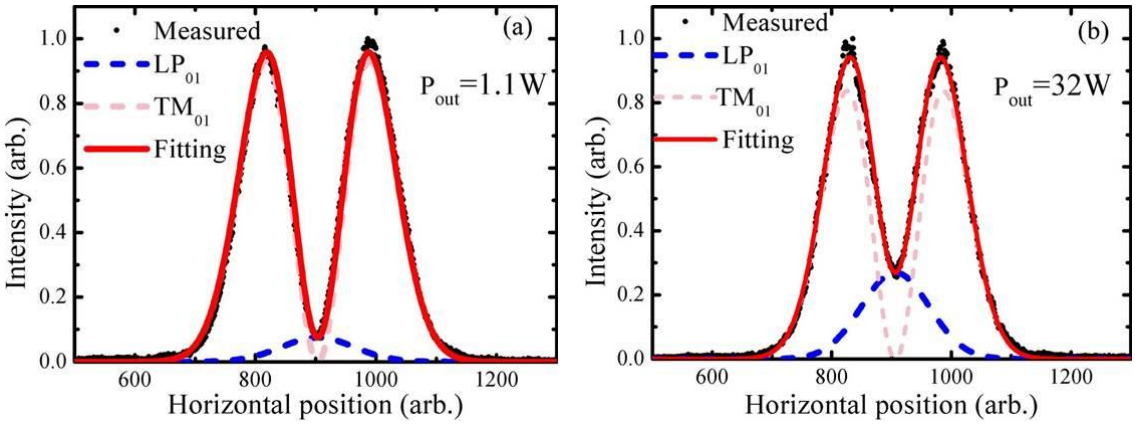

Figure 7.12 Intensity distribution across the beam centre along the x axis. (a) and (b) correspond to the conditions of Figure 7.11(a) and Figure 7.11(b), respectively. The dotted black curves are the measured intensity profiles. The pink and blue dashed curves represent the intensity profiles of theoretical TM_{01} and LP_{01} modes. The solid red curves correspond to fitting results to a superposition of TM_{01} and LP_{01} modes.

7.4 Polarization dependent mode-selection in an Yb-doped fibre laser

Here, we report a very simple strategy for achieving lasing on the first higher-order doughnut-shaped LP_{11} mode or the fundamental LP_{01} mode in a few-moded Yb-doped fibre laser with high efficiency and high mode quality using a simple external feedback cavity with a polarization discriminating element. We also show, with the aid of a detailed experimental investigation, that the underlying mechanism for this scheme is consistent with a change in the average birefringence, specifically fast and slow axes directions, with radial position in the core. The latter is believed to be due to the stress distribution resulting from imperfections in the fibre fabrication process [12, 26].

7.4.1 Experimental results

The laser configuration used in our experiment is shown in Figure 7.13. A 1m length of non-PM Yb-doped double-clad fibre was employed as the gain medium, which is the same type of fibre used in the last section but with different length. Feedback for lasing was provided by the ~3.6% Fresnel reflection from a perpendicularly-cleaved fibre facet at the laser output end of the fibre and by an external feedback cavity at the opposite end. The latter incorporated an aspheric collimating lens of focal length, 18.4 mm, a high reflectivity plane mirror, a polarizing beam splitter and a zero-order half-wave ($\lambda/2$) plate at 1064 nm mounted on rotation stage. This combination ensured that a linearly-polarized beam was fed-back into the fibre, which could be aligned at any desired angle via simple adjustment of the half-wave plate. The end of the fibre adjacent to the external cavity was cleaved at 8° to suppress the broadband feedback and hence parasitic

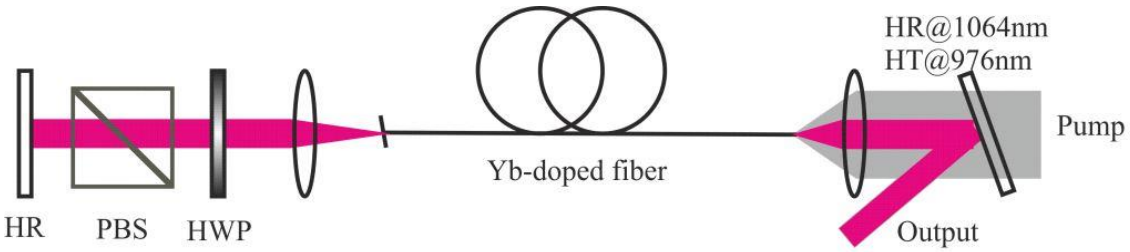

Figure 7.13 Experimental set-up: High reflectivity mirror (HR), polarizing beam splitter (PBS), and half-wave plate (HWP).

lasing between the fibre end facets. Pump light was provided by a 60 W fibre-coupled 976nm laser diode with a 105μm core diameter and 0.12NA, which was free-space coupled into the output end of the fibre via a dichroic mirror. The effective absorption coefficient for pump light launched into the inner-cladding was measured to be ~10 dB/m, hence a fibre length of approximately 1 m was selected for efficient pump absorption. With this arrangement a maximum of 52 W of pump power was absorbed in the Yb fibre.

The laser output beam profile and output power were monitored with the aid of a Spiricon CCD camera and a power meter, respectively. The intensity distribution for amplified spontaneous emission (ASE) from the fibre as illustrated in Figure 7.14 (i.e. with polarization dependent feedback blocked) at relatively low pump power (< 1.5 W) showed a quasi-top-hat profile confirming that there were indeed contributions from the LP_{01} and doughnut-shaped LP_{11} modes. A simple one-dimensional fitting to the measured intensity distribution across the centre of the beam (assuming negligible power in the higher order modes) revealed roughly equal powers for the two modes (~57% for the doughnut-shaped LP_{11} mode and ~43% of the LP_{01} mode) indicating that both fundamental LP_{01} and doughnut-shaped LP_{11} modes are extractable.

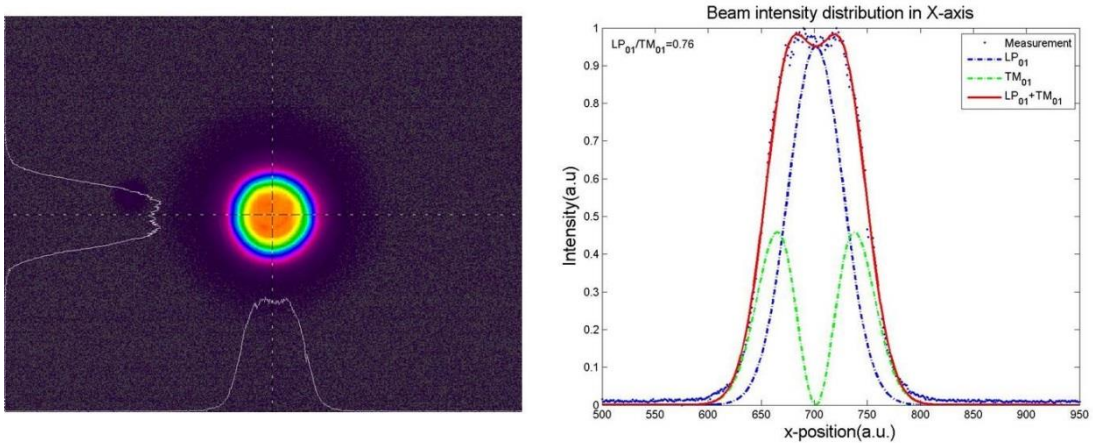

Figure 7.14 (Left) Beam profile for the forward ASE at a pump power of 1.5W; (right) the intensity distribution across the beam centre along the x axis. The dotted black curves is the measured intensity profile. The blue and green dashed lines represent the intensity profiles of theoretical LP_{01} and doughnut-shaped LP_{11} modes, respectively. The solid red line corresponds to the fitting result to a superposition of doughnut-shaped LP_{01} and LP_{01} modes.

With polarization-dependent feedback restored for laser operation, it was found that the fundamental LP_{01} or doughnut-shaped LP_{11} modes could be selected by simply rotating the fast-axis of the λ/2 waveplate to different angles. When the orientation of fibre was adjusted properly, the operation on the LP_{01} mode was achieved by setting the fast-axis of λ/2 waveplate to be in horizontal direction (i.e. so that the polarization direction was parallel to the plane of Figure 7.13), where as the doughnut-shaped LP_{11} mode could be selected by adjusting the orientation of fast-axis of the λ/2 waveplate to be ~22.5° (i.e., so that polarization direction for the beam coupled to the fibre was at ~45° to the plane of Figure 7.13). It was evident that both modes had a similar characteristic of output power versus pump power as illustrated in Figure 7.15. Both modes reached threshold at a pump power of ~1.4W (absorbed) and their power increased linearly with pump power to an output power of 36 W at a lasing wavelength of ~1040 nm at the maximum available pump power (52 W absorbed). The corresponding slope efficiency with respect to absorbed pump power is ~74% and hence typical of that achieved with more conventional cladding-pumped Yb fibre lasers employing an external cavity for feedback. Additionally, the output beams of LP_{01} and doughnut-shaped LP_{11} modes demonstrated a linear polarization but with different orientations. The PER was measured to be ~8.7dB for the doughnut-shaped LP_{11} mode and to be ~10.5dB for

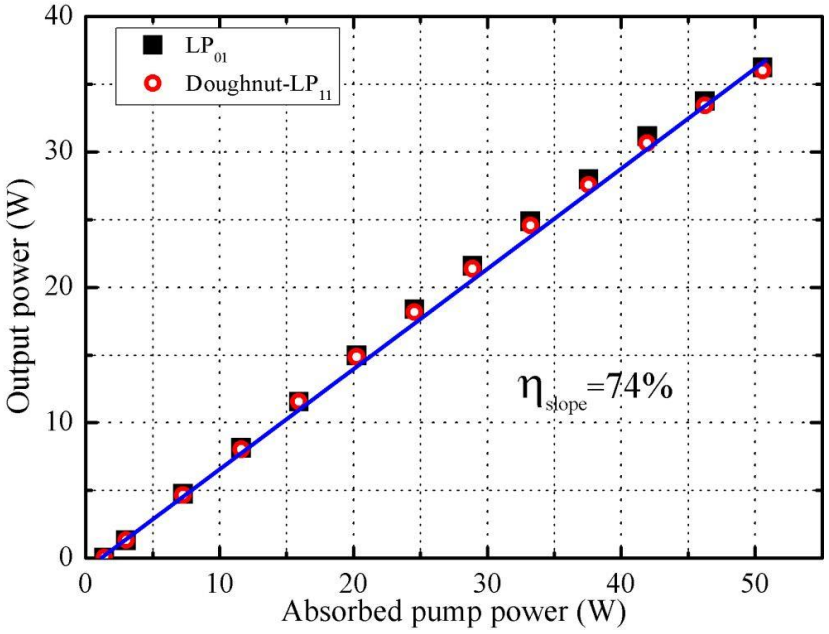

Figure 7.15 Output power for LP_{01} and doughnut-shaped LP_{11} modes as a function of absorbed pump power.

the fundamental LP_{01} mode.

Figure 7.16 (a) shows the output beam intensity profile for selective lasing on fundamental LP_{01} mode at the maximum output power of 36W. The M^2 was measured to be 1.35 suggesting that there was a small fraction of higher order mode content due to insufficient discrimination. Figure 7.16(b) and (c) show the intensity distributions for the doughnut-shaped LP_{11} mode measured at low output power (~1 W) and at the maximum output power of 36W, respectively. Both beams show a clear intensity null at the centre and have a pronounced doughnut shape. The fractional content of doughnut-shaped LP_{11} versus parasitic LP_{01} mode was estimated from the measured intensity profile to be ~57:1 corresponding to a mode purity of >98% confirming that the fundamental LP_{01} mode was successfully suppressed. Moreover, the M^2 was measured to be 2.1 over the full range of powers in close agreement with the theoretical value of 2 confirming the high quality of doughnut-shaped LP_{11} mode.

A Mach-Zehnder interferometer was built in order to investigate the phase-front shape of the doughnut-shaped LP_{11} mode. The output beam was interfered with a reference beam with a spherical wavefront and the resulting interference patterns (shown in Figure 7.17) exhibited a distinct spiral fringe pattern in the clockwise or anticlockwise direction, indicating that the excited doughnut-shaped mode had a phase singularity at the centre of beam. The handedness of the vortex beam could be switched from clockwise to anticlockwise (or vice versa) in a repeatable manner by slightly adjusting the angle ($<0.5^o$) of the plane high reflectivity mirror in the external feedback cavity or by deliberately bending the fibre as well. This vortex

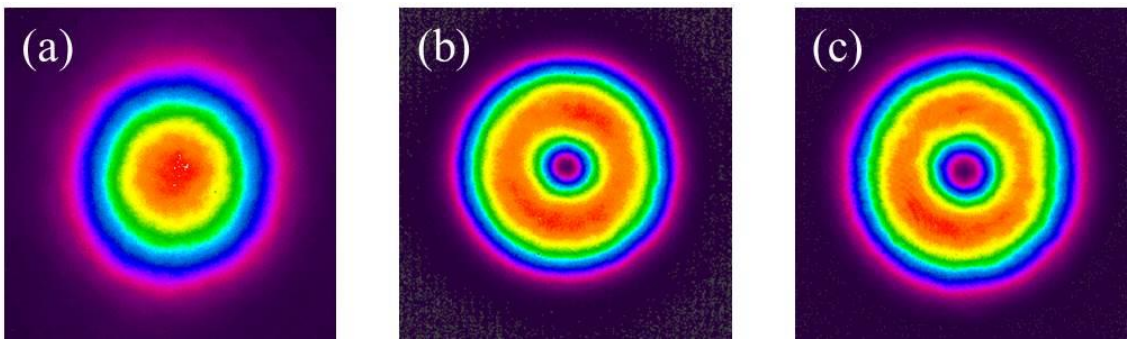

Figure 7.16 Experimental far-field intensity distributions: (a) the LP_{01} mode, (b) doughnut-shaped LP_{11} mode at P_{out}=1 W, and (d) the doughnut-shaped LP_{11} mode at P_{out}=36 W.

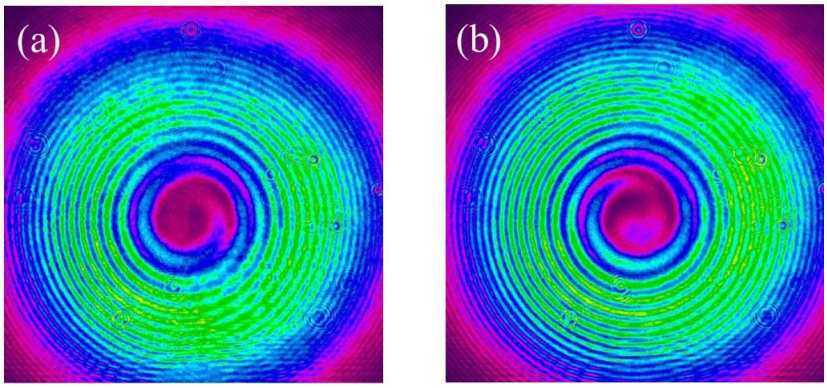

Figure 7.17 Interference patterns of doughnut-shaped LP_{11} modes after superposition with the reference beam with a spherical wavefront.

beam can be considered as a coherent superposition of LP_{11e} and LP_{11o} modes with the same polarization direction and $\pm\pi/2$ phase difference.

7.4.2 Polarization dependent loss measurement

To investigate the underlying mechanism for the polarization-dependent mode selection scheme (described above), we separately launched the LP_{01} and doughnut-shaped LP_{11} modes via a linear polarizer and a half-waveplate on a rotation stage into an unpumped 2-m length of the Yb fibre (i.e. corresponding to one round-trip of the laser resonator) and determined the Stokes parameters for the output polarization in each case and as a function of input polarization direction with the aid of a quarter-wave plate mounted on a rotation stage and a fixed linear polarizer in the manner described in [27]. The Stokes parameters were obtained by fitting the measured power of beam emerging from the fixed linear polarizer to the following formula:

$$P(\theta)=0.5\left\{\left(S_0+\frac{S_1}{2}\right)+\frac{S_1}{2}\cos(4\theta)+\frac{S_2}{2}\sin(4\theta)-S_3\sin(2\theta)\right\} \tag{7.3}$$

where θ is the rotation angle of fast-axis of the quarter-wave plate. The resulting Stokes parameters (S_0 to S_3) were then used to determine the orientation angle ψ and ellipticity angle χ of polarization ellipse for the LP_{01} and LP_{11} mode output beams as a function of the incident beam polarization direction. It should be noted that prior to these experiments, we confirmed, with the aid of a CCD camera, that the LP_{01} and doughnut-shaped LP_{11} mode profiles were preserved with very little

degradation after passage through the fibre confirming that the launch conditions were indeed optimised and that there was no evidence of mode-coupling.

Figure 7.18(a) shows the evolution of experimentally determined Stokes parameters of the output beams as a function of angular orientation of incident linear polarization on the Poincaré sphere. The red curve represents the Stokes parameters of LP_{01} mode and the blue one corresponds to those of doughnut-shaped LP_{11} mode. It is clear that the evolution of Stokes parameters for different modes follow different trajectories on the Poincaré sphere indicating that both modes become different polarization states after passing through the fibre despite having the same wavelength and incident polarization state. The evolution trajectories pass through the equator, north and south poles of Poincaré sphere, which means that the output polarization state could be either linear or elliptical with different handedness depending on the incident beam polarization state. The different evolution of polarization states indicate that there is a different effective birefringence for each mode. The results of most significance are shown in Figure

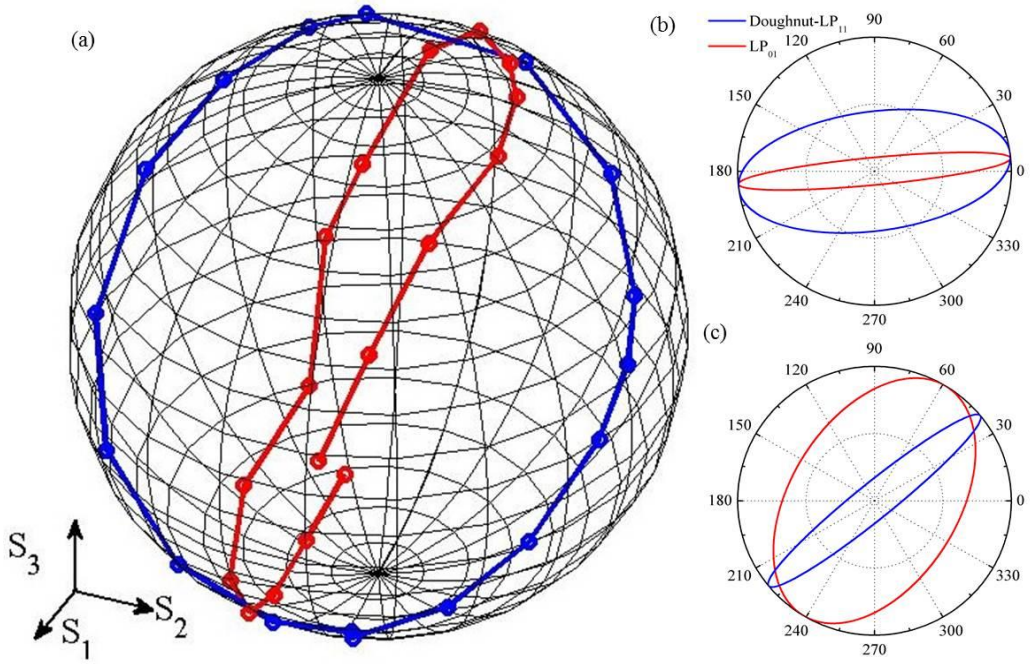

Figure 7.18 (a) Poincaré sphere representation of experimentally measured polarization state of output beams for different angular orientations of the linearly polarized incident LP_{01} mode (red circle line) and doughnut shaped LP_{11} mode (blue circle line); (b) and (c) the derived polarization ellipses of output for specific incident linear polarization orientation at 0° and 45°, respectively.

7.18(b) and (c), which depict the polarization ellipses for both modes when the orientation angles of incident linear polarization are 0°and 45°, respectively. When the incident linear polarization is set at 0°, the LP_{01} mode exits the fibre with nearly the minimum variation of polarization state with an ellipticity angle $\chi = 5.8°$ and orientation angle $\psi = 5.5°$ corresponding to a PER of 19.9 dB; while the PER for the doughnut-shaped LP_{11} mode is dramatically decreased to 7 dB with $\chi = -24°$ and $\psi = 7.7°$. The opposite situation occurs when the incident linear polarization is rotated to 45° (as shown in Figure 7.18(c)), where the doughnut-shaped LP_{11} mode had minimum variation of polarization state with a PER of 17.6 dB ($\chi = 7.6°$ and $\psi = 39.4°$), but LP_{01} mode's polarization becomes elliptical ($\chi = -31.6°$ and $\psi = 58.8°$) with a PER of 4.2 dB.

Figure 7.19 shows the calculated losses for both modes emerging from the Yb-doped fibre after passing through a linear polarizer based on the measured Stokes parameters. The linear polarizer transmission axis was always oriented to the same as the orientation angle of incident linear polarization to mimic the situation in the laser resonator. The red dot-line and blue-circle line in Figure 7.19 represent the loss of LP_{01} and doughnut-shaped LP_{11} modes as a function of orientation of

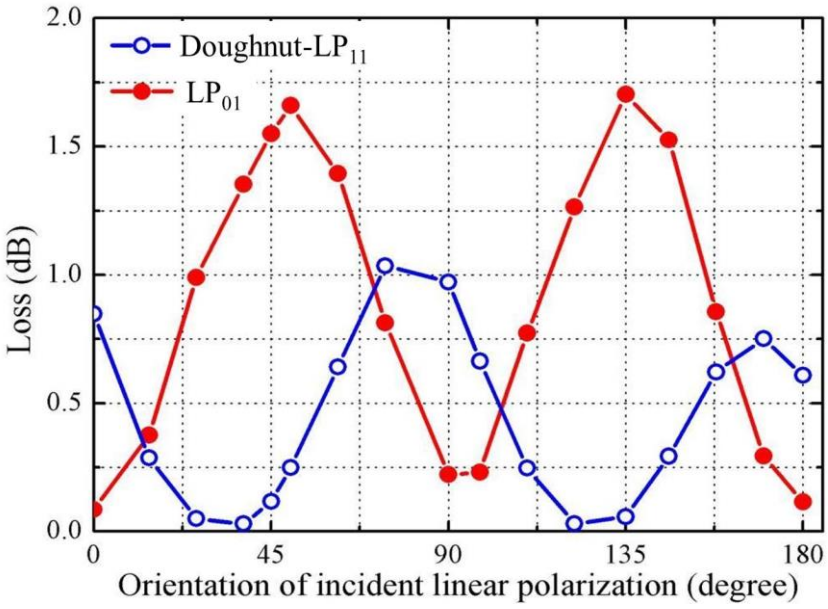

Figure 7.19 Derived loss of each mode emerging from the few-moded Yb-doped fibre after passing through a linear polarizer with the transmission axis aligned in the same orientation as the incident linear polarization.

incident linear polarization. Because both modes evolves to different polarization state after propagating through the fibre they generally experience different loss when passing through the linear polarizer. The minimum loss for LP_{01} mode occurs when the orientation of incident linear polarization is around ~0° or ~90°, which correspond to the maximum loss for the doughnut-shaped LP_{11} mode. However, the minimum loss for the doughnut-shaped LP_{11} mode occurs approximately ~45° or ~135° orientation of incident linear polarization, which correspond to the maximum loss for the LP_{01} mode. This result is in good agreement for our experimental observations for mode selection in the Yb fibre laser. It is also worth noting that that the maximum loss discrimination for lasing on the doughnut-shaped LP_{11} mode is ~1.7 dB and therefore somewhat higher than the loss discrimination (<1 dB) for lasing on the LP_{01} mode. This may explain the differences in modal purity observed for the laser. The different polarization evolutions observed for the LP_{01} and doughnut-shaped LP_{11} modes are consistent with a radial variation in birefringence in the fibre with a change in the average fast and slow axis directions by ~45° for the regions of the core that have a strong spatial overlap with the two modes. This could be due to stress distributions in the fibre resulting from the fabrication process. Normally, this birefringence is rather small. We tried to measure the birefringence by the standard method of spectral interferometry according to [28]. However, none of clear interference pattern was observed over the wavelength from 1200nm to 2000nm on the spectrum analyser indicating that the birefringence should be less than 1×10^{-5}. Note, it is difficult to avoid this small residual birefringence during the fibre fabrication process, and the value and direction of the fast axis of birefringence tend to be different for different fibres. However, the principle of polarization dependent transverse mode selection affords some clues to design special fibres that different modes have different birefringence, which needs further investigations in future.

7.5 Discussions

7.5.1 Numerical model for transverse mode competition

In few mode fibre lasers, it is usual to excite a few transverse modes simultaneously due to effects of mode coupling and transverse spatial hole burning in fibres. Several papers have analytically and numerically investigated transverse

mode competition in multimode fibres to better understand the conditions of fundamental mode selection [5, 29, 30]. The aim of this section is to discuss a numerical model to investigate transverse mode competition in end-pumped fibre lasers with emphasis on doughnut-shaped LP_{11} mode selection. This model is based on spatially-dependent rate equations in a two-level system. To simplify the model, ASE and polarization effects are ignored, and only a single operation wavelength is considered.

A typical linear cavity configuration as illustrated in Figure 7.20 is used in our model. The pump beam can be coupled into any fibre end facet. The fibre has a length of L, and the feedback mirrors at z=0 and z=L have reflectivities of R_1 and R_2, respectively.

In the steady-state case, the two-level spatial dependent rate equations can be written as [29, 30]:

$$\frac{n_2(r,\varphi,z)}{n_1(r,\varphi,z)}=\frac{\dfrac{[P_p^+(z)+P_p^-(z)]\sigma_{ap}\Gamma_p(r,\varphi)}{h\nu_p}+\sum_i\dfrac{[P_{si}^+(z)+P_{si}^-(z)]\sigma_{as}\Gamma_{si}(r,\varphi)}{h\nu_s}}{\dfrac{[P_p^+(z)+P_p^-(z)]\sigma_{ep}\Gamma_p(r,\varphi)}{h\nu_p}+\dfrac{1}{\tau}+\sum_i\dfrac{[P_{si}^+(z)+P_{si}^-(z)]\sigma_{es}\Gamma_{si}(r,\varphi)}{h\nu_s}} \tag{7.4}$$

$$\pm\frac{dP_p^{\pm}(z)}{dz}=\left\{\int_0^{2\pi}\int_0^{a}\left[\sigma_{ep}n_2(r,\varphi,z)-\sigma_{ap}n_1(r,\varphi,z)\right]\Gamma_p(r,\varphi)rdrd\varphi\right\}P_p^{\pm}(z) -\alpha_p P_p^{\pm}(z) \tag{7.5}$$

$$\pm\frac{dP_{si}^{\pm}(z)}{dz}=\left\{\int_0^{2\pi}\int_0^{a}\left[\sigma_{es}n_2(r,\varphi,z)-\sigma_{as}n_1(r,\varphi,z)\right]\Gamma_{si}(r,\varphi)rdrd\varphi\right\}P_{si}^{\pm}(z) -\alpha_{si}P_{si}^{\pm}(z) \tag{7.6}$$

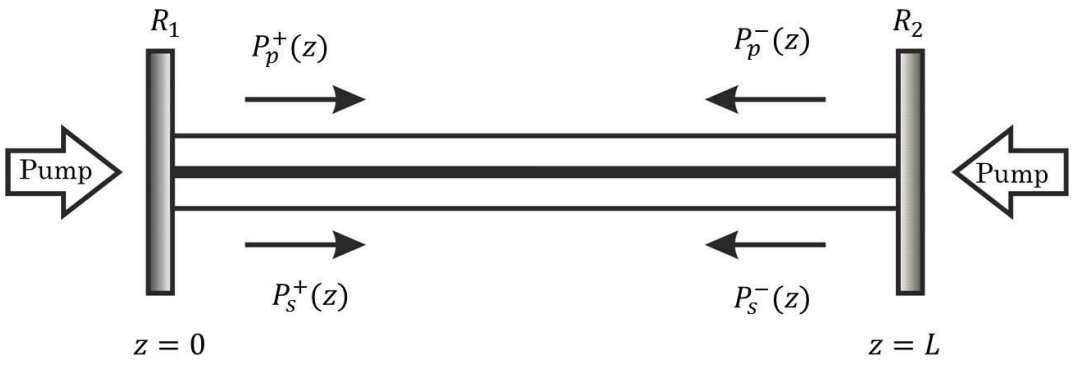

Figure 7.20 Schematic of typical fibre laser.

where $n_1(r,\varphi,z)$ and $n_2(r,\varphi,z)$ are the Yb ion density in the ground-level and upper-level as a function of spatial position, respectively. $n(r,\varphi,z) = n_1(r,\varphi,z) + n_2(r,\varphi,z)$ is the total Yb ion density, h is Planck constant; v_p and v_s are the pump and laser frequency; σ_{ap} (σ_{ep}) and σ_{as} (σ_{es})are the pump absorption (emission) and the signal absorption (emission) cross-sections of Yb ions, respectively; τ is the upper-state lifetime. $P_s^+(z)$ ($P_p^+(z)$) and $P_s^-(z)$ ($P_p^-(z)$) are the signal (pump) forward and backward powers, respectively; α_p and α_{si} are the loss factors for the pump and the ith signal mode. $\Gamma_p(r,\varphi)$ and $\Gamma_{si}(r,\varphi)$ are the spatial overlap factors for the pump and the ith signal mode which can be written as follows:

$$\Gamma_p(r,\varphi) = \frac{1}{A_{clad}}, \qquad \int_0^{2\pi}\int_0^{a} \Gamma_p(r,\varphi) r dr d\varphi = \frac{A_{core}}{A_{clad}} = \Gamma_p \tag{7.7}$$

$$\Gamma_{si}(r,\varphi) = \frac{I_i(r,\varphi)}{\int_0^{2\pi}\int_0^{\infty} r I_i(r,\varphi) dr d\varphi}, \qquad \int_0^{2\pi}\int_0^{a} \Gamma_{si}(r,\varphi) r dr d\varphi = \frac{P_i^{core}}{P_i^{core} + P_i^{clad}} = \Gamma_{si} \tag{7.8}$$

where A_{core} and A_{clad} are the areas of fibre core and inner cladding, respectively;. The pump power is assumed to be homogeneously distributed in the cladding. $I_i(r,\varphi)$ is the normalized intensity distribution of the ith signal mode which can be derived by solving the wave equation Eq. (7.1). Eq. (7.4) describes the population density in ground-level and upper-level as a function of pump and signal power. It contains the information about the small signal gain and the transverse spatial hole burning. Eqs. (7.5) and (7.6) express the evolution of the pump and signal power in the fibre, respectively.

As it is rather difficult to derive an analytically solution for the complicated differential equations written in Eqs.(7.4)-(7.6), we numerically solve these equations using self-compiled differential equation solver in Matlab. Since the intensity distribution of each transverse mode is cylindrically symmetric, the three dimensions can be equivalently simplified to two dimensions that is the propagation distance and the cross-section. Thus the fibre core-section is divided into a number of thin annular layers in which the population inversion and dopant concentration are considered to be constant. The details of this numerical algorithm can be referred to [29]. With the boundary conditions: $P_{si}^+(0) = R_1 P_{si}^-(0)$ and $P_{si}^-(L) = R_2 P_{si}^+(L)$, the set of rate equations can be solved. The parameters used in our numerical simulations are listed in Table 7.2.

Table 7.2 Parameters used in simulations

Parameter	Value	Parameter	Value
a_{core} (μm)	10	a_{clad} (μm)	62.5
NA	0.08	λ_s(nm)	1064
σ_{ap} (m^{-2})	2.6×10^{-24}	σ_{ep} (m^{-2})	2.6×10^{-24}
σ_{as} (m^{-2})	1×10^{-27}	σ_{es} (m^{-2})	1.6×10^{-25}
λ_p(nm)	976	τ (ms)	0.8
α_p (m^{-1})	0.002	L(m)	1
n_t (m^{-3})	5.54×10^{25}		

First, a 1m length of standard step-index circular-core Yb-doped fibre with 20μm core diameter and 125μm cladding was investigated in our model. The Yb-ion doping concentration is considered to be uniform within the fibre core. The fibre has a V-number of 4.6 at 1.064μm that can guide four LP modes, but only the two lowest-order LP modes (the LP_{01} and LP_{11} modes) are considered in our model as the other two higher-order modes are near to the cut-off, and thus the propagation loss can be much higher by just coiling the fibre with the appropriate diameter. The signal loss coefficient(α_s) including the propagation loss, diffraction loss and other losses introduced by intracavity optical elements is assumed to be $0.2m^{-1}$ and $0.3m^{-1}$ for the LP_{01} and LP_{11} modes, respectively. With these assumptions, we calculated the power distribution of each transverse mode as a function of pump power in a counter-propagation pumping configuration as illustrated in Figure 7.21. It can be seen that the fundamental LP_{01} mode reaches the threshold firstly due to its relatively lower loss. Further increasing the pump power saturates the centre part of population inversion leading to a higher gain for the LP_{11} mode which has an intensity null at the beam centre, and consequently the LP_{11} mode is excited. The output powers of both modes increase linearly with the increase of pump power. At 60 W pump power, it yields 39.8W of output power containing 16.5 W (41%) of the LP_{01} mode and 24.26 W (59%) of the LP_{11} mode respectively. The results show that

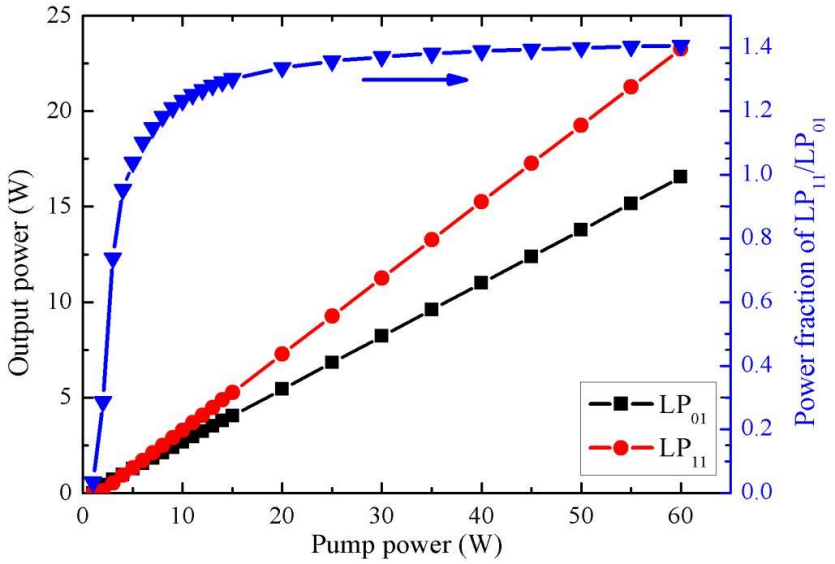

Figure 7.21 Power distribution of each transverse mode as a function of pump power.

the few-mode fibre is no longer operating on the single fundamental mode. In order to get a single transverse mode output (either fundamental mode or any other higher-order mode), the unwanted mode should be effectively suppressed.

As the objective of this chapter is to introduce alternative methods to generate the doughnut-shaped LP_{11} mode in fibre lasers, the first thing is to supress the unwanted fundamental LP_{01} mode. This can be achieved by introducing discriminative loss for each transverse mode as we discussed in section 7.4. In order to provide us with a guidance that how much differentiated loss is required, we calculated it by our numerical model. Figure 7.22 shows the relations of fraction of output power for the doughnut-shaped LP_{11} mode with respect to intracavity losses for both modes. At each fixed loss (α = 0.2, 0.4, and 0.6 m^{-1}) for the doughnut-shaped LP_{11} mode, slightly increasing the loss for the LP_{01} mode will dramatically increase the fraction of output power for the doughnut-shaped LP_{11} mode. It can be seen that the minimum loss for LP_{01} mode is 0.5 m^{-1}, 0.8m^{-1} and 0.9m^{-1} in order to completely suppress the LP_{01} mode in situations with varied intracavity losses for the doughnut-shaped LP_{11} mode.

Although the method of discriminative loss is an effective way to exclusively excite doughnut-shaped LP_{11} mode in fibre lasers, achieving higher loss for the fundamental mode while keeping small loss for the doughnut-shaped LP_{11} mode is rather challenging. Moreover, at relatively high pump power, the undepleted

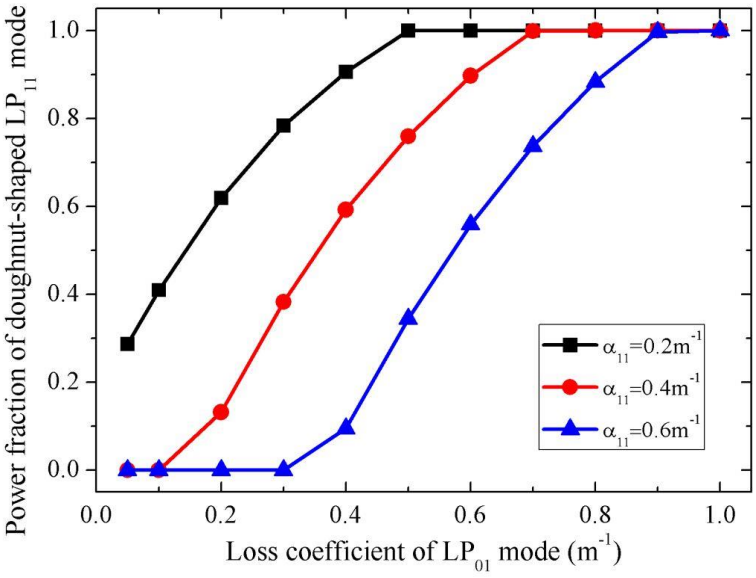

Figure 7.22 Output power fraction of doughnut-shaped LP_{11} as a function of loss for LP_{01} mode.

population inversion at the centre of the fibre core will lead to strong ASE or even parasitic oscillation and hence deteriorate the mode purity. Therefore, effective control of the gain distribution to favour the oscillation for the doughnut-shaped LP_{11} mode is more desirable. The fundamental LP_{01} mode selection in multi-mode fibres by spatially tailoring the radial dopant distribution has been investigated in several papers [5, 29]. Similarly, we simulated the selection of doughnut-shaped LP_{11} mode by tailoring the dopant distribution in a few-moded fibre.

The schematic of the dopant density distribution in a fibre core is illustrated in Figure 7.23(a), which has a ring shape described as:

$$n(r) = n_t \begin{cases} 1-\Delta & r < r_a \\ 1 & r > r_a \end{cases} \tag{7.9}$$

where Δ is the modulation depth of dopant density, r_a is the ring inner radius. Within the circle areas of $r<r_a$, the dopant density is dopped by Δ. We calculated the output powers of the doughnut-shaped LP_{11} mode with various dopant distributions in the few-mode fibre laser under 60 W of pump power. The results are shown in Figure 7.23(b). It can be seen that the output power for the doughnut-shaped LP_{11} mode and the mode purity are related to the modulation depth and modulation area. The maximum output power for the doughnut-shaped LP_{11} mode is achieved when Δ=1 and $r_a = 0.2r_{core}$. When the modulation depth is too small (i.e. Δ=0.25), LP_{01} mode cannot be completely suppressed. Furthermore, a smaller Δ

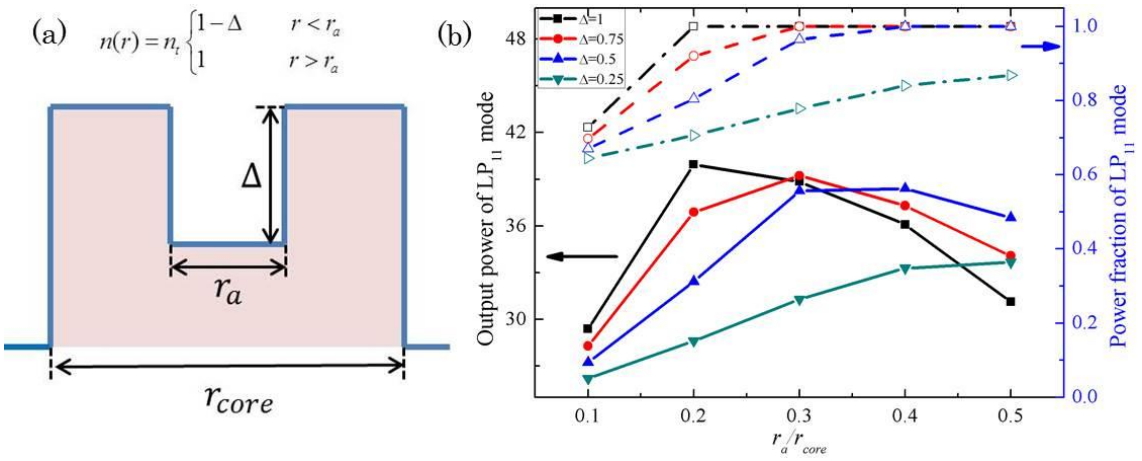

Figure 7.23 (a) Schematic of tailored dopant density distribution; (b) the absolute and percentage of output powers of doughnut-shaped LP_{11} mode in case of various dopant density distributions.

requires a larger modulation area to reach high mode purity at an expense of decreasing the output power due to the lower overlap of doughnut-shaped LP_{11} mode with the population inversion. Therefore, a high modulation depth is more desirable in order to efficiently excite the doughnut-shaped LP_{11} mode. This is just a simple simulation for us to have some clues that how the dopant distribution affects the mode selection for the doughnut-shaped LP_{11} mode in few mode fibre lasers.

7.5.2 Mode splitting

As has been demonstrated within this chapter, direct generation of a doughnut-shaped beam with either radial polarization or a vortex phase front in standard few-mode fibre lasers is achievable. However, due to the weakly guiding properties, the generated mode is nearly degenerate and thus mode coupling within the mode group is rather strong under any slight perturbations resulting in distorted output beam profiles with degradation in polarization state and distortion of phase front. The ability to maintain the propagation of the doughnut-shaped beam with unique polarization state and phase front requires the fibre can provide large mode splitting within the LP mode group, which is not achievable in standard few mode fibres.

Ramachandran and etc. [18, 31] demonstrated a solid ring core fibre that can propagate a radially polarized beam (TM_{01}) or a vortex beam over 1km length of

fibre. The underlying mechanism is to design an appropriate index profile to lift the difference of propagation constant for the vector modes within the LP_{11} mode group. It is well known that the propagation constant of a mode indicates its phase accumulation along the propagation distance within the fibre, and the phase shifts at the interface of index discontinuities are strongly dependent on the polarization state of the incident beam according to the Fresnel law. As the vector modes TE_{01}, TM_{01} and HE_{21} modes have different polarization states, it is possible to design an index-profile that substantially separates the propagation constant for these vector modes. For example, an index profile similar to the distribution of the electric field of the TM_{01} mode itself can substantially lift the difference of propagation constant for the LP_{11} group modes because of high electric field amplitude and gradient at the discontinuity index interface.

7.6 Conclusion

In this chapter, we have successfully demonstrated direct generation of high power doughnut-shaped mode with either a radial polarization or a helical phase front in Yb-doped fibre lasers.

We first experimentally investigated the propagation of a radially polarized beam in both few mode non-PM and PM fibres. When launching a radially polarized beam into both kinds of fibre, the radially polarized beam could be successfully produced on the opposite end of fibres under condition of deliberately manipulating the fibre including bending and applied pressure. Otherwise a distorted beam profile occurred due to severe mode coupling. In the PM fibre, the radially polarized output beam was actually a result of coherent superposition of $\hat{x}LP_{11e}$ and $\hat{y}LP_{11o}$ modes with exact zero phase shift on the fibre output facet. As a result, the polarization state was rather sensitive during the experiment. In contrast, the radial polarization state and doughnut-shaped beam profile could be maintained once appropriate perturbation was applied on the non-PM fibre in the lab environment.

We further demonstrated an alternative method for generating high power radially polarized beam in a few mode fibre laser. The S-waveplate described in Chapter 6 was employed to an Yb-doped fibre laser oscillator comprised a 1.5m length of non-PM Yb-doped few mode silica fibre and an external feedback cavity was used as an

intracavity polarization selection element to allow only radially polarized TM_{01} mode to be fed-back. With this arrangement, a maximum power of 32 W radially polarized beam was obtained with a slope efficiency of 66%. The doughnut-shaped mode purity was >89.5% and the polarization purity was >95%. To the best of our knowledge, this is the highest power and highest slope efficiency for the radially polarized fibre lasers to date.

Within the final section of this chapter, we have demonstrated a simple technique for selecting different transverse modes from a few mode Yb-doped fibre laser using an intracavity polarization filter to exploiting the difference in polarization behaviour believed to be due to different effective birefringence and orientation of the fast and slow axes for each mode. Using this approach we have successfully operated a cladding-pumped Yb-fibre laser on the doughnut-shaped LP_{11} mode with high mode purity (>97%) and controllable handedness of the helical phase front. A maximum power of 36W was obtained with a slope efficiency of 74%. To the best of our knowledge, this is the first demonstration of direct generation of optical vortices from a fibre laser oscillator.

Bibliography

1. D. J. Richardson, J. Nilsson, and W. A. Clarkson, "High power fiber lasers: current status and future perspectives," J. Opt. Soc. Am. B **27**, B63-B92 (2010).

2. D. Marcuse, "Influence of curvature on the losses of doubly clad fibers," Applied Optics **21**, 4208-4213 (1982).

3. J. P. Koplow, D. A. V. Kliner, and L. Goldberg, "Single-mode operation of a coiled multimode fiber amplifier," Optics Letters **25**, 442-444 (2000).

4. J. C. Knight, T. A. Birks, R. F. Cregan, P. S. Russell, and J. P. Sandro, "Large mode area photonic crystal fibre," Electronics Letters **34**, 1347-1348 (1998).

5. J. R. Marciante, "Gain filtering for single-spatial-mode operation of large-mode-area fiber amplifiers," IEEE. J. Sel. Top. Quant. **15**, 30-36 (2009).

6. D. G. Grier, "A revolution in optical manipulation," Nature **424**, 810-816 (2003).

7. G. Molina-Terriza, J. P. Torres, and L. Torner, "Twisted photons," Nature Physics **3**, 305-310 (2007).

8. J. Hamazaki, R. Morita, K. Chujo, Y. Kobayashi, S. Tanda, and T. Omatsu, "Optical-vortex laser ablation," Optics Express **18**, 2144-2151 (2010).

9. J. Bures, *Guided Optics: Optical Fiber and All-fiber Components* (WILEY-VCH, 2009).

10. R. J. Black and L. Gagnon, *Optical Waveguide Modes* (McGraw-Hill, 2010).

11. C. Jocher, C. Jauregui, M. Becker, M. Rothhardt, J. Limpert, and A. Tunnermann, "An all-fiber Raman laser for cylindrical vector beam generation," Laser Physics Letters **10**, 125108 (2013).

12. N. Andermahr, T. Theeg, and C. Fallnich, "Novel approach for polarization-sensitive measurements of transverse modes in few-mode optical fibers," Applied Physics B: Lasers amd OPptics **91**, 353-357 (2008).

13. R. J. Black, C. Veilleux, J. Bures, and J. Lapierre, "Radially Anisotropic Lightguide Mode Selector," Electronics Letters **21**, 987-989 (1985).

14. Y. Fujii, "Optical fibers with very fine layered dielectrics," Applied Optics **25**, 1061-1065 (1986).

15. F. K. Fatemi and G. Beadie, "Spatially-resolved Rayleigh scattering for analysis of vector mode propagation in few-mode fibers," Optics Express **23**, 3831-3840 (2015).

16. G. Volpe and D. Petrov, "Generation of cylindrical vector beams with few-mode fibers excited by Laguerre-Gaussian beams," Optics Communications **237**, 89-95 (2004).

17. C. Jocher, C. Jauregui, C. Voigtlander, F. Stutzki, S. Nolte, J. Limpert, and A. Tunnermann, "Fiber based polarization filter for radially and azimuthally polarized light," Optics Express **19**, 19582-19590 (2011).

18. S. Ramachandran, P. Kristensen, and M. F. Yan, "Generation and propagation of radially polarized beams in optical fibers," Optics Letters **34**, 2525-2527 (2009).

19. J. M. O. Daniel and W. A. Clarkson, "Rapid, electronically controllable transverse mode selection in a multimode fiber laser," Optics Express **21**, 29442-29448 (2013).

20. J. Li, K. Ueda, M. Musha, A. Shirakawa, and L. Zhong, "Generation of radially polarized mode in Yb fiber laser by using a dual conical prism," Optics Letters **31**, 2969-2971 (2005).

21. R. Zhou, B. Ibarra-Escamilla, J. W. Haus, P. E. Powers, and Q. Zhan, "Fiber laser generating switchable radially and azimuthally polarized beams with 140 mW output power at 1.6 μm wavelength," Applied Physics Letters **95**, 191111 (2009).

22. M. Fridman, G. Machavariani, N. Davidson, and A. A. Friesem, "Fiber lasers generating radially and azimuthally polarized light," Applied Physics Letters **93**, 191104 (2008).

23. D. Lin, K. Xia, J. Li, R. Li, K. Ueda, G. Li, and X. Li, "Efficient, high-power, and radially polarized fiber laser," Optics Letters **35**, 2290-2292 (2010).

24. M. B. Shemirani, W. Mao, R. A. Panicker, and J. M. Kahn, "Principal modes in graded-index multimode fiber in presence of spatial- and polarization-mode coupling," J. Lightwave Technol. **27**, 1248-1261 (2009).

25. M. Beresna, M. Gecevicius, P. G. Kazansky, and T. Gertus, "Radially polarized optical vortex converter created by femtosecond laser nanostructuring of glass," Applied Physics Letters **98**, 201101 (2011).

26. N. Andermahr and C. Fallnich, "Interaction of transverse modes in a single-frequency few-mode fiber amplifier caused by local gain saturation," Optics Express **16**, 8678-8684 (2008).

27. B. Schaefer, E. Collett, R. Smyth, D. Barrett, and B. Fraher, "Measuring the Stokes polarization parameters," American Journal of Physics **75**, 163 (2007).

28. S. C. Rashleigh, "Wavelength dependence of birefringence in highly birefringent fibers," Optics Letters **7**, 294-296 (1982).

29. M. L. Gong, Y. Y. Yuan, C. Li, P. Yan, H. T. Zhang, and S. Y. Liao, "Numerical modeling of transverse mode competition in strongly pumped multimode fiber lasers and amplifiers," Optics Express **15**, 3236-3246 (2007).

30. Z. Jiang and J. R. Marciante, "Impact of transverse spatial-hole burning on beam quality in large-mode-area Yb-doped fibers," J. Opt. Soc. Am. B **25**, 247-254 (2008).

31. S. Ramachandran and P. Kristensen, "Optical vortices in fiber," Nanophotonics, **2**, 455-474 (2013).

Chapter 8: Conclusion and future work

Laser beams characterized by a doughnut-shaped intensity profile due to phase or polarization singularities at the centre of beam have significant advantages over traditional Gaussian-shaped laser beam in a wide range of applications. The aim of this thesis was to develop simple, robust and low-cost techniques to directly generate doughnut-shaped beams in solid-state and fibre lasers. In this chapter, we will summarise the key results obtained throughout this thesis as well as providing insight into promising work for the future.

8.1 Conclusion

In chapter 2, the relevant background on doughnut-shaped beam generation was presented. It started with a general overview of diode end-pumped solid-state lasers that discussed laser diodes, gain materials and some key laser performance characteristics including threshold pump power and slope efficiency. The electric field expressions of the doughnut-shaped mode with a helical phase front or radial polarization state were derived by solving the scalar or vector Helmholtz equations in the cylindrical coordinates in the paraxial approximation, respectively. The most important properties including the OAM and tight focusing features of these beams were then discussed in detail. This was followed by a review of past work on the doughnut-shaped mode generation directly from solid-state lasers and a discussion on the applications of these beams.

Chapter 3 discussed the concept of using a ring-shaped pump beam in end-pumped solid-state lasers. The ring-shaped pump beam was obtained using a novel all fibre-based beam conditioning element based on a capillary silica fibre having 105 μm diameter of inner-hole and 200 μm diameter of annular silica guide which was tapered down to a solid core with a diameter of 105 μm and was then spliced to a fibre-coupled laser diode. First, analytical formulas for transverse temperature distribution, phase differences and resulted thermal lens focal length were derived in case of the ring-shaped pumping scheme. The averaged effective focal length for the TEM_{00} and LG_{01} modes were numerically estimated showing that the thermal lens strength is 47% and 31% weaker for the TEM_{00} and LG_{01} modes compared with the case of top-hat shaped pump beam, respectively. The degradation in beam quality for the TEM_{00} and LG_{01} modes in both ring-shaped and top-hat shaped

pump beam were numerically analysed as well showing less aberration in the former. The principles of transverse mode selection in the case of ring-shaped pump beam was then briefly discussed. The results indicate that different LG beams can be selected by tailoring the ring-shaped pump beam to optimise the spatial overlap for the desired transverse mode.

In chapter 4, the criteria for the fundamental TEM_{00} mode selection in the case of the ring-shaped pumping scheme was discussed in detail. The experimental proof-of-principle for this technique was implemented in an end-pumped Nd:YVO_4 laser oscillator with a Z-folded cavity architecture. The dioptric power of the thermal lens was measured to be ~0.17 D/W for a ring-shaped pumping scheme and be ~0.24 D/W for a traditional fibre-coupled laser diode with a quasi-top-hat profile, which was ~30% weaker than the latter. Meanwhile, the M^2 of the TEM_{00} mode passing through the end-pumped laser crystal was measured confirming less degradation in beam quality in the case of the ring-shaped pumping scheme. For the maximum available 31 W of the absorbed pump power, it yielded 14.2W of TEM_{00} mode with a slope efficiency of 53% and $M^2<1.1$ in case of the ring-shaped pump beam, a comparing 9.4 W of TEM_{00} mode with a slope efficiency of 57% obtained in case of traditional fibre-coupled laser diode. Such a pumping scheme would be a very attractive technique to reduce the thermal lensing effects and hence scale output power in end-pumped solid-state lasers.

Chapter 5 discussed the generation of a doughnut-shaped LG_{01} scalar mode with well-determined helical phase front and LG_{01} vector mode with radial polarization in end-pumped Nd:YAG lasers using the ring-shaped pumping scheme. The validity of the principle for doughnut-shaped LG_{01} mode selection discussed in chapter 3 was first verified using a plane-concave resonator from which 1.7 W non-polarized doughnut-shaped LG_{01} mode was achieved with a slope efficiency of 57% and $M^2=2.1$. An investigation of the mode composition was carried out by measuring the phase front and intensity profile for each longitudinal mode using a Mach-Zehnder interferometer together with an astigmatic mode-converter. The results showed that the doughnut-shaped output beam was always a 'hybrid' mode consisting of the TEM_{01} mode with orthogonal orientations and LG_{01} mode with opposite handedness of helical phase front at different frequencies, which could be attributed to inhomogenous axial gain within the crystal due to spatial hole

burning. A single-frequency Nd:YAG laser was employed to obtain the LG_{01} mode with a well-determined helical phase front.

Furthermore, by exploiting the fact that standing-wave intensity distribution for the LG_{01}^{+} and LG_{01}^{-} modes inside the laser resonator are different, a novel mode selection element consisting of two nanoscale thickness aluminium strips was developed to provide discrimination between the LG_{01}^{+} and LG_{01}^{-} modes. This scheme has been applied to a diode-pumped Nd:YAG laser to generate and switch between LG_{01} modes with opposite handedness at output powers ~1 W at 1064nm. Direct generation of radially polarized LG_{01} beam was presented in the final section. This was achieved in a particular plane-plane cavity design so that the spatial overlap of two orthogonal polarization modes with the ring-shaped pump beam were slightly different even when thermally induced bifocoussing was rather weak.

Chapter 6 investigated the extracavity conversion to radially polarized beam using an S-waveplate designed for use in the ~1μm or ~2μm wavelength band. In the ~1μm regime, both λ/2 and λ/4 S-waveplates were utilized. The λ/4 S-waveplate converted a circularly polarized LG_{01} optical vortex beam into radial polarization with total conversion efficiency of 86%, PER of 8dB and M^2=2.9, while the λ/2 S-waveplate converted a linearly polarized TEM_{00} mode to radial polarization with efficiency of 75%, PER of 14dB and M^2=2.7. The slightly lower PER for the λ/4 S-waveplate could be attributed to a resultant helical phase existing in the output beam. The main loss can be attributed to the Rayleigh scattering of nanogratings, which was estimated to ~7.6% and ~13.5% for the λ/4 and λ/2 S-waveplates, respectively. In addition, we demonstrated a highly efficient conversion to radial polarization in the 2μm band with wavelength tunable from 1950nm to 2100nm. The resultant radially polarized beam had a M^2 of 2.1 and a maximum PER of 17.5dB at 2050nm with a variation of less than 3dB from 1950nm to 2100nm. The total conversion efficiency was measured to be ~86%. This shows that the S-waveplate is a very effective radial polarization converter across a wide wavelength band.

Chapter 7 focused on directly generating doughnut-shaped beams in fibre lasers. We first investigated the propagation of radially polarized TM_{01} mode in both non-PM and PM few-moded passive fibres. In both cases, the intensity profile and polarization state of output beam were prone to be impacted by external perturbations including bending, twisting and applied stress. However, by

appropriately manipulating the fibre, when launching a radially polarized TM_{01} mode into both types of fibre, the desired doughnut-shaped TM_{01} mode could be obtained on the fibre exit facet in both cases. The results showed that the doughnut-shaped intensity profile is relatively more stable in PM fibres, while the polarization state is more stable in non-PM fibres. Then, the S-waveplate designed for 1 μm region was employed as an intracavity polarization selective element in an Yb-doped fibre laser to allow radially polarized TM_{01} mode to be excited. A maximum power of 32 W radially polarized beam was obtained with a slope efficiency of 66% and a polarization purity >95%. Furthermore, we exploited the difference in polarization behaviour of individual transverse modes believed to be due to different effective birefringence and orientation of fast and slow axes. Using this approach we have successfully demonstrated a cladding pumped Yb fibre laser generating the fundamental LP_{01} mode or the first higher-order doughnut-shaped LP_{11} mode with higher mode purity and controllable handedness of helical phase front. A maximum power of 36 W was obtained with a slope efficiency of 74% for both output beams.

8.2 Future work

The work undertaken in this thesis is only the beginning of the story, and it has paved the way for a number of potential interested research projects in future which will be discussed briefly in this section.

The numerical modelling and experiments undertaken in chapter 3 and chapter 4 have demonstrated that the adverse thermal lensing effects were much weaker in a ring-shaped pumping scheme compared with a traditional fibre coupled laser diode pumping scheme. As this pump beam re-shaping technique is rather simple, robust and low-cost, it is likely that may be used in any end-pumped laser configuration, in combination with other existing thermal mitigation techniques, to further scale the output powers to much higher levels (great than a hundred watts).

Chapter 5 mainly investigated the generation of doughnut-shaped LG_{01} optical vortex beam in solid-state lasers. The results of mode characterization show that an output beam with doughnut-shaped intensity pattern may not be indicative of the presence of a pure optical vortex. It indicates that the mode composition analysis is required when claiming an optical vortex beam generation in

experiments. With appropriate ratio of r_a/r_b for newly designed capillary fibres, the ring-shaped pump beam could be applied to generate very higher-order doughnut-shaped modes (LG_{0m}, e.g. m=10) which are favourable for applications such as laser micromachining due to a steeper intensity profile and optical manipulation due to increased OAM per photon. Breaking the degeneracy for the opposite handedness modes is still critical to allow the laser to oscillate on optical vortex beam with a well-determined helical phase front. For high-order LG_{0m} mode, the mode selection with two strips seems to be rather challenging. It becomes more sensitive to the optical alignment and environmental perturbations as the petal-like intensity distribution of the standing wave rotate $2m\pi$ every wavelength in propagation distance. However, it is still worth having a try to test the performance of this mode selection for high-order LG_{0m} optical vortex modes. For specific applications such as material processing, highly intense laser radiation is necessary to reach or exceed the ablation threshold. It is worth testing the power scaling capability of this mode selection technique especially in Q-switched operating mode as it is capable of offering nanosecond pulses with over hundred-kilowatts peak power which is very useful in material processing. Moreover, the damage threshold of the MSE should be investigated as the intracavity intensity is rather high during pulsed operation.

In chapter 6, we successfully demonstrated generation of a radially polarized beam in an external cavity by using S-waveplatess in both 1μm and 2μm regions. The Rayleigh scattering loss might lead to serious problems for its use at high power levels required for most application. It limits the total conversion efficiency. Moreover, the scattered light might be absorbed by the silica glass and be dissipated as heat. This might induce adverse thermal lensing effects that degrade the polarization purity and beam quality. Therefore, optimizing the fabrication of S-waveplate with low scattering loss is essential. As the scattering loss is due to nanograting structures, it might be reduced when the density of nanograting structure is lower. This would be easily achieved just by reducing the femtosecond writing resolution. However, the lower resolution of nanograting structure might have deleterious effect on polarization purity. Thus it might be a trade-off between low scattering loss and high polarization purity.

Chapter 7 investigated the direct generation of high power doughnut-shaped beam with either radial polarization or a helical phase front in an Yb-doped fibre laser.

The preliminary results showed the advantages of fibre lasers in high power continuous-wave operation. Higher output power would be achievable with higher pump power. However, before we further scale output powers to even higher levels, one fundamental issue that the strong mode coupling between the nearly degenerate modes should be addressed. This can be achieved by designing specific few-moded Yb-doped fibre with a ring-shaped doping profile and particular refractive index profile that the desired doughnut-shaped mode is favourable for exciting and the mode coupling is avoided due to highly lifted mode splitting. Fibre amplifier systems offer very flexibility on pulse repetition rate, pulse duration and shape. By employing the S-waveplate in fibre amplifier systems, it is able to simultaneously control the spatial, temporal and polarization properties of the output beam. With this method, doughnut shaped pulsed beams with a few nanosecond to hundreds nanosecond duration, hundred microjoules pulse energy and a few tens of kilowatts peak power is expected be achieved to benefit for particular light-matter interactions and hence improve the efficiency and processing quality during the material processing. As the pulse energy is limited by the energy storage in fibres, a new type of fibre capable of propagating vector modes with large effective mode area is really desirable for practice use

Appendix

List of Publications

Journal Papers

1. **Di Lin** and W. A. Clarkson, "Polarization-dependent transverse modes selection in an Yb-doped fiber laser," **Optics Letters** 40(4), 498 (2015).
2. **Di Lin**, J. M. O. Daniel, M. Gecevicius, M. Beresna, P. G. Kazansky, and W. A. Clarkson, "Cladding-pumped ytterbium-doped fiber laser with radially-polarized output," **Optics Letters** 39(18), 5359 (2014).
3. **Di Lin**, J. M. O. Daniel, W. A. Clarkson, "Controlling the handedness of directly excited-Laguerre-Gaussian modes in a solid-state laser," **Optics Letters** 39(13), 3903 (2014).
4. **Di Lin** and W. A. Clarkson, "Efficient TEM_{00} mode operation in a Nd:YVO_4 laser end pumped by a ring-shaped pump beam," **Optics Letters** (draft).

Conference Papers

1. W. A. Clarkson, **Di Lin**, Martynas Bersesna, Peter Kazansky, Peter Shardlow, "Cladding-pumped radially-polarized fibre laser," ASSL Adlershof-Berlin, 04-09 October, 2015. AW2A.4 (Invited).
2. **Di Lin**, P. Shardlow, M. Beresna, P. G. Kazansky, W. A. Clarkson, " Tm-doped fibre lase with radially-polarized output beam at 2μm," CLEO-Europe/IQEC 2015 Munich 21-15 June, 2015, CJ-P.10 WED (Poster).
3. A. C. Butler, R. Uren, **Di Lin**, J. R. Hayes, W. A. Clarkson, "Simple technique for high-order ring-mode selection within solid-state laser resonators," CLEO-Europe/IQEC 2015 Munich 21-15 June, 2015, CA-7.5 MON.
4. **Di Lin**, W. A. Clarkson, "Cladding-pumped Yb-doped fiber laser with vortex output beam," CLEO:2015 San Jose, 10-15 May 2015, STh4L.1.
5. **Di Lin**, P. Shardlow, A. Butler, M. Beresna, P. G. Kazansky, and W. A. Clarkson, "Generation of radially-polarized and azimuthally-polarized

beams in the two-micron band using a space-variant half-wave plate," SPIE Photonics West 2015 San Francisco 7-12 Feb 2015, 9342-38.

6. **Di Lin**, P. Shardlow, M. Beresna, P. G. Kazansky, and W. A. Clarkson, "Efficient conversion to radial polarization in the two-micron band using a continuously space-variant half-waveplate," 6th EPS-QEOD Europhoton Neuchatel, Switzerland 24-29 Aug 2014 WeD-T2-O-06.

7. **Di Lin**, J. Daniel, M. Gecevičius, M. Beresna, P. G. Kazansky, and W. A. Clarkson, "High power radially-polarized Yb-doped fiber laser," 6th EPS-QEOD Europhoton Conference Neuchatel, Switzerland 24-29 Aug 2014 ThA-T2-O-05.

8. **Di Lin**, J. M. O. Daniel, M. Gecevičius, M. Beresna, P. G. Kazansky, W. A. Clarkson, "Direct generation of radially-polarized output from an Yb-doped fiber laser," CLEO:2014 San Jose, 8-13 Jun 2014 JW2A.22 (Poster).

9. **Di Lin**, J. M. O. Daniel, W. A. Clarkson, "Controlling the handedness of directly excited Laguerre Gaussian modes in a solid-state laser," CLEO-Europe/IQEC 2013 Munich 12-16 May 2013 CA-10.2.

10. **Di Lin**, J. M. O. Daniel, W. A. Clarkson, "Single-frequency Nd:YAG laser with LG_{01} donut mode output," SPIE Photonics West 2013 San Francisco 1-6 Feb 2013, 8599-51.